ATOMIC STRUCTURE AND NON-ELECTRONIC PROPERTIES OF SEMICONDUCTORS

Distinctive features of the creation of radiation-induced defects in p-Si by photon-assisted low-dose ion implantation

M. Yu. Barabanenkov, A. V. Leonov, V. N. Mordkovich, and N. M. Omelyanovskaya

Institute of Microelectronics Technology and High Purity Materials, Russian Academy of Sciences, 142432 Chernogolovka, Russia

(Submitted February 13, 1998; accepted for publication October 8, 1998)
Fiz. Tekh. Poluprovodn. **33**, 897–899 (August 1999)

Deep-level transient spectroscopy (DLTS) was used to investigate how temperature and *in situ* photoexcitation affect the creation of radiation-induced defect complexes in *p*-Si during low-dose ion implantation. Samples of *p*-Si were simultaneously irradiated by Ar^+ ions accelerated to 150 keV in doses of 7×10^{10} cm^{-2} and photoexcited with ultraviolet light at temperatures of 300 and 600 K. It was found that nonradiative heating of the samples by the implanted ions increases the total concentration of defect complexes while simultaneously changing the nature of the dominant complex. In contrast, ultraviolet illumination of the semiconductor suppresses defect formation. It was observed that *in situ* photoexcitation has a progressively smaller effect on the formation of radiation-induced defect complexes as the target temperature increases. The dependence of the concentration of secondary defects created as the accelerated ions are incorporated into the *p*-Si on the UV illumination intensity is found to be nonmonotonic. The results obtained for *p*-Si were analyzed and compared with previously known data for *n*-Si. © *1999 American Institute of Physics.* [S1063-7826(99)00108-8]

1. INTRODUCTION

Erokhin et al.[1] and Danilin et al.[2] investigated the formation of defect complexes in Si when the latter was simultaneously implanted with ions and photoexcited by ultraviolet light via the semiconductor electronic subsystem. In these studies, the authors saw no features connected with the initial conductivity type of the silicon. It is likely that the lack of correlation between specific properties of *n*- and *p*-Si and the final state of the radiation-induced defects was due to the high implantation doses used in these studies, for which the concentration of electrically active radiation-induced defects was much higher than the concentration of doping impurities. Under these conditions, the electrical properties of the Si layer are no longer determined by the starting conductivity type of the semiconductor or its level of doping. The only time when this should not be so is the very last stage of implantation, during which the number of defects drops below the impurity concentration. In a previous paper we focused on this final stage and investigated how effectively *in situ* photoexcitation of *n*-Si can affect the behavior of semiconductor defects, in particular, point defects, at various temperatures.

In this paper we discuss the formation of simple defect complexes in *p*-Si implanted with a low dose of ions, in particular, those distinctive features associated with temperature and *in situ* photoexcitation of the semiconductor during implantation.

2. EXPERIMENTAL CONDITIONS

We irradiated *p*-Si films (KDB-20, ⟨100⟩) with Ar^+ ions at doses of $7\times10^{10}\,cm^{-2}$, using an ion current density of $1\ nA/cm^2$ and ion acceleration energies of 150 keV. During implantation, the *p*-Si targets were held at temperatures $T_i = 300$ and 600 K by preheating in a furnace (resistive heating). The *n*-Si samples were photoexcited by light from a high-pressure lamp. Optical power flux densities at the target surface were 4, 10, and $25\,mW/cm^2$.

Capacitance-voltage measurements made on control samples showed that the degree of compensation of the Si did not exceed 15% after ion implantation. The concentration of electrically active defects in $p-Si$, like the analogous case of $n-Si$ (Ref. 3), was considerably lower than the concentration of doping impurities.

The parameters of the deep levels created by radiation-induced defects were determined by deep-level transient spectroscopy (DLTS). In order to make these measurements, Schottky barriers were created by vacuum thermal sputtering of Au on the front side of the illuminated samples, while on the back side Ohmic contacts were made. The DLTS spectra were measured at a constant reverse bias of +2V and a level-filling pulse amplitude of -2V. The DLTS spectra, which we present later in the text, exhibit the following peaks: H_1 ($E_v+0.1$ eV), H_2 ($E_v+0.28$ eV), and H_3 ($E_v+0.38$ eV). Each of these peaks has been associated with the creation of a specific defect.[4–6] According to Ref. 4, the ''shallow'' hole trap H_1 is associated with Fe_i-B_S pairs. Peak H_2 is usually assigned to the complex $V+O+B$ (Ref. 5), where V is a

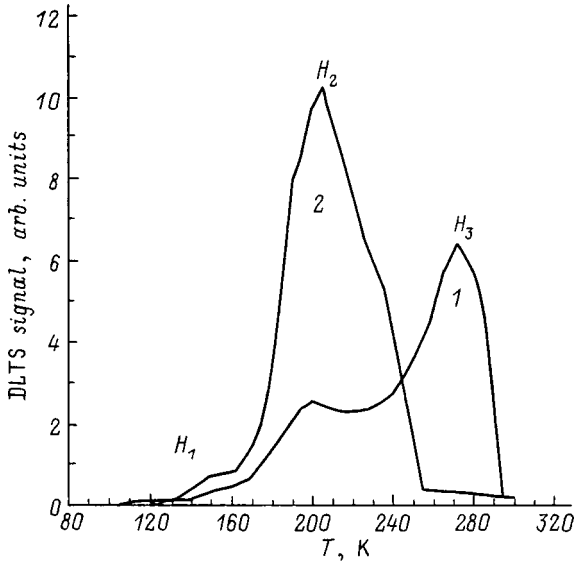

FIG. 1. DLTS spectra of *p*-Si samples implanted with Ar^+ ions at a dose of $7\times10^{10}\,cm^{-2}$ and energy 150 keV at T_i= 300 K (*1*) and 600 K (*2*).

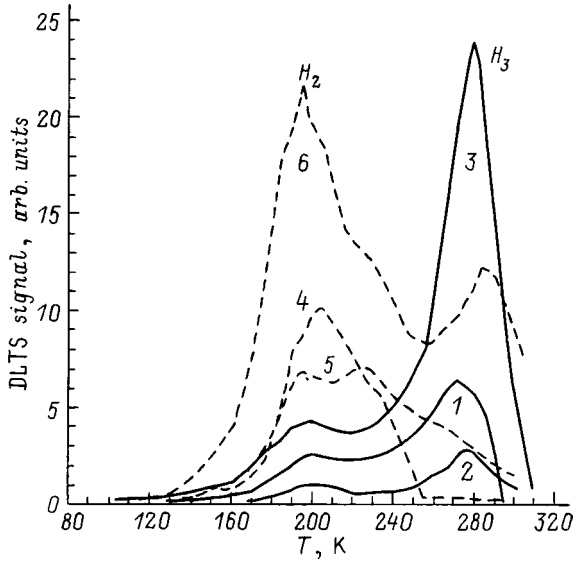

FIG. 2. DLTS spectra of *p*-Si samples implanted with Ar^+ ions at a dose of $7\times10^{10}\,cm^{-2}$ with energy 150 keV at temperatures T_i= 300 and 600 K (4–6). UV illumination power densities in mW/cm^2: *1, 4* — 0; *2* — 4; *3, 5* — 10; *6* — 25.

vacancy. Finally, peak H_3 corresponds to *K*-centers ($V+O+C$) or complexes ($C+V_2+O$), where V_2 is a divacancy.[6]

3. EXPERIMENTAL RESULTS AND DISCUSSION

Figure 1 shows how the DLTS spectra of $p-Si$ samples implanted with Ar^+ ions change when the silicon is heated from room temperature (curve *1*) to 600 K (curve *2*). It is clear from Fig. 1 that increasing the sample temperature T_i leads to replacement of H_3, the dominant peak in the DLTS spectrum, by H_2. This implies that *K*- centers (peak H_3) form more efficiently at room temperature.

As the temperature increases, it is primarily $V+O+B$ complexes (peak H_2) that form. In this case the total number of defects increases (the ratio of areas under curves *1* and *2* in Fig. 1 is ~ 1.3).

The effect of *in situ* photoexcitation of *p*-Si during implantation on the generation of radiation-induced defect complexes is shown in Fig. 2. It is clear from this figure that the effects of UV illumination and heating of the silicon during bombardment with Ar^+ ions are independent in a certain sense: whereas the target temperature determines which peak is highest (H_3 at 300 K and H_2 at 600 K), illumination scales the entire spectrum along the ordinate. In the latter case, increasing the illumination power density first suppresses the spectral amplitude (a scaling coefficient that is less than 1) and then amplifies it (a scaling coefficient greater than 1). In all cases the scaling coefficient is independent of the *p*-Si temperature. As we see from Fig. 2, curve *2* lies below curve *1*, while curve *3* lies above it. Curves *5* and *6* are located analogously relative to curve *4*.

Thus, photoexcitation of *p*-Si at low light intensities decreases the concentration of radiation-induced defect complexes.

The spectra shown in Fig. 2 allow us to estimate the effectiveness of UV light in generating defects during ion implantation of *p*- Si. In fact, let us consider curves *3* and *5* in Fig. 2, which correspond to the same photoexcitation conditions but different sample temperatures during the ion bombardment. The ratio of the areas under curves *3* and *1* is almost five times larger than the ratio of areas bounding curves *5* and *4*. This implies that the effectiveness of the illumination (at least in this case) in generating defects decreases markedly with increasing target temperature.

To complete this section, we emphasize our main results. First of all, resistive heating of *p*-Si to 600 K during ion implantation increases the concentration of secondary defects, while low-intensity UV illumination, conversely, suppresses their formation. Secondly, the effectiveness of *in situ* photoexcitation of *p*-Si in generating defect complexes decreases markedly with increasing semiconductor temperature. Thirdly, the change in the concentration of radiation-induced defects is nonmonotonic with increasing illumination intensity (in the range of optical power densities from 0 to $25\,mW/cm^2$).

4. CONCLUSIONS

In this paper we have investigated how resistive heating and *in situ* photoexcitation of the electron-hole subsystem affect the formation of the simple radiation-induced defect complexes in *p*-Si when the latter is implanted with low doses ($\sim10^{11}\,cm^{-2}$) of Ar^+ ions. Our primary results, which we summarized at the end of the previous section, reveal the following contrasting features of these phenomena in *p*-Si as compared to *n*-Si.[3]

1) Increasing the temperature and increasing the illumination (at low intensities) of the silicon during implantation are found to have opposite effects on complex formation in *n*- and *p*-type Si materials: whereas heating of *p*-Si samples and UV illumination of *n*-Si stimulate defect formation, UV illumination of *p*-Si and heating of *n*-Si suppress it. Moreover, in contrast to *n*-Si, increasing the temperature of *p*-Si

leads to changes in the relative heights of the various peaks in the DLTS spectra, so that one peak replaces another as the highest. In other words, in *p*-Si samples with the same initial content of primary radiation-induced defects, temperature determines which complex is formed most efficiently.

2) With increasing temperature, photoexcitation of silicon affects the formation of defect complexes more strongly for *n*-Si and less strongly for *p*-Si.

3) In *n*-Si, the concentration of all radiation-induced defect complexes depends monotonically on UV illumination intensity in the range of optical power densities from 0 to $25\,\mathrm{mW/cm^2}$, and eventually saturates, while in *p*-Si this dependence is nonmonotonic, decreasing at low light intensities and increasing at higher optical power densities.

This work was supported in part by the program ''Physics of Solid-State Nanostructures'' (Project 97-1062).

[1] Yu. N. Erokhin, A. G. Ital'yantsev, and V. N. Mordkovich, Pis'ma Zh. Tekh. Fiz. **14**, 835 (1988) [Sov. Tech. Phys. Lett. **14**, 372 (1988)].
[2] A. B. Danilin, Yu. N. Erokhin, V. N. Mordkovich, N. Hatzopoulos, and P. L. F. Hemment, Nucl. Instrum. Methods Phys. Res. B **69**, 268 (1992).
[3] M. Yu. Barabanenkov, A. V. Leonov, V. N. Mordkovich, and N. M. Omel'yanovskaya, Fiz. Tekh. Poluprovodn. **32**, 523 (1998) [Semiconductors **32**, 466 (1998)].
[4] L. C. Kimerling and J. L. Benton, Physica B **116**, 297 (1983); A. Kaniava, A. L. P. Rotondaro, J. Vanhellemont, U. Menczigar, and E. Gaubas, Appl. Phys. Lett. **67**, 3930 (1995).
[5] F. P. Anre and P. M. Mooney, J. Appl. Phys. **55**, 984 (1983).
[6] R. L. Wang, Y. S. Lin, G. E. Possin, J. Cerins, and J. Corbett, J. Appl. Phys. **54**, 3839 (1983).

Translated by Frank J. Crowne

Structure and properties of InGaAs layers grown by low-temperature molecular-beam epitaxy

M. D. Vilisova, I. V. Ivonin, L. G. Lavrentieva, S. V. Subach, and M. P. Yakubenya

Siberian Physicotechnical Institute at Tomsk State University, 634050, Tomsk, Russia

V. V. Preobrazhenskiĭ, M. A. Putyato, and B. R. Semyagin

Institute of Semiconductor Physics, Siberian Branch of the Russian Academy of Sciences, 630090 Novosibirsk, Russia

N. A. Bert, Yu. G. Musikhin, and V. V. Chaldyshev

A. F. Ioffe Physicotechnical Institute, Russian Academy of Sciences, 194021 St. Petersburg, Russia
(Submitted February 16, 1999; accepted for publication February 18, 1999)
Fiz. Tekh. Poluprovodn. **33**, 900–906 (August 1999)

This paper describes studies of InGaAs layers grown by molecular-beam epitaxy on InP (100) substrates at temperatures of 150−480 °C using various arsenic fluxes. It was found that lowering the epitaxy temperature leads to changes in the growth surface, trapping of excess arsenic, and an increased lattice parameter of the epitaxial layer. When these low-temperature (*LT*) grown samples are annealed, the lattice parameter relaxes and excess arsenic clusters form in the InGaAs matrix. For samples grown at 150 °C and annealed at 500 °C, the concentration of these clusters was $\sim 8\times 10^{16}\,\mathrm{cm}^{-3}$, with an average cluster size of ~5 nm. Assuming that all the excess arsenic is initially trapped in the form of antisite defects, the magnitude of the *LT*–grown InGaAs lattice parameter relaxation caused by annealing implies an excess arsenic concentration $(N_{\mathrm{As}}-N_{\mathrm{Ga}}-N_{\mathrm{In}})/(N_{\mathrm{As}}+N_{\mathrm{Ga}}+N_{\mathrm{In}})=0.4$ at.%. For layers of InGaAs grown at 150 °C, a high concentration of free electrons ($\sim 1\times 10^{18}\,\mathrm{cm}^{-3}$) is characteristic. Annealing such layers at 500 °C decreases the concentration of electrons to $\sim 1\times 10^{17}\,\mathrm{cm}^{-3}$. The results obtained here indicate that this change in the free-electron concentration correlates qualitatively with the change in excess arsenic concentration in the layers. © *1999 American Institute of Physics.* [S1063-7826(99)00208-2]

In recent years the growth of III–V layers by low-temperature molecular-beam epitaxy (MBE) has attracted considerable interest.[1–3] Layers of gallium arsenide grown at temperatures of 150−200 °C (the so-called *LT* GaAs) possess high structural perfection and interesting electrical and optical properties (high resistivity and short charge carrier lifetimes). Such materials can be used, for example, to make ultrafast photodetectors in the near-infrared region.[4] The desire to shift the sensitivity of these photodetectors to the wavelength range 1.5–1.7 μm, which is important from the practical point of view, has sparked interest in low-temperature epitaxial growth of InGaAs solid solutions, notably those that are lattice-matched to InP substrates.

The unique properties of *LT* GaAs arise from trapping of a large amount (up to 1.5 at.%) of excess arsenic during epitaxial growth, with subsequent redistribution of this material in the GaAs lattice after annealing with the formation of nanosized arsenic clusters.[1–3] More recently, investigations have shown that low-temperature growth of InGaAs solid solutions also results in a large excess of arsenic trapped in the crystal; however, the properties of *LT* InGaAs differ from those of *LT* GaAs.[5–8]

In this paper we discuss the effect of growth temperature and arsenic vapor pressure on the structure and electrical properties of InGaAs layers grown by low-temperature MBE.

EXPERIMENTAL PROCEDURE

Layers of InGaAs were grown in a two-chamber ''Katun'' MBE machine on substrates of semi-insulating InP with orientation (001). The fluxes of arsenic, gallium, and indium were set by the source temperatures. The In and Ga sources were calibrated prior to each cycle of growth experiments based on the period of oscillation of reflection high-energy electron diffraction (RHEED) patterns. Pre-epitaxial preparation of the substrates consisted of two stages: chemical processing (etching in a solution of $H_2SO_4 : H_2O_2 : H_2O$ with proportions 3:1:1) and driving off of the passivating oxide by heating of the substrate in the growth temperature immediately before epitaxy (the anneal temperature was 500 °C). The rate of growth of the films was $\approx 1\mu$m/h. The growth temperature T_g was varied from 150 to 480 °C and the arsenic vapor pressure P_{As_4} was varied from 1.3×10^{-6} to 1.1×10^{-5} Torr. Typical film thicknesses were $\sim 1\mu$m.

After deposition, the samples were removed from the chamber and cut into two parts. One part was studied immediately after growth (''as grown'' material), while the other

was studied after a ten-minute anneal in the growth chamber at a temperature of 500 °C and an arsenic pressure of 5.3×10^{-6} Torr.

For all the samples we used RHEE patterns to study the structure of surface layers *in situ*. The relief of the growth surface was studied by electron-microscopy, using the method of platinum-darkened angular replicas. The internal structure of the layers was studied by transmission electron microscopy (TEM) using a Philips EM420 machine operated with an accelerating voltage of 100 kV. The samples were studied in the planar geometry and in the cross-sectional geometry. In the first case, the samples were prepared by chemical etching in a solution of $HBr : K_2Cr_2O_7$ (1:1), in the second case by sputtering with 4-keV Ar^+ ions at glancing incidence. The structures were also studied by two-crystal x-ray diffractometry using CuK_α radiation and reflection (004). The electrical parameters were determined by measuring the electrical conductivity and Hall coefficient using the Van der Pauw method.

SURFACE INVESTIGATIONS

After a pre-growth anneal, the RHEED pattern at the surface of the InP substrates exhibited a well- defined superstructure (2×4)P, indicating the absence of any trace of oxide. This superstructure was preserved as the substrate was cooled to 480 °C. Further reduction of the substrate temperature led to changes in its surface structure. At $T_g \sim 200$ °C the surface remained atomically smooth, but with a (1×3) superstructure. At $T_g = 150$ °C this superstructure disappeared from the substrate surface.

When the InGaAs layers were grown at temperature $T_g \geqslant 300$ °C, the *in situ* RHEED patterns exhibited superstructure reflections, specular reflection, and Kikuchi lines, all of which were evidence of an atomically smooth crystallization front. For layers grown at $T_g \leqslant 200$ °C, no superstructure reflections were observed during the growth process, but specular reflection and Kikuchi lines were observed in the RHEED pattern for $P_{As_4} \leqslant 2.7 \times 10^{-6}$ Torr. This implies that although the ordered structure of the surface was washed out at the atomic level, the crystallization front was planar as a whole. As the As_4 pressure was increased to 5.3×10^{-6} Torr and higher, a diffuse background and point reflections appeared in RHEED patterns, whose intensity increased with time. It thus follows that the surface develops a macroprofile (i.e., regions of three-dimensional growth) which evolves during the growth.

Electron-microscopy studies of the growth surface of InGaAs layers agreed with the RHEED data. Layers grown at high (480 °C) temperature had planar uniform surfaces over the entire range of arsenic pressures investigated (Fig. 1a), whereas the profiles of surface layers grown at low temperatures depended on the arsenic vapor pressure. At $T_g = 150$ °C and $P_{As_4} = 1.3 \times 10^{-6}$ Torr the surface was microscopically rough, but without any macrodefects. Increasing the arsenic vapor pressure to 5.3×10^{-6} Torr led to the appearance of a sizable number $(2.5-3) \times 10^8$ cm^{-2} of large-scale funnel-shaped pits (with diameters of ≈500 nm) distributed individually or in groups (Fig. 1b). Additional increases in P_{As_4} did not result in any appreciable increase in the density of these pits. However, the isometrically shaped pits were now accompanied by pits (~20% of the total number) which were elongated along ⟨110⟩ and which were surrounded by outcroppings (Fig. 1c).

After annealing at 500 °C, the surface micromorphology of films grown at high temperatures was qualitatively unchanged. In contrast, at the surface of layers grown at low temperatures we see a characteristic streaking which is generated by a system of parallel depressions (grooves) as long as 150 nm (Fig. 1d).

INVESTIGATION OF INTERNAL STRUCTURE OF THE LAYERS

The rocking curves of all the samples exhibited two reflection peaks—one from the epitaxial layer of InGaAs solid solution and one from the InP substrate. The lattice parameter mismatch between the substrate and the layer $\Delta a/a = (a_{InGaAs} - a_{InP})/a_{InP}$ was $(3.5-4) \times 10^{-3}$ at $T_g = 200 - 480$ °C, and increased to $(5-6) \times 10^{-3}$ at $T_g = 150$ °C.

The dependence of the half-width of the diffraction peak Θ on growth temperature is shown in Fig. 2. At $T_g = 480$ °C the magnitude of Θ was 24–30 arc-seconds. Decreasing the growth temperature increased the magnitude of Θ (to 80–100 arc-seconds at $T_g = 150$ °C), i.e., the structural perfection was considerably degraded.

We found that varying the arsenic vapor pressure in the range $1.3 \times 10^{-6} - 1.1 \times 10^{-5}$ Torr did not affect the structural perfection of the layers significantly: at all arsenic pressures the quantity Θ was larger at low epitaxial temperature than it was at high temperature.

Post-growth annealing of the InGaAs layers in the MBE chamber had only a slight effect on their total structural perfection (Fig. 2), but caused large changes in their lattice constants. The change in the lattice parameter of the layers ($\Delta a = a_i - a_{ann}$) during annealing depended on the growth temperature (Fig. 3). We observed a minimum $\Delta a \approx 0$ at $T_g = 480$ °C, and a maximum $\Delta a \approx 3 \times 10^{-3}$ Å at $T_g = 150$ °C.

Electron-microscopy studies showed that the primary defects in the structure of the unannealed layers are dislocations inherited from the substrate. Figure 4 shows an electron-microscope image of a sample grown at 150 °C and annealed at 500 °C. The image shows contrast in the form of a mass of dark dots ~5 nm in size, with a density $\sim 8 \times 10^{16}$ cm^{-3}. In addition, light bands elongated along the direction ⟨110⟩ can be seen. Electron-microscopy studies of these samples in cross section show that the light bands are caused by the presence of grooves on the surface, while the dark dots are distributed throughout the volume of the epitaxial films. We conclude that the contrast in the form of dark dots arises primarily from arsenic clusters that form in the InGaAs matrix.

ELECTRICAL PROPERTIES

Measurements of the electrical properties showed that all the layers of InGaAs, both before and after annealing, have electronic-type conductivity and rather high concentrations

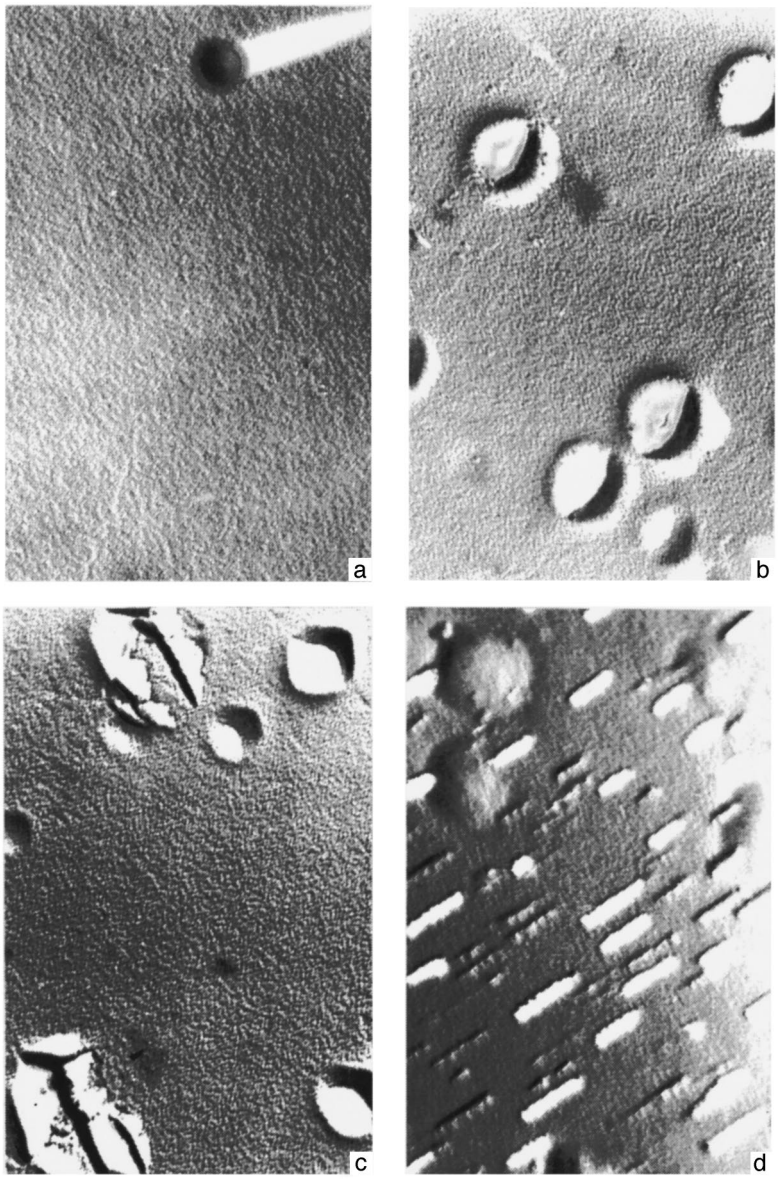

FIG. 1. Microphotographs of the surface of InGaAs layers (a — ×60 000, $T_g = 480\,^\circ\mathrm{C}$, $P_{\mathrm{As}_4} = 1.3\times10^{-6}$ Torr; b — ×20 000, $T_g = 150\,^\circ\mathrm{C}$, $P_{\mathrm{As}_4} = 5.3\times10^{-6}$ Torr; c — ×20 000, $T_g = 150\,^\circ\mathrm{C}$, $P_{\mathrm{As}_4} = 1.1\times10^{-5}$ Torr; d — ×60 000, $T_g = 150\,^\circ\mathrm{C}$, $P_{\mathrm{As}_4} = 1.1\times10^{-5}$ Torr, anneal).

of charge carriers, although the materials are undoped during deposition. Figure 5 shows how the concentration and mobility of electrons in the layers depend on the growth temperature (curves *1*). The electron concentration increases with decreasing growth temperature from $8\times10^{15}\,\mathrm{cm}^{-3}$ ($T_g = 480\,^\circ\mathrm{C}$) to $1\times10^{18}\,\mathrm{cm}^{-3}$ ($T_g = 150\,^\circ\mathrm{C}$), while the mobility decreases by roughly an order of magnitude. The arsenic vapor pressure during epitaxy has only a slight effect on the electron concentration in the layers (Fig. 6). It is nevertheless worth noting that the electron concentration increases with increasing P_{As_4} for epitaxy at low temperatures.

As shown in Fig. 6, annealing at 500 °C has only a slight effect on the electrical parameters of layers grown at high temperature, whereas for layers grown at 150 °C the carrier concentration is observed to decrease to $2\times10^{17}\,\mathrm{cm}^{-3}$ with a corresponding increase in mobility.

DISCUSSION OF THE RESULTS

From these data it follows that decreasing the epitaxy temperature changes the growth surface and structure of the

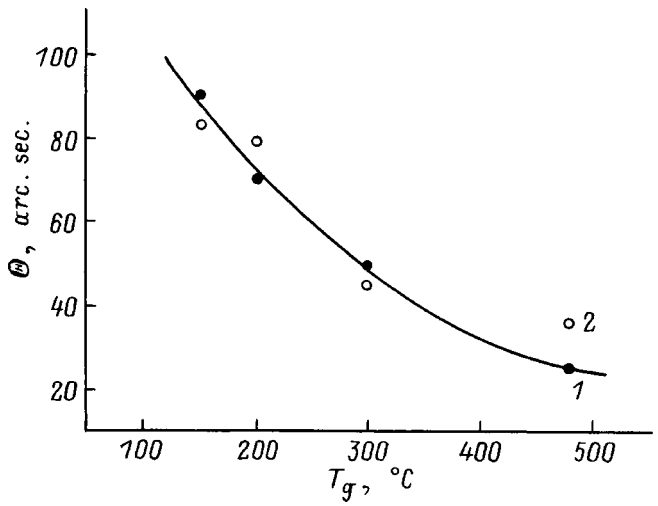

FIG. 2. Dependence of the half-width of the *x*-ray diffraction peak on growth temperature for layers before (*1*) and after (*2*) annealing at 500 °C.

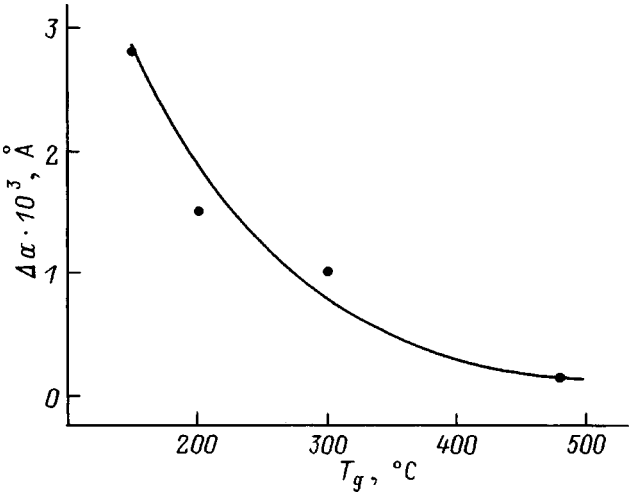

FIG. 3. Change in lattice parameter of layers after annealing as a function of growth temperature.

InGaAs layers. The growth front, which is atomically smooth at high temperatures, becomes atomically rough at $T_g < 473$ K. The defect content of the layer surfaces increases, and characteristic growth pits appear with submicron dimensions. The half-width of the x-ray diffraction peaks increases, which is evidence of an increase in the defectiveness of the layers. The mismatch of lattice parameters between the InGaAs layers and InP substrate increases. Annealing of layers grown at low temperatures leads to relaxation of the lattice parameter of epitaxial films and the appearance of a characteristic contrast on the electron-microscope images, which could be due to the formation of clusters in the volume of the epitaxial films. The conclusions regarding formation of As clusters in an InGaAs matrix are in agreement with the results of previous studies.[8]

It should be noted that phenomena similar to those described above were observed previously[3] for low-temperature epitaxy of GaAs layers. The increase in the GaAs lattice parameter during low-temperature epitaxy is usually associated with trapping of excess arsenic in the growing film in the form of point defects, whose concentrations reach $10^{20}\,\mathrm{cm}^{-3}$. The authors of Ref. 9 proposed that the dominant type of point defect is the antisite defect As_{Ga}, noting that the length of the $As_{Ga}-As_{As}$ bonds surrounding

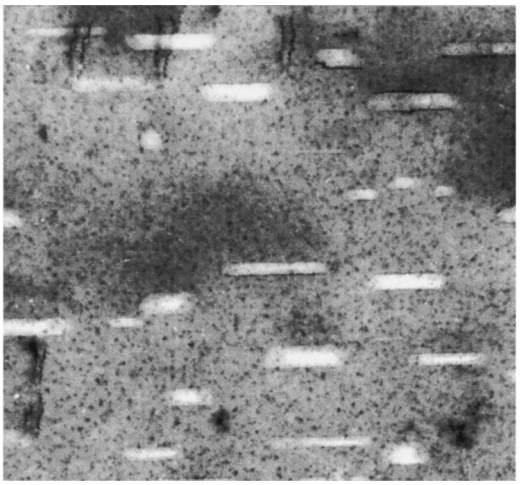

FIG. 4. Electron-microscope image of an InGaAs layer grown at 150 °C and annealed at 500 °C.

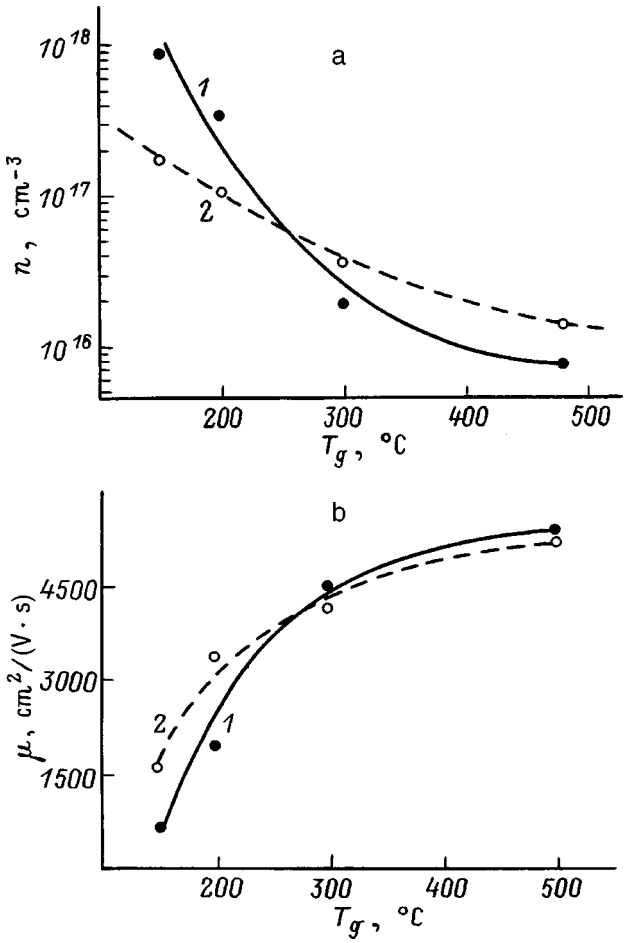

FIG. 5. Dependence of the electron concentration (a) and their mobility (b) on growth temperature for InGaAs layers before (*1*) and after (*2*) annealing at 500 °C.

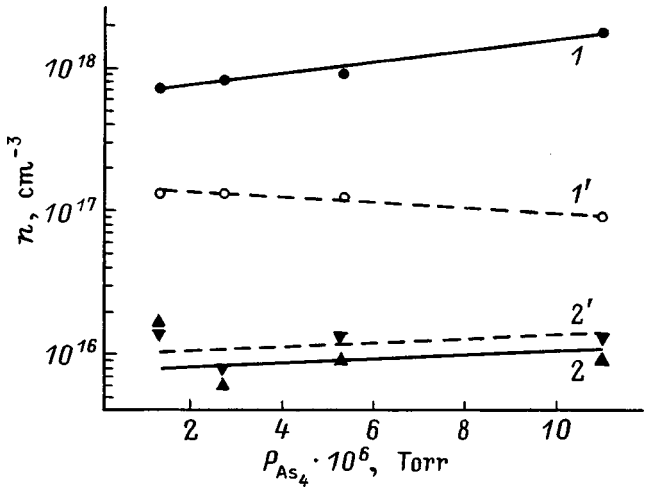

FIG. 6. Effect of As_4 vapor pressure during epitaxy on the electron concentration in InGaAs layers before (*1*, *2*) and after (*1′*, *2′*) annealing at 500 °C. Growth temperature, °C: *1*, *1′* — 150, *2*, *2′* — 480.

such a defect is ~ 8% larger than the normal Ga–As bond length in the GaAs lattice. During annealing of *LT* GaAs, the lattice parameter relaxes to a value close to that of the stoichiometric material, due to the formation of clusters of excess arsenic in the GaAs matrix.

Let us compare data for InGaAs and GaAs layers grown at 150 °C quantitatively. After annealing of a GaAs layer at 500 °C, the change in lattice parameter is 9×10^{-3} Å, which, according to the calibration of Ref. 9, corresponds to an excess arsenic concentration $(N_{As}-N_{Ga})/(N_{As}+N_{Ga})=0.6$ at.%. In doing such calculations for the solid solution InGaAs we must take into account that the lattice parameter of stoichiometric InGaAs is close to the lattice parameter of the InP substrate (5.869 Å), and that it is considerably larger than the GaAs lattice parameter (5.653 Å). If we use the fact that the As–As bond length for an antisite defect is the same in both materials, then the change in lattice parameter of the InGaAs layer as a result of annealing at 500 °C is 3×10^{-3} Å which corresponds to an excess arsenic content $(N_{As}-N_{Ga}-N_{In})/(N_{As}+N_{Ga}+N_{In})=0.4$ at.%. The concentration of antisite defects in this case comes to $\sim0.8\times10^{20}\,cm^{-3}$.

The high concentration of excess arsenic in InGaAs layers must lead to formation of clusters during the annealing process. Such clusters are probably the same ones we observe in TEM. A comparison of TEM images of InGaAs and GaAs layers grown and annealed at the same temperatures shows that the concentration and average size of the clusters is somewhat smaller in the first case, which agrees with the results of an analysis of x-ray diffraction data. It is well known that MBE growth of structurally perfect stoichiometric GaAs layers is usually done at a temperature of 580–600 °C, and for InGaAs layers at a temperature 480–500 °C. This implies that epitaxy at 150 °C entails a stronger departure from stoichiometric growth conditions for GaAs than for InGaAs. The amount of excess arsenic in InGaAs layers grown at 150 °C is close to the amount[3] that is characteristic of GaAs layers grown at 200 °C.

Over a very wide range, changing the arsenic flux for low-temperature MBE of InGaAs layers has only a slight effect on the concentration of excess arsenic. Similar weak dependences were observed previously[3,10] for low-temperature MBE of GaAs in the range of high V/III molecular flux ratios. Note, however, that the V/III molecular flux ratio turns out to have a marked effect on the generation of defects at the growth surface, and hence on the overall structural perfection of the epitaxial layer. For an optimum choice of this ratio no macrodefects are present at the growth surface, which ensures a rather high level of structural perfection of the resulting epitaxial layers, despite the low growth temperature of 150 °C and the high concentrations of excess arsenic.

It is worth noting that annealing of *LT* InGaAs leads not only to the formation of clusters in the bulk of the film, but also to the appearance of characteristic grooves at the surface of the annealed layers (see Fig. 1d and Fig. 4). These surface defects are probably connected with the formation of layer-like accumulations of arsenic near the surface.[8]

Thus, the MBE growth of InGaAs layers on InP substrates at low temperature leads to trapping of a large amount of excess arsenic in the epitaxial layers. Annealing of the material leads to the formation of As clusters in the InGaAs matrix. The trapping of excess arsenic and formation of clusters in InGaAs is qualitatively similar to what happens during low-temperature MBE of GaAs followed by annealing. However, the electronic properties of *LT* GaAs and *LT* InGaAs differ significantly. It is known[3,9,11] that unannealed *LT* GaAs has a resistivity of 10–1000 Ω·cm, and that after annealing at 500–600 °C it becomes semi-insulating. In contrast, *LT* InGaAs has a low resistivity due to the high $(10^{18}\,cm^{-3})$ concentration of free electrons. During annealing, the concentration of free charge carriers decreases; however, it remains extremely high $(10^{17}\,cm^{-3})$ as before. Such a high concentration of electrons cannot be connected with uncontrolled contamination of the sample by background impurities. Measurements of control samples grown at ordinary temperatures showed that the concentration of background impurities in our samples was only $\sim10^{15}\,cm^{-3}$.

It is usually assumed[12] that the electrical properties of *LT* GaAs are a consequence of the high concentration of antisite As_{Ga} defects, which create deep donor levels near the middle of the band gap. Analogously, we may assume that the reason for the high concentration of electrons in *LT* InGaAs is likewise the high concentration of antisite defects, but under conditions where they form rather shallow donor levels. During annealing, the excess arsenic forms clusters and the concentration of antisite defects decreases markedly. This correlates with our observation that the concentration of free electrons in InGaAs decreases after annealing (Figs. 5 and 6). The concentration of antisite defects also decreases with increasing epitaxy temperature. The decrease in concentration of free electrons with increasing T_g was also observed by us experimentally (Fig. 5). Thus, a model based on the electrical activity of antisite defect As_{Ga} will qualitatively describe the change in electrical properties of InGaAs layers as a function of growth temperature and during annealing. However, the reason for the substantial quantitative difference between the concentration of antisite defects $(0.8\times10^{20}\,cm^{-3})$ determined from x-ray diffraction data and the concentration of free electrons $(0.9\times10^{18}\,cm^{-3})$ measured by the Van der Pauw method remains unclear.

CONCLUSIONS

Our studies of InGaAs layers grown by molecular-beam epitaxy on InP (100) substrates at temperatures of 150–480 °C and various arsenic fluxes show that decreasing the epitaxy temperature leads to a change in the growth surface, to trapping of excess arsenic, and to an increase in the lattice parameter of the epitaxial layers. Annealing of samples grown at low temperature leads to relaxation of the lattice parameter and formation of arsenic clusters in the InGaAs host. For samples grown at 150 °C and annealed at 500 °C, the concentration of clusters amounts to $\sim8\times10^{16}\,cm^{-3}$, with an average size of ~5 nm. Assuming that the excess arsenic is primarily trapped in the form of antisite defects, from the values of the lattice parameter relaxation in *LT* InGaAs during annealing we can determine the concentration of excess arsenic, which turns out to be $(N_{As}-N_{Ga}$

$-N_{\mathrm{In}})/(N_{\mathrm{As}}+N_{\mathrm{Ga}}+N_{\mathrm{In}})=0.4$ at.%. The concentration of antisite defects in this case amounts to $\sim 0.8\times 10^{20}\,\mathrm{cm}^{-3}$. Changing the arsenic fluxes within certain ranges has only a slight effect on the concentration of excess arsenic; however, it affects the creation of defects at the growth surface and the structural perfection of the epitaxial layers.

Layers of InGaAs grown at 150 °C characteristically have a high concentration of free electrons ($\sim 1\times 10^{18}\,\mathrm{cm}^{-3}$). Annealing such layers at 500 °C leads to a decrease in the concentration of electrons to $\sim 1\times 10^{17}\,\mathrm{cm}^{-3}$. We have established that changes in the concentration of free electrons correlate qualitatively with the change in concentration of excess arsenic in the layers.

This work was carried out in the framework of the program ''Fullerenes and Atomic Clusters'' of the Russian Science Ministry, and with the support of the Russian Fund for Fundamental Research.

[1] M. Kaminska, Z. Liliental-Weber, E. R. Weber, T. George, J. B. Kortright, F. W. Smith, B.-J. Tsaur, and A. R. Calawa, Appl. Phys. Lett. **54**, 1881 (1989).
[2] Kin Man Ju, M. Kaminska, and Z. Liliental-Weber, J. Appl. Phys. **72**, 2850 (1992).
[3] N. A. Bert, A. I. Veĭnger, M. D. Vilisova, S. I. Goloshchapov, I. V. Ivonin, S. V. Kozyrev, A. E. Kunitsyn, L. G. Lavrent'eva, D. I. Lubyshev, V. V. Preobrazhenskiĭ, B. R. Semyagin, V. V. Tret'yakov, V. V. Chaldyshev, and M. P. Yakubenya, Fiz. Tverd. Tela (St. Petersburg) **35**, 2609 (1993) [Phys. Solid State **35**, 1289 (1993)].
[4] Y. J. Chin, S. B. Fleischer, D. Lasaosa, and J. Bowers, Appl. Phys. Lett. **71**, 2508 (1997).
[5] R. A. Metzger, A. S. Brown, W. E. Stanchina, M. Liu, R. G. Wilson, T. V. Kargodorian, L. G. McCray, and J. A. Henige, J. Cryst. Growth **111**, 445 (1991).
[6] H. Künzel, J. Böttcher, R. Gibis, and G. Urmann, Appl. Phys. Lett. **61**, 1347 (1992).
[7] R. A. Metzger, A. S. Brown, L. G. McCray, and J. A. Henige, J. Vac. Sci. Technol. B **11**, 798 (1993).
[8] N. D. Zakharov, Z. Liliental-Weber, W. Sweder, A. S. Brown, and R. A. Metzger, Appl. Phys. Lett. **63**, 2809 (1993).
[9] X. Liu, A. Prasad, J. Nishio, E. R. Weber, Z. Liliental-Weber, and W. Walukiewicz, Appl. Phys. Lett. **67**, 279 (1995).
[10] M. Luysberg, H. Sohn, A. Prasad, P. Specht, Z. Liliental-Weber, E. R. Weber, J. Gebauer, and R. Krause-Rehberg, J. Appl. Phys. **83**, 561 (1998).
[11] J. Betko, M. Morvic, J. Novak, A. Forster, and P. Kordos, Appl. Phys. Lett. **69**, 2563 (1996).
[12] X. Liu, A. Prasad, W. M. Chen, A. Kurpiewski, A. Stoschek, Z. Liliental-Weber, and E. R. Weber, Appl. Phys. Lett. **65**, 3002 (1994).

Translated by Frank J.Crowne

ELECTRONIC AND OPTICAL PROPERTIES OF SEMICONDUCTORS

Band-edge photoluminescence of heavily doped $In_xGa_{1-x}As_{1-y}P_y$ ($\lambda = 1.2\ \mu m$)

M. V. Karachevtseva, V. A. Strakhov, and N. G. Yaremenko

Institute of Radioengineering and Electronics, Russian Academy of Sciences, 141120 Fryazino, Russia
(Submitted November 30, 1998; accepted for publication January 20, 1999)
Fiz. Tekh. Poluprovodn. **33**, 907–912 (August 1999)

Band-edge photoluminescence spectra of heavily donor-doped samples of $In_xGa_{1-x}As_{1-y}P_y$ ($x=0.77$, $y=0.53$) were investigated in the temperature range (77–300) K. A theory of luminescence that takes into account fluctuations in the band-edge potentials due to nonuniform distribution of impurities is used to calculate temperature dependences of the positions and half- widths of peaks in these spectra. Good agreement is obtained between experimental and calculated curves. For heavily doped $In_xGa_{1-x}As_{1-y}P_y$ samples with either *p*- or *n*-type conductivity, the peak energy of the band-edge PL is observed to shift towards lower frequencies at low temperatures. This shift is accompanied by broadening of the spectra and a decrease in the photoluminescence intensity compared to the analogous parameters for the spectra of undoped material. Possible mechanisms for radiative recombination are analyzed. [S1063-7826(99)00308-7]

In the last two decades, $In_xGa_{1-x}As_{1-y}P_y$ solid solutions have been actively investigated and included in practical applications. $In_xGa_{1-x}As_{1-y}P_y$ heterostructures with optical response at wavelengths longer than 1 μm are widely used for making high-efficiency heterostructure lasers, light-emitting diodes, and photodetectors for fiber-optic communication lines. However, despite the great interest in this material, at this time there is almost no data on the electronic energy spectrum of heavily doped $In_xGa_{1-x}As_{1-y}P_y$, although many applications call for rather high concentrations of impurities.

It is known that heavily doped semiconductors exhibit fluctuations at the edges of the allowed energy bands, caused by a nonuniform distribution of impurities. These fluctuations lead to ''tailing'' of the density of states into the band gap.[1] Information about these fluctuation-induced ''band-tail'' states can be obtained by studying the spectrum of band-edge luminescence as a function of temperature and level of excitation. The mechanisms for interband radiative recombination in heavily doped semiconductors are considerably more complicated and peculiar than in pure or lightly doped semiconductors, where band-edge luminescence is determined only by recombination of free electrons and holes (*BB*-transitions), and where the spectral intensity energy maximum is close to the width of the band gap in magnitude and tracks the temperature dependence of the latter. In heavily doped semiconductors, these fluctuation-induced tails give rise to additional transitions connected with recombination of carriers localized in the band-tail states. The contribution of these quasi-interband recombination channels to the band-edge luminescence spectra increases with decreasing temperature, causing the maximum to shift to lower frequencies. In addition, its temperature dependence no longer reproduces the temperature dependence of the width of the band gap, and can be nonmonotonic in form. Fundamental expressions that relate the luminescence characteristics of a heavily doped semiconductor to the parameters of the band tails were derived in the theoretical paper.[2] This theory was successful in explaning qualitatively many of the peculiarities observed in studies of the emission spectra of various heavily doped semiconductors. However, quantitative comparisons of experimental results with this theory were as a rule unsuccessful. This was partially due to the incompleteness of initial information about the level of doping, compensation, concentration of nonequilibrium carriers, and other parameters, without whose knowledge a rigorous analysis is impossible. Moreover, in the majority of cases the complete emission spectra arises from several recombination channels, whose relative contributions are difficult to determine. It is worth noting that in several papers the authors were unable to obtain agreement with the theory not only at the quantitative but even at the qualitative level, and it was necessary for them to turn to other approaches and models of the energy spectra of electronic states in order to describe their experimental results.[3] Of all the treatments of the theory of luminescence in heavily doped semiconductors that we are familiar with, the one with the most convincing conceptual basis was given by Korolev and Sidorov,[4] who undertook a rather rigorous quantitative analysis of the photoluminescence spectra of heavily doped and heavily compensated GaAs. In contrast, studies of the properties of heavily doped multicomponent solid solutions of binary compounds, in particular, $In_xGa_{1-x}As_{1-y}P_y$, lag significantly behind their practical applications, as we have noted above. The number of papers containing a discussion of the luminescence from $In_xGa_{1-x}As_{1-y}P_y$ compounds with spectral components in the wavelength range $\lambda > 1\ \mu$m is extremely small. Moreover, the systems investigated in these papers were primarily

TABLE I.

Sample Parameters				
Sample No.	Conductivity Type	Doping Impurity	Impurity Concentration, 10^{17} cm^{-3}	γ, meV
1	*p*	Zn	20	29
2	*n*	Sn	7	19
3	*n*	···	~1	···

undoped or lightly doped layers, in which impurity fluctuations are insignificant, and their authors generally restricted the analysis to room-temperature studies, i.e., the temperature range of practical interest (see, e.g., Ref. 5). Such studies naturally miss the peculiarities in the luminescence connected with recombination of localized carriers, which should manifest themselves only at lower temperatures.

In this work we measure the band-edge photoluminescence spectra of heavily doped $In_xGa_{1-x}As_{1-y}P_y$ layers ($x=0.77$, $y=0.53$) of *p*- and *n*-type conductivity in the temperature range $T=$ 77–300 K, and analyze them within the framework of the luminescence theory of Ref. 2. The samples were grown by liquid-phase epitaxy on InP substrates, and were lattice-matched with InP. The composition of the solid solution was designed for an emission wavelength of 1.2 μm at room temperature, and the layer thicknesses were 5–7 μm. In order to obtain layers with *p*- and *n*-type conductivity, the layers were doped with zinc or tin, respectively, during the epitaxy process. The impurity concentration and degree of compensation were controlled by galvanomagnetic measurements. In all the samples the degree of compensation did not exceed 0.1.

We will discuss the results for three samples whose parameters are listed in Table I. Along with the doped samples 1 and 2, we measured spectra of nominally undoped sample 3 for comparison, whose conductivity was *n*-type. In $In_xGa_{1-x}As_{1-y}P_y$, as in the majority of direct-gap semiconductors with $m_e \gg m_h$, the strong-doping condition $Na^3>1$ can be satisfied in *n*-type material with a rather low donor concentration $N_d>10^{17}$ cm^{-3}, while for *p*-type material this condition is satisfied only at acceptor concentrations $N_a>10^{19}$ cm^{-3} (here m_e and m_h are the effective masses of electrons and holes, and N and a are the concentration and Bohr radius of an impurity). Thus, whereas the strong-doping condition is well satisfied by the donors in *n*-type sample 2, *p*-type sample 1 is only lightly doped with regard to acceptors. Moreover, residual donors, whose concentration is estimated to be $\sim 10^{17}$ cm^{-3}, make it heavily donor-doped despite its conductivity type. This so-called intermediate-doping case is the one most often encountered in practice.[2]

Luminescence was excited by a cw argon laser with a wavelength of 488 nm. The laser light was modulated by a mechanical chopper at a frequency of 1000 Hz and focused down to a spot on the sample with a diameter of ~ 200 μm. The sample was located in an optical cryostat, allowing us to vary the temperature from that of liquid nitrogen to room temperature. The excitation power density could be varied in the range $P=10-10^3$ W/cm^2. Spectral measurements were made using an MBR-23 monochromator. As a photodetector we used an FD-10G germanium photodiode. The process of measuring the spectra was automated by a KAMAK system and a computer.

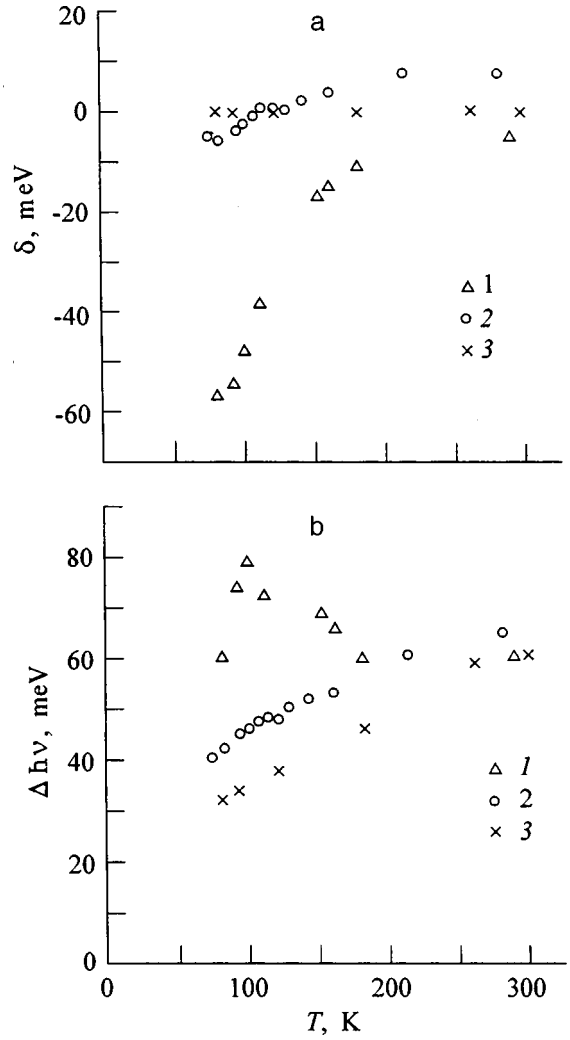

FIG. 1. Temperature dependences of the energy deficit at the peak of the PL spectral intensity δ (a) and the spectral half-width $\Delta h\nu$ (b) for $In_xGa_{1-x}As_{1-y}P_y$ samples. Samples: *1*—sample 1 (*p*-type), *2*—sample 2 (*n*-type), *3*—sample 3 (*n*-type, undoped).

Figure 1 shows the experimental temperature dependences of the magnitude of the energy deficit δ and half-width $\Delta h\nu$ of the band-edge PL spectrum for the samples under study. The concept of an energy deficit $\delta=h\nu_m-E_{g0}$ (i.e., the difference between the energy position of the spectral peak $h\nu_m$ and the band-gap width for undoped material E_{g0}) is usually introduced in order to track temperature-induced changes in the peak energy due only to the heavy doping, and to eliminate the temperature dependence of the width of the band gap. For $E_{g0}(T)$ we used the energy of the peak in the PL spectrum of the undoped sample 3. It is noteworthy that the width of the spectrum of this sample increases with increasing temperature almost linearly with a coefficient of 1.8, in accordance with the theory of interband recombination in lightly doped semiconductors, although the absolute values of the half-widths were 15 to 20 meV larger than predicted from this theory. At low tempera-

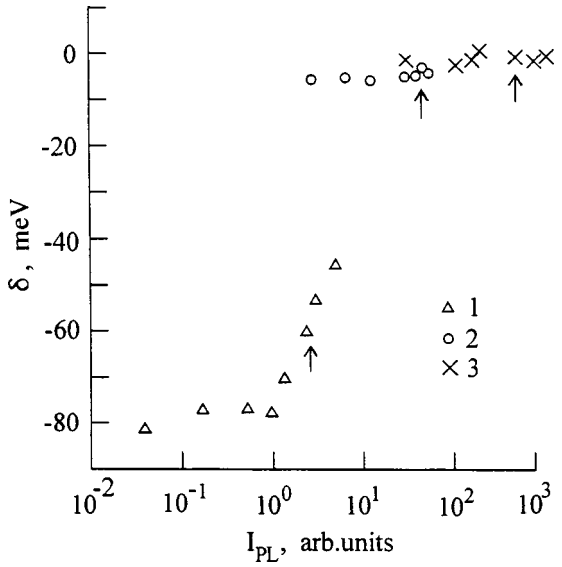

FIG. 2. Dependence of the energy deficit at the peak of the PL spectral intensity δ on the excitation intensity at $T=77$ K for $In_xGa_{1-x}As_{1-y}P_y$ samples. Samples: *1*—sample 1 (*p*-type), *2*—sample 2 (*n*-type), *3*—sample 3 (*n*-type, undoped). The arrows indicate points obtained at an excitation intensity of 500 W/cm^2.

tures, the band-edge PL spectrum of sample 1 (with *p*-type conductivity) is considerably broader than that of the undoped sample 3, and is shifted to lower frequencies. The absolute value of the deficit increases with decreasing temperature, and at nitrogen-temperatures is $\sim$ 60 meV; moreover, the sign of the deficit is negative in the entire range of temperatures investigated. A characteristic of this sample is the presence of a maximum in the temperature dependence of the peak half-width. In contrast, with regard to the magnitude of its deficit and half-width of its band-edge PL line, and the temperature dependences of these quantities, sample 2 (with *n*-type conductivity) does not differ much from the undoped sample 3. The values of δ did not exceed 10 meV, and change sign with increasing temperature.

Figure 2 shows how the energy deficit of the spectral peak depends on the level of excitation at liquid-nitrogen temperatures. The intensity of the excitation is expressed in terms of the PL intensity I_{PL}, whose changes reflect changes in the concentration of nonequilibrium carriers that recombine radiatively. Usually this is done in order to compare samples with different quantum efficiencies, since it eliminates the effect of nonradiative recombination mechanisms on the way the luminescence parameters depend on the excitation intensity. From the figure it is clear that for the samples with *n*-type conductivity (samples 2 and 3), changing the level of excitation over the full available range does not affect the position of the spectral peak; in contrast, sample 1, which is *p*-type, exhibits a shift in the position of the peak toward higher frequencies starting with a certain excitation density. The vertical arrows denote points that correspond to an excitation power density $P=500$ W/cm^2, at which temperature dependences of the PL spectra of all the samples were taken. This rather high level of excitation ensured that a reliable PL signal would be obtained in the entire temperature range up to room temperature. A comparison of samples at different levels of excitation showed that undoped sample 3 possessed the highest PL efficiency, compared to which the PL efficiency of sample 2 was lower by an order of magnitude, and that of sample 1 by almost two orders of magnitude.

Let us discuss the possible channels for recombination in these samples. The mean-square amplitudes of Gaussian fluctuations (γ) were estimated to be 29 and 19 meV for samples 1 and 2, respectively. These estimates were based on the expressions from Ref. 2, taking into account that the screening mechanisms in samples with *p*- and *n*-type conductivity are different. The condition $T \leqslant \gamma$, under which the effect of the fluctuation-induced tail on the luminescence properties can be analyzed, was satisfied for sample 1 over the full range of temperatures under study up to room temperature, while for sample 2 it was satisfied only at lower temperatures.

According to our estimates, the width of fluctuations in nondegenerate $In_xGa_{1-x}As_{1-y}P_y$ with *p*-type conductivity (sample 1) is sufficient to localize the nonequilibrium electrons not only at deep ''point'' fluctuations but also in Gaussian fluctuations with a characteristic amplitude γ. Localized electrons can recombine with holes located on individual acceptors (*TI*- transitions) and in deep states of the valence band tail (*TT*-transitions) as well as with free holes (*TB*-transitions). However, the *TI* mechanism presupposes the presence of a rather deep acceptor level with an ionization energy $I_a > \gamma$. The energy of the acceptor level caused by zinc in $In_xGa_{1-x}As_{1-y}P_y$ material with a composition optimized for the wavelength 1.2 μm comes to $\sim$ 30 meV (Ref. 6), i.e., the acceptor level merges with fluctuations of the valence band edge. Furthermore, it is difficult to believe that *TT* recombination has a strong effect on the spectral characteristics of sample 2, since *TT*- transitions, which involve diagonal tunneling of localized electrons and holes, can efficiently compete with *TB*-transitions only at very low temperatures and excitation levels, or under conditions of strong compensation when the value of γ is especially large.

In degenerate $In_xGa_{1-x}As_{1-y}P_y$ with *n*-type conductivity (sample 2), the emission in the neighborhood of the spectral peak at temperatures $T \leqslant 200$ K is determined by recombination of free electrons with energies near the Fermi level, i.e., deep in the free-carrier band. At the same time, holes, whose concentration is low and determined only by the level of excitation when $T \leqslant \gamma$, are located primarily in localized states of the valence band tail. Under these conditions, when $T \leqslant$ 200 K the primary contribution to the emission should come from *BT*- transitions. The negative sign of δ at low temperatures indicates that the decrease in the transition energy caused by fluctuations exceeds the shift of the Fermi level into the conduction band (the Burstein–Moss shift). With increasing temperature, the fraction of localized holes decreases, and the role of *BB*-transitions increases, changing the sign of δ to positive.

Hence, in order to describe the experimental results we begin with the fact that within our range of temperature and excitation density the *TB* and *BT* recombination mechanisms must play the primary role in generating band-edge PL for samples 1 and 2, respectively. We calculated the spectra

for these mechanisms by using the approach and expressions from the theory of luminescence of heavily doped semiconductors given in Ref. 2. However, in their theory these authors focused primarily on the temperature dependence of the peak energy of the spectral intensity, and unfortunately did not discuss the other important parameter of the spectrum—the half-width of the line. Moreover, the functions $h\nu_m(T)$ obtained in Ref. 2 are correct only over limited temperature ranges, where it was possible to represent them in analytic form. This hinders comparison of the experimental results with theory. Therefore, we addressed the problem of calculating the spectral intensities for *TB*- and *BT*-transitions, and obtained continuous temperature dependences of the peak energy and half-width of the spectra over the entire range of temperature studied. These calculations are of interest because they can be used both to explain the PL spectra of the $In_xGa_{1-x}As_{1-y}P_y$ samples and to obtain more complete information about the influence of impurity fluctuations on the luminescence properties of other heavily doped semiconductors, in particular, information about the *TB*-recombination mechanism, which is the least studied mechanism of all, both experimentally and theoretically. Although the authors of Ref. 7 derived an expression for the spectral intensity of the emission due to *TB*-recombination, they did not analyze its temperature dependence, although they did note that this mechanism can be decisive in nondegenerate, heavily doped, *p*-type semiconductors.

The spectral intensity of the emission was calculated from the expression

$$I(h\nu)=h\nu\int_{\max[(E_{g0}-h\nu),0]}^{\infty}W(E_e,E_h)\rho_c(E_e)q_e(E_e)\times\rho_v(E_h)q_h(E_h)dE,$$

where $h\nu=|E_e-E_h|$; $W(E_e,E_h)$ is the probability of radiative recombination of an electron with energy E_e and a hole with energy E_h; $\rho_c(E_e)$ and $\rho_v(E_h)$ are densities of states for electrons and holes, respectively; and $q_e(E_e)$ and $q_h(E_h)$ are the occupation functions for these states. The integration is carried out over minority-carrier energy. The energies for the *TB*- and *BT*-recombination mechanisms were measured from the bottom of the conduction band E_c and the top of the valence band E_v, respectively, with a plus sign for localized states in the band gap and free carriers in the allowed bands. The upper limit of integration for each frequency was identified as the point where the function being integrated decreased by a factor of 10^{-3}. In this case, for all the samples the interval of integration did not exceed 6γ over the entire spectral range. The spectra were calculated by numerical integration, allowing us to obtain continuous temperature dependences of the spectral parameters over the entire temperature range, and to make quantitative comparisons with experiment.

Following Ref. 2, we treated the distributions of free electrons and holes, and also localized electrons, as quasiequilibrium distributions, i.e., we modeled them as Fermi functions. However, we used a more rigorous expression to calculate the Fermi energy in degenerate *n*-$In_xGa_{1-x}As_{1-y}P_y$, with corrections to take into account

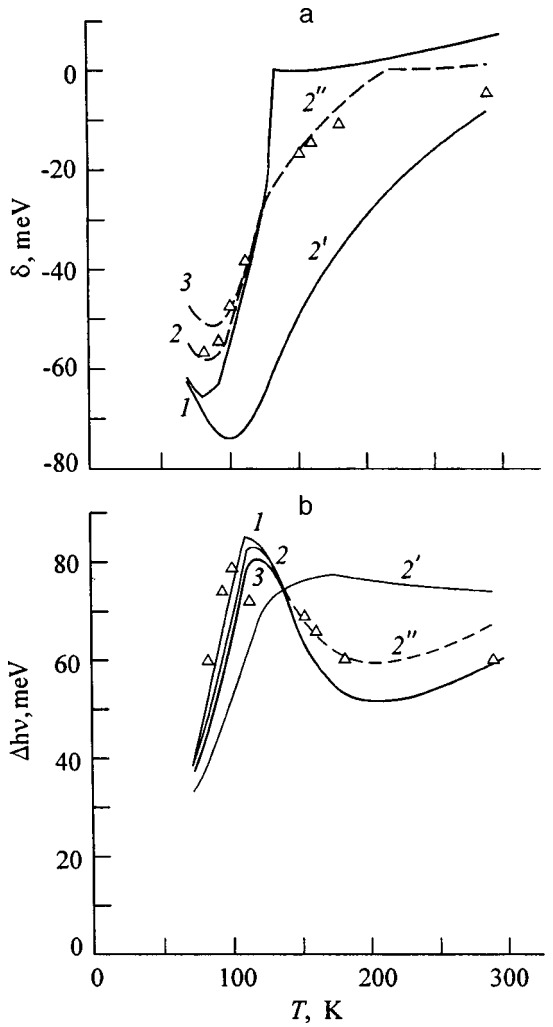

FIG. 3. Computed temperature dependences of the energy deficit at the peak of the PL spectral intensity δ (a) and half-width of the spectrum $\Delta h\nu$ (b) for *TB*-recombination in *p*-type $In_xGa_{1-x}As_{1-y}P_y$ with $N_a=2\times10^{18}$ cm^{-3} and concentrations of nonequilibrium electrons $\Delta n=1\times10^{11}$ (*1*), 5×10^{11} (*2*,*2′*,*2″*), and 2×10^{12} cm^{-3} (*3*). *2′*—calculations without including the dependence of the recombination probability *W* on energy; *2″*—calculations in which we assume $W=$ const for $E_e<\gamma$ and $W=W(E_e,E_h)$ for $E_e>\gamma$. The points are experiment for sample 1.

electron- electron and electron-impurity interactions.[1] Without these corrections, we were unable to obtain quantitative agreement with experiment. For holes localized in states of the band tail, we included the nonequilibrium character of the distribution. For the band-tail densities of states we used expressions that were correct in the range of shallow and Gaussian fluctuations and expressions that were correct in the range of deeper point-like fluctuations. At the boundary between these ranges the expressions were fitted together by choosing a pre-exponential factor. We assumed that the densities of states in the free-carrier bands followed the usual square-root functions. In order to describe the energy dependence of the recombination probability, we used the interpolation expressions from Ref. 7.

Our calculations started with prespecified concentrations of free carriers $n=n_0+\Delta n$, $p=p_0+\Delta p$. Because all the samples were weakly compensated, the concentrations of majority carriers (n_0, p_0) were set equal to the impurity

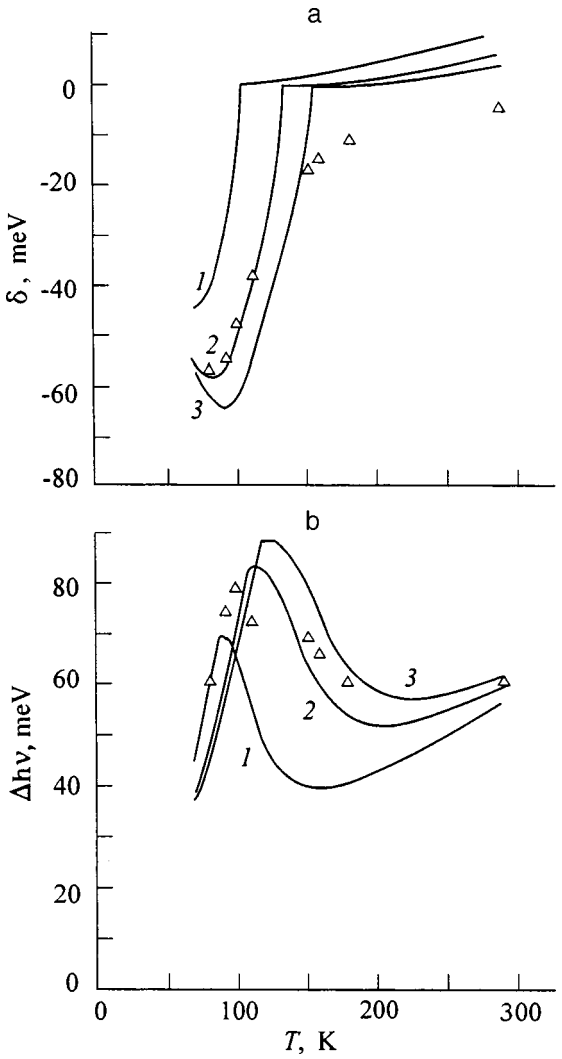

FIG. 4. Calculated temperature dependences of the energy deficit at the peak of the PL spectral intensity δ (a) and half-width of the spectrum $\Delta h\nu$ (b) for *TB*-recombination in *p*-type $In_xGa_{1-x}As_{1-y}P_y$ for $\Delta n = 5\times10^{11}\,cm^{-3}$ and values of N_a, $10^{18}\,cm^{-3}$: *1*—1, *2*—2, *3*—3. The points are experiment for sample 1.

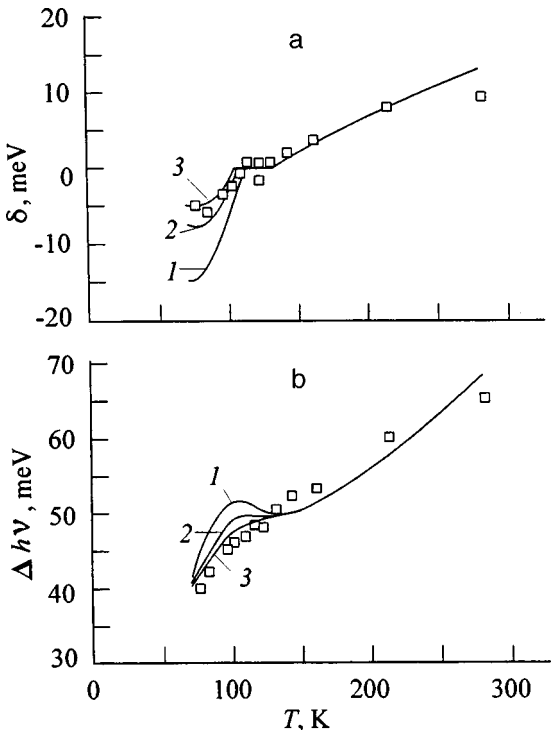

FIG. 5. Calculated temperature dependences of the energy deficit at the peak of the PL spectral intensity δ (a) and half-width of the spectrum $\Delta h\nu$ (b) for *BT*-recombination in *n*-type $In_xGa_{1-x}As_{1-y}P_y$ with $N_d = 7\times10^{17}\,cm^{-3}$ for various values of the parameter θ: *1* — 1×10^{-3}, *2* — 1×10^{-1}, *3* — 2×10^{-1}. The points are from experiment using sample 2.

concentrations. According to our estimates, at the excitation levels we used the concentrations of nonequilibrium carriers Δn, Δp did not exceed $1\times10^{15}\,cm^{-3}$. Consequently, $\Delta n, \Delta p \ll n_0, p_0$, and we could assume that $n = n_0$, $p = \Delta p$ in *n*-type material and $n = \Delta n$, $p = p_0$ in *p*-type material. The rigorous determination of the nonequilibrium carrier concentrations Δn and Δp, in general, constitutes a complex self-consistent problem, and requires knowledge of the mechanisms for nonradiative recombination in each sample. Therefore, in calculating the spectra for *TB*-transitions the concentration of nonequilibrium carriers was treated as a fitting parameter. For *BT*-transitions, as we will show below, they can be disregarded.

Figures 3 and 4 show the calculated temperature dependences of the position of the spectral peak and half-width for *TB*-recombination, and the experimental data for *p*-$In_xGa_{1-x}As_{1-y}P_y$ (sample 1). It is clear that the calculations reproduce the minimum on the curve $\delta(T)$ and maximum on the curve $\Delta h\nu(T)$ observed in experiment. Usually a maximum at the temperature dependence of the half-width is explained by the presence of two recombination mechanisms whose relative contributions change with temperature. From these calculations it follows that for the *TB*- recombination mechanism the temperature dependence of the half-width has a maximum even in the absence of a second competing mechanism. At the same time, these calculations predict a more abrupt change in the energy deficit at high temperatures than is observed in experiment. This stems from the use of the interpolation expression of Ref. 7 for the energy dependence of the recombination probability, which, in general, is correct only at rather high electron energies. Our attempt to wholly ignore the dependence of the recombination probability on energy led to a contradiction with the experimental curves, in particular, to the disappearance of the maximum in the temperature dependence of the spectral half-width (Fig. 3, curves *2′*). The agreement with experiment can be improved if in these calculations we assume that the recombination probability depends on energy only within the electron energy range $E_e \geqslant \gamma$ (Fig. 3, curves *2″*).

In calculating the curves shown in Fig. 3, we varied the concentration of nonequilibrium carriers Δn, while treating the quantity N_a as a constant equal to the acceptor concentration in sample 1. It is clear that at low temperatures $T \leqslant 120\,K$ the magnitude of the energy deficit and half-width of the spectrum depend on the concentration of nonequilibrium carriers. This explains the shift in the peak energy of the band-edge PL spectrum with increasing excitation level observed in sample 1 at liquid-nitrogen temperature (Fig. 2).

The experimental results are closest to the calculated results when $\Delta n = 5 \times 10^{11}\,\mathrm{cm}^{-3}$. This value was used to calculate a family of curves that differ by the concentration of acceptors N_a (Fig. 4). With increasing values of N_a, the absolute values of δ grow; the positions of the minimum of the curve $\delta(T)$ and the maximum of the curve $\Delta h\nu(T)$ shift towards higher temperatures.

We now discuss our computer results for the *BT*- recombination mechanism, the most probable mechanism operating in degenerate *n*-$In_xGa_{1-x}As_{1-y}P_y$ (sample 2). The quantity $(\Delta p + \theta n)$ enters into our computational expression for the spectral intensity when the *BT*-recombination mechanism operates; here θ is the ratio of coefficients of radiative capture of electrons and nonradiative capture of holes in localized states of the valence band tail. If we assume that the quantity θ is bounded by the same limits in $In_xGa_{1-x}As_{1-y}P_y$ as it is in GaAs, the condition $\Delta p \ll \theta n$ will be satisfied for our range of excitation power densities, and hence the quantity Δp can be ignored in these calculations. In this case, the theory predicts that the peak energy of the luminescence spectrum will be independent of pump power, which agrees with experiment. Figure 5 shows the temperature dependences of the peak energy and half-width of the luminescence spectrum, calculated for *BT*-recombination at various values of the parameter θ, and experimental results for sample 2. It is clear that we cannot describe the experimental spectra by choosing θ in the range $10^{-3}-10^{-1}$ as Levanyuk and Osipov did in Ref. 2 for GaAs. The best agreement between theory and experiment is achieved for $\theta = 0.2$, which exceeds somewhat the values indicated above for GaAs.

Thus, our investigations show that at low temperatures $T \leqslant \gamma$, the band-edge PL of heavily doped $In_xGa_{1-x}As_{1-y}P_y$ is associated with recombination of carriers localized in fluctuations of the band-edge potential caused by a nonuniform distribution of impurities.[2] The band-edge PL spectra and their temperature dependences are well described within the theory of luminescence of heavily doped semiconductors. Comparison of calculated and experimental temperature dependences leads us to conclude that *TB*- and *BT*-transitions play a decisive role in creating the band-edge PL spectra of nondegenerate *p*-$In_xGa_{1-x}As_{1-y}P_y$ and degenerate *n*-$In_xGa_{1-x}As_{1-y}P_y$, respectively.

[1] V. N. Shklovskiĭ and A. L. Efros, *Electronic Properties of Doped Semiconductors* (Nauka, Moscow, 1979)
[2] A. P. Levanyuk and V. V. Osipov, Usp. Fiz. Nauk **133**, 427 (1981) [Sov. Phys. Usp. **24**, 187 (1981)].
[3] V. A. Vil'kotskiĭ, D. S. Domanevskiĭ, S. V. Zhokhovets, and M. V. Prokopeva, Fiz. Tekh. Poluprovodn. **12**, 2192 (1984) [Sov. Phys. Semicond. **12**, 1304 (1984)].
[4] V. L. Korolev and V. G. Sidorov, Fiz. Tekh. Poluprovodn. **22**, 1359 (1988) [Sov. Phys. Semicond. **22**, 862 (1988)].
[5] V. P. Evtikhiev, D. Z. Garbuzov, V. A. Agaev, V. B. Khalfin, and V. P. Chalyĭ, Fiz. Tekh. Poluprovodn. **17**, 1652 (1983) [Sov. Phys. Semicond. **17**, 1052 (1983)].
[6] D. Z. Garbuzov, Z. N. Sokolova, and V. B. Khalfin, Zh. Tekh. Fiz. **53**, 315 (1983) [Sov. Phys. Tech. Phys. **28**, 193 (1983)].
[7] V. V. Osipov, T. I. Soboleva, and M. G. Foĭgel', Fiz. Tekh. Poluprovodn. **13**, 542 (1979) [Sov. Phys. Semicond. **13**, 319 (1979)].

Translated by Frank J. Crowne

Determining the position of antimony impurity atoms in PbS by ^{119}Sb(^{119m}Sn) emission Mössbauer spectroscopy

V. F. Masterov, F. S. Nasredinov, P. P. Seregin, N. P. Seregin, A. V. Ermolaev, and S. I. Bondarevskiĭ

St. Petersburg State Technical University, 195251 St. Petersburg, Russia
(Submitted January 19, 1999; accepted for publication January 20, 1999)
Fiz. Tekh. Poluprovodn. **33**, 913–915 (August 1999)

Emission Mössbauer spectroscopy based on the isotope ^{119}Sb(^{119m}Sn) is used to show that the location of antimony impurity atoms in the PbS lattice depends on the conductivity type of the material: in *n*-type samples the antimony is localized primarily on the anion sublattice, while in *p*-type material it is primarily on the cation sublattice. It is noteworthy that when the ^{119m}Sn center appears in the anion PbS sublattice (i.e., as an antisite defect) after radioactive conversion of ^{119}Sb, its charge state does not depend on the position of the Fermi level. When the ^{119}Sb-center is in the cation sublattice of PbS, it acts like an electrically active substitutional impurity: in *n*-type samples the spectrum corresponds to the neutral state of a donor center ($^{119m}Sn^{2+}$), while in *p*-type material it corresponds to the doubly ionized state of this center ($^{119m}Sn^{4+}$). © *1999 American Institute of Physics.* [S1063-7826(99)00408-1]

In recent years much progress has been made in understanding the nature of impurity states in lead chalcogenides formed by group-III and group-IV impurities. In particular, resonance scattering of current carriers by group-III impurities has been observed,[1] while two-electron centers associated with group-IV impurities have been identified with negative correlation energy.[2] However, there are practically no papers that discuss group-V impurities (As, Sb, and Bi) in lead chalcogenides. It is only known that these impurities are donors, although the fraction of electrically active atoms is considerably less than one.[3] Two explanations can be given for this fact: either a significant number of impurity atoms form electrically inactive complexes (e.g., Sb_2Te_3) in the lattice, or the impurities are distributed between the cation sublattice (where they are donors) and the anion sublattice (where they should be acceptors). It is possible to choose between these alternative models once the positions of group-V atoms in the lead chalcogenide lattices are determined. In this paper we make this determination for the case of impurity atoms of antimony in lead sulfide PbS by the method of emission Mössbauer spectroscopy, using the isotope ^{119}Sb(^{119m}Sn). In Fig. 1a we sketch how the Mössbauer level ^{119m}Sn forms, using the parent isotope ^{119}Sb (with a half-life of 38 hours). If we assume that the recoil energy of the daughter ^{119m}Sn atoms arising from electron capture by ^{119}Sb atoms with emission of a neutrino does not exceed 1.4 eV, we can conclude that radioactive transmutation does not lead to a displacement of the tin atoms from the normal sites on the crystal lattice. Then the parameters of the emission Mössbauer spectra of ^{119}Sb(^{119m}Sn) should reflect the valence (charge) state of ^{119m}Sn atoms located at sites occupied by the antimony atoms.

The radioactive isotope ^{119}Sb was obtained from a cyclotron via the reaction ^{120}Sn$(p,2n)^{119}$Sb. In order to precipitate out a carrier-free preparation of ^{119}Sb, the target was dissolved in concentrated hydrochloric acid, and $SbCl_3$ was extracted using isopropyl alcohol; the preparation was then purified by anion exchange. The Mössbauer sources were made by fusing samples of PbS with the carrier-free preparation of $^{119}SbCl_3$ so that the estimated concentration of impurity atoms of antimony did not exceed 10^{17} atoms$\cdot$cm^{-3}.

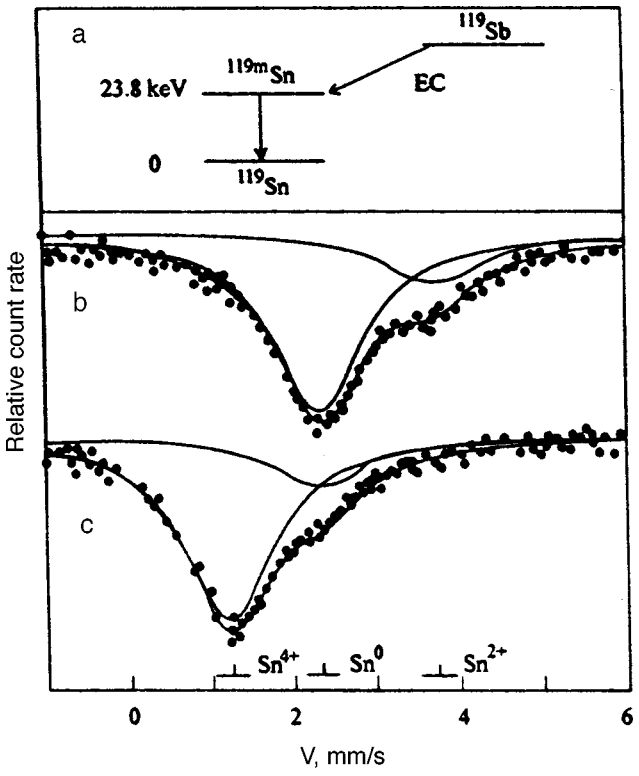

FIG. 1. a—decay scheme for ^{119}Sb; emission Mössbauer spectrum of ^{119}Sb(^{119m}Sn) at $T=80$ K for samples of *n*-PbS (b)—and *p*-PbS (c). The positions of the experimental spectra are shown for components corresponding to $^{119m}Sn^0$, $^{119m}Sn^{2+}$, and $^{119m}Sn^{4+}$.

TABLE I. Parameters of emission Mössbauer spectra of $^{119}Sb(^{119m}Sn)$ in PbS at a temperature of 80 K.

Type of Conductivity	Type of Spectrum	Impurity Center	*I.S.*, mm/s	Γ, mm/s	*S*, %
n	*I*	$^{119m}Sn^{0}$	2.34	1.34	78
	II	$^{119m}Sn^{2+}$	3.73	1.33	22
p	*I*	$^{119m}Sn^{0}$	2.33	1.33	21
	III	$^{119m}Sn^{4+}$	1.23	1.32	79
Error			±0.01	±0.02	±2

Note: I.S. stands for isomeric shift relative to $CaSnO_3$, Γ is the spectral width at half-height (FWHM), and *S* is the area under the spectrum.

The initial PbS samples were *n*-type (with an excess of lead and an electron concentration $n \simeq 5\times10^{18}\,cm^{-3}$) and *p*-type (with an excess of sulphur and a hole concentration $p \simeq 10^{18}\,cm^{-3}$).

Mössbauer spectra of $^{119}Sb(^{119m}Sn)$ were measured on an industrial SM-2201 spectrometer at 80 K with a $CaSnO_3$ absorber (the surface density with respect to tin was 5 mg $\cdot cm^{-2}$). The spectra of both the absorber and the source Ca $^{119m}SnO_3$ consisted of the same line, with a FWHM $\Gamma = 0.79 \pm 0.01$ mm/s, which we took to be the instrument width of the spectral line. Typical spectra of PbS: ^{119}Sb samples are shown in Figs. 1b and 1c, and the results of their analysis are listed in Table I.

The spectrum of an *n*-type sample consists of a superposition of two lines. The widths of both lines considerably exceed the instrument width, which indicates distortion of the cubic environment of the ^{119m}Sn daughter atoms. The reason for this distortion is unclear—it could be, e.g., a noncentral position of the tin ions caused by the large size difference between a tin ion and the Pb^{2+} or S^{2-} ion it replaces. One of these lines (which dominates in *n*-type samples, and is referred to as spectrum *I*) exhibits an isomeric shift that is characteristic of alloys and intermetallic compounds with tin, so we must assign it to $^{119m}Sn^{0}$ centers in the anion sublattice of PbS (lead atoms located in the immediate vicinity of these centers interact with them, leading to a tin isomeric shift that is typical of metallic alloys with tin). It is obvious that $^{119m}Sn^{0}$ atoms can form from ^{119}Sb atoms located in the PbS anion sublattice. The second line (spectrum *II*) exhibits an isomeric shift that is characteristic of compounds with divalent tin, and so we should assign it to $^{119m}Sn^{2+}$ centers in the cation sublattice of PbS (sulfur atoms located in the immediate vicinity of these centers interact with them, leading to a tin isomeric shift that is close to the isomeric shift in the spectrum of ^{119}Sn taken from the compound SnS). It is obvious that $^{119m}Sn^{2+}$ atoms can form from ^{119}Sb atoms located in the PbS cation sublattice.

The spectrum of the *p*-type sample also consists of a superposition of two broad lines. One of these lines has parameters close to those of the type-*I* spectrum (although its intensity in *p*-type samples is considerably lower than it is in *n*-type samples, where it dominates). This spectrum must be assigned to $^{119m}Sn^{0}$-centers that form from ^{119}Sb atoms located in the anion sublattice of PbS. The second line (spectrum *III*) has an isomeric shift that is characteristic of compounds with quadrivalent tin, and so we must assign it to $^{119m}Sn^{4+}$-centers that form from ^{119}Sb atoms located in the cation sublattice of PbS.

Thus, localization of impurity atoms of antimony in the PbS lattice depends on the character of the loss of stoichiometry of the material: in samples with excess lead the antimony is localized predominantly on the anion sublattice, while in the samples with excess sulphur it localizes predominantly on the cation sublattice (and plays the role of a donor). The fraction of antimony atoms that are electrically active depends on the distribution of antimony between sublattices, but it is always less than unity, so that even in *p*-type samples a significant number of antimony atoms are located on the anion sublattice.

It is worth noting that an ^{119}Sn center in the anion sublattice of PbS (which corresponds to a type *I* spectrum) is an antisite defect. It follows from the fact that the isomeric shift of spectrum *I* is independent of the conductivity type of the material that the charge state of the antisite defect does not depend on the position of the Fermi level. In contrast, ^{119m}Sn-centers in the cation PbS sublattice (which corresponds to type-II and type-III spectra) are isoelectronic substitutional impurities. It follows from the data we presented in Ref. 3 that the isoelectronic tin impurity in PbS is an electrically active center, behaving as a two-electron donor with negative correlation energy. This explains the observed dependence of the isomeric shift in the spectra of both centers on the conductivity type of the material: in *n*-type samples the spectrum corresponds to the neutral state of the donor center ($^{119m}Sn^{2+}$), while in *p*-type material it corresponds to the doubly ionized state ($^{119m}Sn^{4+}$).

[1] V. I. Kaĭdanov, S. A. Nemov, and Yu. I. Ravich, Fiz. Tekh. Poluprovodn. **26**, 201 (1992) [Sov. Phys. Semicond. **26**, 113 (1992)].
[2] V. F. Masterov, F. S. Nasredinov, S. A. Nemov, and P. P. Seregin, Fiz. Tekh. Poluprovodn. **31**, 327 (1997) [Semiconductors **31**, 420 (1997)].
[3] V. F. Masterov, F. S. Nasredinov, S. A. Nemov, and P. P. Seregin, Fiz. Tekh. Poluprovodn. **30**, 840 (1996) [Semiconductors **30**, 450 (1996)].

Translated by Frank J. Crowne

Intrinsic photoconductivity of copper-doped gallium phosphide

N. N. Pribylov, V. A. Buslov, S. I. Rembeza, A. I. Spirin, and S. A. Sushkov

Voronezh State Technical University, 394026 Voronezh, Russia
(Submitted August 5, 1998; accepted for publication February 2, 1999)
Fiz. Tekh. Poluprovodn. **33**, 916–920 (August 1999)

Studies of the intrinsic photoconductivity of copper- doped gallium phosphide reveal that increasing the light intensity incident on the sample leads to the appearance of an additional photoconductivity peak in the fundamental absorption band, which can be viewed as anomalous. It is found that the line shape of this new peak in the photoconductivity spectrum depends on the photon energy of the additional illumination. These results are explained by variations in the lifetime of minority carriers over the sample bulk due to reconstruction of copper centers. An expression, which qualitatively describes the experiment, is derived for the photoconductivity spectrum. © *1999 American Institute of Physics.* [S1063-7826(99)00508-6]

Anomalies in the kinetics of intrinsic photoconductivity in GaP:Cu and its infrared quenching have been reported previously.[1,2] In this paper we derive and discuss new photoconductivity spectra which we have observed in compensated samples of this material.

FUNDAMENTAL EXPERIMENTAL RESULTS

Our starting gallium phosphide samples consisted of 1-mm-thick plates cut from a single crystal grown by the Czochralsky method and doped with tellurium, with an electron concentration of $4\times10^{17}\,\mathrm{cm}^{-3}$ and a Hall mobility of $130\,\mathrm{cm}^2/(\mathrm{V}\cdot\mathrm{s})$. The samples were diffusion-doped with copper to saturation in vacuum quartz cells from a layer of metal sputtered onto the sample surface. A doping temperature of 900–910 °C was maintained for 24 hours. At the end of this diffusive anneal, the samples were quenched by dropping the cells into water, then processed with abrasive powders, polished, and etched in a mixture of hydrofluoric and nitric acids. Contacts were deposited from a In–Ga eutectic onto the polished surface of the samples in the form of two parallel strips with width 6–8 mm and a gap between them of 2–3 mm. The primary focus of our interest is that region of the photocurrent spectrum arising from interband transitions, because the shape of the spectrum in this range, is a function of the light intensity and can be controlled by varying the size of the monochromator gap. We measured the photoconductivity signal in the constant-field regime, using a modulation method with synchronous detection. The light flux of a 500-W halogen incandescent lamp was focused onto the input gap of an MBR-23 monochromator and modulated after it left the gap. Light modulated at a frequency of about 300 Hz passed through an optical filter and was focused onto the sample surface. Figure 1 shows spectra obtained for uniform illumination of the interelectrode gap with normally incident light. All the spectra presented in this paper correspond to the strong-excitation regime, i.e., when the sample was illuminated, the current in the circuit greatly exceeded its value in the dark.

An important feature of our samples was their long electron lifetimes $\tau_n\sim$ 1 s, which correspond to a value of the diffusion length $L_n=\sqrt{D_n\tau_n}=\sqrt{\mu_n kT\tau_n/e}\approx1$ cm (where D_n is the diffusion coefficient, μ_n is the electron mobility, and T is the temperature) that exceeds all the characteristic dimensions of the sample. Confirmation of this comes from our ability to record the photoconductivity spectrum of a sample with thickness $\sim$ 1 mm in the intrinsic regime, when it is illuminated with light from the side opposite the side on which the contacts were deposited.

Increasing the optical flux intensity leads to the appearance of an additional peak in the photoconductivity spectrum in the neighborhood of the fundamental transition bands. By picking an arbitrary optical wavelength, we can use the data shown in Fig. 1 to obtain the superlinear lux-ampere charac-

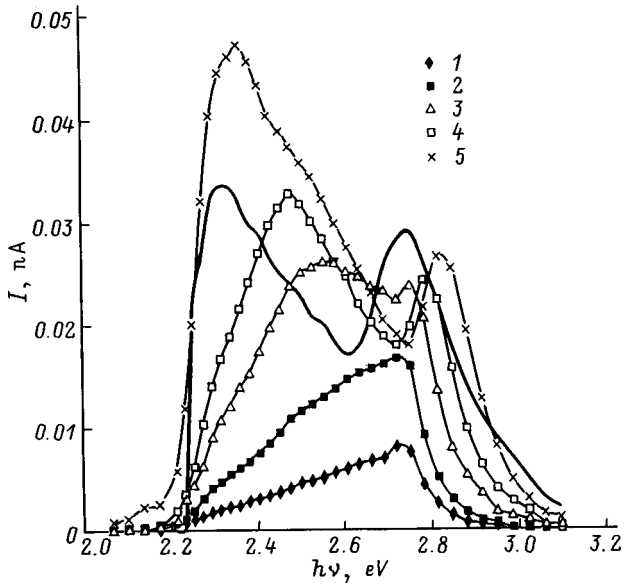

FIG. 1. Photocurrent spectra (I) of a GaP sample doped with Cu at 900 °C as a function of the size of the monochromator gap d, mm: *1* — 0.5, *2* — 0.6, *3* — 0.7, *4* — 0.8, *5* — 1.1. The solid curves are derived from calculations using Eq. (1).

teristic deduced from the results of Ref. 1. The appearance of features in the spectral dependence of the photocurrent in the region of intrinsic absorption of GaP can be regarded as anomalous, since the condition for generation near the surface is satisfied in this region, and saturation of the photoconductivity should take place.[3] We assume that this anomaly arises from the specific behavior of copper, which sensitizes the intrinsic photoconductivity of gallium phosphide. In order to identify possible reasons for the appearance of these spectral features, we measured the photoconductivity in the presence of an additional illumination of the sample surface with monochromatic light, and studied the influence of contacts on the shape of the spectrum.

We found that in the intrinsic region of the spectrum the photoconductivity caused by the modulated light increased abruptly when an additional source of unmodulated short-wavelength light from a second source illuminated the sample surface. The shape of the spectrum in this case is a strong function of the optical wavelength of the unmodulated-light flux (Fig. 2). Illumination by intrinsic light, which is comparatively weakly absorbed, simply increases the value of the photoconductivity over its value recorded without the illumination. In contrast, shifting the illumination wavelength to the short-wavelength region (photon energies $h\nu_0 \geqslant 2.58$ eV), where the absorption coefficient of gallium phosphide begins to exceed ~ 800 cm^{-1} (Ref. 4), leads to a qualitative change in the shape of the spectrum and to the appearance of well-defined structure in the latter. It is clear from Fig. 2 that the positions of the peaks in the observed bands are found to depend on the photon energy $h\nu_0$ of the unmodulated illumination.

The current-voltage characteristics of a sample with contacts measured at constant current have a nearly linear shape in the dark; however, measurements of the frequency dependence of the total resistance show that the contacts to the sample are blocking. The lowest photocurrent is observed for local illumination of the region near the contact with negative potential by a strip of modulated light. Shifting the optical probe to the opposite electrode is accompanied by an increase of photocurrent with simultaneous changes in its spectrum (Fig. 3).

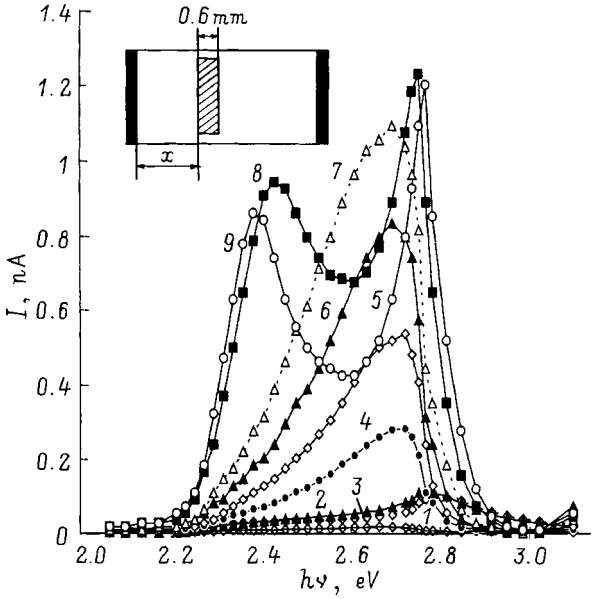

FIG. 3. Photocurrent spectra (I) of GaP : Cu as a function of the distance x from the optically excited region to the contact with negative potential. x, mm: *1* — 0, *2* — 0.2, *3* — 1, *4* — 1.4, *5* — 1.5, *6* — 1.6, *7* — 1.7, *8* — 1.9, *9* — 2.

In order to clarify the role of contacts in this effect, we measured the magnitude of the photocurrent caused by intrinsic modulated light with a fixed wavelength. The light was directed into the gap between electrodes, and unmodulated light was focused into a bounded region near the positive contact and scanned over the spectrum. Figure 4 clearly shows that additional local illumination of the sample near the contact always increases the photocurrent in the circuit in the same way, independent of the photon energy $h\nu_0$. This is due to the increased concentration of electrons in the con-

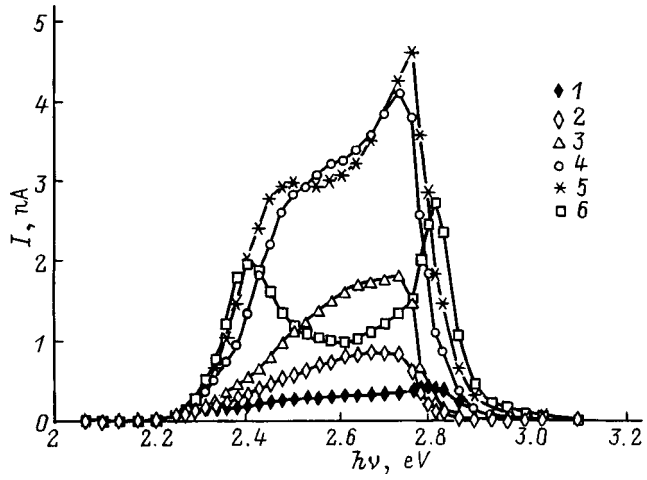

FIG. 2. Shape of the photocurrent spectrum (I) of a GaP : Cu sample without illumination (1) and with unmodulated illumination at the following photoenergies $h\nu_0$, eV: *2* — 2.29, *3* — 2.38, *4* — 2.53, *5* — 2.58, *6* — 2.88.

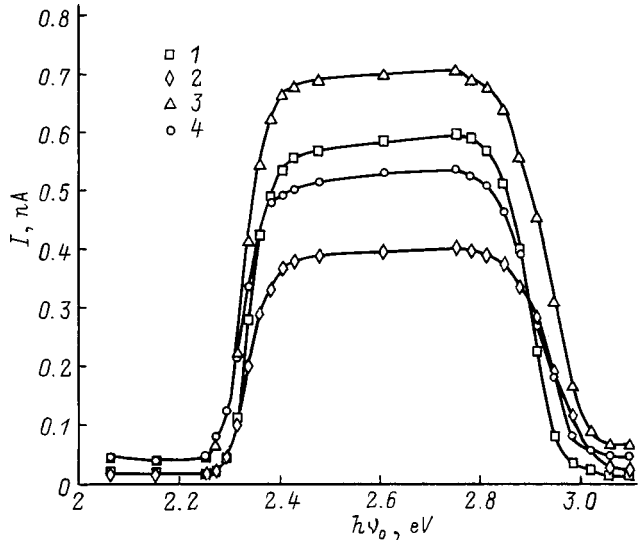

FIG. 4. The effect of unmodulated illumination of a contact on the photocurrent (I) caused by photons with various energies $h\nu$, eV: *1* — 2.58, *2* — 2.48, *3* — 2.34, *4* — 2.29.

duction band caused by optical excitation, which can only happen because the electron lifetime is so long.

This illumination has little effect on the photoconductivity current I at the negative contact. In our view, this is a consequence of the short lifetime of electron-hole pairs there.

DISCUSSION OF EXPERIMENTAL DATA

There are several possible reasons for the observed regularities: an abrupt increase in the rate of surface recombination of gallium phosphide induced by light within a narrow spectral range, a manifestation of the light-induced excitation of the *d*-shell of the copper impurities, or nonuniformity of the material caused by impurities.

The first assumption is purely hypothetical in character, since as far as we know nothing similar has ever been observed in samples of GaP. If optical suppression of surface recombination were to take place, then the shape of the spectra in Fig. 4 would repeat the trace of the functions in Figs. 1–3, which in fact does not happen.

The second assumption can be partially justified by the fact that the energy of the short-wavelength resonance-shaped peak, which is $\sim$ 2.7–2.8 eV, is close to the excitation energy of the $3d^9$- shell of copper in inorganic compounds.[5] In view of the comparatively high solubility of copper in the samples, this assumption is not so far-fetched; however, it is difficult to argue that the intracenter excitation of an impurity is capable of dominating a band of intrinsic transitions. Moreover, the position of an intracenter excitation line should not change.

The effect of nonuniformity of the semiconductor material on its photosensitivity spectrum was considered in Ref. 6, where it was shown for the example of gallium arsenide that a distribution of recombination parameters and absorption characteristics throughout the sample can result in observation of additional extrema in the photoconductivity spectra beyond the fundamental absorption band edge.

In our case we can use the scheme of Kustov et al.[6], where each ith layer of the sample is characterized by its own relaxation time τ_i, but with the same absorption coefficient α. These authors assumed that the generation density was reduced to unit area, the quantum yield η was constant in each layer, and the change in mobility μ from layer to layer is small.

Absorption of light in the sample can be expressed in the form $G_i = J_i[1-\exp(-\alpha t_i)]$ and, accordingly, the transparency of a semiconductor layer to the light flux is $J_{i+1} = J_i \exp(-\alpha t_i)$. Here G_i is the absorbed flux of photons in the ith layer, and J_i, J_{i+1} are, respectively, the incident and transmitted photon fluxes through the ith layer of thickness t_i.

Expressing the photoconductivity $\Delta\sigma$ of the entire sample as a sum of additive contributions from each layer, we can write

$$\Delta\sigma = A\{1-\exp(-\alpha t_1) + \theta_2\exp(-\alpha t_1)[1-\exp(-\alpha t_2)] + \theta_3\exp(\alpha t_1-\alpha t_2)[1-\exp(-\alpha t_3)]+\ \dots\}, \qquad (1)$$

where $A = J_1 e\mu\eta\tau_1$, and $\theta_i = \tau_i/\tau_1$.

In our case, explaining the observed experimental extrema in the spectral dependence of the photocurrent requires that we consider at least a four-layer structure, which is complex enough to provide qualitative agreement with experiment. Conditions for observing the extrema are described by the expression

$$\alpha_{\text{extr},j} = \frac{1}{t_{i+1}}\ln\left[\frac{\theta_{i+1}}{\theta_{i+1}-1}\left(1+t_{i+1}\Big/\sum_{i=1}^{4}t_i\right)\right]. \qquad (2)$$

It follows from Eq. (2) that a four-layer structure with a monotonic spectral dependence of α can have three extrema when the conditions $\tau_1<\tau_2>\tau_3<\tau_4$ are satisfied. Since the magnitude of the absorption coefficient α for interband transitions varies over a wide range, features of the sort described in Ref. 6 will appear in the photoconductivity spectrum.

1) $\alpha(\lambda)\leqslant\alpha_{\text{extr1}}$. In this case the photoconductivity spectrum repeats the trace of $\alpha(\lambda)$ via the relation $\Delta\sigma\sim[\alpha(\lambda)]^n$. This is the region of weak absorption, where optical generation takes place primarily in the sample bulk (layer t_4) where the constant lifetime of electron τ_4 is large. Here and in what follows $n\geqslant 1$ (Ref. 6).

2) $\alpha(\lambda)\sim\alpha_{\text{extr1}}$. At the point where $\alpha(\lambda)=\alpha_{\text{extr1}}$ a peak in the photoconductivity appears, while for $\alpha_{\text{extr2}}>\alpha(\lambda)>\alpha_{\text{extr1}}$ the trace of the photoconductivity spectrum is mirror-reversed with respect to $\alpha(\lambda)$ via $\Delta\sigma\sim[\alpha(\lambda)]^{-n}$. In this region the illumination is primarily absorbed in layer t_3 with a small electron lifetime τ_3.

3) $\alpha_{\text{extr3}}>\alpha(\lambda)>\alpha_{\text{extr2}}$. The photoconductivity spectrum has the form of the function $\alpha(\lambda)$ via $\Delta\sigma\sim[\alpha(\lambda)]^n$. In this case, generation takes place in layer t_2 with a long lifetime for electrons τ_2.

4) $\alpha(\lambda)>\alpha_{\text{extr3}}$. The spectrum has the form $\Delta\sigma\sim[\alpha(\lambda)]^{-n}$ and corresponds to a falloff in photoconductivity in region 2 due to strong absorption of light in the skin layer t_1 with small electron lifetime τ_1.

This stratification with regard to properties of the recombination parameter of a sample illuminated by intrinsic light can be explained by starting from the description of the behavior of impurity copper-centers given previously in Ref. 2. Although the spectrum of a compensated GaP : Cu sample contains shallow energy levels from ionized tellurium inpurity atoms, its dominant features come from photosensitizing deep A^- levels of copper-center acceptors ($E_A = E_v + 0.51$ eV) when the concentration of recombination-induced ionized copper-centers, i.e., the donors B^+ ($E_B = E_v + 0.7$ eV), is relatively low. Let us assume that there is a reversible conversion of a *A*-center to a *B*-center, which lowers the energy of the crystal. Under equilibrium conditions these centers will be distributed throughout the volume of the sample almost uniformly, maintaining a concentration balance with each other.

Photogeneration of electron-hole pairs takes place within a layer whose width is determined by the absorption of the excitation light at the wavelength of the latter. Once the intrinsic photoconductivity has been sensitized in the material, photogenerated holes in this layer are almost all trapped at copper centers in the A^- state. Meanwhile, electrons with

their longer relaxation time diffuse against the field of the trapped holes into the sample bulk, where they are trapped primarily at B^+ centers. As the intensity of the illumination increases, the *B* levels become occupied by electrons, and the bulk of the sample acquires *n*-type conductivity. The accumulation of excess electrons, which continue to diffuse out of the region of optical generation, leads to reconstruction of *B* centers into *A* centers. Since these centers are hole traps in their ionized state, the photoconductivity is sensitized and the lifetime of electrons in the sample bulk increases.

When the light is absorbed strongly and optical generation takes place at the surface of the sample in space-charge regions t_1 and t_2, nonequilibrium holes accumulate in *A*-centers beyond these layers due to diffusion and drift. This process gives rise to layer t_3, with hole-type conductivity, in which the *A* trapping centers are reconstructed into *B* recombination centers. Hence, the lifetime of electron-hole pairs in layer t_3 will decrease. The illumination therefore ''stratifies'' the sample with regard to lifetimes of electrons and holes. This layering should be enhanced with increasing intensity of light incident on the surface. Near the surface, in a layer whose thickness is the Debye screening length $\sim L_D = \sqrt{\varepsilon_r \varepsilon_0 kT/\varepsilon^2 n_0}$, accumulation of holes counters the field of the surface potential; hence, the copper impurities should be predominately in the A^- acceptor state even in the absence of illumination. The results shown in Fig. 3 suggest this possibility in that the sensitivity of the sample to light increases near the contact with positive potential. We thus see that the lifetime of conduction electrons in GaP:Cu samples can vary in the direction of propagation of the incident light, passing through a maximum in the Debye screening layer and a minimum in neighboring regions where reconstruction of copper centers takes place. In situations where the sample is excited by two optical fluxes, spatial nonuniformity of the recombination parameter is induced by the unmodulated light, whereas for a single light flux the nonuniformity is generated by the same process that leads to the observed dependence of the shape of the spectrum on the excitation level. If in Eq. (1) we choose for t_1 the thickness of the damaged layer $\sim 0.3\mu$m, for t_2 the Debye screening length $L_D \sim 3\mu$m, for t_3 the size of the reconstruction region $\sim 20\mu$m, and for t_4 the thickness of the sample, i.e., 1 mm, we can use the known form of the absorption spectrum $\alpha(\nu)$ (Ref. 4) to calculate the spectral dependence of the photocurrent (Fig. 1). The parameters $\theta_1 = 10^{-4}$, $\theta_2 = 5$, $\theta_3 = 10^{-2}$, $\theta_4 = 3.5$, and $A = 10^{-2}$ are selected to obtain agreement between the computed dependence and experiment. It is clear from the spectra shown in Fig. 1 that within limited ranges of photon energies we can observe both superlinear increase of the photocurrent and differential negative photoconductivity. In each case this occurs because of changes in the lifetime of electrons in the different layers of the sample. The experimental data we have discussed have certain analogies with the previously observed appearance of additional extrema in the spectrum of intrinsic photoconductivity in germanium.[7] In these experiments recharging of surface states took place when a voltage was fed to a cell containing a Ge-electrolyte contact, altering the bending of allowed energy bands of the semiconductor.

[1] B. Goldstein and S. S. Perlman, Phys. Rev. **148**, 715 (1966).
[2] N. N. Pribylov, S. I. Rembeza, A. I. Spirin, V. A. Buslov, and S. A. Sushkov, Fiz. Tekh. Poluprovodn. **32**, 1165 (1998) [Semiconductors **32**, 1192 (1998)].
[3] I. Aut, D. Gentsov, and K. German, *Photoelectric Phenomena* (Mir, Moscow, 1980).
[4] V. V. Sobolev, *Optical Fundamental Spectra for Group $A^{III}B^V$ Compounds* (Shtinitsa, Kishinev, 1979, p. 46).
[5] D. T. Sviridov, R. K. Sviridova, and Yu. F. Smirnov, *Optical Spectra of Transition-Metal Ions in Crystals* (Nauka, Moscow, 1976, p. 119).
[6] K. Kustov, V. P. Orlov, V. A. Presnov, and B. S. Azikov, Fiz. Tekh. Poluprovodn. **4**, 669 (1970) [Sov. Phys. Semicond. **4**, 567 (1970)].
[7] G. G. Kareva and P. P. Konorov, Fiz. Tekh. Poluprovodn. **4**, 271 (1972) [Sov. Phys. Semicond. **6**, 233 (1972)].

Translated by Frank J. Crowne

Determining the energy levels of elementary primary defects in silicon

V. V. Luk'yanitsa

Minsk State Medical Institute (Chair of Physics), 220116 Minsk, Belarus
(Submitted April 7, 1998; accepted for publication February 18, 1998)
Fiz. Tekh. Poluprovodn. **33**, 921–923 (August 1999)

The purpose of the experiments described here was to determine the energy level spectrum of elementary primary Frenkel defects in the band gap of silicon, based on whether or not the rate of direct annihilation of these defects depends on their charge state. The results were obtained by jointly analyzing the states of the atomic and electronic subsystems of the crystal under varying conditions of irradiation of the sample with high-energy particles. It was established that these elementary primary defects have energy levels near $E_c-0.28$ eV, $E_c-0.44$ eV, $E_c-0.65$ eV, and $E_c-0.86$ eV. © *1999 American Institute of Physics.* [S1063-7826(99)00608-0]

Despite vigorous efforts by investigators over the past several decades in the area of semiconductor research, there remain several fundamental properties and characteristics of elementary primary defects— Frenkel pairs and their component elements, i.e., vacancies (V) and intrinsic interstitial atoms (I)—that no one has been able to identify with assurance, even for such well-studied semiconductor materials as silicon. Although it has been established that V and I are amphoteric defects with migration energies that depend on their charge state,[1,2] at present our knowledge of the spectrum of energy levels of these defects is far from complete, as was pointed out in the review article by Emtsev *et al.*[3] The purpose of this paper is to determine the position of energy levels of these elementary primary defects in the band gap of silicon. The n-type (with $\rho=100\,\Omega\cdot$cm) and p-type (with $\rho\approx 8-30\,\Omega\cdot$cm) silicon crystals we used were grown by the Czochralsky (crucible) method and zone melting in vacuum. Elementary primary defects were generated within the crystal volume by irradiating it with high-energy electrons ($E_e=9.8$ MeV) in the pulse regime ($t_{\rm pls}=1\,\mu$s, off-duty cycle $\sim 10^4$). In the control experiments the samples were irradiated with ^{60}Co gamma rays corresponding to internal irradiation of silicon by Compton electrons with an average energy $E_e\approx 0.8$ MeV. These types of irradiation are used to obtain genetic Frenkel pairs with different average distances between the components, i.e., so-called ''distant'' pairs (for $E_e=9.8$ MeV) and ''nearby'' pairs (for $E_e=0.8$ MeV). The sample temperature was set during irradiation and maintained with an accuracy of $\pm 1\,^\circ$C by special instruments. During the irradiation time the system also monitored the nonequilibrium conductivity of the irradiated crystal via a matched measurement circuit and a memory oscilloscope. By analyzing the oscillograms we were able to estimate the concentration and lifetime of nonequilibrium charge carriers in the crystal under the electron beam (including the regime where electrons were sent one at a time, which could be implemented in the accelerator).

In order to obtain information about the nature of the radiation-induced defects (RD) and their rates of formation ($\eta=N/\Phi$, where N is the concentration of RD, and Φ is the flux) we analyzed the temperature ($T=78-400$ K) and dose dependences of the concentration (n) and lifetime (τ) of charge carriers in the crystals under study by Hall and phase measurements, respectively.

Two types of primary experiments were carried out: 1) while holding the temperature $T_{\rm irr}$ of the crystal and the integrated flux Φ constant, we varied the irradiation intensity J; 2) holding J and Φ constant, we irradiated the samples at various fixed temperatures within the interval $T_{\rm irr}=100-350\,^\circ$C.

In these experiments we measured the rate of formation of RD, the so-called coefficients of radiative carrier concentration change $K_n=(n_0-n_\Phi)/\Phi$ and carrier lifetime change $K_\tau=(1/\tau-1/\tau_0)/\Phi$, and the concentration of nonequilibrium carriers in the crystals under various irradiation conditions (J, $T_{\rm irr}$). In the experiments with a fixed value of $T_{\rm irr}$ and fixed values of the irradiation flux Φ, we replaced K_n with the dimensionless parameter $\delta_n=K_n(T_{\rm irr})/K_n(T_{\rm irr}=20\,^\circ\text{C})$, which is the ratio of K_n at a given $T_{\rm irr}$ to K_n at $T_{\rm irr}=20\,^\circ$C.

Our data on the energy spectrum of elementary primary defect levels was obtained by jointly analyzing the states of the crystal atomic and electronic subsystems as a function of the irradiation conditions.

Changing the conditions (J and $T_{\rm irr}$) under which the crystal was irradiated led to shifts in the quasi-Fermi levels F_n^* and F_p^* in the band gap of silicon. As they shift towards the edges of the band gap with increasing J or towards the center of the band gap with increasing $T_{\rm irr}$, the quasi-Fermi levels can cross energy levels of the elementary primary defects. This results in charging of these defects. Changing the charge state of an elementary primary defect must cause a change in its direct annihilation rate, which in turn must affect the rates of formation of stable defects in the irradiated crystals.[4] In fact, the authors of Refs. 5 and 6 concluded that when silicon is irradiated, efficient direct annihilation of elementary primary defects takes place, and that the observed nonmonotonic dependences of the rates of formation of radiation defects of various kinds on J or $T_{\rm irr}$ are primarily

determined by changes in the annihilation rate.

It thus follows that irradiation of silicon crystals can under certain conditions be accompanied by charging of the elementary primary defects, which for radiation defects of different kinds should be accompanied by abrupt and uniform (''simultaneous'') changes in the partial rates η at which they are introduced. This makes it possible to experimentally record the charging of elementary primary defects based on these characteristic changes in η.

On the other hand, by monitoring the electronic subsystem of these crystals during the irradiation process we can identify those states that record the event, i.e., charging of the primary radiation-induced defects, and use these states to determine the position of the elementary primary defect energy levels in the band gap of silicon.

Analysis of the values of η obtained when the irradiation conditions were varied for crystals grown by various methods led us to conclude that the dependence of η on J or T_{irr} had the same form for radiation defects of either type, i.e., vacancy (A- and E-centers) or interstitial (C_i-C_s complexes). For this reason, it is more convenient to use integrated parameters to characterize the rate of formation of electrical and recombination-induced active radiation defects. Three parameters that are sensitive to the minimum concentration of radiation defects are the coefficient of radiation-induced concentration change K_n, the ratio δ_n, and the coefficient of carrier lifetime change K_τ.

Figure 1 are plots of the radiative change in concentration of K_n and δ_n, and of the carrier lifetime K_τ as a function of the intensity and irradiation temperature. In the same figure we show the positions of the quasi-Fermi levels for electrons (F_n^*) and holes (F_p^*) in the crystals under these conditions, calculated by measuring the nonequilibrium concentration of charge carriers and crystal temperature during the initial stage of irradiation (when $\Delta n/n_0<10\%$).

Analysis of these data, in which we assumed that charging of the elementary primary defects takes place when the quasi-Fermi levels cross their energy levels, shows that the energy levels of the elementary primary defects are as follows (see Fig. 1):

$$E_1=E_c-(0.28\pm0.03)\text{ eV},\quad E_2=E_v+(0.24\pm0.03)\text{ eV},$$

and

$$E_3=E_c-(0.44\pm0.05)\text{ eV},\quad E_4=E_v+(0.45\pm0.05)\text{ eV}.$$

The reliability of these results was confirmed by data from additional experiments in which the functions $K_n=f(J)$ and $\delta_n=f(T_{\text{irr}})$ were recorded at other values of the fixed parameters T_{irr} or J. We established that in the second type of experiment (trials with fixed irradiation temperature) decreasing the irradiation intensity from $J_1=5\times10^{11}$ $\text{cm}^{-2}\cdot\text{s}^{-1}$ to $J_2=3.85\times10^{10}\,\text{cm}^{-2}\cdot\text{s}^{-1}$ causes the minimum on the curve $\delta_n=f(T_{\text{irr}})$ to shift (Fig. 1c) to the temperature region $T_{\text{irr}}=190-200\,^\circ\text{C}$. However, our calculations, which took into account the new irradiation conditions, led to the same positions for the energy levels of elementary primary defects in the band gap of silicon—E_3 and E_4. On the other hand, varying the fixed crystal temperature in trials with variable irradiation intensity [$K_n=f(J)$] also had no effect on the final results, and we once more obtained the same values of E_1 and E_2.

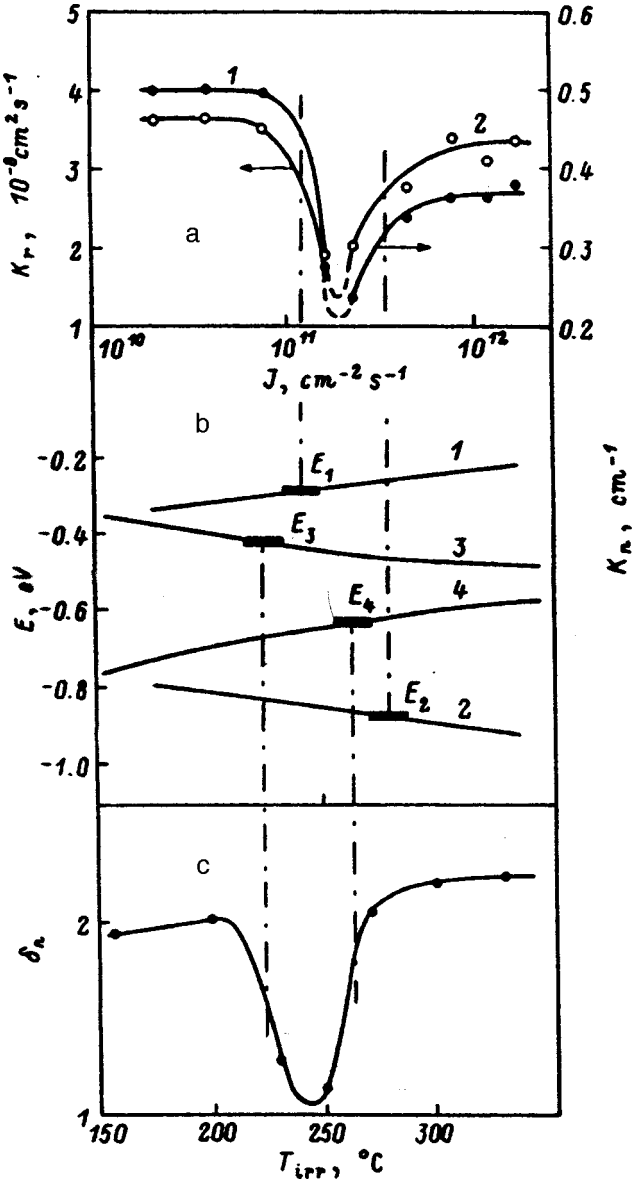

FIG. 1. Temperature dependence of the coefficients of radiation-induced change (a): *1*— concentration K_n for zone-melted, ''vacuum-grown'' n-type Si with $\Phi=8\times10^{13}\,\text{cm}^{-2}$, *2*—lifetime K_τ for crucible-grown n-Si with $\Phi=10^{13}\,\text{cm}^{-2}$, $T_{\text{irr}}=50\,^\circ\text{C}$; b—dependence of the quasi-Fermi levels on irradiation intensity J: *1*—for electrons $F_n^*(J)$, *2*—for holes $F_p^*(J)$, and on irradiation temperature: *3*—$F_n^*(T_{\text{irr}})$, *4*—$F_p^*(T_{\text{irr}})$; c—dependence of the coefficient σ_n on irradiation temperature T_{irr} for crucible-grown n-Si at $\Phi=4\times10^{13}\,\text{cm}^{-2}$, $J=5\times10^{11}\,\text{cm}^{-2}\cdot\text{s}^{-1}$.

In interpreting these results we must keep in mind two possibilities. The first is that the levels we observe could belong to vacancies and interstitial atoms that enter into the composition of relatively strongly bound Frenkel pairs. In this case, in order to find the energy levels of V or I defects we must take into account their interaction energy (Coulomb, polarization, or strain).[3]

In our view, however, the second possibility is more likely, namely, that to first approximation these levels correspond to levels of ''free'' defects V and I. In fact, with in-

creasing energy of the bombarding electrons, the average distance between components of a Frenkel pair increases and the interaction energy between them decreases.[4] This behavior is attributable to the fact that contributions from flexoelectricity and strain to the interaction energy fall off rapidly with increasing intercomponent distance r ($\sim r^{-3}$), and can be important only at distances less than two crystal lattice constants.[3] In contrast, the Coulomb contribution to the interaction of Frenkel pair components with opposite charges, even when screening is taken into account, can be ''sensed'' at distances of greater than three lattice constants. Additionally, irradiation of silicon by electrons with energy $E_e = 9.8\,\text{MeV}$ primarily leads to generation of ''distant'' genetic Frenkel pairs with intercomponent distances close to the maximum possible. This is because irradiation of silicon crystals by electrons with $E_e > 10\,\text{MeV}$ is well known to result in disordered regions, due to the effect of atomic recoil.[7] This implies that for $E_e \approx 10\,\text{MeV}$ even the Coulomb interaction energy between components of a Frenkel pair is relatively small (it probably exceeds the thermal energy kT by no more than a few hundredths of an eV), and that the components of the Frenkel pairs that form can reasonably be treated as quasi-free components. Taking this into account, we must expect that the energy spectra of V and I obtained for $E_e \approx 10\,\text{MeV}$ are insignificantly perturbed, i.e., they differ very little from the energy spectra of the free defects V and I.

Further evidence in favor of the second possibility comes from results of control experiments using ^{60}Co gamma rays, in which E_2 levels are charged by varying the initial concentration of holes p_0 in p-type silicon. Gamma rays with energies $E_\gamma \approx 1.25\,\text{MeV}$ create ''nearby'' Frenkel pairs in silicon, whose large values of interaction energy between components (several tenths of an eV; see Ref. 3) can lead to energy levels that in no way coincide with those we find. However, as p_0 increases, there is a rather narrow range of concentrations (within which $E_v + 0.255\,\text{eV} > F_p > E_v + 0.217\,\text{eV}$, i.e., F_p crosses level E_2) from $4\times10^{14}\,\text{cm}^{-3}$ to $1.5\times10^{15}\,\text{cm}^{-3}$, where an exponential increase is observed [from $(2-3)\times10^{-5}\,\text{cm}^{-1}$ to $2.5\times10^{-4}\,\text{cm}^{-1}$] in the rate of escape of boron atoms $\eta_B = (N_B^0 - N_B)/\Phi$ from sites at the crystal lattice. This fact is evidence of charging of a defect that interacts with boron. The most likely candidate for such a defect is the free intrinsic interstitial silicon atom I, which appears (and is charged) after a nearby Frenkel pair decomposes and then induces a boron atom to move from its lattice site to an interstitial position in accordance with the Watkins reaction: $B_s + I \rightarrow B_I$.[8] In fact, the Coulomb interaction between the reacting centers makes the efficiency of this reaction depend on the charge state of I, since the defect B_s is always negatively charged. In our view, this implies that the level $E_2 \approx E_v + 0.24\,\text{eV}$ should most likely be assigned to the free intrinsic interstitial silicon atom I.

Differentiating among the levels of elementary primary defects we have identified:

$$E_1 \approx E_c - 0.28\,\text{eV},\quad E_3 \approx E_c - 0.44\,\text{eV},$$

$$E_4 \approx E_c - 0.65\,\text{eV},\quad E_2 \approx E_c - 0.86\,\text{eV}$$

and obtaining information about charge states that distinguish them are subjects for future research, in which we plan to use charge-dependent selective drains (trapping centers) for defects of type V and type I.

This work was carried out using the experimental facilities of the NII for Applied Physics Problems in the State University of Belarus (city of Minsk) and the Khar'kov Physicotechnical Institute.

We wish to thank N. I. Maslov for help in measuring the nonequilibrium conductivities and lifetimes of nonequilibrium charge carriers in crystals under the electron beam. We also thank I. I. Kolkovskiĭ for collaboration in measuring the lifetimes in the initial and irradiated samples.

[1] G. D. Watkins, *Deep Levels in Semiconductors* (London–N.Y.–Tokyo–Toronto, 1986).
[2] V. A. Panteleev, S. N. Ershov, V. V. Chernikhovskiĭ, and S. N. Narodnykh, JETP Lett. **23**, 633 (1976).
[3] V. V. Emtsev, T. V. Mashovets, and V. V. Mikhnovich, Fiz. Tekh. Poluprovodn. **26**, 20 (1992) [Sov. Phys. Semicond. **26**, 12 (1992)].
[4] V. V. Emtsev, T. V. Mashovets, and V. V. Mikhnovich, Fiz. Tekh. Poluprovodn. **27**, 708 (1993) [Semiconductors **27**, 390 (1993)].
[5] P. F. Lugakov and V. V. Luk'yanitsa, Fiz. Tekh. Poluprovodn. **18**, 345 (1984) [Sov. Phys. Semicond. **18**, 215 (1984)].
[6] P. F. Lugakov and V. V. Luk'yanitsa, Fiz. Tekh. Poluprovodn. **20**, 742 (1986) [Sov. Phys. Semicond. **20**, 469 (1986)].
[7] *Physical Processes in Irradiated Semiconductors* (Nauka, Novosibirsk, 1977, p. 153).
[8] G. D. Watkins, Conf. Ser. No. 23, Inst. Phys. ''*Lattice Defects in Semiconductors*'' (London–Bristol, 1975).

Translated by Frank J. Crowne

The influence of an external electric field and irradiation energy on the efficiency of Frenkel pair formation in silicon crystals

Z. V. Basheleishvili and T. A. Pagava

Georgian Technical University, 380075 Tbilisi, Georgia
(Submitted November 30, 1998; accepted for publication February 18, 1999)
Fiz. Tekh. Poluprovodn. **33**, 924–926 (August 1999)

indent 0 pt Local irradiation of *p*-Si and *n*-Si followed by measurement of the bulk photovoltage along the sample is used to show that the Coulomb interaction energy between unlike charged components of Frenkel pairs is negligible compared to energies imparted to a silicon atom when *n*-Si is irradiated with electrons having energies of 6–8 MeV. It is asserted that when *n*-Si is irradiated by 8-MeV electrons, the cascade mechanism for defect formation prevails over the diffusion mechanism. © *1999 American Institute of Physics.* [S1063-7826(99)00708-5]

Decisive roles are played in the appearance, stabilization, and reconstruction of defects by the initial interaction events involving fast particles (after which primary radiation defects remain, i.e., Frenkel pairs that have avoided annihilation immediately after formation), and secondary processes in which the interaction of migrating components of Frenkel pairs with one another, and also with impurity atoms or initial imperfections, give rise to various electrically active complexes or even regions of bulk charge.[1–3]

The most tenable theoretical picture of these events is one in which irradiation of silicon generates Frenkel pairs, most of which disappear when their components, i.e., vacancies and interstitial atoms, annihilate with each other immediately after creation, primarily due to Coulomb interaction forces.[4] This assumption forms the basis for a large body of contemporary work that explains the various experimental data, including the data confirming the fact that charged components of Frenkel pairs in silicon do indeed exist (unlike-charged components in *n*-Si, and like-charged, i.e., positive, components in *p*-Si).[5–9]

In this paper we use local irradiation of a silicon sample followed by measurement of the bulk-gradient photovoltage U_{ph} along the sample to continue our study of the properties of primary radiation-induced defects. In particular, we seek to determine the charge states of intrinsic interstitial atoms and vacancies in silicon crystals, and also to find out how the phenomenon of annihilation of Frenkel-pair components depends on the energy of incoming electrons and the application of external electric fields during irradiation. This method was used for the first time in Ref. 5.

In order to conduct these experiments we used single-crystal silicon samples, batch labels BKD-500 and BKEF-150, with hole and electron concentrations of $\sim 5\times 10^{13}$ and $\sim 10^{13}\,\mathrm{cm}^{-3}$, respectively, grown by crucible-free floating-zone method. These samples were irradiated with 2, 6, and 8-MeV electrons at room temperature. The flux density of electrons in all these experiments was the same: $\varphi = 5\times 10^{12}\,\mathrm{cm}^{-2}\cdot\mathrm{s}^{-1}$.

The curves plotted in Fig. 1 illustrate how the magnitude of the photovoltage U_{ph} increases with dose when *n*- and *p*-type silicon samples are irradiated by electrons with various energies. It is clear from this figure (curves *1–3*) that an external electric field applied to a sample of *p*-Si during the irradiation does not change the value of the bulk photovoltage. For samples irradiated in the presence of an external electric field ($E = 110$ V/cm) and in its absence ($E = 0$), the curves $U_{ph} = f(\Phi)$ superimpose on one another for a given

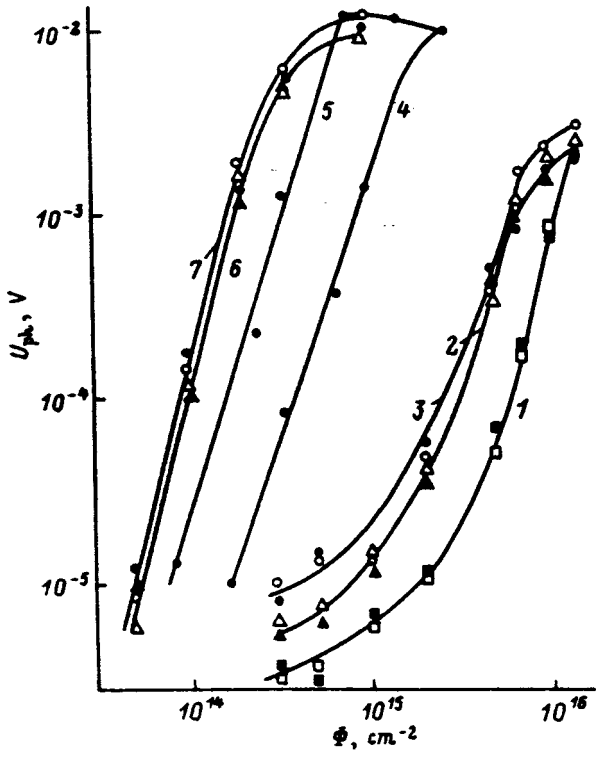

FIG. 1. Dependence of the bulk photovoltage U_{ph} on irradiation dose Φ in samples of *p*-Si (*1–3*) and *n*-Si (*4– 7*) irradiated at $T_{irr} = 300$ K by electrons with the following energies E_{irr}, MeV: *1, 4, 5* — 2.2; *2, 6* — 6; *3, 7* — 8. All measurements of $U_{ph}(\Phi)$ were made for electric fields $E = 0$ and 110 V/cm, and no dependence $U_{ph}(E)$ was observed. *4,5*— the functions $U_{ph}(\Phi)$ for *n*-Si when $E_{irr} = 2.2$ MeV, taken from Ref. 5, measured at electric fields *E*, V/cm: 4 – 0; 5 – 110.

electron irradiation energy. For samples of *n*-type silicon (curves *6* and *7* in the figure) irradiated with 6- and 8-MeV electrons, the situation is analogous to that of *p*-type silicon, i.e., an external electric field has no effect on the function $U_{ph}=f(\Phi)$. Contrast this with the work of Milevskiĭ and Garnik,[5] who reported that when a certain voltage is applied across the sample while it is being irradiated with 2.2-MeV electrons, the resulting electric field shifts the position of the maximum of $U_{ph}=f(\Phi)$ towards lower doses (see the figure, curves *4* and *5*).

It is well known that the value of the bulk photovoltage is directly proportional to the resistivity gradient and the minority current carrier lifetime τ, but in fact the magnitude of U_{ph} is mainly determined by the resistivity gradient because τ is only a weak function of the irradiation dose Φ (Ref. 10). Consequently, any increase in the magnitude of U_{ph} is connected with increases in the resistivity gradient, which in turn increases with decreasing free carrier concentration in the irradiated portion of the sample due to formation of secondary radiation-induced defects. Starting from this information and the prevailing viewpoint regarding the creation of primary radiation-induced defects, we explain the data we obtained from experiment as follows: when silicon is irradiated by fast electrons with various energies, primary defects—Frenkel pairs—are created with differing separation distances between their components, depending on how much the energy transferred to an atom by elastic collisions with the incoming particles exceeds the threshold energy for the formation of primary defects. In this case, as noted by Corbett in Ref. 4, immediately after their formation the components of Frenkel pairs in crystals of *p*-type silicon are both charged positively, while in *n*-type silicon their signs are opposite—vacancies are charged negatively, while interstitial atoms are charged positively.

When the energy of the incoming electrons is ~ 2 MeV, the probability of forming nearby Frenkel pairs is larger than the probability of forming free vacancies and interstitial atoms, i.e., separated Frenkel pairs.

The subsequent fate of ''nearby'' Frenkel pairs— spontaneous recombination, dissociation into free vacancies and interstitial atoms, or persistence in the form of metastable pairs—depends on the charge states of the components of the Frenkel pair and the conditions of the experiment, in particular, the presence or absence of an external electric field in the sample at the time it is irradiated.[5]

For all the energies used in our experiments, the presence of an external electric field in *p*-type silicon samples did not influence the generation of secondary radiation-induced defects (i.e., U_{ph} was unaffected by the presence of an external electric field in the sample during irradiation). For irradiation by electrons with energies on the order of ~ 2 MeV, this behavior is consistent with vacancies and interstitial atoms that are both charged positively after generation. It is known[3] that the stable charge states in *p*-silicon are the defects V^{++} and V^0 resulting from the decay of the unstable vacancy V^+. Based on our data, we can then assume that interstitial atoms are also charged positively, and hence nearby Frenkel pairs decay into their components immediately after appearance. Therefore, it is logical (we claim) that Frenkel pairs created in *p*-type silicon irradiated with fast electrons separate even at very low temperatures, and that intrinsic interstitial atoms and vacancies interact with impurities.[6]

When samples of either *p*- or *n*-type silicon are irradiated by electrons with energies of 6–8 MeV, the presence or absence of an external electric field within them during the irradiation has no observable effect on the value of U_{ph}. To explain this fact, we note that when silicon crystals are irradiated by electrons with these energies, the distance between Frenkel-pair components is large. Despite the fact that these components are oppositely charged in *n*-type silicon crystals, the Coulomb interaction forces between them immediately after the appearance is insignificant. Vacancies and interstitial atoms have a higher probability of interacting with impurity atoms than they do of annihilating each other immediately after appearance, and if they annihilate, they do so via annihilation centers.[2] It is notable that for the same irradiation dose, electrons with energies 6–8 MeV lead to values of U_{ph} that are an order of magnitude higher than electrons at energies ~ 2 MeV. Consequently, the function $U_{ph}=f(\Phi)$ shifts towards lower irradiation doses for both types of silicon.

It is known that the electron energy $E_{irr}=9$ MeV is a threshold above which regions of disorder can appear in silicon.[11] Consequently, we anticipate that when silicon crystals are irradiated by 8-MeV electrons, the cascade mechanism for defect formation prevails over the diffusion mechanism. This also explains why plots of the function $U_{ph}=f(\Phi)$ are found to shift toward lower doses with increasing irradiation energy.

[1] V. S. Vavilov, *The Effect of Light on Semiconductors* (Nauka, Moscow, 1963).
[2] *Physical Processes in Irradiated Semiconductors*, edited by L. S. Smirnov (Novosibirsk, 1977).
[3] V. V. Emtsev and T. V. Mashovets, *Impurities and Point Defects in Semiconductors* (Nauka, Moscow, 1981).
[4] J. W. Corbett, *Radiation Effects in Semiconductors* (1976), p. 1.
[5] L. S. Milevskiĭ and V. S. Garnyk, Fiz. Tekh. Poluprovodn. **13**, 1369 (1979) [Sov. Phys. Semicond. **13**, 801 (1979)].
[6] V. V. Emtsev, T. V. Mashovets, and E. Kh. Nazaryan, Fiz. Tekh. Poluprovodn. **16**, 687 (1982) [Sov. Phys. Semicond. **16**, 440 (1982)].
[7] Z. V. Basheleĭshvili, T. L. Bzhalava, T. A. Pagava, and V. V. Sanadze, Repts. Acad. Sci. of the Georgian SSR **116**(2), 297 (1984).
[8] P. F. Lugakov and V. V. Luk'yanitsa, Fiz. Tekh. Poluprovodn. **18**, 345 (1984) [Sov. Phys. Semicond. **18**, 215 (1984)].
[9] P. F. Lugakov and V. V. Luk'yanitsa, Electrical Engineering Ser. 6, No. 2, p. 38 (1982).
[10] Z. V. Basheleĭshvili, V. S. Garnyk, V. S. Gorin, and T. A. Pagava, Fiz. Tekh. Poluprovodn. **18**, 1714 (1984) [Sov. Phys. Semicond. **18**, 1074 (1984)].
[11] G. M. Ivanov and N. N. Sirota, *Radiative Defects in Semiconductors* (Minsk, 1972), p. 56.

Translated by Frannk J. Crowne

Electrical properties of InSb irradiated with fast neutrons from a nuclear reactor

N. G. Kolin and D. I. Merkurisov

Affiliate of the State Science Center of the Russian Federation, ''Karpov Institute of Physical Chemistry,'' 249020 Obninsk, Russia

S. P. Solov'ev*

Institute of Nuclear-Power Engineering, 249020 Obninsk, Russia

(Submitted January 11, 1999; accepted for publication February 18, 1999)
Fiz. Tekh. Poluprovodn. **33**, 927–930 (August 1999)

The effect of fast neutrons, having the full spectrum of neutrons from a reactor, on the formation and annealing of radiation defects and on the nuclear-transmutation doping of InSb single crystals is determined. The character of the change produced in the electrical properties of the material by irradiation and subsequent heat-treatments is determined. © *1999 American Institute of Physics.* [S1063-7826(99)00808-X]

The radiation defects (RDs) in indium antimonide have now been studied extensively. The effect of various types of radiation — electrons,[1–3] ions,[4,5] protons,[6] and neutrons[7–10] — on the properties of InSb has been studied. It has been shown that room-temperature irradiation with low-energy ($E<5$ MeV) electrons produces in the material predominantly simple radiation defects in the indium lattice and complexes of such defects with oxygen atoms (M_1 centers with a level $E_c-0.05$ eV) that are acceptors and lead to $n\rightarrow p$ conversion, while irradiation with neutrons, protons, ions, and high-energy electrons produces more complicated radiation defects – so-called disordered regions (DRs) and clusters of defects with an average radius 150–200 Å which give rise to $p\rightarrow n$ conversion.

Complex RDs continue to be annealed up to the melting point, and they therefore have a strong effect on the electrical, optical, and structural properties of the material, as well as on the operational parameters of devices and parts based on it. For this reason it is important to study the mechanisms leading to the formation and annealing of RDs in InSb, especially for the practical implementation of the possible advantages of nuclear-transmutation doping material. In this connection, our objective in the present work is to determine the effect of fast neutrons with a reactor spectrum on the formation of radiation defects and the nuclear-transmutation doping of InSb single crystals, as well as to establish the character of the change produced in the electrical properties of materials by irradiation and subsequent heat-treatments.

The starting materials consisted of $\sim 40-$mm-diam, *n*- and *p*-type InSb single crystals Czochralski grown in the [211] direction and doped with Sn and Zn, respectively, to different densities. The properties of the startin samples are presented in Table I.

Irradiation was conducted in Cd containers at temperatures no higher than 70 °C in the vertical channels of a VVR-ts nuclear reactor. The samples 3–5 (see Table I) were irradiated in a core channel with fast-neutron ($E>0.1$ MeV) flux density $\varphi_f=5\times10^{13}\,\mathrm{cm^{-2}\cdot s^{-1}}$; all other samples were irradiated in a peripheral channel with flux density $\varphi_f=7\times10^{11}\,\mathrm{cm^{-2}\cdot s^{-1}}$. The irradiation time was chosen so that the fast-neutron flux (F_f) ranged from 1.8×10^{16} to $1.26\times10^{18}\,\mathrm{cm^{-2}}$. The use of 1-mm-thick Cd containers prevented nuclear-transmutation doping due to reactions occurring on thermal neutrons. The contribution of the resonant neutrons ($E=1.46$ eV, $\sigma=2.2\times10^4$ b) to nuclear-transmutation doping[11] was eliminated by grinding off at least 50-μm-thick layer from both sides of the irradiated sample. In connection with the high induced radioactivity, before work commenced the irradiated samples were held in special containers for periods ranging from 3–4 to 10–12 months, depending on the neutron flux. The electrical parameters were measured by the van-der-Pau method at liquid-nitrogen temperature.

The density n and mobility μ of charge carriers in the InSb samples as a function of the fast-neutron flux are presented in Fig. 1 (curves *1′*, *1″*). It is evident that for neutron flux $1.8\times10^{16}\,\mathrm{cm^{-2}}$ $p\rightarrow n$ conversion has already occurred in the InSb samples, and as the flux continues to icnrease, the carrier density increases linearly and the carrier mobility decreases linearly for all experimental samples, irrespective of the initial type of conductivity.

This picture differs from some of the published data obtained as a result of bombardment by neutrons with a different spectral composition or with initial *n*-InSb samples with a high charge-carrier density ($n\geqslant10^{14}\,\mathrm{cm^{-3}}$), where for low neutron flux ($F\leqslant10^{14}\,\mathrm{cm^{-2}}$) the charge-carrier density was observed to decrease with increasing flux.

To determine the radiation processes occurring in InSb under irradiation and subsequent heat-treatments we performed isochronous annealing of irradiated samples for 20 min in the temperature range 20–450 °C. Curves of the charge-carrier density and mobility versus the annealing temperature in InSb samples irradiated with different fast-neutron fluxes are shown in Figs. 2 and 3, respectively. It is evident that the charge-carrier density and mobility increase with the annealing temperature. This testifies that the annealing of the radiation defects introduced by irradiation is effective. Even though the RDs anneal in the entire experimental

TABLE I.

Sample No.	Initial values of the electrical parameters		Initial Dopant	Type of conductivity	Fast neutron flux, F_f, 10^{16} cm^{-2}	Electrical parameters after iradiation and annealing at 400–450 °C	
	n, 10^{13} cm^{-3}	μ, 10^5 cm^2/(V·s)				n, 10^{16} cm^{-3}	μ, 10^4 cm^2/(V·s)
1	8.72	6.12	Sn	*n*	5.00	1.00	5.60
2	8.72	6.12	Sn	*n*	25.00	4.00	3.40
3	31.00	4.70	Sn	*n*	1.80	0.50−0.60	15.00
4	31.00	4.70	Sn	*n*	12.60	3.00	7.30
5	31.00	4.70	Sn	*n*	126.00	50.00−60.00	1.30
6	40.00	5.00	Sn	*n*	5.00	1.00	6.00
7	40.00	5.00	Sn	*n*	25.00	6.00	5.50
8	5.50	0.01	Zn	*p*	5.00	1.20	4.90
9	5.50	0.01	Zn	*p*	25.00	5.00	8.70

temperature range, two main stages of annealing of radiation defects can be distinguished: first stage — 100–200 °C and second stage — 250–350 °C. The annealing temperature dependences of n and μ are of the same character for different neutron fluxes. It should be noted that, just as in GaAs,[12] the temperature at which restoration of μ commences decreases with increasing neutron flux.

The substantial (by one or two orders of magnitude) changes in n and μ after heat-treatment of the irradiated samples shows that the RDs introduced during irradiation make a large contribution. It is known[7–10] that RDs in neutron-irradiated InSb are annealed in our temperature range, but in our case the charge-carrier densities and mobilities after annealing at 300–400 °C are not restored, but rather they saturate at a level that depends linearly on the neutron flux (Fig. 1, curves *2′* and *2″*). The latter testifies that for irradiation under our conditions a definite density of impurities as products of nuclear reactions on intermediate neutrons is introduced into InSb. The number of such neutrons in the total flux depends on the type of reactor, the location of the channel, and the apparatus used for irradiation.

Chemical-spectral analysis showed that after heat-treatment the samples contained a stable tin donor impurity, whose concentration depends linearly on the neutron flux. The dependence of the onset temperature of the restoration of μ is apparently determined by the different density of the impurity introduced into the material. Generalization of our experimental results allows us to use the empirical formula to describe the dependence of the charge-carrier density in the InSb samples, irradiated in Cd containers and then annealed, on the fast-neutron flux:

$$n_{(Cd)} \approx 0.2 F_f .$$

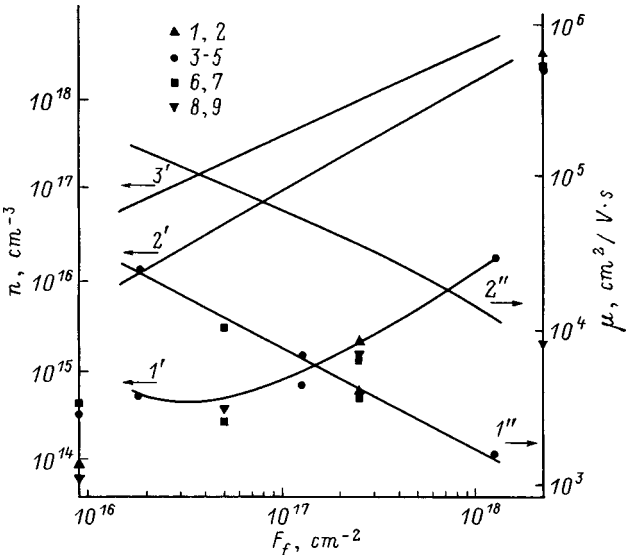

FIG. 1. Density (n, curves *1′*–*3′*) and mobility (μ, curves *1″*, *2″*) of charge carriers in the InSb samples, presented in Table I, as a function of the fast neutron flux (the initial values of n and μ are indicated on the axes). The symbol numbers for the experimental points correspond to the sample numbers in Table I. The following curves were measured: *1′*, *1″* — after irradiation; *2′*, *2″* — after irradiation and heat-treatment at $T \approx 400-450$ °C; *3′* — after irradiation with the full neutron spectrum of the reactor (no Cd screens) and heat-treatment.

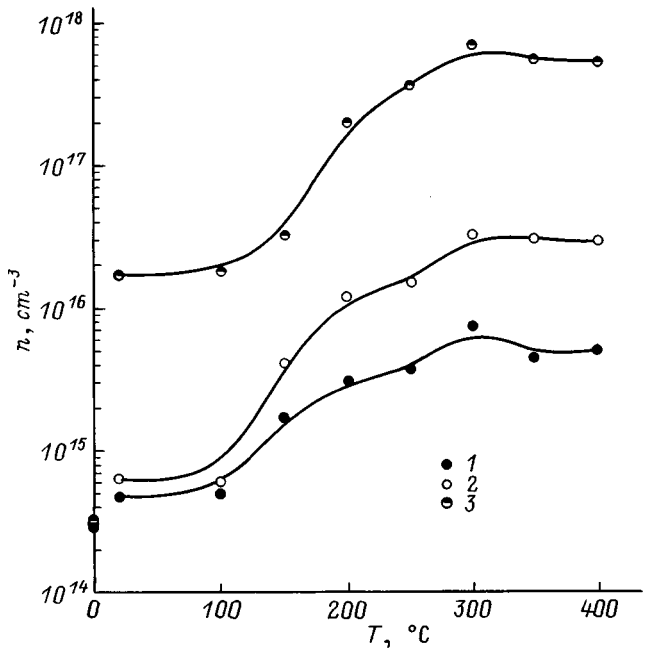

FIG. 2. Charge carrier density n versus the isochronous annealing temperature for InSb samples *3–5*, presented in Table I, after irradiation with fast neutron flux F_f, 10^{16} cm^{-2}: *1* — 1.8, *2* — 12.6, *3* — 126. The initial values of n are indicated on the axes.

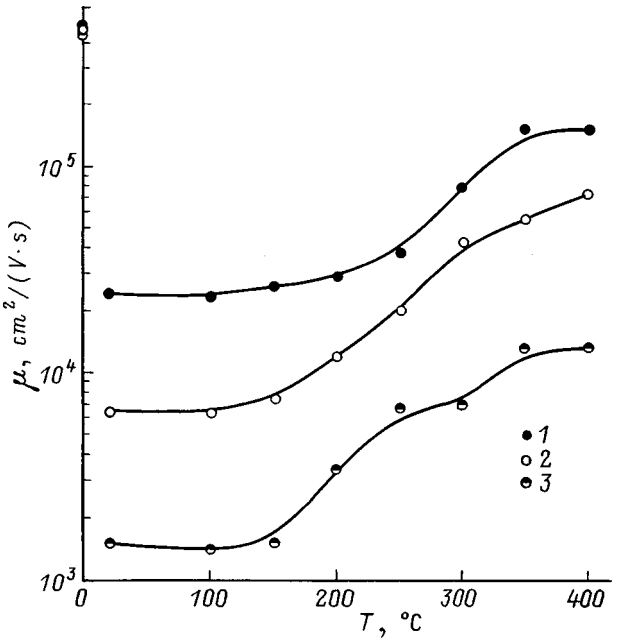

FIG. 3. Charge-carrier mobility μ versus the isochronous annealing temperature for the same InSb samples as in Fig. 2. The initial values of μ are indicated on the axis.

For a comparative estimate of the effectiveness of nuclear-transmutation doping of InSb by reactions on intermediate neutrons, the charge carrier density as a function of the fast-neutron flux in samples of nuclear-transmutation doped InSb, obtained by irradiating with the full neutron spectrum of the reactor (no Cd containers), is shown in Fig. 1 (curve $3'$). In previous studies[11] we derived the experimental dependence of the charge-carrier density introduced by nuclear-transmutation doping on the thermal neutron flux F_s as $n_{tr} \approx 2.1F_s$. Since the ratio of the thermal and fast neutron flux densities is known ($k=\varphi_s/\varphi_f=F_s/F_f$) for a definite reactor channel where the samples are irradiated, the effect of the additional doping due to intermediate neutrons during nuclear-transmutation doping of indium antimonide can be determined by comparing these two dependences:

$$\frac{n_{(Cd)}}{n_{tr}}=\frac{0.2F_f}{2.1kF_s}\approx 0.1/k.$$

Therefore, depending on the ratio of the thermal and fast neutron flux densities in a particular channel, the contribution of nuclear-transmutation doping due to superthermal neutrons ranges from 5% (for $k\approx 2$ — peripheral channels) to 10% ($k\approx 1$ — core channels).

The following conclusions can be drawn from the results obtained in this study.

1. In contrast to nuclear-transmutation doping of InSb during irradiation with the full neutron spectrum of the reactor, so that the electrical parameters of the irradiated material are determined mainly by the density of the impurity (Sn) introduced, elimination of the effect due to thermal and resonant neutrons makes it possible to study more deeply the kinetics of the formation and annealing of RDs in a wide range of flux.

2. Under irradiation with the full neutron spectrum of the reactor the contribution of intermediate neutrons to the total level of nuclear-transmutation doping in each specific case depends on the ratio of the thermal and fast neutron flux densities and reaches 5–10% for the VVR-ts reactor.

We wish to thank I. I. Kuz'min and O. L. Kukhto for participating in a discussion of the results.

This work was supported by the Ministry of Science and Technology Policy of the Russian Federation according to the State Science and Technology Program ''Investigations and developments in priority directions of development of science and technology for civilian applications'' (Project No. 045) and the Association of the US Chamber of Commerce (USIC) as part of subcontract No. 4616510 with the Lawrence National Laboratory in the U.S.A (Berkeley, California).

*E-mail: FCI@meteo.ru; Fax: (08439) 6-39-11

[1] E. P. Skipetrov, V. V. Dmitriev, F. A. Zaitov, G. I. Kol'tsov, and E. A. Ladygin, Fiz. Tekh. Poluprovodn. **20**, 1787 (1986) [Sov. Phys. Semicond. **20**, 1120 (1986)].
[2] G. A. Vikhliĭ, A. Ya. Karpenko, I. G. Megela, and L. I. Tarabrova, Neorg. Mater. **21**(8), 1279 (1985).
[3] N. A. Vitovskiĭ, T. V. Mashovets, O. V. Oganesyan, and N. Kh. Pambukhchyan, Fiz. Tekh. Poluprovodn. **12**, 1861 (1978) [Sov. Phys. Semicond. **12**, 1106 (1978)].
[4] A. N. Blaut-Blachev, N. N. Gerasimenko, L. V. Lezheĭko, E. V. Lyubopytova, and V. I. Obodnikov, Fiz. Tekh. Poluprovodn. **14**, 306 (1980) [Sov. Phys. Semicond. **14**, 179 (1980)].
[5] A. B. Korshunov, G. M. Kuznetsov, A. G. Makarov, V. V. Olenin, and I. V. Postnikov, Fiz. Tekh. Poluprovodn. **12**, 938 (1978) [Sov. Phys. Semicond. **12**, 554 (1978)].
[6] V. A. Bogatyrev and G. A. Kachurin, Fiz. Tekh. Poluprovodn. **11**, 1360 (1977) [Sov. Phys. Semicond. **11**, 798 (1977)].
[7] J. W. Cleland and J. H. Crawford, Phys. Rev. **95**(5), 1177 (1954).
[8] N. I. Kurdiani, Fiz. Tekh. Poluprovodn. **3**, 1683 (1969) [Sov. Phys. Semicond. **3**, 1415 (1969)].
[9] N. A. Vitovskiĭ, A. P. Dolgolenko, T. V. Mashovets, and O. V. Oganesyan, Fiz. Tekh. Poluprovodn. **13**, 1958 (1979) [Sov. Phys. Semicond. **13**, 1141 (1979)].
[10] V. N. Brudnyĭ, N. V. Kamenskaya, and N. G. Kolin, in *Electric Properties of Strongly Irradiated InSb* (USSR Academy of Sciences, Pavlodar, 1989), Part 2, p. 140.
[11] N. G. Kolin, V. B. Osvenskiĭ, N. S. Rytova, and E. S. Yurova, Fiz. Tekh. Poluprovodn. **20**, 822 (1986) [Sov. Phys. Semicond. **20**, 519 (1986)].
[12] N. G. Kolin, L. V. Kulikova, V. B. Osvenskiĭ, S. P. Solov'ev, and V. A. Kharchenko, Fiz. Tekh. Poluprovodn. **18**, 2187 (1984) [Sov. Phys. Semicond. **18**, 1364 (1984)].

Translated by M. E. Alferieff

Avalanche light-emitting diodes operating at room temperature based on single-crystal Si:Ho:O

N. A. Sobolev,* A. M. Emel'yanov, and Yu. A. Nikolaev**

A. F. Ioffe Physicotechnical Institute, Russian Academy of Sciences, 194021 St. Petersburg, Russia
(Submitted April 13, 1999; accepted for publication April 15, 1999)
Fiz. Tekh. Poluprovodn. **33**, 931–932 (August 1999)

Electroluminescence of Ho^{3+} ions has been observed for the first time in diode structures based on single-crystal silicon doped with holmium and oxygen. The product of the effective cross-section for excitation of Ho^{3+} ions and the lifetime of the first excited state was determined under avalanche breakdown conditions. © *1999 American Institute of Physics.* [S1063-7826(99)00908-4]

INTRODUCTION

We report the first observations of photoluminescence (PL) and injection electroluminescence (EL) in a semiconductor containing Ho^{3+} ions. In our experiments, direct current was passed through a $p-n$-junction in a structure based on Si:Ho:O at temperatures 4.2–150 K.[1,2] Electronic transitions within the inner $4f$-shell of a Ho^{3+} ion from the first excited state($^5I_7$) to the ground state ($^5I_8$) give rise to a line in the luminescence spectrum whose wavelength is close to $\lambda = 2\ \mu$m. For both the PL and injection EL spectra in Si:Ho:O, the peak intensity was recorded at $\lambda \approx 1.96\ \mu$m. In this paper we describe the first observations and studies of room-temperature EL of Ho^{3+} ions in diode structures based on Si:Ho:O in the avalanche breakdown regime.

EXPERIMENTAL CONDITIONS

Implantation of holmium ions (with energies $E=2.0$ and 1.6 MeV, in doses $D=1\times10^{14}\,\mathrm{cm}^{-2}$) and oxygen ($E=0.28$ and 0.22 MeV, $D=1\times10^{15}\,\mathrm{cm}^{-2}$) into n-type silicon films with resistivities of 5 $\Omega\cdot$cm oriented in the (111) plane results in amorphization of the surface layer. Annealing at temperature/times of 620 °C/1 h + 900 °C/0.5 h leads to recrystallization of the amorphous layer via the mechanism of solid-phase epitaxy and the formation of holmium-containing, optically and electrically active, donor-like centers in the n^+-layer. The $p^{++}-n^+$ structures are created by implantation with boron ions ($E=40$ keV, $D=5\times10^{15}$ cm^{-2}). Defects that form during boron implantation disappear after annealing in the regime 900 °C/0.5 h. Contacts were made by deposition of aluminum. The mesa diodes had working areas of 5.3 mm^2. Electroluminescence was excited by rectangular current pulses with duration 8 ms at a frequency of 32 Hz. Emission from the diode structures was focused by a lens system on the input gap of an MDR-23 monochromator. Light at the output of the monochromator was recorded by an InGaAs photodetector (covering the wavelength range $\lambda = 1.0-1.6\ \mu$m with 7-nm resolution) and a PbS photodetector (covering the wavelength range $\lambda = 1.6-2.4\ \mu$m with 14-nm resolution). Measurements of the EL spectrum made with the PbS photodetector were not corrected for the spectral sensitivity functions of the devices recording the EL, but were scaled in such a way that the EL intensity at $\lambda = 1.6\ \mu$m measured in relative units coincided for the different photodetectors. A selective amplifier was used to record the photodetector current.

EXPERIMENTAL RESULTS AND DISCUSSION

Figure 1 shows the reverse branch of the I–V characteristics of one of the diode structures at two temperatures. The room-temperature breakdown voltage, obtained by extrapolating the linear portion to zero current, amounted to ~8 V. The breakdown voltage was observed to decrease with decreasing temperature. This value of the breakdown voltage, and its temperature dependence indicated that avalanche breakdown takes place in this diode structure at 300 K. Figure 2 shows the EL spectrum of this reverse-biased diode at 300 K and a current of 300 mA. In addition to light in the wavelength range $\lambda = 1.85-2.15\ \mu$m with a maximum at $\lambda \approx 1.96\ \mu$m, caused by radiative transitions of electrons between levels $^5I_7$ and $^5I_8$ of the Ho^{3+} ions split in the crystal field, within the range of transparency of silicon we observe a relatively weak emission caused by transitions of ''hot'' electrons within the silicon conduction band (so-called ''hot'' EL).[3] Passage of a forward-bias current of 300 mA at 300 K through the structure generated no EL.

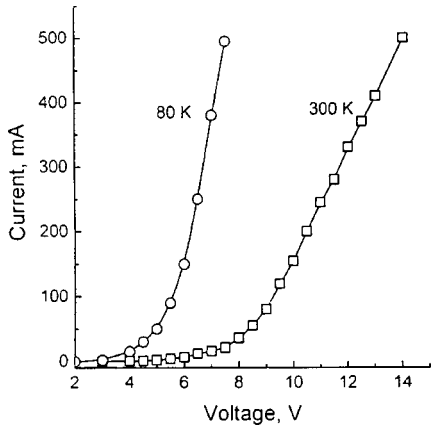

FIG. 1. Reverse branches of diode I–V characteristics at temperatures 300 K and 80 K.

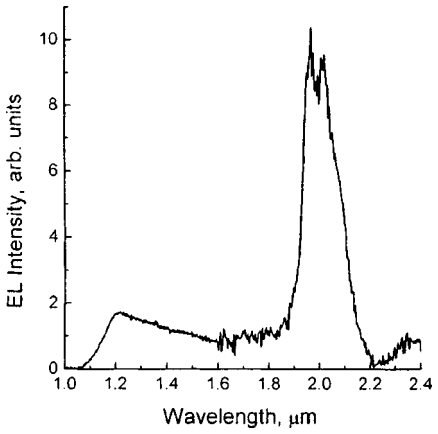

FIG. 2. Electroluminescence (EL) spectra of a reverse-biased diode at 300 K and 300 mA.

These results lead us to suggest that the mechanism for exciting EL from the holmium ions is collisions with these hot carriers.

In Fig. 3 we plot the holmium EL intensity at $\lambda = 1.96\,\mu$m and the hot EL intensity at $\lambda = 1.75\,\mu$m versus the density of reverse current passing through the diode

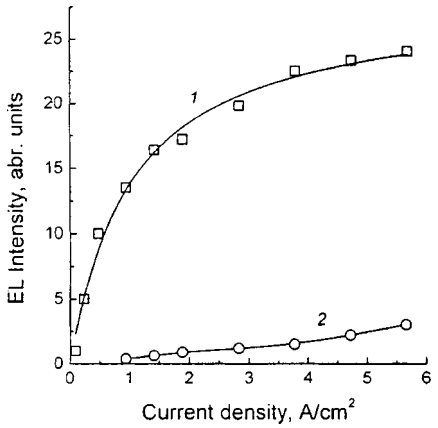

FIG. 3. Plots of the electroluniescence (EL) intensity of holmium (*1*) at $\lambda = 1.96\,\mu$m and light from the same diode at $\lambda = 1.75\,\mu$m (*2*) versus current density.

structure at 300 K. According to Ref. 4, when the collision mechanism drives the excitation of the rare-earth element ions, the dependence of the EL intensity (I_{EL}) on current density (j) is given by the expression

$$I_{EL}/I_{EL}^{max} = (\sigma\tau j/q)/(\sigma\tau j/q + 1), \quad (1)$$

where I_{EL}^{max} is the maximum EL intensity, q is the electron charge, τ is the lifetime of Ho^{3+} ions in the first excited state, and σ is the effective cross section for excitation of EL in holmium ions. Curve *1* in Fig. 3 best approximates the experimental results when $\sigma\tau \approx 1.5\times10^{-19}\,\mathrm{cm}^2\cdot\mathrm{s}$. For comparison we note that in avalanche diode structures based on Si:Er:O the value of $\sigma\tau$ for EL of Er^{3+} ions at $\lambda = 1.54\,\mu$m and 300 K comes to $8.7\times10^{-20}\,\mathrm{cm}^2\cdot\mathrm{s}$ (Ref. 5), i.e., it is smaller by a factor of ~ 1.7.

CONCLUSION

In summary, diode structures based on Si:Ho:O, operating in the avalanche breakdown regime at room temperature, were found to emit hot EL and EL in the wavelength range $\lambda \approx 1.85-2.15\,\mu$m with a peak at $\lambda \approx 1.96\,\mu$m as a result of transitions of Ho^{3+} ions from the first excited state to the ground state. The value of $\sigma\tau$ for holmium EL in these structures was $1.5\times10^{-19}\,\mathrm{cm}^2\cdot\mathrm{s}$.

This work was supported in part by the Russian Fund for Fundamental Research (Grant 99-02-17750).

*Fax: (821) 247 1017
**E-mail: nick@sobolev.ioffe.rssi.ru

[1] B. A. Andreev, N. A. Sobolev, D. I. Kuritsyn, M. I. Makhoviĭchuk, Yu. A. Nikolaev, and E. O. Parshin, Fiz. Tekh. Poluprovodn. **33**, 420 (1999) [Semiconductors **33**, 462 (1999)].
[2] N. A. Sobolev, A. M. Emel'yanov, R. N. Kyutt, Yu. A. Nikolaev, E. I. Shek, O. V. Aleksandrov, A. O. Zakhar'in, V. I. Vdovin, M. I. Makoviĭchuk, E. O. Parshin, and A. N. Yakimenko, *Abstracts of the Conference ''Nanostructures''* (Nizhniĭ Novgorod, 1999, p. 71).
[3] F. G. Chynoweth and K. G. McKay, Phys. Rev. **102**, 369 (1956).
[4] G. Franzo, S. Goffa, and F. Priolo, J. Appl. Phys. **81**, 2784 (1997).
[5] N. A. Sobolev, Yu. A. Nikolaev, A. M. Emel'yanov, K. F. Shtel'makh, P. E. Khakuashev, and M. A. Trishenkov, J. Lumin. **80**, 315 (1999).

Translated by Frank J. Crowne

SEMICONDUCTOR STRUCTURES, INTERFACES AND SURFACES

Conductivity of the insulating (oxide) layer on the surface of a semiconductor caused by electron-ion interaction at the insulator-semiconductor boundary

E. I. Goldman, A. G. Zhdan, and G. V. Chucheva

Institute of Radioengineering and Electronics, Russian Academy of Sciences, 141120 Fryazino, Russia
(Submitted January 12, 1998; accepted for publication December 8, 1998)
Fiz. Tekh. Poluprovodn. **33**, 933–939 (August 1999)

The creation of neutral electron-ion complexes at the boundary between the semiconductor and its surface insulating layer, the diffusion of these complexes, and their decay in the bulk of the insulator are discussed. An ion that appears after the decay of one of these complexes either returns to the semiconductor-insulator (SI) boundary or drifts toward the opposite electrode under the action of the electric field in the insulator layer, depending on the direction of this field. In the first case, a peculiar ion circulation takes place at the surface of the semiconductor within a layer whose thickness is of the same order of magnitude as the diffusion length for electron-ion complexes. This circulation manifests itself in the form of a stationary current through the insulator that depends only slightly on the electric field. In the second case, the transient ion current acquires a component that is independent of the magnitude of the electric field; this component is attributable to the diffusion and decay of the complexes. These effects are observed in insulating layers on silicon MOS structures. © *1999 American Institute of Physics.* [S1063-7826(99)01004-2]

The influence of ions, which are present in the insulating layer that covers most semiconductors, on the electrical properties of the semiconductor-insulator boundary (e.g., its spectrum of localized electronic states, carrier scattering ability, etc.) is now receiving considerable attention as a topic of investigation.[1–8] In contrast, there has been almost no discussion in the literature of the opposite side of the electron-ion interaction, i.e., how semiconductor electrons affect the ion subsystem in the insulator, in particular, ion migration. Diametrically opposing opinions have been expressed (at least with regard to the Si/SiO_2 boundary) about the possibility of an ion being neutralized when it captures an electron from the semiconductor in the capture center it creates along with its insulator environment. In Refs. 9 and 10, Hino, Yamashita, and DiMaria asserted that neutralization does take place, while in Refs. 3, 11, and 12 Nicollian, Chou, and Vertoprakhov claim it does not. Resolution of these two opposing claims can only come from direct observation of features in the electrical conductivity of the insulating layer arising from the neutralization effect.

In this paper we look for possible evidence of electron-ion interactions at the insulator-semiconductor boundary in the ionic conductivity of the insulating layer of an MOS structure. We assume that mobile ions are present in the insulator, with an elementary positive charge for definiteness. At sufficiently high temperatures, polarizing fields (appearing when the potential of the field electrode $V_g > 0$) gives rise to a quasi-two-dimensional layer of free ions at the boundary. In principle, tunneling transitions, in which an electron tunnels from the surface accumulation (inversion) layer of the semiconductor to a localized state (trap) created by the ion and its insulating environment, are now possible. As a result, neutral electron-ion complexes (EIC) form in the insulator. The existence of these complexes requires a new picture of the ion transport mechanism in the insulator. When a complex diffuses into the insulator interior, it can thermally decay into an ion and an electron (the latter departs for the corresponding electrode in a time that is nearly instantaneous compared to the characteristic ion transport time). Under the action of an electric field, depending on the direction of the latter, the newly-formed ion will either return to the boundary (for a polarizing voltage), or depart for the opposite contact (for a depolarizing voltage). In the first case (Fig. 1a), a peculiar nonattenuating circulation of ions occurs at the semiconductor surface within a layer whose thickness is of the same order of magnitude as the diffusion length for the complexes (λ). This causes a stationary current to flow through the insulator, which is a weak function of electric field. In the second case (Fig. 1b), the transient ion current is augmented by a component determined by diffusion and decay of complexes, which is also independent of electric field.

Let us consider the quantitative consequences of this model. Let $z=0$ be the coordinate of the boundary; the region $z<0$ consists of semiconductor, while the region $z>0$ is insulator (Fig. 1). Let us denote the bulk concentrations of ions and complexes in the insulator by N and M. The system of equations that describes electron transport in the insulator has the form

$$\frac{\partial M}{\partial t} - D\frac{\partial^2 M}{\partial z^2} + \frac{M}{\tau} + \frac{M}{\tau_i} - \frac{N}{\tau_n} = 0, \tag{1}$$

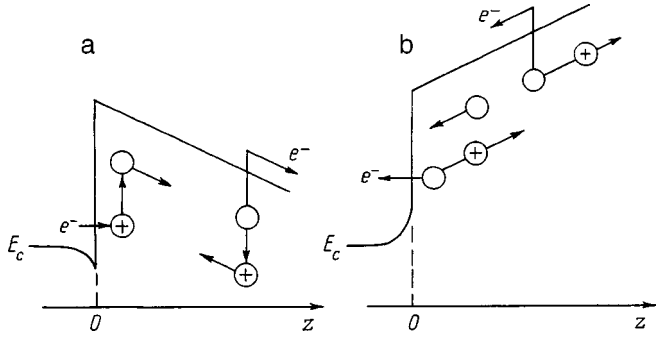

FIG. 1. Band diagrams that illustrate the transport of electrons, ions, and neutral complexes in an insulator at the boundary with a semiconductor for polarizing (a) and depolarizing (b) voltages: $z<0$ is semiconductor, $z>0$ is insulator, and E_c is the bottom of the conduction band of the semiconductor. The arrows parallel to the bottom of the conduction band of the insulator indicate the direction of spatial drift of charges and complexes. The horizontal arrows correspond to the direction of tunneling transitions for electrons: a—from the semiconductor to the insulator (in this case the reverse transition, in which electrons tunnel from a complex to the semiconductor, also occurs. This is not shown in the figure); b—from the insulator (with complexes) to the semiconductor. The vertical curves show the conversion of ions to complexes and complexes to ions.

$$\frac{\partial N}{\partial t}+\frac{1}{q}\frac{\partial j}{\partial z}-\frac{M}{\tau}-\frac{M}{\tau_i}+\frac{N}{\tau_n}=0. \tag{2}$$

Here t is time, D is the diffusion coefficient of the complexes, τ is the characteristic time for decay of a complex connected with the transition of the electron to the conduction band of the insulator, $\tau_i(z)$ is the characteristic ionization time of a complex located a distance z from the boundary ($z=0$) due to escape of its electron into the semiconductor, $\tau_n(z)$ is the characteristic time for neutralization of an ion located a distance z from the boundary ($z=0$) due to arrival of an electron from the semiconductor, q is the elementary charge, j is the ion current density $j=q\mu N\mathcal{E}-\mu T\partial N/\partial z$, μ is the mobility of the ions, $\mathcal{E}$ is the electric field in the insulator, and T is the temperature in energy units. The probabilities of ionization $\tau_i^{-1}(z)$ and neutralization $\tau_n^{-1}(z)$ fall off abruptly with increasing z. This is due to the assumed tunneling nature of electron transitions from the semiconductor to a positive ion and from a complex to the semiconductor, and, e.g., the shift in electronic levels due to hybridization of the wave functions of localized (virtual) states with the wave functions of the allowed band of the semiconductor. Under conditions where the tunneling effect predominates, good approximations for $\tau_n(z)$ and $\tau_i(z)$ are the exponential functions $\tau_n(z)=\tau_{n0}\exp(z/\delta)$ and $\tau_i(z)=\tau_{i0}\exp(z/\delta)$; the characteristic distance δ is the effective tunneling length. The ratio of pre-exponential factors is $\tau_{n0}/\tau_{i0}=\exp(\Delta E/T)$, where ΔE is the distance from an electronic level of the complex to the Fermi level at the boundary ($z=0$). It thus follows that control of the degree of neutralization of ions at the boundary is possible by varying the position of the Fermi level at the phase boundary. Of course, if the energy level of an electron in a complex is located sufficiently high above the bottom of the semiconductor conduction band, neutralization is impossible.

Boundary conditions for the system of equations (1) and (2) are: at $z=0$, $j=0$, and $D(\partial M/\partial z)=0$ (the absence of mass transport through the boundary); at $z=\infty$ we have $M=0$ and $N=0$.

Let us consider the steady-state distribution of ions and complexes at the boundary in a polarizing field $\mathcal{E}<0$, which compresses the ions against the boundary (Fig. 1a). Assuming that the diffusion length $\lambda=(D\tau)^{1/2}\gg\delta$, taking into account the boundary conditions, we obtain the following expressions from Eqs. (1) and (2):

$$\frac{\partial^2 M}{\partial z^2}-\frac{M}{\lambda^2}-\frac{M_0}{D\tau_i(z)}+\frac{N}{D\tau_n(z)}=0, \tag{3}$$

$$j-qD\frac{\partial M}{\partial z}\equiv q\mu N\mathcal{E}-\mu T\frac{\partial N}{\partial z}-qD\frac{\partial M}{\partial z}=0, \tag{4}$$

where $M_0=M|_{z=0}$. Equation (4) (i.e., the total particle current, including ions and complexes, equals zero) is also, in fact, the condition for the circulation of ions at the boundary ($z=0$). The replacement $M\to M_0$ in the third term of Eq. (3) is justified by the smallness of the decrease in M within the characteristic length over which $\tau_i(z)$ changes. The solution to Eq. (3) has the form

$$M=\frac{M_0}{2}(e^{z/\lambda}+e^{-z/\lambda})+\frac{\lambda}{2D}\int_0^z\left[\frac{M_0}{\tau_i(z_1)}-\frac{N}{\tau_n(z_1)}\right]\times[e^{(z-z_1)/\lambda}-e^{(z_1-z)/\lambda}]dz_1. \tag{5}$$

From Eq. (5) and the condition $M|_{z=\infty}=0$ we find the relation between M_0 and N:

$$\frac{\lambda}{D}\int_0^\infty\frac{e^{-z/\lambda}N}{\tau_n(z)}dz=M_0\left[1+\frac{\lambda}{D}\int_0^\infty\frac{e^{-z/\lambda}}{\tau_i(z)}dz\right], \tag{6}$$

or approximately, because $\delta\ll\lambda$,

$$M=M_0e^{-z/\lambda}, \tag{5a}$$

$$\frac{\lambda}{D}\int_0^\infty N\tau_n^{-1}(z)dz=M_0\left[1+\frac{\lambda}{D}\int_0^\infty\tau_i^{-1}(z)dz\right]. \tag{6a}$$

The profile of the distribution of ion concentration in sufficiently strong fields $|\mathcal{E}|\gg 4\pi qN_s/\kappa$ (where $N_s=\int_0^\infty Ndz$ is the surface density of ions and κ is the dielectric permittivity of the insulator) is determined from Eqs. (4) and (5a):

$$N=N_0e^{-q|\mathcal{E}|z/T}+\frac{qDM_0}{\mu T}\frac{[e^{-z/\lambda}-e^{-q|\mathcal{E}|z/T}]}{(q|\mathcal{E}|\lambda/T-1)}. \tag{7}$$

From this we have $N_s=(N_0T/q|\mathcal{E}|)+(DM_0/\mu|\mathcal{E}|)$. Using Eq. (5a), we find the ratio of surface densities of free ions and ions bound at the complex:

$$\frac{N_s}{M_0\lambda}=\left(\frac{\delta}{\lambda}+\frac{T}{q|\mathcal{E}|\lambda}\right)\left(\frac{\tau_{n0}}{\tau_{i0}}+\frac{D\tau_{n0}}{\lambda\delta}\right)+\frac{\lambda}{\mu|\mathcal{E}|\tau}. \tag{8}$$

Thus, nearly all the ions are neutralized ($N_s\ll M_0\lambda$) in strong polarizing fields if the decay time of a complex τ is much longer than the time of flight of an ion over a diffusion length $\lambda/\mu|\mathcal{E}|$ and the neutralization time τ_{n0}, and the ratio

of the ionization probability to neutralization probability τ_{n0}/τ_{i0} turns out to be considerably smaller than λ/δ.

The current density through the insulator is determined by the rate of bulk generation of electrons as the complexes decay:

$$J=\frac{qM_0\lambda}{\tau}; \tag{9}$$

if $N_s \ll M_0\lambda$, then $M_0\lambda \simeq \mathcal{N}$ is the total surface density of particles (ions and complexes) and $J \simeq q\mathcal{N}/\tau$.

Let us now consider the transient process of ion transport after switching from a polarizing field to a depolarizing field ($\mathcal{E}>0$, Fig. 1b). We assume that the drift time of the ions through the insulating layers $\tau_d = h/\mu\mathcal{E}$ (where h is the thickness of the dielectric layer) is considerably smaller than the decay time for a complex τ and the ionization time $\tau_i(\lambda)$ at a distance on the order of the diffusion length λ measured from the SI boundary. For $t \gg \tau_d$ we then can ignore the terms $\partial N/\partial t$ and N/τ_n in Eqs. (1) and (2).

The current density through the insulator is determined by the flux of ions at distances $z \gg \lambda$, i.e., $J=j|_{z=\infty} = q\int_0^\infty M(1/\tau+1/\tau_i)dz$; see Eq. (2). Let us introduce the time t_* at which the decay time for a complex located at $z=z_*$ equals the diffusion time of the complex over a distance z_*, $t_*^{-1}=\tau_i^{-1}(z_*)+\tau^{-1}=(z_*^2/D)^{-1}$. For $t \ll t_*$ (but for $t \gg \tau_d$, of course) diffusion of the complexes can be ignored, and the solution of Eq. (1) has the form

$$M=M_i(z)\mathrm{e}^{-t[1/\tau_i(z)+1/\tau]},$$

where $M_i(z)$ is the initial distribution of complexes. Assuming in accordance with Eq. (5a) that $M_i(z)=M_0\exp(-z/\lambda)$, we obtain an expression for the transient current density through the insulator:

$$J=q\int_0^\infty M_0\mathrm{e}^{-z/\lambda}\left[\frac{1}{\tau_i(z)}+\frac{1}{\tau}\right]\mathrm{e}^{-t[1/\tau_i(z)+1/\tau]}dz. \tag{10}$$

Equation (10) is typical of relations that describe transient processes in electronic systems with dispersion of the lifetimes. Under conditions where the decay time of a complex varies with coordinate z much more rapidly than the initial profile $M_i(z)$ for the complexes, i.e., $|\partial\ln(1/\tau+1/\tau_i)/\partial z| \gg |\partial\ln M_i(z)/\partial z|$,[1)] it follows from the theory of relaxation spectroscopy for systems with distributed lifetimes[13] that

$$J=\frac{qM_0\xi}{t}\,\mathrm{e}^{-z_m/\lambda}. \tag{11}$$

Here z_m is the coordinate that separates the region where the complexes have already disappeared due to ionization ($z<z_m$) from the region where decay of the complexes has not yet occurred ($z>z_m$). The value of z_m is determined from the condition $t[\tau_i^{-1}(z_m)+\tau^{-1}]=1$, from which $z_m = \delta\ln[t\tau/(\tau-t)\tau_{i0}]$; $\xi=\delta[1+\tau_i(z_m)/\tau]$ is the effective thickness of the transition layer from the region in which $M(z)=0$ to the region in which $M=M_i(z)$. When condition $t \ll \tau$ is satisfied, i.e., $\tau_i(z_m) \ll \tau$, Eq. (11) simplifies:

$$J=\frac{qM_0\delta\tau_{i0}^{\delta/\lambda}}{t^{1+\delta/\lambda}}. \tag{12}$$

Now let $t \gg t_*$; in the layer $(0, z_*)$ the complexes have already decayed, while for $z>z_*$ their diffusion takes place more rapidly than their ionization via escape of their electrons into the semiconductor. The transient process is determined by diffusion of complexes through the insulator under the conditions $M|_{z=z_*}=0$ and their decay in the bulk with a characteristic time τ. Within the framework of this standard diffusion problem, the expression for the transient current has the form

$$J=\frac{qM_*\sqrt{D}}{\sqrt{\pi t}}\,\mathrm{e}^{-t/\tau}, \quad M_*=M_0\mathrm{e}^{-z_*/\lambda}, \tag{13}$$

where M_* is the initial concentration of complexes in the plane $z=z_*$. In Eq. (13) we have already taken into account the fact that within the time period $(0,t_*)$ the concentration of complexes decreases by a factor of $\exp(t_*/\tau)$ due to their decay in the bulk. We note that in this regime ($t \gg t_*$) the complexes diffuse from the insulator bulk to the boundary, in contrast to the steady-state situation considered previously, where the current is determined by diffusion of complexes from the boundary into the bulk of the dielectric.

These features of the electrical conductivity of the insulator associated with the formation of clusters were observed, as predicted, in insulating layers at the Si/SiO_2 boundary. The experiments were carried out on MOS structures based on *n*-Si(100) using a field electrode (Al) with an area $S=2.4\times10^{-2}\,\mathrm{cm}^2$. An insulating layer with thickness $h=1700$ Å was created by thermal oxidation in dry oxygen at 1100 °C. At 300 K, the concentration of electrons in *n*-Si comes to $10^{13}\,\mathrm{cm}^{-3}$. Immobile ions are not introduced intentionally into the SiO_2 layer; for these investigations samples were selected with negative values of the flat-band potential $|V_{fb}| \geqslant 1$ V. Details of the measurement technique and methods can be found in Refs. 14 and 15. The most obvious consequences of ion neutralization and formation of complexes implied in the analysis given above are the following: the presence of a steady-state ion current in polarizing voltages given by Eq. (9), hyperbolic kinetics for the attenuation of the depolarizing current (in the regime of isothermal relaxation), and the latter's independence of electric field, i.e., Eq. (12).

Identification of a stationary current under conditions where the time-dependent ionic polarization of the oxide approaches its final stages extremely slowly[15] gives rise to certain difficulties: it is unclear which current the measurement device is recording—the steady-state or extremely slow relaxation current. This problem was solved by the method of thermal-modulation measurements. After being polarized at a preset temperature of 423 K, the sample was first cooled down to a temperature at which the current became unrecordable, and then heated back to the original temperature. Regardless of how the temperature varies, under steady-state conditions the values of current at identical temperatures (including the original temperature) should coincide for arbitrarily large numbers of cooling-heating cycles. These assertions are superbly reproduced in the experiment: current levels at the same temperatures coincide. Their activation

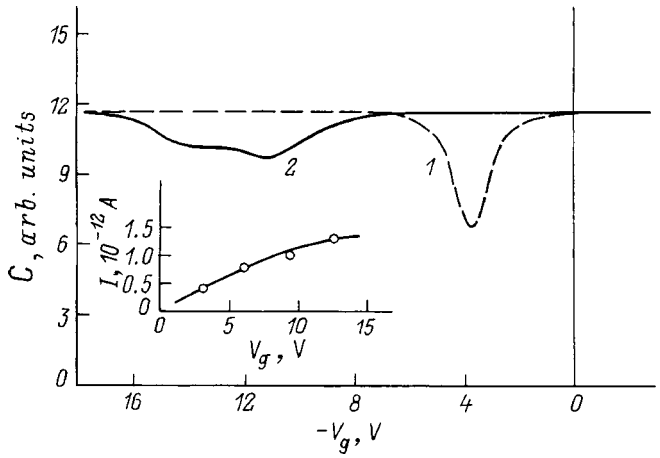

FIG. 2. Quasistatic C–V characteristics of a silicon MOS structure at 300 K before (*1*) and after (*2*) polarization. Regime of polarization: temperature 400 K, voltage +3 V, time 3 min. The linear sweep rate of the voltage V_g is 0.025 V/s. The inset shows I–V characteristics for the steady-state ion current. Polarizaton regime: temperature 423 K, time 30 min.

energy E_τ, determined from data taken during nine successive measurement cycles, comes to 1.19 ± 0.03 eV.

The qualitative changes in the shape of the quasistatic capacitance-voltage (CV) characteristic that appear after the sample is polarized constitute direct evidence of neutralization of ions at the SiO_2 / Si boundary. It is clear from Fig. 2 that the CV characteristic is significantly broadened after transport of the ions to the interphase boundary, and the minimum value of the MOS structure capacitance increases significantly. Most of this broadening of the CV characteristic takes place at voltages for which the silicon surface is still in accumulation.[2)] This is characteristic of MOS structures with localized states at the boundary that are distributed within a range of energies concentrated above the Fermi level of the semiconductor under flat-band conditions. An estimate of the total number of these states based on the usual method of processing CV characteristics[16] gives a value $\sim 1.1 \times 10^{11}\,\mathrm{cm}^{-2}$. The closeness of this value to the total density of ions $2 \times 10^{11}\,\mathrm{cm}^{-2}$ (for this trial) indicates a high degree of neutralization of the ions. We note that this electronic charge cannot be localized in wells of the fluctuating potential caused by ions, since at 300 K the amplitude of this potential is $\leqslant T$.

From the theory we have developed it follows that as the polarizing field increases, the degree of neutralization of ions increases as well—see Eq. (8). Therefore, the dc I–V characteristics of an MOS structure in the polarization regime should have the shape of a curve with saturation. The experimental data (see the inset in Fig. 2) completely confirm this assertion. The sublinear nature of the current's field dependence excludes the possibility of interpreting it as an electron leakage current, for which exponential dependences on voltage are typical consequences of most field transport mechanisms—Frenkel, tunneling, etc.[16]

Thus, the observed steady-state current should be regarded as resulting from thermal decay of complexes that diffuse away from the boundary into the SiO_2 bulk. Assuming that $M_0 \lambda \simeq \mathcal{N}$ and, in agreement with the experimental

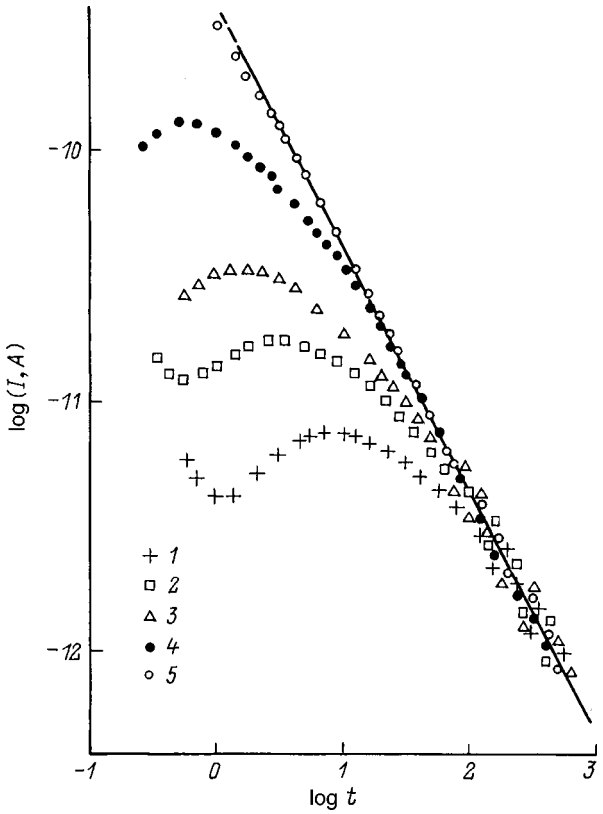

FIG. 3. Kinetics of relaxation of the depolarization current at a temperature of 333 K. Depolarization voltage $|V_g|$, V: *1* — 0.77; *2* — 1.56; *3* — 3.12; *4* — 4.85; *5* — 15.9. Polarization regime: temperature 423 K, voltage +5 V, time 5 min. The initial density of ions at the SiO_2/Si boundary $\mathcal{N} \simeq 10^{12}$ cm^{-2} (obtained by integrating the depolarization current according to the method of Refs. 14 and 15). The initial falloff of the current, which is significant for the relaxation curves when $V_g = -0.77$ and -1.56 V, is caused by differentiation of the step in the depolarizing voltage by the geometric capacitance of the sample.

data, that $\mathcal{N} = 1 \times 10^{12}\,\mathrm{cm}^{-2}$,[3)] we find $\tau = \tau_0 \exp(E_\tau / T) = 3.6 \times 10^3$ s. Using the value $E_\tau = 1.19 \pm 0.03$ eV determined previously, we obtain $\tau_0 = (1.7 - 8.7) \times 10^{-11}$ s.

We now turn to analyzing the experimental data derived from isothermal relaxation. As before, the samples were polarized at 423 K. The direction of the field was then switched and the time dependence of the depolarizing current was measured for various values of the potential on the field electrode V_g ($V_g < 0$). A typical family of these depolarizing curves is shown for a temperature of 333 K in Fig. 3. Two features attract our attention.

1. At the initial stage of the relaxation we observe a typical time-drift effect:[17,18] The dependence of the drift time of the ions τ_d (points where the transient characteristics are maxima) on V_g follows the classical law $\tau_d^{-1} \sim V_g$ (Fig. 4). When the mobility of the ions found from the relation $\mu = h/(\tau_d \mathcal{E})$ is plotted as a function of temperature, it follows the Arrhenius law with activation energy $E_\mu = 0.8$ eV (Fig. 5). The pre-exponential factor in the expression $\mu = \mu_0 \times \exp(-E_\mu / T)$, obtained by extrapolating the straight line in Fig. 5 to high temperatures ($T^{-1} \to 0$), is $\mu_0 = 72.5$ $\mathrm{cm}^2/(\mathrm{V} \cdot \mathrm{s})$. This value allows us to determine $\mu(423\,\mathrm{K}) = 2.7 \times 10^{-8}$ and $\mu(453\,\mathrm{K}) = 1 \times 10^{-7}\,\mathrm{cm}^2/(\mathrm{V} \cdot \mathrm{s})$. These val-

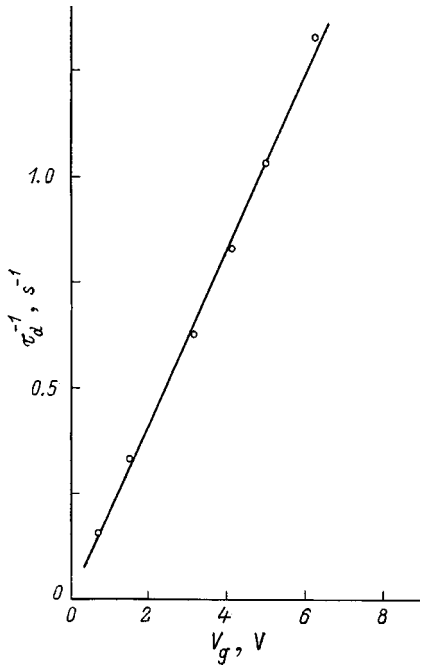

FIG. 4. Dependence of the inverse drift time τ_d^{-1} on the depolarizing voltage $|V_g|$ ($V_g<0$) according to the data of Fig. 3.

ues, like the value $E_\mu=0.8$ eV, are in excellent agreement with the values determined previously by an independent method:[15] $\mu(423\,\mathrm{K})=2.5\times10^{-8}$ and $\mu(453\,\mathrm{K})=1.1\times10^{-7}\,\mathrm{cm^2/(V\cdot s)}$, $\mu_0=85.5\,\mathrm{cm^2/(V\cdot s)}$, and $E_\mu=0.8\,\mathrm{eV}$. They also agree with the most reliable literature data for Na^+ ions.[8]

2. After the front of free ions has passed, the depolarizing current first decays, while remaining a function of the applied voltage V_g. Eventually, however, all the relaxation curves are asymptotic to a single straight line independent of V_g, on which the current I follows the hyperbolic law $I\sim t^{-(1+\alpha)}$, $\alpha\ll1$, in exact agreement with the theoretical expression (12). At a temperature of 333 K (Fig. 3) we have $\tau\simeq2.2\times10^7$ s and it is impossible to observe an exponential region of depolarization kinetics corresponding to diffusion and decay of complexes [see Eq. (13)] in the range of real

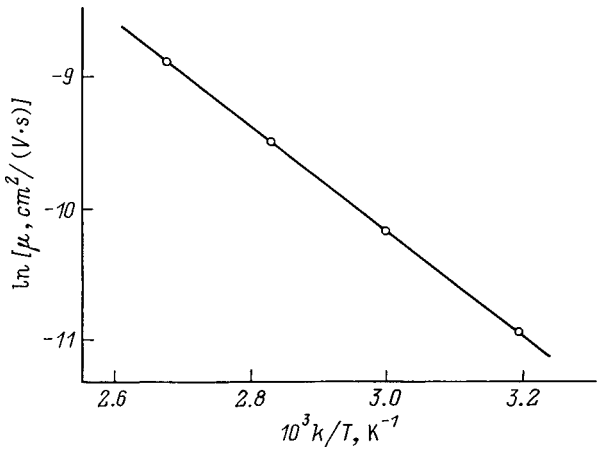

FIG. 5. Temperature dependence of the ion mobility determined by the time-of-flight method. The polarization regime is the same as in Fig. 3.

times. Therefore, the ionic charge that remains at the SiO_2/Si boundary after a lapse of 10^3 s (Fig. 3) is determined by integrating the curve for the thermal-stimulated depolarization current. The density of free ions is found by integrating the relaxation curve from time $t\simeq0$ to the time at which the time-flight and hyperbolic curves merge; the remaining area under the relaxation curve before $t\simeq10^3$ s is added to the area under the thermal-stimulated depolarization curve, which allows us to determine the value of $\mathcal{N}$. It turned out that in the polarization state the total ion density $\mathcal{N}=1\times10^{12}\,\mathrm{cm^{-2}}$, of which $8\times10^{11}\,\mathrm{cm^{-2}}$ of them are neutralized. Expressed as in percentage ratios, these data agree with the results of previous estimates based on CV characteristics.

The slope of the straight line $\log I$ — $\log t$ in Fig. 3 equals 1.08, i.e., $\delta/\lambda=0.08$ for the initial spatial distribution of complexes at 423 K—see Eq. (12); the quantity λ used here corresponds to the polarization condition. Setting $\delta\simeq1$ Å (Ref. 19), we have $\lambda\simeq12.5$ Å. Consequently, the diffusion coefficient for complexes at 423 K is $D=\lambda^2/\tau=4.3\times10^{-18}\,\mathrm{cm^2\cdot s^{-1}}$, which is eight orders of magnitude smaller than the diffusion coefficient for free ions.[18]

The comparison we have made of theory and experiment has shown good qualitative and quantitative agreement between the two, which points directly to a fundamental role for complexes in electrical transport in insulator layers.

The picture we have developed here allows us to explain the anomalously large width (up to $\lesssim50$ Å) of the region of the spatial localization of ions near the surface in a natural way.[10] In fact, after polarization of the MOS structure at a temperature T in a field $\mathcal{E}$, the characteristic decay length of the ion density from the boundary into the depth of the insulator is $T/q|\mathcal{E}|\ll\lambda$. However, cooling the sample shifts the equilibrium of the ionization/neutralization processes towards an increased role for ionization, since neutralization requires some thermal activation. As a result, the complexes will decay and the ions that form in this case will appear to be ''frozen'' at the positions of their parent complexes, which under polarization conditions are distributed at the boundary over a layer whose thickness is on the order of several $\lambda=12.5$ Å, i.e., on the order of 50 Å.

The model we have considered agrees with previously known observations of a characteristic asymmetry in the polarization and depolarization processes in silicon MOS structures: when other conditions are kept the same, polarization takes place much more slowly than depolarization.[14,15,20] Increasing the depolarizing field causes the electron concentration at the semiconductor surface to fall off; consequently, the rate of decay of complexes with respect to the rate of neutralization increases. The position of the Fermi level in the metal (gate) is fixed; therefore, the equilibrium of the ionization-neutralization processes at the SiO_2/Me boundary is unaffected by the polarizing electric field.

We should not identify the experimental value $E_\tau\simeq1.19$ eV we have found, at least at $z=0$, with the distance from the energy level of an electron in a complex to the bottom of the insulator conduction band (Fig. 1). Since the observed degree of neutralization of the ions is quite high, this distance should be much larger. This fact could be associated either with ionization of the complexes in the bulk of

the insulator due to transitions of electrons to a band of delocalized states in the energy gap of SiO_2,[21,22] or with a strong reconstruction of the (virtual) electronic state localized on the complex at the phase boundary, for example, as a result of hybridization of its wave function with wave functions of allowed bands of the semiconductor. For the latter reason, the passage of a complex from the surface to the bulk of the insulator can be contingent on the overcoming of a certain energy barrier. However, this barrier is not manifested in the experiment if the limiting step for steady electrical transport is diffusion and decay of complexes in the insulator bulk rather than their escape from the phase boundary.

We note in conclusion that the hyperbolic law observed experimentally for the relaxation of the depolarization current $I \sim t^{-(1+\alpha)}$, $\alpha < 1$, is typical of bulk dispersive transport.[21–24] Nevertheless, the model we have developed in this paper makes it plain that the physical nature of this law is entirely different here: it is connected with the dispersive nature of the contact conditions, which manifest themselves in the form of a distribution of tunneling ionization times. It is for this reason that we do not see the other relaxation regime that is characteristic of disperive transport, i.e., $I \sim t^{-(1-\alpha)}$.

CONCLUSIONS

1. Electron-ion exchange at the SiO_2/Si phase boundary leads to the formation and decay of neutral ion + electron complexes in the insulator.

2. In polarizing fields, diffusion of neutral complexes into the SiO_2 bulk with their subsequent decay leads to a nonattenuating circulation of ions at the Si surface, giving rise to a steady-state current through the insulator that is only a weak function of the electric field.

3. In depolarizing fields, the decay of neutral complexes via tunneling transitions of electrons into the Si manifests itself in the form of a quasihyperbolic dispersion law for the decrease of the depolarizing current with time. Under these conditions the depolarizing current does not depend on the magnitude of the electric field.

4. The degree of initial neutralization of ions at the SiO_2/Si boundary is determined by the polarization conditions. In relatively weak polarizing fields the number of neutral complexes can be small. In this case the depolarization process will be determined basically by free-ion transport.

We wish to thank N. F. Kukharskaya for a great variety of constructive assistance.

[1)] This inequality is satisfied for $\tau_{i0} \ll \tau$ and $\delta \ll \lambda$.

[2)] This circumstance does not allow us sufficient precision to use the standard method of Ref. 16, i.e., to compare the shift in C–V characteristics based on the field electrode voltage ΔV_g caused by polarization with the magnitude of the ionic charge qN_sS (here $\Delta V_g = qN_sS/C_{SiO_2}$, where C_{SiO_2} is the capacitance of the dielectric layer.

[3)] The quantity $\mathcal{N}$ is determined from independent measurements by integrating the depolarization current; see Ref. 15.

[1] A. Hartstein and A. B. Fowler, Surf. Sci. **73**, 19 (1978).
[2] V. A. Gerel' and R. A. Suris, Zh. Éksp. Teor. Fiz. **75**, 191 (1978) [Sov. Phys. JETP **47+48**, 95 (1978)]; Zh. Éksp. Teor. Fiz. **84**, 719 (1983) [Sov. Phys. JETP **57**, 415 (1983)].
[3] E. H. Nicollian and J. R. Brews, *MOS (Metal-Oxide Semiconductors) Physics and Technology* (N. Y., 1982).
[4] T. Ando, A. Fowler, and F. Stern, *Electronic Properties of Two-Dimensional Systems* (Mir, Moscow, 1985).
[5] V. D. Dobrovol'skiĭ and V. G. Litovchenko, *Electron and Hole Transport at Semiconductor Surfaces* (Naukova Dumka, Kiev, 1985).
[6] J. F. Verwey, E. A. Amerasekera, and J. Bisschop, Rep. Prog. Phys. **53**, 1297 (1990).
[7] V. A. Gerel' and G. V. Shpatkovskaya, Zh. Éksp. Teor. Fiz. **102**, 640 (1992) [Sov. Phys. JETP **75**, 342 (1992)].
[8] E. Atanassova and A. Paskaleva, Solid-State Electron. **39**, 1033 (1996).
[9] T. Hino and K. Yamashita, J. Appl. Phys. **50**, 4879 (1979).
[10] D. J. DiMaria, J. Appl. Phys. **52**, 7251 (1981).
[11] N. J. Chou, J. Electrochem. Soc. **118**, 601 (1971).
[12] V. N. Vertoprakhov, B. M. Kuchumov, and V. G. Sal'man, *Fabrication and Properties of Si–SiO$_2$-M Structures* (Nauka, Novosibirsk, 1981).
[13] E. I. Goldman and A. G. Zhdan, Semicond. Sci. Technol. **5**, 675 (1990).
[14] E. I. Goldman, A. G. Zhdan, and G. V. Chucheva, Prib. Tekh. Eksp. No. 6, 110 (1997).
[15] E. I. Goldman, A. G. Zhdan, and G. V. Chucheva, Fiz. Tekh. Poluprovodn. **31**, 1468 (1997) [Semiconductors **31**, 1520 (1997)].
[16] S. M. Sze, *Physics of Semiconductor Devices* (Wiley, New York, 1969; Mir, Moscow, 1984).
[17] R. J. Kriegler and T. F. Devenyi, Thin Solid Films **36**, 435 (1976).
[18] S. R. Hofstein, Appl. Phys. Lett. **10**, 291 (1967).
[19] I. Lundstrom and C. Svensson, J. Appl. Phys. **43**, 5045 (1972).
[20] M. Kuhn and D. J. Silversmith, J. Electrochem. Soc. **118**, 966 (1971).
[21] P. Nagels, in the collection: *Amorphous Semiconductors* (Mir, Moscow, 1982).
[22] V. A. Gritsenko, *Fabrication and Electronic Structure of Amorphous Insulators in Silicon MOS Structures* (Nauka, Novosibirsk, 1993).
[23] H. Scher and E. W. Montroll, Phys. Rev. B **12**, 1255 (1975).
[24] I. P. Zvyagin, *Kinetic Phenomena in Disordered Semiconductors* (Moscow State Univ. Publ., Moscow, 1984).

Translated by Frank J. Crowne

Determination of the valence-band offset and its temperature dependence in isotypic heterojunctions p-$Al_xGa_{1-x}As$/p-$Al_yGa_{1-y}As$ from $C-V$ measurements

V. I. Zubkov,*) M. A. Mel'nik, A. V. Solomonov, and A. N. Pikhtin

St. Petersburg State Electrotechnical University, 197376 St. Petersburg, Russia

F. Bugge

Ferdinand-Braun-Institut für Höchstfrequenztechnik, Berlin, Germany
(Submitted January 18, 1999; accepted for publication January 20, 1999)
Fiz. Tekh. Poluprovodn. **33**, 940–944 (August 1999)

The isotypic heterojunctions p-$Al_xGa_{1-x}As$/p-$Al_yGa_{1-y}As$, grown by MOVPE on n-GaAs substrates, have been investigated by the voltage–capacitance method at temperatures ranging from 300 to 100 K. To determine the valence-band offset ΔE_V and the built-in charge in the heterojunction, the Poisson equation was solved numerically on a nonuniform coordinate grid. The incomplete ionization of the acceptors and the different magnitude of the permittivity in different layers of the heterostructure were taken into account in the calculation. It was found that for a p-$Al_{0.2}Ga_{0.8}As$/p-$Al_{0.5}Ga_{0.5}As$ heterojunction ΔE_V at room temperature is 39% (113 meV) of the total gap ΔE_g and decreases monotonically to 35% at $T=120$ K. © *1999 American Institute of Physics.* [S1063-7826(99)01108-4]

1. INTRODUCTION

The ratio of the valence- and conduction-band offsets is a key parameter that controls the operation of modern devices based on heterostructures, specifically, laser heterodiodes. Despite the large number of publications on the determination of the band offset in heterojunctions based on AlGaAs and InGaAs solid solutions (see Refs. 1–3 and the references cited there), the magnitudes and temperature and composition dependences of the band offsets in these materials are still not completely clear. As a rule, in most previous publications n–n type heterojunctions were considered, and the effect of incomplete ionization of the impurity was ignored. In addition, the dopant profile near the heterojunction has a considerable effect on the results of fitting calculations of the energy parameters of the heterojunctions.

The subject of the present investigation is the accurate determination of band offsets in AlGaAs and InGaAs heterostructures. To this end, heterojunctions and quantum wells with an active region as in laser diode structures and a controllable dopant density, as well as single quantum wells with a constant dopant density and quantum wells not doped deliberately were prepared specially. The present paper is part I of a study of the parameters of isotypic heterojunctions and simulation of their $C-V$ characteristics. Part II will be devoted to profiling of the impurity near quantum wells and the self-consistent solution of the Schrödinger and Poisson equations.

2. EXPERIMENTAL RESULTS

We measured the $C-V$ characteristics of laser heterostructures $Al_xGa_{1-x}As$ containing a quantum well (QW). The structures were grown by the MOVPE method on n-GaAs substrates.[4,5] The sequence of grown layers for one structure is presented in Fig. 1.

In asymmetric p–n structures the space-charge region was 0.19–0.20 μm wide at zero bias. A quantum well was located deep inside the depleted region; this is confirmed by SIMS measurements (Fig. 2).[6] As the reverse bias was increased, the boundary of the space-charge zone shifted into the weakly doped region p-$Al_{0.2}Ga_{0.8}As$ and crossed the isotypic heterojunction p-$Al_{0.2}Ga_{0.8}As$/p-$Al_{0.5}Ga_{0.5}As$.

To determine the valence-band offset ΔE_V and the built-in charge N_{ss} in the heterojunction, numerical simulation of the $C-V$ characteristic was performed by solving the one-dimensional Poisson equation neglecting the contribution of the minority charge carriers

$$\varepsilon_0\varepsilon\frac{d^2\varphi(x)}{dx^2}=e[N_A^-(x)-p(x)] \tag{1}$$

with boundary conditions on the potential $\varphi(x)$. In the relation (1) $p(x)$ is the hole density and $N_A^-(x)$ is the density of the ionized part of the dopant.

Since band bending near a heterojunction often causes a level corresponding to the band edge to cross the Fermi level, degeneracy must be taken into account. Moreover, the possibility of incomplete ionization of the impurity must be taken into account in the simulation, since in many solid solutions the depth of the dopant is appreciable (about 40 meV for zinc in $Al_xGa_{1-x}As$[7]) and impurity centers are not completely ionized even at room temperature. Taking these circumstances into account, the mobile charge carriers and the ionized part of the impurity were calculated according to the equations

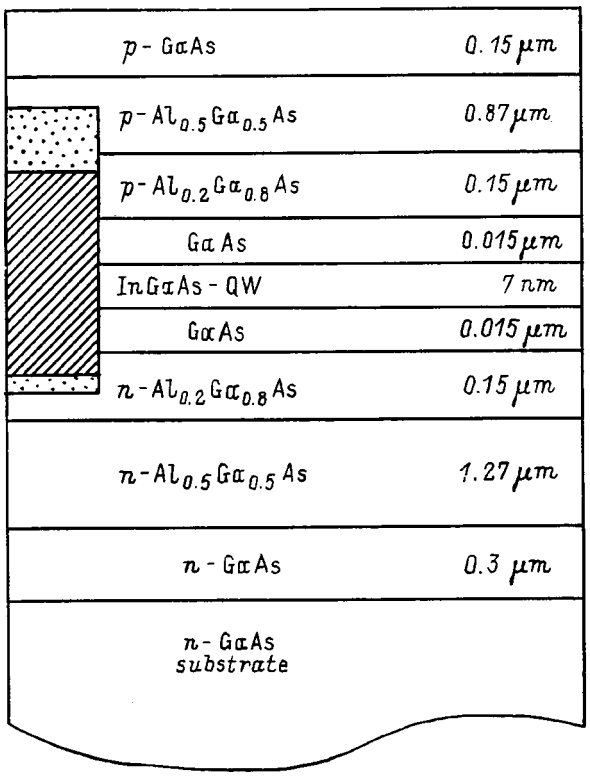

FIG. 1. Layer sequence in the heterostructures (sample No. 020100). The space-charge regions with $U_s=0$ V (wall area) and $U_s=-9$ V (larger area) are hatched.

$$p(x)=N_V\frac{2}{\sqrt{\pi}}\mathrm{F}_{1/2}\left(\frac{E_V-E_F-e\varphi(x)}{kT}\right), \tag{2}$$

$$N_A^-(x)=\frac{N_A}{1+g_A\exp\left(\dfrac{E_A-e\varphi(x)}{kT}\right)}, \tag{3}$$

where $\mathrm{F}_{1/2}$ is the Fermi–Dirac integral with index 1/2 (Ref. 8), g_A is the degeneracy factor of the acceptor level with energy E_A, and all other notation is standard.

We then linearized Eq. (1); accordingly, we represented the potential as a sum:

$$\varphi(x)=\varphi_0(x)+\Delta\varphi(x), \tag{4}$$

where φ_0 is the initial approximation, and $\Delta\varphi$ is a correction ($\Delta\varphi\ll\varphi_0$). As usual, the initial approximation was obtained by solving the Poisson equation in an approximation with a space-charge region with sharp boundaries.

Expanding the Fermi–Dirac integral in a series and dropping the nonlinear terms, we can write the Poisson equation as follows:

$$\varepsilon_0\varepsilon\left[\frac{d^2\varphi_0(x)}{dx^2}+\frac{d^2\Delta\varphi(x)}{dx^2}\right]=e\left\{N_A^-(x)-p(x)\left[1+\frac{\Delta\varphi(x)e}{kT}\right]\right\}. \tag{5}$$

This equation, which is linear in the correction $\Delta\varphi$, was solved by the finite-difference method on a nonuniform coordinate grid. A nonuniform grid must be introduced because of the nearly exponential dependence of the charge-carrier density on the potential in the expression (2).

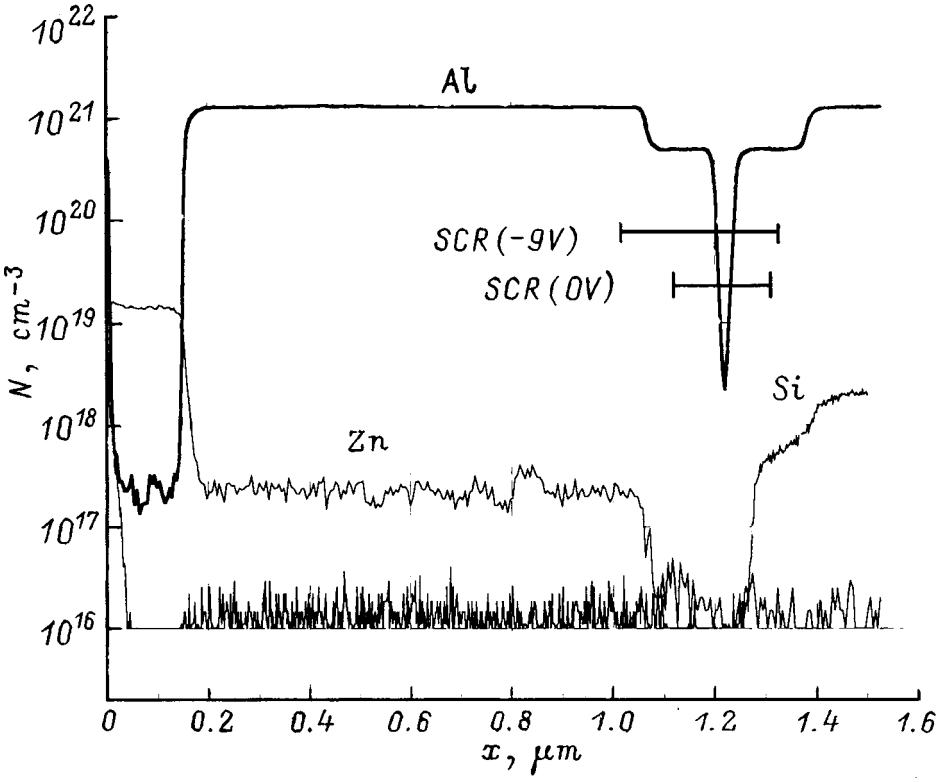

FIG. 2. Results of SIMS measurements of the dopant composition and profile in the laser heterostructure $Al_xGa_{1-x}As$ (sample No. 020100). The width of the space-charge region with reverse biases $U=0$ and -9 V is shown.

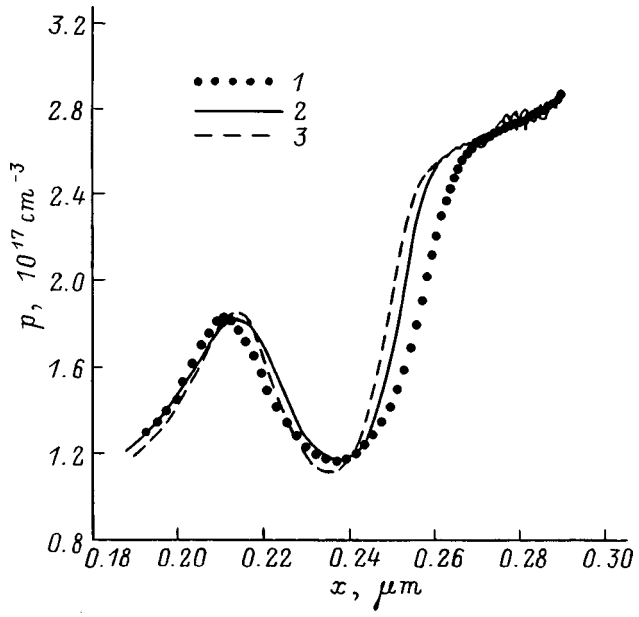

FIG. 3. Measured and computed hole density profiles near the p-$Al_{0.2}Ga_{0.8}As$/p-$Al_{0.5}Ga_{0.5}As$ heterojunction: *1* — experiment at $T=300$ K, *2* — calculation with $\Delta E_{Zn}=40$ meV and partial ionization, *3* — calculation with complete ionization.

Discretization of the linearized Poisson equation gives a system of linear equations with a tridiagonal matrix. The system was solved by the elimination method. Iterations were repeated until the correction $\Delta\varphi(x)$ became comparable to machine accuracy ($\approx 10^{-10}$ V). The iteration process based on Eq. (4) converges superlinearly near the solution, so that four or five iterations suffice to find the potential distribution.

To obtain the potential distribution in a structure containing a heterojunction, the Poisson equation (5) must be solved for each layer of the material and boundary conditions of the form

$$e\varphi_l(x_j)=e\varphi_{\text{sub}}(x_j)+\Delta E_i, \tag{6}$$

$$\varepsilon_0\varepsilon_l\frac{d\varphi_l(x_j)}{dx}=\varepsilon_0\varepsilon_{\text{sub}}\frac{d\varphi_{\text{sub}}(x_j)}{dx}+\sigma \tag{7}$$

must be satisfied at the heterojunction. Here ΔE_i is the total difference in the band gaps of the layers, and σ is the built-in surface charge density. The subscript l refers to one layer and ''sub'' refers to the other layer. Thus, the iteration process consists of solving the Poisson equation for each layer of the semiconductor, with allowance for the boundary conditions on the potential, and then correcting the solution to ensure that the boundary conditions on the first derivative of the potential are satisfied.

A modified Newton's method was used to match the solutions in individual layers. Numerical experiments show that the iteration process converges stably when the potential on the heterojunction is initially set equal to the value U_0 in the interior volume of the semiconductor. To start the iteration process Poisson's equations were solved for both layers with the potential difference kT/e in the heterojunction,

$$\varphi_{\text{iter}=1}=U_0, \quad \varphi_{\text{iter}=2}=\varphi_{\text{iter}=1}+kT/e. \tag{8}$$

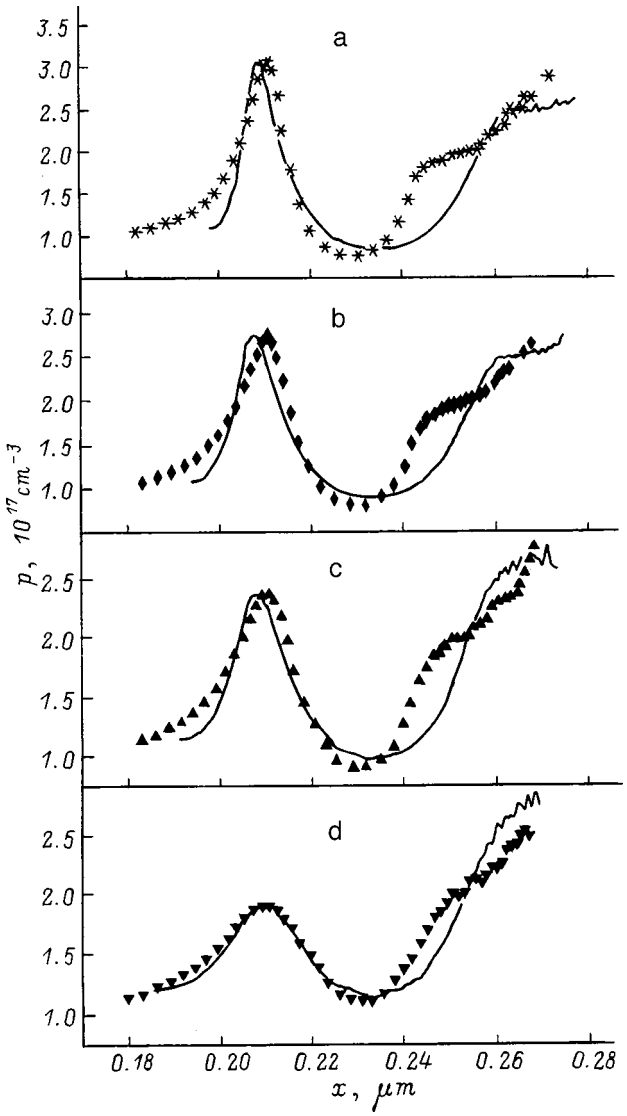

FIG. 4. Experimental hole density profiles in the p-$Al_{0.2}Ga_{0.8}As$/p-$Al_yGa_{1-y}As$ heterojunction (dots) and computed curves (solid lines) at temperatures T, K: a — 120, b — 150, c — 190, and d — 290.

In the numerical calculations the derivative was again replaced by a difference relation calculated on the basis of the results of the two preceding iterations:

$$\frac{d}{d\varphi}\left[\frac{d\varphi(x)}{dx}\right]=\frac{\varepsilon_l\left(\frac{d\varphi_{i-1}}{dx}\right)-\varepsilon_s\left(\frac{d\varphi_{i-1}}{dx}\right)-\varepsilon_l\left(\frac{d\varphi_i}{dx}\right)+\varepsilon_s\left(\frac{d\varphi_i}{dx}\right)}{\varphi_{i-1}-\varphi_i}. \tag{9}$$

The coordinate grid was constructed on a logarithmic scale. This saved time and increased the computational accuracy substantially. Ordinarily, we chose a voltage step of 0.1 V and 200 points along the coordinate axis. The corresponding values of the direct and indirect band gaps and of the other parameters of $Al_xGa_{1-x}As$ solid solutions, required for the calculations, were taken from Refs. 1 and 7. The calculations showed that the incomplete ionization of acceptors (Zn) in $Al_xGa_{1-x}As$, especially near a heterojunction,

decreases the depletion and enrichment regions at the heterojunction. For this reason, the valence-band offset ΔE_V determined without regard for this effect is too large. It should be noted that we have observed that this phenomenon depends on the ratio of the effective hole masses m_{lh} and m_{hh}. The effect of ΔE_V and N_{ss} on the observed carrier profile was demonstrated in detail. It was found that the effect of these two quantities is fundamentally different, and the two effects are weakly correlated. This enabled us to determine separately the contribution of each parameter.

The experimentally observed (apparent) profile, determined from $C-V$ measurements, of the majority charge carriers (holes) near a p-$Al_{0.2}Ga_{0.8}As/p$-$Al_{0.5}Ga_{0.5}As$ heterojunction for sample No. 020100 is presented in Fig. 3. To construct the profile $p(x)$ we took account of the fact that the permittivity ε is different on each side of the heterojunction.[9] The hole density profile calculated by solving the Poisson equation is also shown in Fig. 3. The band offset and the amplitude of the built-in charge at the heterojunction served as adjustable parameters. The valence-band offset ΔE_V at $T=300$ K was found to be 113 meV (39% of ΔE_g). We estimated the built-in charge at the heterojunction as $\leqslant 10^{11}\,\mathrm{cm}^{-2}$. The samples possessed a relatively high hole density ($>10^{17}\,\mathrm{cm}^{-3}$). For this reason, the calculations showed that N_{ss} less than $10^{11}\,\mathrm{cm}^{-2}$ has no effect on the carrier profile near the heterojunction, and for $N_{ss} > 10^{11}\,\mathrm{cm}^{-2}$ the computed spectrum started to differ substantially from the experimental spectrum. The electric field at the heterojunction was approximately 50 kV/cm with zero bias.

The isotypic heterojunction p-$Al_{0.2}Ga_{0.8}As/p$-$Al_{0.5}Ga_{0.5}As$ was studied in detail in the temperature range 300–120 K. The hole distribution, determined from the $C-V$ measurements, near the heterojunction at various temperatures, is shown in Fig. 4. The amplitude of the signal from the enriched layer increased by 60% as temperature decreased from 290 to 120 K. The results of fitting the computed curves to the experimental dependences are shown in Fig. 4 for four temperatures. We found that the relative valence-band offset in p-$Al_{0.2}Ga_{0.8}As/p$-$Al_{0.5}Ga_{0.5}As$ was temperature dependent. The offset ΔE_V decreased monotonically from 39 to 35% (of ΔE_g) as temperature decreased from 300 to 120 K. The absolute values of the valence-band offset, as shown in Fig. 5, were determined on the basis of the data from Ref. 7. In addition, Fig. 5 shows the temperature dependence of the total band gap ΔE_g.

3. CONCLUSIONS

The capacitance–voltage characteristics were studied in detail and simulated for specially prepared heterostructures.

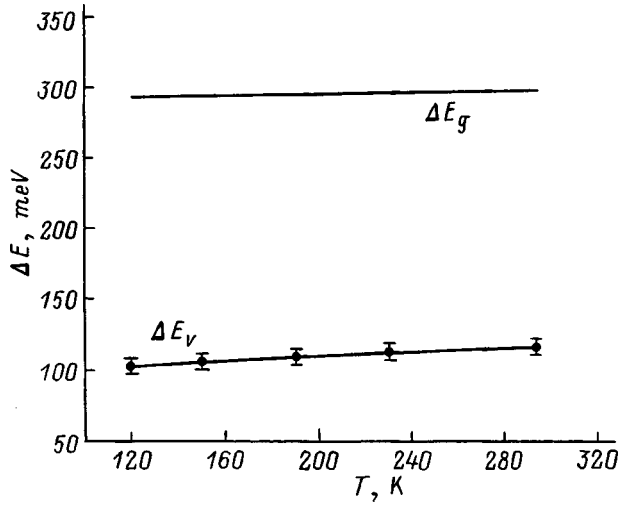

FIG. 5. Temperature dependence of the valence-band offset ΔE_V and the total band gap ΔE_g of a p-$Al_{0.2}Ga_{0.8}As/p$-$Al_{0.5}Ga_{0.5}As$ heterojunction.

The results of $C-V$ measurements on p-$Al_{0.2}Ga_{0.8}As/p$-$Al_{0.5}Ga_{0.5}As$ heterojunctions in the temperature range 120–300 K are presented. The computational results obtained taking into account the incomplete ionization of acceptors and the different values of the permittivity of the layers are presented. It was found that the relative valence-band offset at 300 K is 39% of ΔE_g and decreases monotonically to 35% at 120 K.

*)E-mail: zubkov@fvleff.etu.spb.ru; Fax: (812)-234-30-16

[1] *Numerical Data and Functional Relationships in Science and Technology*, edited by Landolt-Börnstein, 22a (1986).
[2] *Properties of Lattice-Matched and Strained Indium Gallium Arsenide*, edited by P. Bhattacharya (EMIS Datareviews Series, INSPEC, 1993).
[3] *Properties of Aluminium Gallium Arsenide. EMIS Data Reviews Series* (INSPEC, 1993).
[4] F. Bugge, G. Erbert, S. Gramlich, I. Rechenberg, U. Zeimer, and M. Weyers, Inst. Phys. Conf. Ser., No. 145, 167 (1996).
[5] F. Bugge, U. Zeimer, M. Sato, M. Weyers, and G. Tränkle, J. Cryst. Growth **183**, 511 (1998).
[6] M. A. Melnik, A. N. Pikhtin, A. V. Solomonov, V. I. Zubkov, and F. Bugge, in *Proceedings of the International Symposium ''Nanostructures: Physics and Technology''* (St. Petersburg, Russia, 1997), p. 263.
[7] S. Adachi, J. Appl. Phys. **54**, 1844 (1983).
[8] S. M. Sze, *Physics of Semiconductor Devices* [Wiley, New York, 1969; Mir, Moscow, 1984].
[9] V. I. Zubkov, M. A. Mel'nik, and A. V Solomonov, Fiz. Tekh. Poluprovodn. **32**, 61 (1998) [Semiconductors **32**, 52 (1998)].

Translated by M. E. Alferieff

Langevin-recombination-controlled explosive kinetics of electroluminescence in organic semiconductors

V. I. Arkhipov and V. R. Nikitenko*)

Moscow State Engineering-Physics Institute (Technical University), 115409 Moscow, Russia
(Submitted December 21, 1998; accepted for publication January 31, 1999)
Fiz. Tekh. Poluprovodn. **33**, 945–947 (August 1998)

The kinetics of electroluminescence in organic semiconductors is investigated theoretically taking into account the strong dependence, characteristic of these materials, of the charge-carrier mobility on the electric field strength. Recombination of electron-hole pairs under the influence of an external electric field and the electric field due to the Coulomb interaction is investigated on the basis of the Langevin theory. It is shown that as a result of the nonuniformity of the field and the field-dependence of the mobility, the recombination kinetics after the external field is switched off is explosive. © *1999 American Institute of Physics.* [S1063-7826(99)01208-9]

It is well known that the rate of recombination of electron-hole pairs in disordered materials is determined by the convergence time of recombining carriers, i.e., the process is diffusion-controlled. Two types of recombination are conventionally distinguished: 1) geminal recombination of an electron and a hole created in the same photoionization event and 2) bimolecular recombination, where there is no correlation between the origin and annihilation of the carriers. As a rule, the models describing geminal recombination are based on an analysis of the kinetics of drift and diffusion of individual carriers in each individual geminal pair.[1–4] Conversely, as a rule, the average electron and hole densities are used to study bimolecular recombination.[5,6]

From the physical standpoint, however, both recombination mechanisms mentioned above are similar. At least at the final stage, in both cases one carrier and one recombination center participate in the process (most often, this carrier is of opposite sign and is trapped in a deep trap). Mathematically, these processes differ only by the initial and boundary conditions for the distribution function of carriers in a pair.

Previous works have shown that the kinetics of geminal recombination exhibits a variety of interesting features, for example, negative nonstationary photoconductivity.[1,2,7] This gives a basis for expecting that even under the conditions of bimolecular recombination the kinetics of drift and diffusion of pairs of recombining carriers in the Coulomb field coupling them can lead to effects that are not described by models that operate with the volume-averaged electron and hole densities. One such effect is studied in the present paper — explosive carrier-recombination kinetics in single-layer electroluminescence structures based on disordered organic materials. The fact that the mobility of the charge carriers in organic semiconductors depends strongly on the electric field strength is taken into account.[8,9]

The motion of a pair of two charges of opposite sign in an electric field consisting of a superposition of an applied field $\mathbf{E}_0$ and the intrinsic Coulomb field of the charges is described by the continuity equation in the form

$$\frac{\partial f(\mathbf{r},t)}{\partial t}+\operatorname{div}\left[\mu\left(\mathbf{E}_0+\frac{e\mathbf{r}}{4\pi\varepsilon_0\varepsilon r^3}\right)f(\mathbf{r},t)\right]=0, \tag{1}$$

where $\mathbf{r}$ is the radius vector of the more mobile carrier, measured from the position of the lower-mobility carrier; $f(\mathbf{r},t)$ is the space–time distribution function of the higher-mobility carrier (hole); μ is the carrier mobility, which, in general, depends on the field; ε is the permittivity of the material; ε_0 is the permittivity of empty space; and e is the electron charge. When the transient processes occurring after the external field is switched on have ended, stationary distributions of the average electron and hole densities are established in the sample. In what follows we assume that the characteristic scale of variation of these densities is much greater than the average distance between pairs of recombining carriers and the size of the pairs themselves. Introducing a cylindrical coordinate system (ρ,z) with the $\mathbf{z}$ axis directed along the external electric field, we write the boundary condition for the distribution function of the mobile carriers as

$$f(\rho,-\infty)=\text{ const}=p_0, \tag{2}$$

which corresponds to a stationary hole flux directed toward a stationary recombination center (electron). Making the substitution

$$\varphi(\rho,z)=\frac{f(\rho,z)\mu[E(\rho,z)]}{\mu_0}, \tag{3a}$$

where

$$\mathbf{E}=\mathbf{E}_0+\frac{e\mathbf{r}}{4\pi\varepsilon_0\varepsilon r^3} \tag{3b}$$

and μ_0 is the mobility in the weak-field limit, the stationary problem (1) and (2) for the function φ $(\partial\varphi/\partial t=0)$ reduces to a problem with a constant (field-independent) mobility μ_0 and can be easily solved by the method of characteristics. As a result of the homogeneity of Eq. (1) and the condition (2), the solution is a constant $\varphi_{st}(\rho,z)=\varphi_0=p_0\mu(E_0)/\mu_0$ and,

correspondingly, the stationary electron distribution is determined by the field-dependence of the mobility

$$f_{st}(\mathbf{r}) = p_0 \mu(E_0)/\mu[E(\mathbf{r})]. \quad (4)$$

We note that for a field-independent mobility the stationary distribution function is uniform: $f_{st}(\mathbf{r}) = p_0$.

The stationary distribution function must be used as an initial condition in the problem of the temporal evolution of a pair after the external field is switched off. The continuity equation and the initial conditions can be written in a spherical coordinate system as

$$\partial\varphi(r,\theta,t)/\partial t - E_q(r)\,\mu[E_q(r)]\partial\varphi(r,\theta,t)/\partial r = 0, \quad (5)$$

$$\varphi(r,\theta,0) = f_{st}(r,\theta)\,\mu[E_q(r)]/\mu_0, \quad (6)$$

where $\varphi(r,\theta,t) = f(r,\theta,t)\mu[E_q(r)]/\mu_0$ and $E_q(r) = e/4\pi\varepsilon\varepsilon_0 r^2$ is the Coulomb field, and the polar angle θ is measured from the direction of the field $\mathbf{E}_0$. The moment at which the external field is switched off is taken as the origin point for measuring time.

From the practical standpoint, the most important characteristic of a light-emitting structure is the time-dependence of the intensity of electroluminescence (EL). In what follows, we assume that the intensity of EL is proportional to the pair recombination rate, which in the Onsager approximation,[10] as follows from Eq. (5), is determined as

$$R(t) = -(d/dt)\int d\mathbf{r}\, f(\mathbf{r},t) = \frac{e\mu_0}{2\varepsilon\varepsilon_0}\int_{-1}^{1} du\, \varphi(0,u,t), \quad (7)$$

where $u = \cos\theta$. Using the system of equations (5)–(7) it is easy to show that the function $R(t)$ can be written as

$$R(t) = \frac{e\mu\{E_q[r_0(t)]\}}{2\varepsilon\varepsilon_0}\int_{-1}^{1} du\, f_{st}[r_0(t),u], \quad t>0. \quad (8)$$

Here r_0 is the distance between the particles that merge at time t after the field is switched off, i.e., $r_0(t)$ is the reciprocal of the convergence time $t(r_0)$ defined as

$$t(r_0) = \int_0^{r_0} dr\, \mu^{-1}[E_q(r)]E_q^{-1}(r). \quad (9)$$

The equation (9) determines the function $r_0(t)$ implicitly. We note that in the limit $t\to 0$, when $r_0(t)\to 0$ and $\mu(E_q)/\mu(E)\to 1$, we obtain from Eqs. (4), (6), and (8) the passage to the limit of a stationary recombination rate

$$R(t) = R_0 = e\mu(E_0)p_0/\varepsilon\varepsilon_0 = K_L(E_0)p_0, \quad t\leqslant 0, \quad (10)$$

where K_L is the Langevin recombination constant.

The system of equations (2), (4), and (8)–(10) is the analytic solution of the problem of the kinetics of EL for an arbitrary field dependence of the mobility. We shall now examine the case, which is important for practical applications, where the mobility depends on the field as

$$\mu(E_0) = \mu_0 \exp(\sqrt{E_0/F_0}), \quad (11)$$

which is characteristic for a wide class of organic semiconductors.[8,9] Substituting the function (11) into Eqs. (4), (8), and (9) gives the following expression for the ratio $I(t)/I_0$ of the nonstationary and stationary EL intensities:

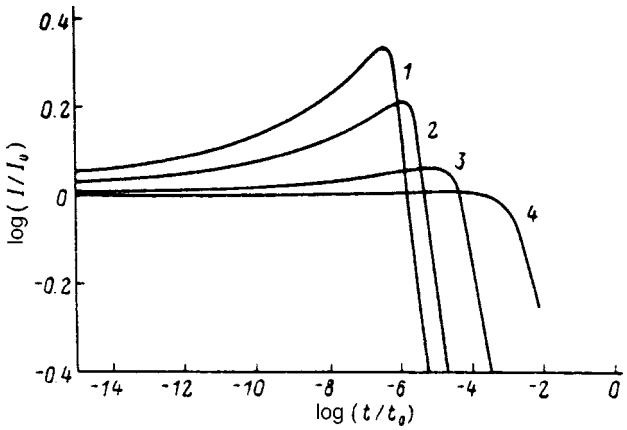

FIG. 1. Time dependences of EL intensity, scaled to the stationary level I_0, for several values of the parameter $F = F_0/E_0$: *1* — 40, *2* — 30, *3* — 15, *4* — *5*; $t_0 = \mu_0^{-1}(e/\varepsilon F_0^3)^{1/2}$.

$$I(t)/I_0 = R(t)/R_0 = e^s[g(a) - g(b)]/Fs^2. \quad (12)$$

Here we give the notation

$$g(x) = e^{-x}(x^3 + 3x^2 + 6x + 6), \quad (13a)$$

$$a(s) = \sqrt{F + s^2}, \quad b(s) = \sqrt{|F - s^2|}, \quad (13b)$$

$F = E_0/F_0$ and the dimensionless function of time s is determined by the equation

$$t/t_0 = s^{-3}\int_1^{\infty} d\tau \exp(-s\tau)/\tau^4 = E_4(s)/s^3, \quad (14)$$

$t_0 = \mu_0^{-1}(e/4\pi\varepsilon\varepsilon_0 F_0^3)^{1/2}$, and $E_4(s)$ is the exponential integral.

The time dependences of I/I_0 calculated using Eqs. (12)–(14) for several values of the external electric field strength E_0 are shown in Fig. 1. The curves possess a maximum. The distance of the maximum above the stationary level increases strongly with the field. The physical reason for the appearance of such ''explosive'' kinetics of EL is easy to understand. Under stationary conditions (before the external field is switched off) holes accumulate in the region of weakest field E (at locations where $E<E_0$ as a result of the influence of the Coulomb field of the pair) on account of the low mobilities in these regions — see Eqs. (4) and (11). After the field E_0 is switched off, these carriers rapidly recombine, producing a peak in the EL intensity. It is obvious that the stationary hole density p_{st} is maximum near the point A, where $E=0$ (behind the electron, looking from the negative side of the z axis), and the convergence time $t(r_A)$ of the carriers from the point A with electrons, where $r_A = \sqrt{e/4\pi\varepsilon\varepsilon_0 E_0}$ [see Eq. (9)], determines the time at which the maximum is reached. As a result of the decrease of r_A, this time decreases with increasing field E_0 and therefore the height of the peak increases with E_0. The relative height of the peak is limited, however, by the fact that the transfer of charge carriers in the semiconductors under study is of a hopping character, and the characteristic hopping distance r_h must be shorter than the distance r_A. This condition places an upper bound on the range of fields under study:

$$E_0 < e/4\pi\varepsilon\varepsilon_0 r_h^2. \quad (15)$$

Numerically, for $r_h \simeq 1$ nm and $\varepsilon = 2$ the condition (15) leads to the limit $E_0 < 5 \times 10^6$ V/cm. In the case of the typical (at room temperature) value $E_0 \simeq 10^5$ V/cm (Ref. 9), the latter condition gives an upper bound ~ 5 on the relative magnitude $I_{\max}/I_0$ of the peak.

The explosive kinetics of EL after the applied field is switched off has been observed experimentally in bilayer light-emitting structures.[11,12] However, these results cannot be explained on the basis of the Langevin model of recombination because 1) $I_{\max}/I_0$ decreases and does not increase with increasing external field strength E_0 and 2) $I_{\max}/I_0$ can reach values of the order of 100. The indicated regularities of the explosive kinetics of EL in bilayer structures can be explained on the basis of recombination of electrons and holes which have accumulated near the interface between the materials forming the bilayer structure.[12] The observation of explosive EL kinetics in single-layer light-emitting structures under conditions precluding the possibility of macroscopic spatial separation of electrons and holes could provide an experimental confirmation of the theoretical model proposed in the present paper.

*)Fax: (095) 324 21 11

[1] B. S. Yakovlev and G. F. Novikov, Fiz. Tverd. Tela (Leningrad) **17**, 3070 (1985) [Sov. Phys. Solid State **17**, 2035 (1985)].
[2] V. I. Arkhipov, V. R. Nikitenko, and A. I. Rudenko, Fiz. Tekh. Poluprovodn. **21**, 1125 (1987) [Sov. Phys. Semicond. **21**, 685 (1987)].
[3] A. P. Tyutnev, V. I. Arkhipov, V. R. Nikitenko, and D. N. Sadovnichiĭ, Khim. Vys. Energ. **29**, 351 (1995).
[4] K. M. Hong and J. Noolandi, Chem. Phys. **69**, 5026 (1978).
[5] A. P. Tyutnev, A. V. Vannikov, and G. S. Mingalev, *Radiation Electrophysics of Organic Dielectrics* (Moscow, 1989), p. 190.
[6] V. I. Arkhipov, Yu. A. Popova, and A. I. Rudenko, Fiz. Tekh. Poluprovodn. **17**, 1817 (1983) [Sov. Phys. Semicond. **17**, 1159 (1983)].
[7] V. I. Arkhipov, Yu. A. Popova, and A. I. Rudenko, Fiz. Tekh. Poluprovodn. **21**, 1625 (1987) [Sov. Phys. Semicond. **21**, 984 (1987)].
[8] A. Peled and L. B. Schein, Chem. Phys. Lett. **153**, 422 (1988).
[9] P. M. Borsenberger, L. Pautmeier, and H. Baessler, J. Chem. Phys. **94**, 447 (1991).
[10] L. Onsager, Phys. Rev. **54**, 554 (1938).
[11] Y. H. Tak, J. Pommerehne, H. Vestweber, R. Sander, and H. Baessler, Appl. Phys. Lett. **69**, 1291 (1996).
[12] V. R. Nikitenko, V. I. Arkhipov, Y. H. Tak, J. Pommerehne, H. Baessler, and H.-H. Horhold, J. Appl. Phys. **81**, 7514 (1997).

Translated by M. E. Alferieff

Formation and thermal stability of contacts based on titanium borides and titanium nitrides with gallium arsenide

E. F. Venger, V. V. Milenin, I. B. Ermolovich, R. V. Konakova,*) V. N. Ivanov, and D. I. Voĭtsikhovskiĭ

Institute of Semiconductor Physics, Ukrainian National Academy of Sciences, 252650 Kiev, Ukraine
(Submitted January 11, 1999; accepted for publication February 2, 1999)
Fiz. Tekh. Poluprovodn. **33**, 948–953 (August 1999)

The formation mechanisms and thermal stability of contacts, fabricated by ion-plasma sputtering of titanium borides and nitrides on gallium arsenide, are investigated by structural, secondary-emission, photoluminescence, and electrical methods. A physical model, according to which the solid solutions $B_xGa_{1-x}As$ and GaN_xAs_{1-x} are formed in the process of deposition on the phase boundary, is proposed on the basis of the data obtained. It is shown that the correlation between the physicochemical interactions at the phase boundaries of the contacts and their electrical parameters is due to defects that arise in the contact layers of the semiconductor during the formation of the heterostructures and subsequent treatments. It is established that the high thermal stability of the experimental objects is due to their bilayer structure, which sharply decreases interdiffusion processes at the phase boundary.
 [S1063-7826(99)01308-3]

1. INTRODUCTION

It has now been established that the degradation of metal–semiconductor structures during operation under extreme conditions (high temperatures, high-power electromagnetic radiations, radiation field, and so on) is due to the characteristics of mass-transfer processes and the character of the solid-phase reactions in the contiguous pairs.

External perturbations alter the structural-phase states and the degree of local nonuniformity of a boundary, the impurity-defect composition of the contact region of the semiconductor, and other characteristics, which ultimately changes (degrades) the electrical parameters of the contacts. Stable perturbation-resistant metal–III-V structures can now be obtained by selecting metallic alloys and compositions that could greatly diminish the diffusion interaction of the metal–semiconductor layers. These include alloys based on titanium borides and nitrides. The present paper is devoted to a comparative analysis of these materials in $TiB_x(TiN_x)$–GaAs structures.

2. OBJECTS AND METHODS OF INVESTIGATION

Epitaxial GaAs:Te structures with *n*-layer thickness 1.6–2.5 μm and carrier density in the active layer $(0.7-1.1)\times10^{16}$ cm^{-3} were used to prepare the samples. TiB_x and TiN_x layers were deposited, by magnetron sputtering of powdered pressed targets in argon or a mixture of argon with nitrogen in the first case and by thermionically active synthesis in the second case, on the surface of an epitaxial layer, subjected to photonic cooling, at substrate temperature $T_s=200\,^\circ$C. The metal layers were no more than 0.1 μm thick. The contacts were annealed in a hydrogen stream at temperatures up to $T_a=800\,^\circ$C for 1 min.

A combination of methods, including structural (electron diffraction, x-ray phase analysis), optical (photoluminescence), and electrical (current–voltage characteristics) methods as well as methods for analyzing the atomic composition of prepared objects (Auger spectroscopy combined with etching with 3-keV Ar^+ ions, secondary-ion mass spectrometry) and atomic-force microscopy was used to study the mechanisms leading to the formation and thermal stability of contact structures.

3. RESULTS AND DISCUSSION

The electron-diffraction and x-ray-phase analysis data show that the deposited films are in a quasiamorphous state. The ratio of the amorphous and polycrystalline phases changes with increasing thickness of the deposited films and the annealing temperature. For example, the ratio is 70:30 for 1-μm-thick TiN_x films. Annealing of these films resulted in a redistribution of the amorphous and crystal phases and the formation of new, larger, and structurally more perfect grains. For thin layers ($\ll1$ μm), characterized by especially small crystallite sizes (grain size $\simeq0.03$ μm), the recrystallization process proceeds more intensely.

The structured changes occurring in the deposited layers as a result of annealing are accompanied by changes in the planar-stressed state of the film (a transition occurs from macrocompression to macrotension). These changes can be substantial. A qualitative confirmation of this process is, for example, the image shown in Fig. 1 of the surface of Au–Mo–TiB_x–GaAs structures annealed at $T_a=800\,^\circ$C. This image was obtained with an atomic-force microscope. As one can see, the thermal stresses arising can be so stong that the deposited TiB_x layers crack.

The Auger-spectroscopy concentration profiles of the deposited titanium boride (Fig. 2) and nitride layers over thickness *d* show that besides the main components the layers contain substantial quantities of oxygen and carbon. Since Ti

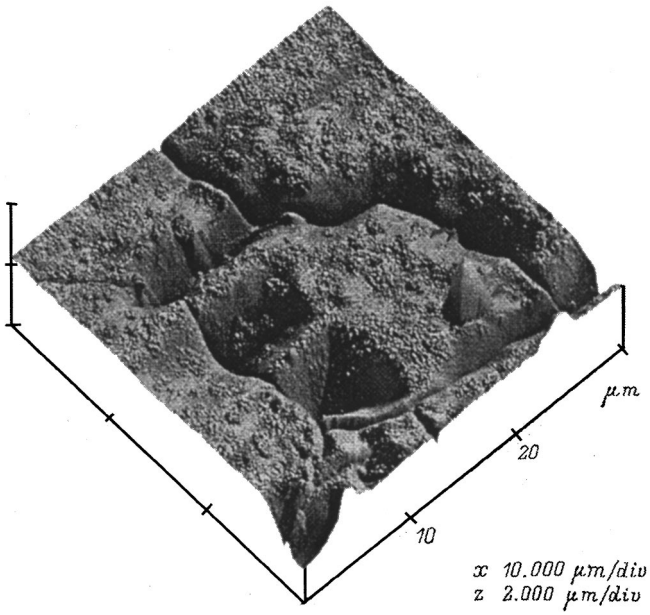

FIG. 1. Morphology of an Au–Mo–TiB_x–GaAs structure after annealing at $T_a = 800\,^\circ$C.

has a high affinity to oxygen, the presence of oxygen in the reaction zone at the film formation stage leads to the formation of oxide phases, and the presence of a carbon impurity (chemically inert) impedes completion of the structural changes occurring in the deposited layers. Annealing of such layers stimulates their further structural-chemical rearrangement, in which the variable-composition phases Ti–O–N(B) play the dominant role. The structural-phase modification occurring in the deposited layers as a result of anneals does not result in substantial smearing of the phase boundaries right up to temperatures $T_a = 600\,^\circ$C. As temperature increases to $T_a = 800\,^\circ$C, the barrier properties of the deposited layers sharply degrade, and a substantial mixing of the components of heteropairs is observed. This mixing is stronger in structures based on titanium borides. The structural-phase rearrangement of the condensed layers results in a transformation of the impurity-defect composition of the contact regions of the semiconductor.

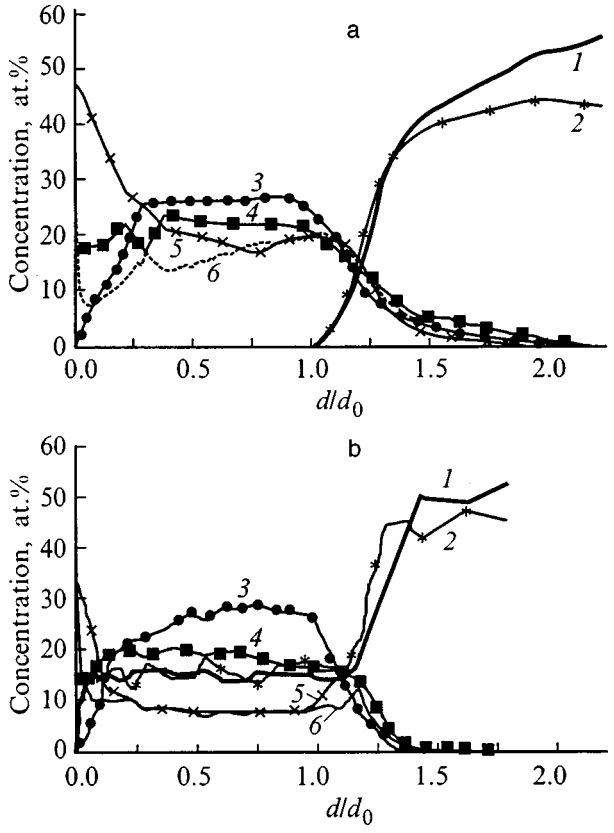

FIG. 2. Atomic profiles of the components of a TiB_x–GaAs contact before (a) and after (b) a 60-s anneal at $T_a = 800\,^\circ$C: *1* — Ga, *2* — As, *3* — B, *4* — Ti, *5* — O, *6* — C.

Figure 3 shows as an example the photoluminescence (PL) spectra, measured at $T = 77$ K, from the contact region of TiB_x–GaAs structures. Five bands with energies $h\nu_{max} = 1.54$, 1.33, 1.20, 1.01, and 0.765 eV can be distinguished in the spectra from both structures. The annealing temperature dependences of the intensities W of these bands are presented in Fig. 4. The main features of the PL from the experimental structures are as follows.

1. The PL spectra contain a large number of wide, overlapping bands. This indicates the presence of a large quantity of structural defects in the contact regions of GaAs.

2. In the initial state of the structures the strongest band is the 1.01-eV band, which in the literature[1] is attributed to radiative capture of a free electron on an isolated acceptor center Cu_{Ga}. Apparently, copper is an uncontrollable impurity in the structures investigated. Another PL band which we observed with $h\nu_{max} = 1.33$ eV is also attributed to copper. Its centers are the complexes ($Cu_{Ga} + D$), where D is an intrinsic (V_{As}) or impurity (Te, Sn, Si) donor.[2] In the initial state this is most likely Te, since the initial epitaxial layers are doped with Te.

3. Anneals at $T_a = 400\,^\circ$C intensify and redistribute the intensities of the PL bands. This is especially clearly expressed in TiB_x–GaAs structures. This shows that TiN_x–GaAs structures are more stable than TiB_x–GaAs structures against thermal perturbations relative to restructuring of the spectra of the defect states. On the other hand, apparently, the intensification of PL occurs in TiB_x–GaAs structures in the entire spectral range because of the greater structural ordering in the contact region and the consequent weakening of the nonradiative recombination channel.

After annealing at $T_a = 400\,^\circ$C, the 1.20-eV band, whose luminescence centers are the complexes ($V_{Ga} + D$),[3] is intensified more strongly than the other impurity-defect bands in the contact regions of both types of structures. This could stem from the enrichment of the contact region with gallium vacancies because of the fact that in the presence of interphase interactions of metallic layers with a semiconductor, gallium diffuses from the contact region and possibly from the interior volume into the metal layer. Taking account of the isoelectronic similarity of B and Ga, it can also be assumed that in the presence of an excess of Ga vacancies a $B_xGa_{1-x}As$ solid solution can form at the early stages of growth of a boride film (see below).

At $T_a = 600\,^\circ$C the intensities of all impurity–defect bands in TiB_x–GaAs structures decrease, with the exception

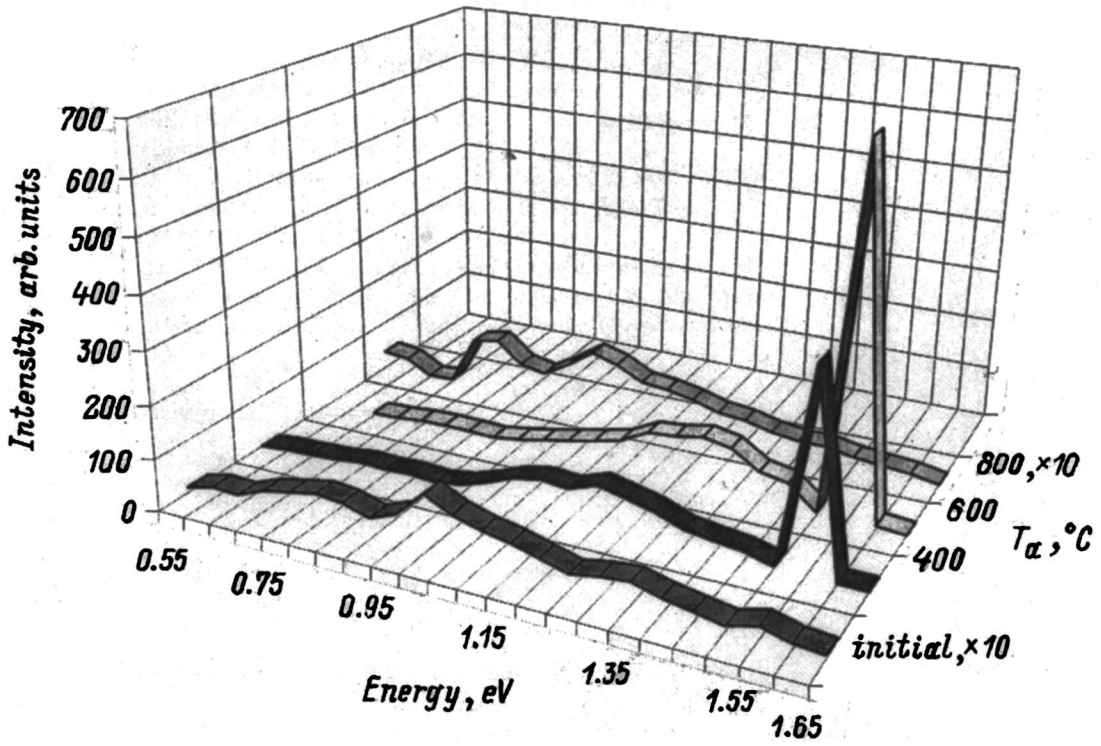

FIG. 3. Photoluminescence spectra of the contact layers of TiB_x–GaAs structures, initial structures and after anneals at $T_a = 400$, 600, and 800 °C. Measurement temperature: $T = 77$ K.

of the 1.33-eV band, which intensifies slightly, probably because of the formation of $(Cu_{Ga} + V_{As})$ complexes. This conclusion is based on the fact that at these temperatures the arsenic atoms start to interact effectively with Ti from the metallic layer, forming Ti–As compounds,[4] and the semiconductor is enriched with V_{As}. The 1.01-eV band weakens because some of the luminescence centers responsible for it participate in the formation of the complexes mentioned.

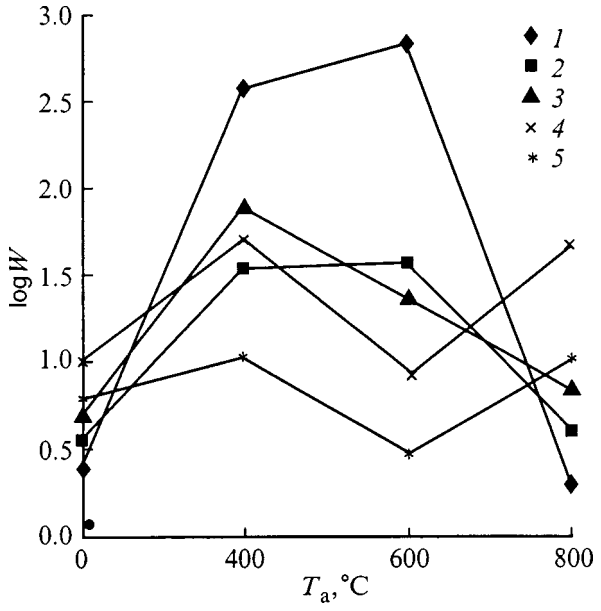

FIG. 4. Intensities of PL bands with $h\nu_{max} = 1.54$ (*1*), 1.33 (*2*), 1.20 (*3*), 1.01 (*4*), 0.765 eV (*5*) of TiB_x–GaAs structures versus the anneal temperature.

This out-of-phase behavior of the 1.01 and 1.33-eV bands as a result of heat treatment was also observed in TiN_x–GaAs structures.

Note the analogy in the behavior of the 1.01 and 0.765-eV bands in both structures, which shows that they are related. We assume that the 0.765-eV band is due to radiative intracenter transitions in a Cu^{2+} ion (this center is responsible for the 1.01-eV band), whose unfilled $3d^9$ shell splits in the crystal field and as a result of the spin-orbit interaction, similarly to CdS:Cu.[5]

Annealing at $T_a = 800$ °C results in decomposition of complexes of centers of 1.20 and 1.33-eV bands; the intensities of the bands decrease (the intensity of the 1.01-eV band increases) and they remain virtually the same as in the initial state.

4. The main feature of the PL spectra of the contact regions of the structures investigated is the presence of a free-exciton emission band with $h\nu_{max} = 1.54$ eV in a TiB_x–GaAs structure and 1.57 eV in a TiN_x–GaAs structure, while the band gap in GaAs at $T = 77$ K is 1.51 eV.[6] We assume that this is direct evidence that thin layers of the solid solutions $B_xGa_{1-x}As$ and GaN_xAs_{1-x} are formed with high crystalline perfection and corresponding structure at the phase boundary. The sharp quenching of the excitonic band as a result of annealing at $T_a = 800$ °C, just as other bands, attests to the appearance of a large number of additional nonradiative recombination centers.

The formation of solid solutions at the phase boundary of the structures investigated, just as the possible presence of Cu in it, was confirmed by secondary-ion mass spectra ob-

TABLE I. Mass-spectrometric data for TiN_x–GaAs and TiB_x–GaAs heterostructures.

Structure	Element compound	Mass, amu	Intensity of the ion current in the transitional layer, arb. units			
			initial state	T_a, °C		
				400	600	800
TiN_x–GaAs	TiN	62	1×10^4	1×10^4	1×10^4	1.2×10^4
	GaN	84	4×10	4×10	3×10	5×10
	GaAsN	159	10	8	5	7
	GaAsTi	192	5×10	3×10	1×10	…
	Cu(TiO)	64	5×10^4	8×10^4	6×10^4	1.2×10^4
TiB_x–GaAs	TiB	54	4×10^4	1×10^5	7×10^4	2×10^4
	BAs	86	…	…	…	…
	GaBAs	155	5×10	8×10	8×10	9×10
	GaAsTi	192	3×10^2	3×10^2	3×10^2	8×10^2
	Gu(TiO)	64	4×10^5	4×10^5	6×10^5	4×10^5

tained in the contact regions of the structures investigated (see Table I).

The presence of peaks due to ions with masses 84, 159, and 155 in the spectra could be an argument in support of the conclusion drawn above, just as the appearance of peaks corresponding to clusters with atomic mass 192 (apparently, GaAsTi), formed by Ti atoms which are not bound with nitrogen, in the secondary-ion spectra.

The identification of Cu impurity, whose mass spectra overlap with the mass spectra of TiO oxides, is less definite. Apparently, signals from TiO and Cu are superimposed in the characteristic spectra measured. The small variations in the intensities of the spectral lines observed after annealing and the intensity ratio of the lines, which is different from that of a natural composition of Cu isotopes, confirm the presence of an uncontrollable Cu impurity in the samples.

The results obtained, taken together, indicate that the electrical parameters of diode structures formed using antidiffusion barriers based on TiB_x and TiN_x will shown enhanced resistance to thermal perturbations. This conclusion has been checked by measurements of the current–voltage characteristics (IVCs) on Au–TiB_x–GaAs contact structures.

The direct branches of the current–voltage characteristics of diodes before and after annealings are shown in Fig. 5. In the initial structures they are nonlinear in the $\ln I-V$ coordinates. At small biases there is a section of excess current, and at high biases the current is virtually independent of the voltage. For the reverse branch of the I-V characteristic the current exhibits a power-law dependence on the bias voltage. Annealing changes the form of the direct branches of the I-V characteristic. For the reverse branches the power-law dependence on the applied bias remains, only the magnitude of the reverse current changes. On the basis of the PL data it can be inferred that the basic reason for the deviation of the I-V characteristic from the form characteristic for the simple thermal-emission mechanism of current, which ordinarily occurs in GaAs-based diodes with the chosen doping level,[7] is a change in the density and type of defects that form deep local levels in the band gap in GaAs. It is well known and has been shown in the present work by the PL method that when a metal film is deposited on a semiconductor surface, deep centers that participate in current transport through the interface appear in the contact region of the semiconductor as a result of interphase reactions and mechanical stresses, as well as possible contamination of the semiconductor surface by uncontrollable impurities from the surrounding fixtures.[7] Judging from the characteristic features of the nucleation and growth of film coatings by magnetron sputtering, a nonuniform distribution of impurities (for example, Cu, which we discovered) and defects in the contact GaAs layers should be expected, i.e., the appearance of local regions with high defect density in the space-charge region is completely realistic. This changes (compared with an ideal contact) the differential slope of the straight

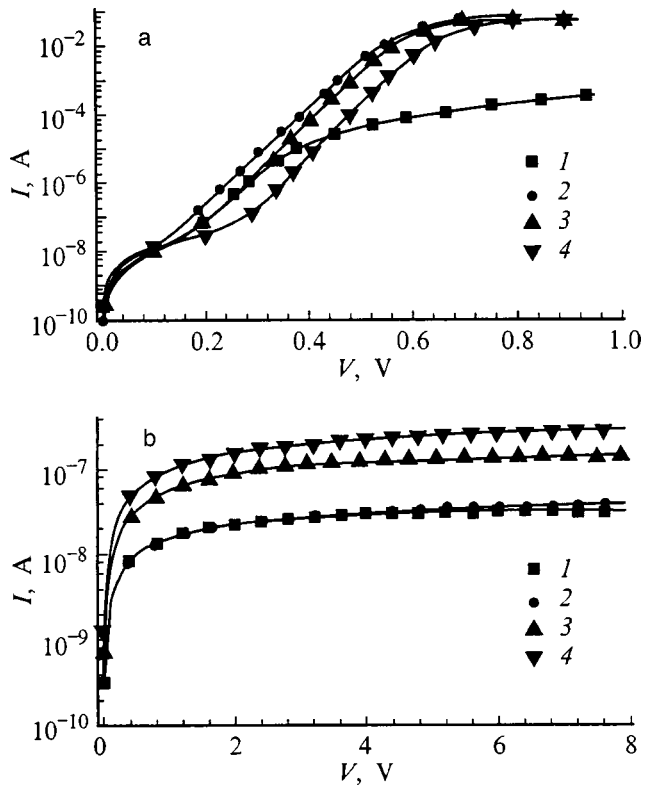

FIG. 5. Direct (a) and reverse (b) branches of the current–voltage characteristics of Au–TiB_x–GaAs contacts before (*1*) and after anneals at temperatures $T_a=400$ (*2*), 500 (*3*), and 600 °C (*4*).

branches of the I-V characteristic ($1/n = d \ln I/dV$), i.e., it leads to the appearance of an additional component in the current and therefore to a decrease in the effective Schottky barrier. Annealings at moderate temperatures ($T_a \sim 400\,^\circ$C) partially remove the defects introduced, including compensating acceptors in the diode base. The structural nonuniformity of the contact GaAs layers increases (as is indicated by the PL data), and the current–voltage characteristics approach the ''ideal'' curves, as is observed experimentally (see Fig. 5).

As the anneal temperature increases, additional defects appear or existing defects with a different ionization energy are restructured (in our samples, the density of the complexes $Cu_{Ga} + V_{As}$ increases). This results in the appearance and growth of a section of excess currents on the direct branch of the I-V characteristic. However, the thermionic mechanism of current flow remains dominant. At annealing temperature $T_a = 800\,^\circ$C the device parameters degrade appreciably. In this case, as follows from Auger-spectroscopy data, the antidiffusion properties of the layer that produces the barrier degrade sharply, which intensifies the interphase interactions. As a result, the structural-phase state of the interface is modified, the complex centers $V_{Ga} + D$ and $Cu_{Ga} + D$ decompose, and other types of defects (including centers of fast nonradiative recombination) form in the contact region of GaAs in substantial quantities. Our results showed that apparently the Cu atoms, which uncontrollably contaminate GaAs-based heterostructures, play an important role in the degradation processes.

In summary, the investigations performed confirm that antidiffusion barrier-forming compositions based on metal borides and nitrides are promising for producing surface-barrier structures with high thermal stability and indicate the need for special methods for prevention of copper contamination of the fabricated heterostructures.

This work was supported by the Ukrainian Science and Technological Center (Project No. 464).

*)E-mail: konakova@eee.semicond.ua; Fax: (044) 2658342

[1] T. N. Morgan, M. Pilkuhn, and H. Rupprecht, Phys. Rev. **138**, 1551 (1965).
[2] N. S. Averkiev, T. K. Ashirov, and A. A. Gutkin, Fiz. Tekh. Poluprovodn. **15**, 1970 (1981) [Sov. Phys. Semicond. **15**, 1145 (1981)].
[3] E. W. Williams, Phys. Rev. **168**, 922 (1968).
[4] C. E. McCants, T. Kindelevicz, P. H. Mahovald, K. A. Bertness, M. D. Williams, N. Newman, S. Lindau, and W. E. Spicer, J. Vac. Sci. Technol. A **6** (3), 1466 (1988).
[5] J. Broser, H. Majer, and H.-J. Schulz, Phys. Rev. **140**, 2135 (1965).
[6] E. Grilli, M. Guzzi, R. Zamboni, and L. Pavesi, Phys. Rev. B **45**, 1638 (1992).
[7] E. H. Rhoderick, *Metal–Semiconductor Contacts* [Oxford, Clarendon Press, 1978; Radio i svyaz', Moscow, 1982, p. 91].

Translated by M. E. Alferieff

Photosensitivity of structures produced by heat treatment of $CuInSe_2$ in different media

V. Yu. Rud'

St. Petersburg State Technical University, 195251 St. Petersburg, Russia

Yu. V. Rud'

A. F. Ioffe Physicotechnical Institute, Russian Academy of Sciences, 194021 St. Petersburg, Russia
(Submitted February 1, 1999; accepted for publication Feburary 3, 1999)
Fiz. Tekh. Poluprovodn. **33**, 954–958 (August 1999)

Photosensitive structures were produced by heat-treatment of polycrystalline *p*- and *n*-$CuInSe_2$ substrates in vacuum and in air at temperatures near 500 °C. The spectral dependences of the photosensitivity of two types of structures in natural and linearly polarized light were investigated and analyzed. The photosensitivity of the best structures reached 16 mA/W at $T=300$ K. The laws of polarization photosensitivity of such structures were determined and discussed in relation to the fabrication conditions of the structures. It was concluded that there is a new possibility of using polarized photoelectric spectroscopy for diagnostics of phase interactions in complex semiconductors and for optimizing the technology for producing photoconversion structures. [S1063-7826(99)01408-8]

Copper and indium diselenide $CuInSe_2$ has become one of the most promising photovoltaic materials because of the optimal combination of its optical and electric properties.[1,2] The technological process has made it possible to increase the efficiency of $CuInSe_2$ solar cells up to 18%.[1,3] However, the behavior of point defects in the lattice in this material is still not completely understood, and it is obvious that any findings in this direction could open up new avenues for increasing the efficiency of $CuInSe_2$-based structures. Questions concerning the interaction of $CuInSe_2$ with various media are no less important for solving this problem.[4] The present work is devoted to experimental investigations of the photoelectric properties of structures arising with heat treatment of bulk $CuInSe_2$ crystals in vacuum and air.

Polycrystalline $CuInSe_2$ ingots were grown by directed crystallization of melt, close to a stoichiometric ternary compound, with a vertical arrangement of a quartz crucible (diameter ≈10 mm). The ingots were then cut into rings (thickness ≈3 mm), whose surface was polished mechanically and then chemically. The *n* and *p*-type crystals were electrically uniform and possessed free-carrier density $\approx 10^{18}\,\mathrm{cm}^{-3}$ at $T=300$ K.

To form photosensitive structures the rings were heat-treated at ≈500 °C in evacuated quartz cells with a standard volume (at pressure $\approx 10^{-4}$ Torr) or directly in air. The results of these investigations can be summarized as follows.

1. Heat-treatment (HT) in evacuated cells is usually accompanied by conversion of the *p*-type conductivity of the crystals, and for HT times $t\approx 1$ min, *n*–*p* junctions can be obtained. As the heat-treatment time increases to 5–10 min, conversion becomes of a volume nature and only isotypic $n'-n$ junctions can be prepared from rings of the size indicated above. It is important to underscore that the surface of the plates after such HT is visually identical to the initial state, and conductivity conversion is due to the formation of intrinsic donor defects in the lattice — vacancies in the selenium sublattice.

A typical stationary current-voltage characteristic (IVC) for one such structure is shown in Fig. 1 (curve *1*). The initial section of the direct IVCs is exponential, and it corresponds to nonideality factor $\beta=3.1-4.4$, while in the forward bias range, $U>0.7$ V, the characteristics follow the relation

$$I=(U-U_0)/R_0, \tag{1}$$

where for *n*–*p* structures the cutoff voltage $U_0\approx 0.6$ V, and the residual resistance $R_0\approx 80-100\ \Omega$ at $T=300$ K. For $n'-n$ structures the corresponding parameters are $U_0\approx 0.1$ V and $R_0\approx 20-40\ \Omega$, and the rectification ratio is substantially lower than for *n*–*p* structures. The reverse branch of the IVC for the aniso- and isotypic structures obtained with vacuum HT has the form $I\sim U^n$, where $n\approx 1.1$ up to voltages ≈1 V. The latter could indicate that the leakage currents affect the flow of reverse current in such structures.

When *n*–*p* and $n'-n$ structures are illuminated, the layer produced by HT is always negatively charged, which corresponds to the direction of rectification. The voltage (S_U) and current (S_I) photosensitivities in these structures (see Table I) dominate for illumination from the side of the layers formed during HT and form narrow bands with total width at half-height $\delta\approx 40$ meV. The energy position $\hbar\omega_{\max}$ of the maximum in the spectrum of the relative quantum photoconversion efficiency η always lies somewhat below the band gap in $CuInSe_2$, equal to $E_G\approx 1.02$ eV[3–5] (Fig. 1, curve *2*). The sharp short-wavelength dropoff of η, which is typical for such structures and is observed upon exposure to light from the side of the layers obtained by HT in vacuum, is due to an increase in the influence of absorption as the photon energy approaches E_G. For HT of $CuInSe_2$ in air, layers whose color depended on the holding time in air and whose

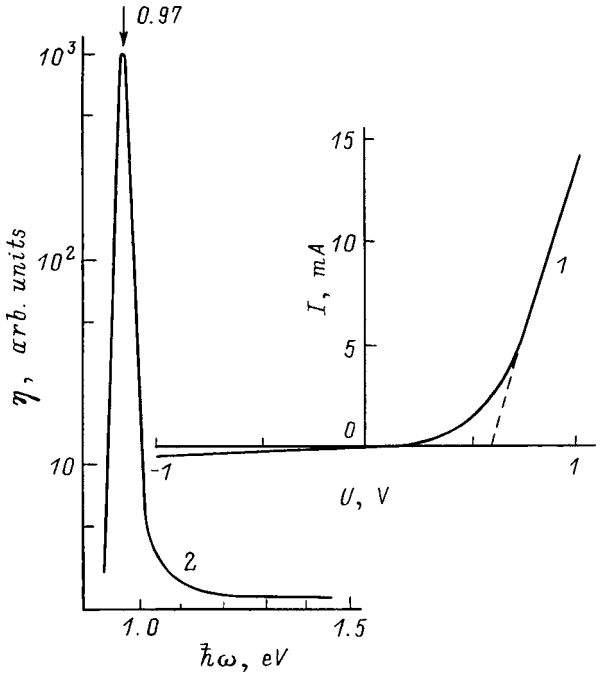

FIG. 1. Stationary current-voltage characteristic of a $n-p$-$CuInSe_2$ structure (curve *1*, sample 10) and the spectrum of the relative quantum photoconversion efficiency for the structure $n'-n$-$CuInSe_2$ (curve *2*, sample 11; illumination from the layer side by unpolarized light). The arrow marks $\hbar\omega_{max}$. The measurements were performed at $T=300$ K.

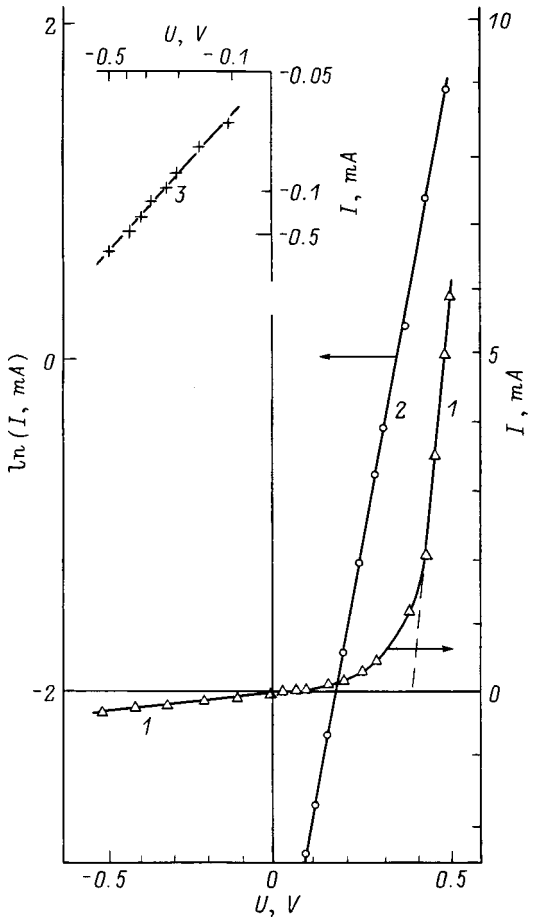

FIG. 2. Stationary current–voltage characteristic of a $p'-p$-$CuInSe_2$ structure at $T=300$ K (sample 1, curve *1*). The direct branch of the IVC is drawn on a logarithmic scale (*2*); reverse branch (*3*).

conductivity type was the same as in the initial state appeared on the surfaces of the rings.

Figure 2 shows the stationary IVC of one of the isotypic $p'-p$ structures. It is evident that the HT regimes used make it possible to obtain rectifying structures (Fig. 2, curve *1*), whose transmission direction always corresponds to positive polarity of the external bias on the layer. The typical parameters of the IVCs of these structures are $\beta=3.0-3.2$, $U_0\approx 0.5-0.6$ V, $R_0\approx 120-250\ \Omega$, and $n\approx 1.1$, which, in general, are quite close to the analogous parameters of structures obtained by heat-treatment of $CuInSe_2$ crystals in vacuum.

2. When isotypic $p'-p$ and $n'-n$ structures obtained by HT of $CuInSe_2$ crystals in air are illuminated, the layers always become positively charged, and this corresponds to the transmission direction for such structures. The maximum photosensitivities S_U^{max} and S_I^{max} were attained in $n'-n$ structures obtained by HT for $t\approx 5$ min (see Table I). The sign of the photovoltaic effect turned out to be independent of the location of the light probe (diameter ≈ 0.2 mm) and the incident photon energy, and therefore it could be due to the formation of an active region as a result of heat-treatment of $CuInSe_2$ in air.

The conversion efficiency spectra η for a number of isotypic structures produced with different HT times are presented in Fig. 3. The main features appearing in these spectra with increasing heat-treatment time t are as follows:

TABLE I. Photoelectric properties of $CuInSe_2$-based structures at $T=300$ K.

Sample No.	Heat-treatment medium	t, min	Type of structure	S_U^{max}, V/W	S_I^{max}, mA/W	$\hbar\omega_{max}$, eV	S, eV^{-1}	δ, meV	η_2/η_{max}	P_I^{max}, %
6	Air	1	$n'-n$	0.2	0.04	0.995	46	440	0.34	20
5	,,	5	$n'-n$	0.4	16	0.995	46	280	0.21	33
4	,,	10	$n'-n$	0.1	1	0.995	50	200	0.12	30
7	,,	40	$n'-n$	0.3	10	0.995	50	290	0.15	38
3	,,	120	$p'-p$	0.05	0.1	0.89	⋯	80	0.0003	25
1	,,	120	$p'-p$	0.05	0.01	0.90	⋯	90	0.001	27
2	,,	120	$p'-p$	0.03	0.02	0.92	⋯	80	0.0005	18
10	Vacuum	1	$n-p$	0.2	0.5	0.97	72	40	0.001	52
11	,,	8	$n'-n$	0.2	1	0.92	⋯	⋯	⋯	53

Note: HT — heat treatment, t — heat-treatment time.

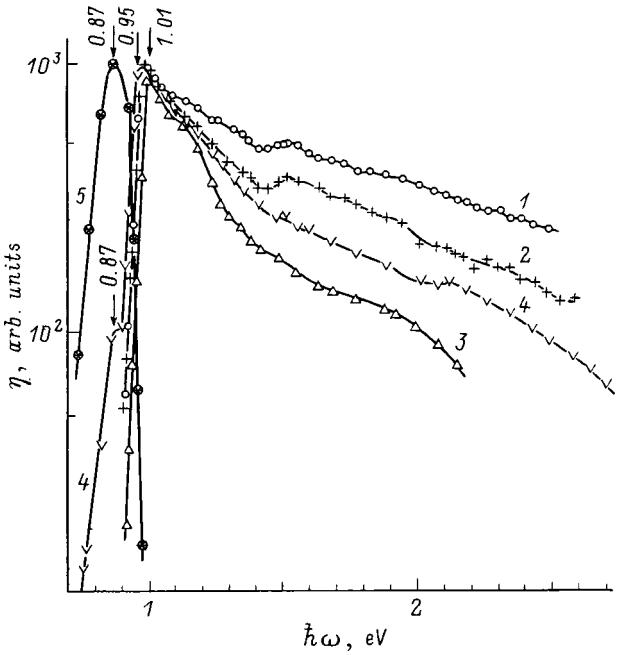

FIG. 3. Spectral curves of the relative quantum photoconversion efficiency of $n'-n$-$CuInSe_2$ (sample numbers: *1* — 6, *2* — 5, *3* — 4, *4* — 7) and $p'-p$-$CuInSe_2$ (curve *5*, sample 3) structures. The measurements were performed at $T=300$ K in unpolarized light (illumination of the structures from the layer side).

a) Intensification of the short-wavelength dropoff of the curve $\eta(\hbar\omega)$ and

b) shift of the long-wavelength photosensitivity edge into the impurity absorption range.

The ratio of η at $\hbar\omega=2$ eV (η_2) to the absolute maximum quantum photoconversion efficiency η_{max}, i.e., η_2/η_{max}, serves as a measure of the short-wavelength dropoff of the photosensitivity in Table I. The long-wavelength photosensitivity edge of $n'-n$ structures is exponential (Fig. 3, curves *1–4*), and its slope $S=\partial(\ln\eta)/\partial(\hbar\omega)$ remains large (see Table I) and corresponds to direct interband transitions in $CuInSe_2$.[6] The observed shift of $\hbar\omega_{max}$ into the long-wavelength region with increasing HT time t could be due to an increase in the density of the corresponding lattice defects of $CuInSe_2$ in the active region of the structures. These features correlate with the corresponding levels of lattice defects of $CuInSe_2$; such levels have been observed in the photoluminescence of $CuInSe_2$.[7] It is also evident from Fig. 3 that the sharp feature arising in the form of a peak at $\hbar\omega\approx0.87$ eV on the long-wavelength shoulder η transforms into an absolute maximum as t increases to 120 min, while the photosensitivity in the fundamental absorption range of $CuInSe_2$ becomes negligible. On the whole, the observed evolution of the spectra η shows that as the HT time for $CuInSe_2$ in air increases, the density of lattice defects and correspondingly the contribution of the long-wavelength sensitivity increase, the width of the bands decreases, and the short-wavelength decay of η intensifies (see Table I) as a result of the shift of the active region of the structures into the interior volume of the substrates.

The investigations of photosensitivity in unpolarized light for two different types of $CuInSe_2$ structures therefore indicate only an increase in the density of lattice defects in this ternary semiconductor as a result of selenium diffusion into the vapor phase. It can be inferred that in the presence of air this process slows down as a result of the appearance of an oxide layer on the $CuInSe_2$ surface. This situation probably accounts for the decrease in the rate of the conversion process $p\rightarrow n$ with HT of $CuInSe_2$ in air.

3. Neither type of structure obtained by illumination with linearly polarized light (LPL) along the normal to the illuminated plane (the angle of incidence $\Theta=0°$) showed any dependence on the spatial orientation of the electric field vector **E** of the light wave. This is due to the deliberate choice of samples with polycrystalline structure for these investigations, which made it possible to mask the natural photopleochroism of $CuInSe_2$ (Ref. 6) and therefore observe only the induced photopleochroism.[5]

The characteristic features of the polarized investigations of the photosensitivity of the two types of $CuInSe_2$ structures are as follows.

In all structures obtained by vacuum HT, the angular dependences of the short-circuit photocurrents i^P [the vector **E** is parallel to the plane of incidence (PI) of the light] and i^S (the vector **E** is perpendicular to the PI) are in agreement with the analysis of the passage of a light wave through the interface between two media (air/$CuInSe_2$) on the basis of the Fresnel relations[8] (Fig. 4a, curves *1* and *2*). In the entire range of photosensitivity the photocurrent i^P at first increases, reaches a maximum near the pseudo-Brewster reflection angle (marked by arrows in Fig. 4) and only then decays, while the current i^S only decreases in the entire range of angles Θ. The angular dependence $i^P(\Theta)$ (Fig. 4, curve *1*), taking into account the results of Ref. 9, indicates a good enough optical quality of the photodetecting surface, produced by vacuum HT of $CuInSe_2$, and the increase in the photocurrent ratio $i^P(55°)/i^P(0°)\approx1.12$ near the peaks in the η spectrum indicates a decrease of reflection losses of LPL.

For structures obtained by heat-treatment of $CuInSe_2$ in air (Fig. 4b, curves *5–8*), for $\Theta>0°$ the photocurrent i^S, just as i^P, is observed to increase in a certain region of variation of Θ, indicating that reflection losses decrease for the *s* wave also. On the basis of the results obtained in Ref. 10 this feature can be attributed to the interference of LPL in the entrance layer of such structures. As one can see from Fig. 4 (curves *3*, *9*, and *10*), the angular dependences of the induced photopleochroism coefficient

$$P_I=(i^P-i^S)/(i^P+i^S), \tag{2}$$

in both types of structures follow the same quadratic law $P_I\sim\Theta^2$, as indicated by the straight lines $P_I^{1/2}=f(\Theta)$ (see Fig. 4, curves *4*, *11*, and *12*).

Figure 5 shows examples of the spectral dependences of the induced photopleochroism coefficient at $\Theta=75°$ for some structures. The maximum value $P_I=53\%$ (see Table I) is characteristic of structures obtained by vacuum HT. This value of P_I corresponds to the theoretical value for the case where the LPL passes through the air/$CuInSe_2$ interface.[11]

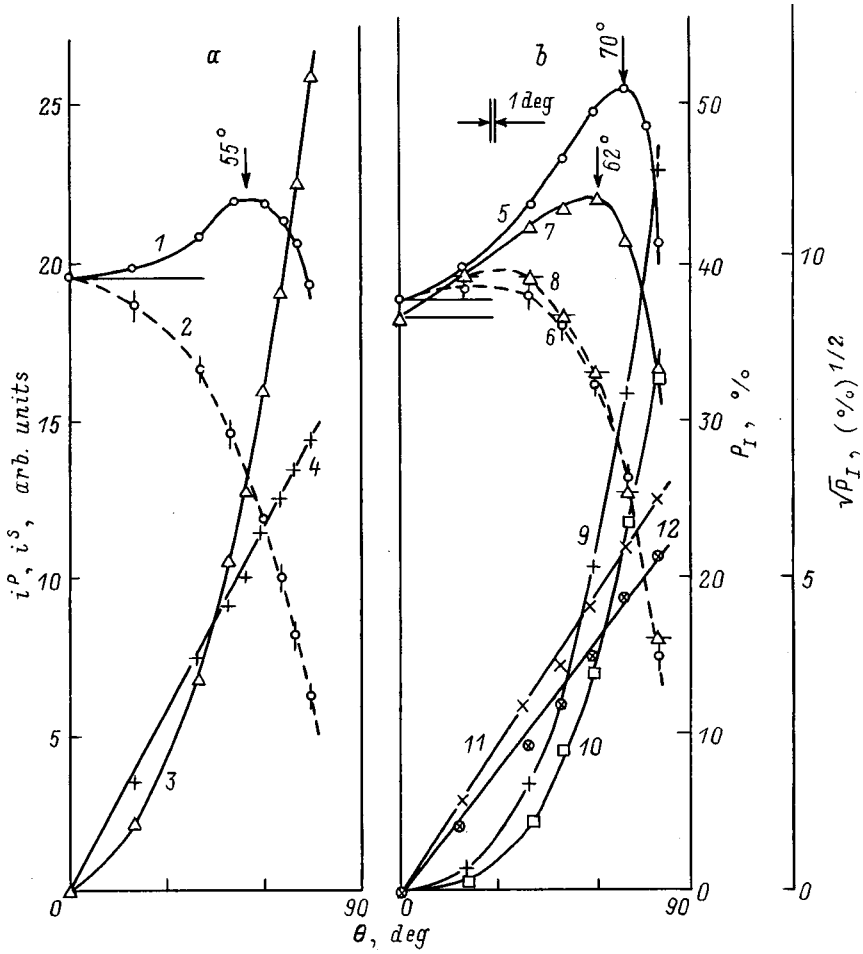

FIG. 4. Angular dependences of the photocurrents $i^P(1,5,7)$ and $i^S(2,6,8)$ and the induced photopleochroism coefficient P_I *(3,9,10)*–$\sqrt{P_1}$ *(4,11,12)* for $CuInSe_2$-based structures at $T=300$ K (a — sample 11; b — sample 5). Illumination was performed by linearly polarized radiation from the layer side; photon energy $\hbar\omega$, eV: *1–4* — 0.92; *5,6,9,11* — 0.955; *7,8,10,12* — 1.08).

For structures obtained by heat-treatment of $CuInSe_2$ in air (Fig. 5, curves *2–7* and in Table I), the experimental values of P_I are less than the theoretical values of P_I for the air/$CuInSe_2$ interface.[11] The fact that P_I changes from one structure to another could itself be due to the formation of oxides with a complicated composition on the $CuInSe_2$ surface, in agreement with the known results of ellipsometric investigations.[12,13] Specifically, the experimental values of P_I for samples 5 and 7 (Fig. 5, curves *2* and *3*) yield, on the basis of the analysis in Ref. 11, the estimate $n\approx 2.1$ for the refractive index, in agreement with the results of Ref. 13. On the other hand, on the basis of Ref. 10 the character of the experimental spectral curves of P_I and the observed sensitivity of the induced photopleochroism to the heat-treatment conditions (medium, time) could be due to interference of LPL in the oxide layers with variable composition that form on the $CuInSe_2$ surface.

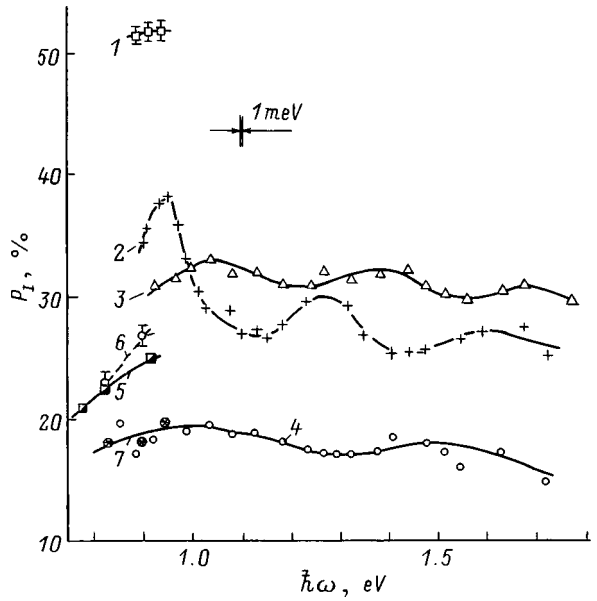

FIG. 5. Spectral curves of the coefficient of induced photopleochroism of $CuInSe_2$-based structures at $T=300$ K. The curves correspond to the following samples in Table I: *1* — 11, *2* — 7, *3* — 5, *4* — 6, *5* — 3, *6* — 1, *7* — 2; $\Theta=75°$.

In summary, the first comparison of the results of experimental investigations of the photosensitivity of two different types of $CuInSe_2$-based structures opens up new possibilities for polarized photoelectric spectroscopy in the diagnostics of phase interaction processes on the surfaces of complex semiconductors and therefore for choosing optimal technologies for producing optical-range photoconverters.

[1] J. R. Tuttle, E. D. Cole, K. R. Ramanathan, M. Contreras, J. Alleman, J. Keane, and R. Noufi, in *Proceedings of the 10th Sunshine Workshop on Thin Film Solar Cells* (Tokyo, Japan, Nov. 8–9, 1996), p. 139.
[2] L. Stolt, in *Proceedings of the 9th International Photovoltaic Science and Engineering Conference* (Niyazaki, Japan, Nov. 11–15, 1996), p. 139.

[3] H. W. Schock, Appl. Surf. Sci. **92**, 606 (1996).
[4] *Copper Indium Diselenide for Photovoltaic Applications*, edited by T. J. Coutts, L. L. Kazmerskii, and S. Wagner (Elsevier, Amsterdam, 1986).
[5] N. N. Konstantinova, M. A. Magomedov, V. Yu. Rud', and Yu. V. Rud', Jpn. J. Appl. Phys. **32**(3), 106 (1993).
[6] I. V. Bondar', A. A. Vaĭpolin, V. Yu. Rud', and Yu. V. Rud', Fiz. Tekh. Poluprovodn. **28**, 1322 (1994) [Semiconductors **28**, 748 (1994)].
[7] A. N. Y. Samaan, R. Waidhyanathan, R. Noufi, and R. D. Tomlinson, Sol. Cells **16**, 181 (1986).
[8] G. S. Landsberg, *Optics* (Vysshaya shkola, Moscow, 1976).
[9] V. Yu. Rud', Yu. V. Rud', and H. W. Schock, in *Abstracts Int. Conf. POLYSE'98* (Schwabisch Gmund, Germany, 1998), p. 37.
[10] V. Yu. Rud', Yu. V. Rud', T. Walter, and H. W. Schock, in *Proceedings of the 11th International Conference on Ternary and Multinary Semiconductors* (Salford, UK, Sept. 8–12, 1997) [Inst. Phys. Ser., No. 152, 971 (1998)].
[11] G. A. Medvedkin and Yu. V. Rud', Phys. Status Solidi A **67**, 333 (1981).
[12] R. N. Bekimbetov, *Author's Abstract of Candidate's Dissertation* (A. F. Ioffe Physicotechnical Institute, Russian Academy of Sciences, St. Petersburg, Russia, 1987).
[13] G. A. Medvedkin, R. N. Bekimbetov, T. L. Makarova, A. D. Smirnova, and V. I. Sokolova, Zh. Tekh. Fiz. **57**, 960 (1987) [Sov. Phys. Tech. Phys. **32**, 583 (1987)].

Translated by M. E. Alferieff

Investigation of the effect of surface treatment of a semiconductor on the characteristics of 6*H*-SiC Schottky diodes

A. A. Lebedev, D. V. Davydov, V. V. Zelenin, and M. L. Korogodskiĭ

A. F. Ioffe Physicotechnical Institute, Russian Academy of Sciences, 194021 St. Petersburg, Russia
(Submitted February 8, 1999; accepted for publication February 15, 1999)
Fiz. Tekh. Poluprovodn. **33**, 959–961 (August 1999)

Capacitance methods are used to investigate Schottky diodes formed on the basis of epitaxial $n-$type 6*H*-SiC layers grown by vapor-phase epitaxy. It is found that the height of the potential barrier and its dependence on the work function of the metal strongly depend on the method used for surface treatment of the semiconductor. © *1999 American Institute of Physics.* [S1063-7826(99)01508-2]

1. INTRODUCTION

It is well known that the pregrowth surface treatment of a semiconductor substrate strongly affects the quality of the epitaxial layer. The surface treatment of a pregrown layer largely determines the parameters of the surface-barrier structures (Schottky diodes) fabricated on its basis.

Investigations of Schottky diodes (SDs) based on 6*H*-SiC epitaxial layers obtained by the sublimation method (SE) have revealed that the height of the potential barrier (φ_b) is essentially independent of the type of metal deposited and is determined primarily by the density of surface states.[1,2] It has also been found that various treatments have virtually no effect on φ_b. At the same time, investigations of SDs based on epitaxial SiC layers obtained by vapor-phase epitaxy (CVD) have shown a strong (more than three orders of magnitude) variation in the reverse currents, depending on the methods used to treat the semiconductor before deposition of the metal.[3] In previous studies we performed comparative investigations of the spectra of deep centers in *n*-type epitaxial layers grown by vapor-phase and sublimation epitaxy methods.[4,5] It was found that the same deep background centers exist in epitaxial layers of both types, but their density is two or three orders of magnitude lower in the samples obtained by vapor-phase epitaxy. The results obtained were explained by the fact that the lower growth temperatures in the case of CVD epitaxy did not create the conditions for the formation of deep centers, and the stresses arising during growth relaxed as a result of the formation of dislocations whose density is much higher in layers of this type. The present study is a continuation of the comparative investigations initiated in Refs. 4 and 5 of the spectra of CVD and SE epitaxial layers of $n-$type 6*H*-SiC by capacitance methods.

2. SAMPLES

6*H*-SiC epitaxial layers grown by the CVD method at the CREE Company[6] (USA) and at A. F. Ioffe Physicotechnical Institute of the Russian Academy of Sciences[7] (PTI) were investigated. Silicon carbide substrates, grown by the Leighly method (PTI) or a modified Leighly method (LM) (CREE Co.) were used for epitaxy. All epitaxial layers were grown on the (0001) face of the Si substrate of 6*H*-SiC. Prior to deposition of the metal, the samples were washed with deionized water. The surface of the epitaxial layers was treated as follows: group 1 — etching in SF_6 plasma (samples 3 and 4); group 2 — conventional cleaning using organic solvents (samples 2 and 5); group 3 — etching in KOH (sample 1).

Before the barrier was created, the samples were annealed in a 10^{-4} Pa vacuum at 500 °C for 1–1.5 min. Deposition was conducted at sample temperature 100 °C. The metals were deposited by the resistance (Au, Al, Cr) or electron-beam (Mo) method.

3. EXPERIMENT

The uncompensated donor impurity density (N_d-N_a) and the height φ_b of the potential barrier were determined by the method of capacitance–voltage characteristics. The capacitive cutoff voltage (U_c) is determined by extrapolating the linear curve $C^{-2}-U$ to $C^{-2}=0$, where C is the differential capacitance of the SD, and U is the voltage on the structure. The barrier height φ_b is related to the capacitive cutoff voltage U_c by the relation $\varphi_b=U_c-\Delta\Phi+\xi+kT/e$, where $\Delta\Phi$ is the decrease of the barrier as a result of image forces, k is Boltzmann's constant, T is the absolute temperature, and e is the electron charge; $\xi=kT\cdot\ln(n/N_c)$, where n is the electron density in the conduction band, and N_c is the density of states in the conduction band.

It was found that the $C-U$ characteristics constructed for the experimental structures in the coordinates C^2-U were linear in the experimental voltage range. The typical $C-U$ characteristics are shown in Fig. 1. The quantity N_d-N_a for all epitaxial layers investigated fell into the range $(1-3)\times10^{16}\,\mathrm{cm}^{-3}$.

The measurements of φ_b for samples in groups 1–3 showed that this quantity depends strongly on the surface treatment method and is ~1.2–1.4 eV for group 1, ~0.7–0.8 eV for group 2, and ~0.4 eV for group 3. The dependence of φ_b on the work function of the metals used (Ti, Al, Au, Mo) (see Figs. 1 and 2) becomes weaker as the average value of φ_b decreases. It should be noted that Schottky diodes based on the CVD epitaxial layers grown on

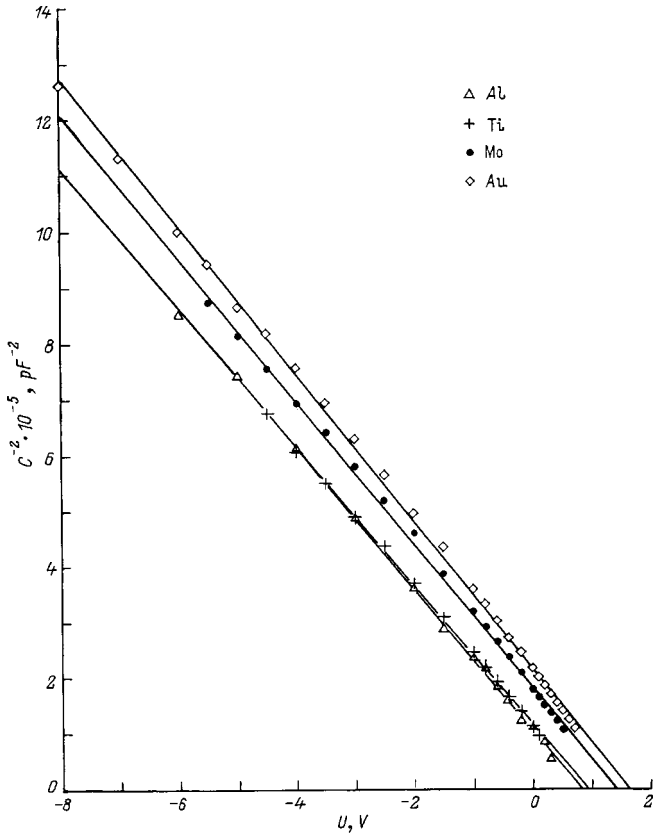

FIG. 1. Capacitance–voltage characteristics of sample 4 in the case of Schottky diodes formed using various metals.

Leighly substrates at the PTI possess essentially the same characteristics as diodes produced on the basis of epitaxial layers grown at CREE on ML substrates (samples 5 and 2, respectively). This indicates that the growth technology chosen has a stronger effect on the properties of epitaxial layers than the type of substrate employed.

4. DISCUSSION

X-Ray investigations of SiC p–n structures prepared by various technological methods have shown[8] that the minimum half-width of the x-ray diffraction peaks was observed primarily in structures with the maximum intensity of ''defect'' electroluminescence (DEL) (high density of i centers). It was inferred in this work that the activation centers of DEL were formed during the relaxation of the stresses arising during the growth of the epitaxial layer. It was also shown previously that the CVD epitaxial layers have a high dislocation density ($\sim 10^3 - 10^4\ \mathrm{cm}^{-2}$), i.e., one or two orders of magnitude higher than in epitaxial layers obtained by sublimation epitaxy.[9]

The CVD SiC layers were grown at lower temperatures than the sublimation layers: $\sim$1500 and $\sim$2000 °C, respectively. Therefore it can be assumed that for vapor-phase epitaxy the temperature is too low for stresses in the crystal lattice to relax via the formation of i centers or other similar defects of an acceptor nature. In this case relaxation occurs via the formation of dislocations. This tentatively explains the low density of deep acceptor centers and the high density of dislocations in CVD SiC layers as compared with layers

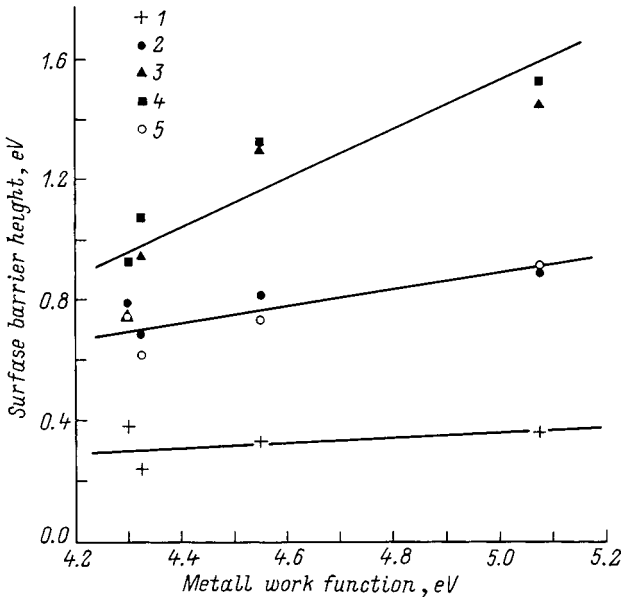

FIG. 2. Height of the potential barrier of the experimental samples versus the work function of the metal for various forms of surface treatment: *1* — after etching in KOH; *2, 5* — without special treatment; *3, 4* — after plasma etching.

grown by sublimation epitaxy. In addition, a high dislocation density could lead to lower mechanical and chemical strength in SiC layers prepared by the CVD method.[10] Because of the lower strength of the CVD films, the density of surface states changes when different forms of chemical treatment of the surface are used. As a result, the Schottky barrier height depends strongly on the method used to treat SiC surfaces.

5. CONCLUSIONS

We have shown here that the height of the potential barriers in Schottky diodes based on CVD epitaxial SiC layers strongly depends on the method of surface treatment of the semiconductor before deposition of the metal. The observed dependence is most likely determined by the structure of the layer and not by the type of substrate employed (Leighly or modified Leighly).

[1] A. L. Syrkin, A. N. Andreev, A. A. Lebedev, M. G. Rastegaeva, and V. E. Chelnokov, Mater. Sci. Eng. **29**, 198 (1995).
[2] A. M. Stelchuk and M. G. Rastegaeva, Mater. Sci. Eng. **46**, 379 (1997).
[3] M. Frischholz, K. Rottner, A. Schoner, T. Dalibor, and G. Pensl, Diamond Relat. Mater. **6**, 1396 (1997).
[4] A. A. Lebedev, D. V. Davydov, and K. I. Ignat'ev, Fiz. Tekh. Poluprovodn. **30**, 1865 (1995) [Semiconductors **30**, 975 (1995)].
[5] A. A. Lebedev and D. V. Davydor, Fiz. Tekh. Poluprovodn. **31**, 1049 (1997) [Semiconductors **31**, 896 (1997)].
[6] J. W. Palmor, J. A. Edmond, H. S. Kong, and C. H. Carter Jr., Physica B **185**, 461 (1993).
[7] V. V. Zelenin, A. A. Lebedev, S. M. Starobinets, and V. E. Chelnokov, Mater. Sci. Eng., B **46**, 300 (1997).
[8] A. A. Lebedev, M. P. Shcheglov, and T. V. Sokolova, Pis'ma Zh. Tekh. Fiz. **21**(16), 48 (1995) [Tech. Phys. Lett. **21**, 654 (1995)].
[9] A. A. Lebedev, M. P. Tregubova, A. A. Glagovskii, M. P. Scheglov, and V. E. Chelnokov, in *Abstracts E-MRS Conference* (Strasburg, France, 1996, p. A-15).
[10] Yu. A. Vodakov and E. N. Mokhov, Inst. Phys. Conf. Ser. **137** (1994), Chap. 3. p. 197.

Translated by M. E. Alferieff

Free ion transport in the insulator layer and electron–ion exchange at an insulator–semiconductor phase boundary produced as a result of thermally stimulated ionic depolarization of silicon MOS structures

E. I. Gol'dman, A. G. Zhdan, and G. V. Chucheva

Institute of Radio Engineering and Electronics, Russian Academy of Sciences, 141120 Fryazino, Russia
(Submitted January 25, 1999; accepted for publication February 18, 1999)
Fiz. Tekh. Poluprovodn. **33**, 962–968 (August 1999)

The nature of thermally stimulated depolarization currents in silicon MOS structures is investigated. The analysis is based on the experimentally established fact that the activation energy of the depolarization current in the initial section of growth is independent of the magnitude of the depolarizing voltage and on the previously discovered phenomenon of the formation of neutral associates ion + electron at the insulator–semiconductor interface. Transport of free ions in the insulator layer (the transit time is of a thermal activation character) and electron–ion exchange processes at the $Si–SiO_2$ phase boundary, which include tunneling ionization (decay) of neutral associates, are studied. The ion transfer in SiO_2 layers, found from the thermally stimulated depolarization curves using the developed theory, agrees well with data from independent experiments. © *1999 American Institute of Physics.* [S1063-7826(99)01608-7]

The advancement of MIS electronics into the submicron region is sharply toughening the requirements for ion contamination levels of the insulator. It is currently thought that the level of such contamination in field-effect transistors with gate length less than 0.1 μm should not exceed 5×10^9 cm^{-2} (Refs. 1 and 2), which is at least an order of magnitude less than the level achieved to date.[3] These circumstances are stimulating special interest in studying the mechanisms of ion generation and migration, as well as in developing reliable methods for investigating ion transport in the subgate oxide of silicon MOS structures and in refining the interpretation of known experimental data.[4–6] One of the most direct methods for investigating ion processes in insulators is observation of the thermally stimulated depolarization (TSD) currents,[7] and the results of such observations are, naturally, quite widely reported.[8–16] As a rule, samples with alkali metal impurities (Na, K) artificially introduced into the SiO_2 layer are investigated. However, irrespective of the method used to introduce the impurities (NaCl deposition on the oxide surface,[8] treatment of SiO_2 in NaCl solutions,[10–12,14] KCl solutions,[12,14] and NaI solutions, Ref. 14.[1)] the use of oxides with natural ionic contamination[5,9–11,13]), two wide, sometimes merging, current peaks are almost always observed on the TSD curves in the temperature range $T=200-675$ K — a low-temperature peak (a) and a high-temperature peak (b), which are associated with thermally stimulated transport of Na^+ and K^+ ions, respectively, from the SiO_2/Si interface (IF) toward the gate electrode.[2)] The localization temperatures of the current peaks exhibit a substantial variance: $T_m=312-450$ K (peak *a*) and $T_m=533-600$ K (peak *b*).[8–14] Apparently, this variance cannot be explained, on the basis of the general laws of TSD,[7] simply by a difference in the experimental conditions (the values of the initial ion density N_{s0} at the IF,[3)] rates of heating of the sample, and depolarizing fields). Therefore the reason for the variance in T_m must be sought in differences in the properties, which are correspondingly manifested in the TSD mechanisms, of the oxide films investigated. Two systems of views were developed concerning such mechanisms.

1. The TSD currents in the *a* peaks (Na^+) are due to depopulation of discrete ion traps (with activation energy $E_i=0.87\pm0.03$ eV)[8] or energy-distributed ion traps (in the band $\Delta E_i=0.75-1.50$ eV)[9,10] concentrated at the SiO_2/Si interface. The energy parameters of the traps for K^+ ions (peak *b*) have not been determined by the TSD method. Moreover, in Ref. 12 peak b ($T_m=573$ K) is associated to not K^+ ions but rather Na^+ ions, thermally activated from deep ''ionic'' states formed at the SiO_2/Si interface by chlorine introduced into the SiO_2 layers in amounts up to $\sim5\times10^{15}$ cm^{-2}. The process leading to trapping of ions in such states is thermally activated (the activation energy is 0.87 ± 0.15 eV) and is completed by neutralization of the states as a result of charge exchange with the Si substrate. Thus, in Ref. 12 the two main peaks of TSD are attributed exclusively to the presence of sodium in SiO_2,[4)] which is localized at the SiO_2/Si phase boundary in the ionized (peak *a*, ''shallow'' traps, $E_i\simeq0.75$ eV) and neutralized (peak *b*, ''deep'' traps, $E_i\simeq1.5$ eV) states. The value $E_i=0.87\pm0.03$ eV (Ref. 8) seems justified, since it was obtained by the standard method of analyzing the ascending branches of the TSD curves on the basis of molecular relaxation kinetics.[7] This approach in principle makes it possible to do without an analysis of the high-temperature shoulder of the peak, though in so doing information about the type of TSD kinetics is lost. In the apparatus, developed in detail, for analyzing thermally stimulated electronic phenomena,[17–19] the broadening and symmetrization of the peaks of ''deexcitation curves'' are attributed to retrapping, i.e., to bimolecular effects. This circumstance was disregarded in all studies concerned with de-

veloping a quantitative interpretation of the experimental data on TSD.[8,9,11,12] Specifically, in Refs. 9 and 12 the broadening of the current peaks *a* and *b* is explained by the presence of an energy distribution for boundary ionic traps. The only argument in favor of such a conclusion is the possibility of fitting quite accurately the computed TSD curves to the experimental curves by varying the spectral density of traps with a prescribed, energy-independent, frequency factor of their distribution $\omega \sim 10^{11}$ s^{-1}. However, as shown in Ref. 20, such a procedure, which evidently is always realizable for TSD curves of any form, is incorrect for nonmonoenergetic traps, so that additional information at least with respect to the spatial distribution of the ions pinned by the polarizing field to the SiO_2/Si interface is required in order to establish the physical nature of the TSD currents reliably. The formation of neutral associates when Cl atoms trap Na^+ ions, i.e., when the latter are localized in deep surface traps,[12] implies the presence of tunneling electron exchange in the semiconductor–insulator system[5)] (other forms of exchange are hardly possible because of the large height of the contact barrier, 3.4 eV (Ref. 21), at the SiO_2/Si phase boundary). Ions at the Si surface are not concentrated in a two-dimensional layer, but rather they are distributed along the normal to the IF in a region ranging in width from 5 Å (Ref. 22) up to 50 Å (Ref. 23) and even 200 Å (Ref. 12). Therefore even for monoenergetic traps the TSD peaks should be broadened as a result of the exponential dependence of tunneling exchange on the tunneling distance, distributed randomly over the surface of the IF and giving rise thereby to a dispersion of contact conditions.[6] This circumstance, just as the possibility of dispersive ion transport in the interior volume of the oxide,[24] if they are disregarded when analyzing the TSD curves, will be manifested in the form of an apparent spectral distribution of ion traps. Therefore, in the absence of information about the spatial distribution of ions at the IF, it is impossible to establish the existence of nonmonoenergetic traps. This information is not so difficult to obtain, since the apparatus for finding the coordinates of the centroid of the spatial localization of charge trapped in the region of the IF of MIS structures is quite well developed.[25,26] The laws of TSD of an insulator containing volume ion traps were analyzed in Ref. 27. It was shown that depending on the polarization regime of the MIS structure and the magnitude of the depolarizing field, the TSD current can describe from one to three of the strongly asymmetric peaks (with smoothly increasing and sharply decreasing branches), the positions of whose maxima are determined by the initial conditions of polarization (by the polarizing field) and by the depolarization conditions. However, TSD peaks of this form have not yet been observed experimentally.

It is evident from this brief analysis that Refs. 8, 9, and 12–14 do not present sufficiently convincing arguments in favor of the limiting stage of TSD processes being thermally activated ejection of ions from boundary traps, and the nature of the boundary traps, just as the mechanism of surface neutralization of ions, has not been identified (the latter, incidentally, is also valid for Ref. 10, where, apparently, the fact that neutralization of ions occurs at the SiO_2/Si interface was first established and confirmed by independent experiments).

2. A different, ''transport,'' concept of the origin of ionic TSD currents, which is developed in Ref. 11, is based on computer simulation of ion transport in the interior volume of the oxide, with allowance for the diffusion and drift of ions in the space-charge field, which varies during thermal stimulation and is produced by the uncompensated positive ions (Na^+). Only the low-temperature peak *a*, arising as a result of ion hops along the system of potential wells of depth E_i, was analyzed. The lifetime of an ion in the well is $\tau = \omega^{-1} \exp(E_i/kT)$, where ω is a frequency factor, k is Boltzmann's constant, and T is the temperature. Even though three adjustable parameters — E_i, ω, and l (the distance between neighboring wells) — are used, a good description of the experimental dependences of the current on the temperature, the depolarizing voltage, and N_{s0} could not be attained. Most importantly, the simulation results approach closest to the experimental data for physically unrealistic values $\omega \sim 10^6$ s^{-1}. On the basis of the model considered in Ref. 11, ω should be of the order of the characteristic phonon frequency, i.e., of the order of $10^{10}-10^{11}$ s^{-1} (Ref. 12). It is interesting that if the computed straight line $\log \omega - E_i$ presented in Ref. 11 is extended to reasonable values of ω (for example, $\omega = 3\times 10^{10}$ s^{-1}),[6)] then one obtains not $E_i = 0.5$ eV, as in Ref. 11, but rather $E_i = 0.87$ eV, i.e., a value which is very close to that observed in Refs. 8, 9, and 12 and obtained by independent methods (see, for example, Ref. 15). Nonetheless, to describe TSD of MOS structures it is necessary to take account of the possibility of volume properties of the oxide being manifested. This is indicated, specifically, by the results of isothermal time-of-flight experiments.[6,15]

Thus, as far as the experimental results are concerned, the systematic features of TSD of Si-based MOS structures are assumed to be known. The characteristics of the current peaks and their dependence on the conditions of polarization (field, temperature, and time) and depolarization (depolarizing voltage and heating rate) have been established. At the same time, information about the nature of the TSD peaks is quite sparse and contradictory; experimental investigations have been performed predominantly at the qualitative level; quantitative data are few and ambiguous.

In this connection, in the present paper new ideas about the mechanism of TSD, which follow from the model of isothermal ionic depolarization of an insulator[6] and permit explaining the basic experimental data, are developed on the basis of detailed investigations of TSD of SiO_2 layers on Si. The measurements were performed on silicon MOS structures, identical to the structures investigated previously:[4–6] Al (gate electrode with area $S = 2.4\times 10^{-2}$ cm^2)/SiO_2 (thermal oxide with thickness $h = 1700$ Å)/Si (100) (free electron density at 300 K $n = 1\times 10^{13}$ cm^{-3}). The measuring system described in Ref. 4 and the traditional method for observing TSD were used.[7] The structure was polarized at temperature $T = 423$ K in the prescribed time t_p with positive potentials V_g ($V_{gp} > 0$) on the gate electrode; the mobile positive ions in the SiO_2 layer shifted to the layer/Si interface. Next, the sample was cooled to temperature $T_0 \simeq 263$ K, V_g abruptly

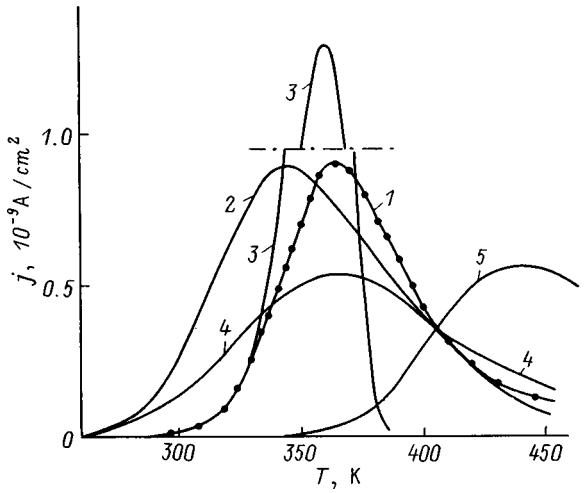

FIG. 1. Typical curves of TSD of *n*-Si-based MOS structures with depolarization voltages $V_{gd}=-1$ (*1*) and -11.2 V (*2*). The structure was polarized at $T=423$ K, $V_{gp}=5$ V, $t_p=5$ min. *3* — Calculation in the monomolecular kinetics approximation with a fit according to the current levels to the experimental data 1 in the region of initial growth. *4* — Data from Ref. 9. *5* — Thermally stimulated polarization current for the investigated structure with $V_{gp}=1.5$ V.

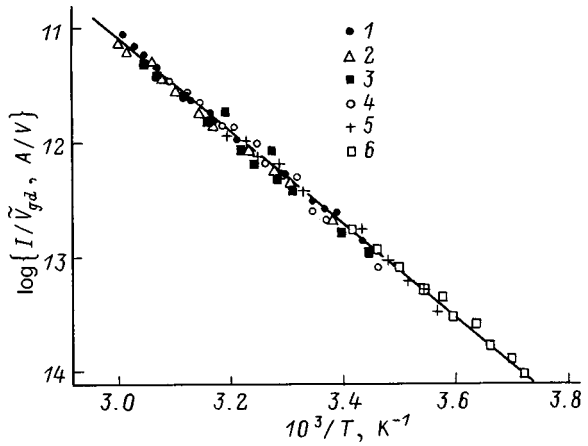

FIG. 2. Temperature dependences of the effective thermally stimulated ion conductivity $\log(I/|\tilde{V}_{gd}|)$, scaled to the same value $N_{s0}^{*}=4.5\times10^{10}$ cm^{-2}, for regions of initial current growth ($T_0\leqslant T\leqslant T_m$) for depolarization voltages $|V_{gd}|$, V: *1* — 0.6, *2* — 1, *3* — 1.5, *4* — 2.5, *5*—5, *6* — 11.2. Polarization regime $T=423$ K, $V_{gp}=5$ V, $t_p=5$ min, $\tilde{V}_{gd}=V_{gd}+V_c$, $V_c\simeq0.4$ V.

changed its sign ($V_{gd}<0$), and in the process of heating at constant rate $\beta_T\simeq0.4\,\mathrm{deg}\cdot\mathrm{s}^{-1}$ the current $I=jS$ flowing in the external circuit (j is the current density) and due to depolarization of SiO_2 (i.e., the motion of ions from the SiO_2/Si interface to the Al electrode) was recorded. The typical TSD curves are presented in Fig. 1 for two values of the depolarizing voltage V_{gd}. The character of the curves, their temperature localization range, the displacement of the temperature T_m of the current maximum with increasing $|V_{gd}|$ to low temperatures, and even the TSD current levels (compare, for example, the curves *1* and *2* with curve *4*) are very close to those known for the TSD peak *a*.[8–14] For this reason, the subsequent discussion will be quite general.

The temperature characteristics of the depolarization current cannot be described by the equations of monomolecular kinetics. This becomes clear when the experimental curves $j(T)$ (Fig. 1, curves *1* and *2*) are compared with the dependence (curve *3*) computed in the monomolecular approximation using the formula[7]

$$j=j_0\exp\left[-\frac{E}{kT}-\frac{\omega}{\beta_T}\int_{T_0}^{T'}\mathrm{e}^{-E/kT}dT'\right]. \qquad (1)$$

The parameters required to calculate $j(T)$ — the activation energy E, the preexponential factor j_0, and the frequency factor ω — were obtained by analyzing the region of the initial growth of the experimental curve *1* [$j\simeq j_0\times\exp(-E/kT)$, $T_m>T\geqslant T_0$]:[7)] $E=0.90$ eV — according to the slope of the straight line plotted in the Arrhenius coordinates $\log j-T^{-1}$; $j_0=qN_{s0}\omega\simeq1.6\times10^4$ A/cm^2 — from the equation $j_{\exp}(\tilde{T})=j_0\exp(-0.90/k\tilde{T})$, where $j_{\exp}$ is the current density measured for any temperature $\tilde{T}$ given in the region of linearity of the plot $\log j-T^{-1}$; $\omega=j_0/qN_{s0}\simeq1\times10^{11}$ s^{-1} (q is the elementary charge) — according to the values of j_0 and $N_{s0}\simeq1\times10^{12}$ cm^{-2} (the latter was found by integrating the experimental curve *1* in Fig. 1 over time). After starting at the same point, which is a natural consequence of the fitting procedure employed, the curves *1* and *3* diverge substantially: The experimental curve is much less steep than the computed curve, especially in the region where the current drops off. Quantitative estimates made of the activation energy using the standard formulas of thermally stimulated conductivity[30] for temperatures of the maximum and the half-heights of the peak give $E=0.62$ and 0.31 eV. For monomolecular kinetics of depopulation of ion traps, these values of E should be the same, within the limits of experimental error, as the value of E found from the Arrhenius straight line. Apparently, the large broadening and the shape of the TSD peaks are responsible for their interpretation on the basis of the idea of energy-distributed surface ion traps.[9,12] However, such an interpretation contradicts a number of experimentally observed results. For traps with a smooth energy distribution, as $|V_{gd}|$ increases, it can be expected that, first, T_m will increase and, second, the apparent activation energy will increase because increasingly deeper trapping centers will be drawn into the TSD current generation process. Even in the region of initial current growth $I\ll I_m$ (I_m is the current at the maximum of the TSD peak) the curves $\log I-T^{-1}$, generally speaking, should be nonlinear Ref. 20.[8)] Experimentally, however, T_m decreases with increasing $|V_{gd}|$ (Fig. 1; see also Ref. 8), the activation energy E does not depend on $|V_{gd}|$, and its value, averaged over the slopes of the six straight lines $\log I-T^{-1}$ obtained in a wide range of values of $|V_{gd}|$ ($0.6\leqslant|V_{gd}|\leqslant11.2$ eV), has a small variance and is 0.87 ± 0.05 eV. Moreover, the dependences $\{\log I/|\tilde{V}_{gd}|\}-T^{-1}$ ($\tilde{V}_{gd}=V_{gd}+V_c$, V_c is the gate–semiconductor contact potential difference) describe a single straight line (Fig. 2). On the descending branches of the TSD curves there is a region where the current is independent of the temperature, of the magnitude of the depolarizing voltage and of the rate β_T of heating of the sample, and is only a function of the time t measured from the moment t_m at which the current reaches its maximum value (Fig. 3). Thus, the experimental data presented are close to the known results of

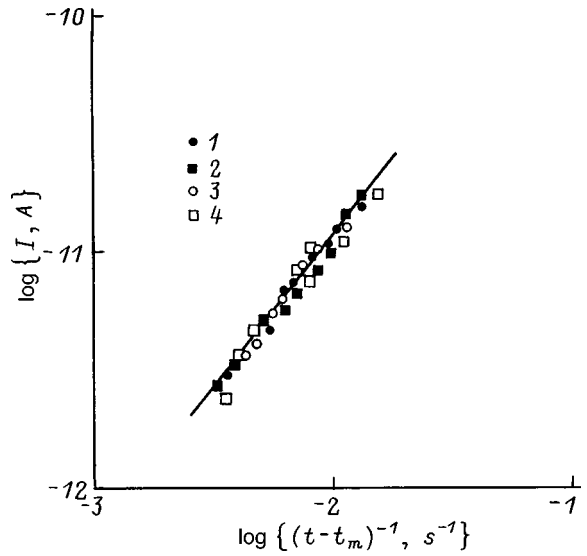

FIG. 3. Quasihyperbolic region of TSD current decay for depolarization voltages $|V_{gd}|$, V: *1* — 0.6, *2* — 1.5, *3* — 2.5, *4* — 11.2. Polarization regime $T=423$ K, $V_{gp}=5$ V, $t_p=5$ min.

similar investigations and, just as these results, do not agree with the presence of discrete ion traps or ion traps distributed over energy at the SiO_2/Si interface.

Turning now to the interpretation of the experiments, we note that in virtually all studies devoted to isothermal observations of ion transport through a dielectric gap[31–33] and the dynamics of the shift of the flat-band voltage[34] due to ion drift, the initial stages of depolarization of SiO_2 are attributed to the transit of free ions. Therefore it it logical to conclude that even the initial stages of TSD current growth can be determined by the time-of-flight effect.

Charge carriers can pass through a dielectric gap in the regimes of drift of small or large charge.[35] The first regime occurs for $4\pi qN_{s0}/\kappa_{SiO_2} \ll \tilde{V}_{gd}/h$ and the second regime occurs for the opposite inequality (κ_{SiO_2} is the permittivity of the oxide). Let us estimate $4\pi qN_{s0}/\kappa_{SiO_2}$. The value of N_{s0} appearing in the inequality should be identified with the value N_{s0}^* for completely free ions. This quantity can be found approximately from the relation

$$N_{s0}^* = (1/q\beta_T)\int_{T_0}^{T^*} I(T)dT,$$

where the temperature T^* corresponds to the moment of arrival of the leading edge of the ion packet at the gate electrode: $\tau_0 = t^* = (T^* - T_0)/\beta_T$. The quantity T^* can be taken as the temperature at which the TSD current no longer follows the Arrhenius law. Estimates give $N_{s0}^* \simeq 4.5\times 10^{10}$ cm^{-2}, $4\pi qN_{s0}^*/\kappa_{SiO_2} \simeq 2\times 10^4$ V/cm ($\kappa_{SiO_2}=3.9$), and as can be easily checked, for $|V_{gd}| \geqslant 1$ V the depolarizing field is greater than $4\pi qN_{s0}^*/\kappa_{SiO_2}$ (the value $V_c \simeq 0.4$ V required for these estimates was calculated, according to Ref. 21, for carrier density $n=1\times 10^{13}$ cm^{-3} and temperature $T\simeq 300$ K, corresponding to the midpoint of the temperature range presented in Fig. 2). For this reason, the small-charge drift regime should occur under the conditions of the present experiments. Then, in accordance with Ref. 35,

$$j = \frac{qN_{s0}^*}{\tau_0} = \frac{qN_{s0}^*\tilde{V}_{gd}\mu_0 \exp(-E_\mu/kT)}{h^2}, \qquad (2)$$

so that in the time-of-flight regime at the initial stages of TSD current growth, irrespective of the value of $\tilde{V}_{gd}$, the Arrhenius plots in the coordinates $\log(I/|\tilde{V}_{gd}|) - T^{-1}$ should be a single straight line whose slope is determined by the value of E_μ. The corresponding dependence presented in Fig. 2 agrees very well with these ideas. The quantity E_μ determined from the slope of the straight line using the least-squares method is 0.87 ± 0.05 eV, and the value of μ_0 found by extrapolating to the $T^{-1}=0$ axis is ~ 3.2 $cm^2/(V\cdot s)$. These values of E_μ and μ_0 agree well with the published values[8,9,12,36,37] and with the values which we obtained previously by independent methods.[5,6] Hence it follows that the initial stages of TSD current growth are due to thermal activation of the time-of-flight of free ions.

The model developed and deduced theoretically and experimentally in Ref. 6 can be used to interpret the laws of variation of the TSD current following the time-of-flight stage. According to Ref. 6, a reversible electron-ion reaction occurs at the insulator–semiconductor interface: In polarizing fields (positive ions are localized at this interface), as a result of tunneling transitions of electrons from the semiconductor to traps produced by ions and their dielectric environment, almost complete neutralization of the boundary ion charge occurs and is accompanied by the formation of the neutral associates (NAs) ion + electron;[9] in depolarizing fields — in the isothermal relaxation and TSD regimes — the depolarization kinetics is determined by drift not of the neutralized part of the ions but by tunneling ionization (decay) of NAs. Since the decay rate of NAs is independent of the magnitude of the depolarizing field and the temperature, the relaxation signal should be a unique function of time. (This fact was established in Ref. 6 on the basis of observations of the isothermal relaxation.)

In accordance with these ideas, tunneling ionization of NAs located directly at the insulator–semiconductor interface should accompany TSD even during the transit of transmission of the leading edge of the initially free ions. Since the electron lifetime on a NA increases exponentially with increasing distance between the NA and the interface, while τ_0 decreases rapidly with temperature, NAs initially decay in a time shorter than τ_0 and then the process starts to lag. This results in a decrease of the growth rate [$j(T)$ deviates from the Arrhenius law; compare curves *1* and *3* in Fig. 1] followed by the appearance of a maximum, after which the TSD current decays. At the stage where τ_0 becomes much less than the tunneling ionization time of NAs, the TSD current j ceases to depend on the depolarizing field, the temperature, and therefore the temperature sweep rate β_T and, according to Ref. 6, is determined by the relation

$$j \sim \tilde{t}^{-(1+\delta/\lambda)}, \qquad (3)$$

TABLE I. Summary data on the characteristics of ionic conduction in oxide layers on a silicon surface.

μ_0, $cm^2/(V \cdot s)$	E_μ, eV	Determination method	References
85.5	0.80 ± 0.05	Dynamic IVCs	Ref. 5
–	$0.75-1.5$	TSD	Refs. 9, 12
3.2	0.87 ± 0.05	TSD	Our work
–	0.87 ± 0.03	TSD	Ref. 8
72.5	0.80 ± 0.05	Time-of-flight	Ref. 6
1.05	0.66	Time of flight	Ref. 32
0.40	0.73	Time of flight	Ref. 31
$3.5 \times 10^{-4}-46$	0.81 ± 0.15	Result of averaging the published data for Na^+ ions	Refs. 8, 12, 31, 32, 37–42

where $\tilde{t}$ is the time measured from the moment of arrival at the given stage (under the present experimental conditions, as one can see from Fig. 3, this time essentially coincides with the time t_m at which the current reaches its maximum value), δ is the effective tunneling length, and λ is the diffusion length of NAs that corresponds to the polarization conditions, i.e., the initial spatial distribution of NAs in the insulator: the concentration $\sim \exp(-z/\lambda)$, z is the coordinate measured from the interface into the interior volume of the insulator. The ''dispersion'' character of the relation (3) is due to two circumstances — the wide (exponential) distribution of tunneling ionization times, on the one hand, and the exponential dropoff of the initial (''frozen'' after polarization) concentration of NAs with characteristic length λ, on the other.

The quasihyperbolic depolarization law (3) is clearly manifested in the experiment: The descending branches of the TSD current constructed in the coordinates $\log I - \log(t - t_m)^{-1}$ describe a single straight line (Fig. 3,) irrespective of the magnitude of the depolarizing voltage. The exponent determined from the slope of this line is $1 + \delta/\lambda = 1.28 \pm 0.04$. The investigations of isothermal depolarization performed by the method of Ref. 6 in the temperature range 333–453 K show that as the temperature is raised, the exponent $1 + \delta/\lambda$ increases from 1.08 to ~ 1.3. In the model developed in Ref. 6, which assumes dispersion of the tunneling ionization times of the NAs, it was not assumed that the parameter δ/λ is a function of temperature. Therefore, the experimentally observed dependence of δ/λ on T can be regarded as being due to thermal tunneling decay of NAs, i.e., $\delta = \delta(T)$.

The parameters of ion conductivity found on the basis of the present and previous works[5,6] are compared in Table I with the most reliable average published data characterizing the transport of Na^+ ions in SiO_2 layers. It is evident from this table that the basic characteristics of ion conduction on SiO_2 layers, determined from the results of three physically independent experiments (dynamic current–voltage characteristics — IVCs, isothermal relaxation, and TSD), agree very well within the limits of experimental error with one another and with the results of independent measurements.

In summary, the initial stages of TSD current growth must be attributed to thermal activation of the time of flight of free ions, and the descending branches to tunneling (or thermotunneling) ionization of NAs. Correspondingly, it is natural to interpret the regions of the extrema as regions of a transition from a regime of thermally activated transit of free ions with gradual depletion of their reservoir in the oxide layer bounding the silicon to a regime of thermotunneling decay of NAs, accompanied by drift of newly formed free ions to the gate electrode. This gives rise to a shape of the peaks of the thermally stimulated relaxation signals that is characteristic of systems with distributed parameters[20] — the slope of the ascending branches of the TSD current is much greater than the slope of the descending branches.

It is interesting that the thermally stimulated polarization (TSP) of silicon MOS structures under otherwise equal conditions occurs at much higher temperatures than TSD (compare curves *1*, *2*, and *4* with curve *5* in Fig. 1). If it is assumed, in accordance with the ideas considered above, that the initial stages of growth of the TSP current are also associated with thermal stimulation of the time of flight of free ions, then in order to remain within the model of Ref. 6 it is necessary to ascertain that the degree of neutralization of ions in the metal (gate electrode) is much higher than at the boundary with silicon. The stage of tunneling ionization of NA following the time-of-flight stage occurs only with sharp electron depletion of the semiconductor surface, which occurs due to switching of the field in the insulator from polarizing to depolarizing. The picture at the insulator–metal contact is different. For any realistic value, the electric field cannot alter the position of the Fermi level of the electrons in the metal at its phase boundary with the insulator and thereby displace the equilibrium of ion neutralization–NA ionization tunneling processes. Hence follows the obvious conclusion, in agreement with existing experimental data, that the process leading to the polarization of the insulator in MIS structures is much slower than the depolarization process[5,42] (see also Fig. 1). In this connection, it is of interest to investigate structures with a strongly doped semiconductor, where definite ''symmetrization'' of polarization–depolarization processes can be expected, as well as *p*-Si-based MOS structures, which thus far have not been studied from this point of view. Specifically, polarization–depolarization experiments on such structures should make it possible to identify directly the presence of mobile negative ions in the oxide. Lacking data from such experiments, at present it is impossible to rule out with certainty either the ''trap'' nature of TSP currents[8,9,11,12] or the model of electrochemical reactions at the gate electrode[40,43] accompanied

by generation of free ions followed by injection of the ions into the oxide layer.

We thank N. F. Kukharskaya and I. N. Tulyakovaya for unfailing and constructive assistance.

[1)]In these cases the nature of the charge carriers responsible for the corresponding current peak was identified according to the growth in the amplitude of the peak with increasing holding time of the sample in the sodium or potassium salt solution (under otherwise equal conditions).

[2)]TSD curves with a more complicated structure are also observed. Besides the main peaks *a* and *b* they show additional peaks, ranging from one peak[10] to several peaks.[8,12]

[3)]Experiments on TSD cover a very wide range of values of N_{s0}: from $\leqslant 1\times10^{10}$ (Ref. 13) to 3×10^{13} cm^{-2} (Ref. 8).

[4)]The authors of Ref. 10 arrived at the same conclusion somewhat earlier but on the basis of different considerations.

[5)]A typical indicator of this mechanism of electronic exchange are very large, essentially independent of the electric field, characteristic response times of the MIS structure to an external perturbation.[20] Precisely such behavior was clearly found to accompany neutralization of Na^+ ions with the participation of Cl.[12]

[6)]A value of ω very close to this value is deduced in Ref. 12.

[7)]For a priori unknown relaxation kinetics the ''method of initial heating'' based on the relation $j \simeq j_0 \exp(-E/kT)$ gives the most reliable information about the value of E.[18,28,29]

[8)]For monoenergetic traps the position of the current maximum T_m should not depend on $|V_{gd}|$.

[9)]According to the data of Ref. 6, the neutralization factor (the ratio of the NA density to the total density of neutralized and free ions) reaches 83%.

[1] G. S. Horner, M. Kleefstra, T. G. Miller, and M. A. Peters, Solid State Technol., N 6, 79 (1995).
[2] G. Ya. Krasnikov, Élektron. tekhn., Ser. 3, No. 1, 67 (1996).
[3] M. Lee, C. H. Lin, B. H. Lei, and C. D. Yang, Jpn. J. Appl. Phys. , **37**, L53 (1998).
[4] E. I. Gol'dman, A. G. Zhdan, and G. V. Chucheva, Prib. Tekh. Eksp. No. 6, 110 (1997).
[5] E. I. Gol'dman, A. G. Zhdan, and G. V. Chucheva, Fiz. Tekh. Poluprovodn. **31**, 1468 (1997) [Semiconductors **31**, 1268 (1997)].
[6] E. I. Gol'dman, A. G. Zhdan, and G. V. Chucheva, Fiz. Tekh. Poluprovodn. **33**, 933 (1999) [Semiconductors **33**, 985 (1999)].
[7] Yu. A. Gorokhovatskiĭ and G. A. Bordovskiĭ, *Thermal-Activation Spectroscopy of High-Resistance Semiconductors and Dielectrics* (Nauka, Moscow, 1991).
[8] T. W. Hickmott, J. Appl. Phys. **46**, 2583 (1975).
[9] M. R. Boudry and J. P. Stagg, J. Appl. Phys. **50**, 942 (1979).
[10] T. Hino and K. Yamashita, J. Appl. Phys. **50**, 4879 (1979).
[11] K. Yamashita, M. Iwamoto, and T. Hino, J. Appl. Phys. **52**, 1429 (1981).
[12] I. P. Stagg and M. R. Bodry, J. Appl. Phys. **52**, 885 (1981).
[13] M. W. Hillen and D. G. Hemmes, Solid-State Electron. **24**, 773 (1981).
[14] C. Choquet, C. Plossu, M. Berenguer, and B. Balland, Thin Solid Films **167**, 45 (1988).
[15] J. F. Verwey, E. A. Amerasekera, and J. Bisschop, Rep. Prog. Phys. **53**, 1297 (1990).
[16] A. G. Zhdan and Yu. V. Markin, Fiz. Tekh. Poluprovodn. **28**, 756 (1994) [Semiconductors **28**, 444 (1994)].
[17] V. V. Antonov-Romanovskiĭ, *Kinetics of Photoluminescence of Crystal Phosphors* (Nauka, Moscow, 1966).
[18] K. H. Nickolas and J. Woods, J. Appl. Phys. **15**, 783 (1964).
[19] R. Chen and Y. Kirsh, *Analysis of Thermally Stimulated Processes* (Pergamon Press, New York, 1981).
[20] E. I. Goldman and A. G. Zhdan, Semicond. Sci. Technol. **5**, 675 (1990).
[21] S. M. Sze, *Physics of Semiconductor Devices* [Wiley, New York, 1969; Mir, Moscow, 1984, Vol. 1].
[22] A. Harstein and A. B. Fowler, Surf. Sci. **73**, 19 (1978).
[23] D. J. DiMaria, J. Appl. Phys. **52**, 7251 (1981).
[24] I. P. Zvyagin, *Kinetic Phenomena in Disordered Semiconductors* (Moscow State University Press, Moscow, 1984).
[25] V. I. Antonenko, A. G. Zhdan, and P. S. Sul'zhenko, Fiz. Tekh. Poluprovodn. **22**, 756 (1988) [Sov. Phys. Semicond. **22**, 473 (1988)].
[26] E. I. Gol'dman, Fiz. Tekh. Poluprovodn. **26**, 766 (1992) [Sov. Phys. Semicond. **26**, 430 (1992)].
[27] E. I. Gol'dman, Fiz. Tekh. Poluprovodn. **31**, 43 (1997) [Semiconductors **31**, 36 (1997)].
[28] L. I. Grossweiner, J. Appl. Phys. **24**, 1306 (1953).
[29] A. G. Zhdan and N. A. Lushnikov, Fiz. Tekh. Poluprovodn. **16**, 793 (1982) [Sov. Phys. Semicond. **16**, 509 (1982)].
[30] A. G. Zhdan, V. B. Sandomirskiĭ, A. D. Ozheredov, and G. N. Yakovleva, Fiz. Tekh. Poluprovodn. **3**, 1755 (1969) [Sov. Phys. Semicond. **3**, 1486 (1969)].
[31] S. R. Hofstein, Appl. Phys. Lett. **10**(10), 291 (1967).
[32] J. P. Stagg, Appl. Phys. Lett. **31**(8), 532 (1977).
[33] V. G. Litovchenko and A. P. Gorban', *Principles to the Physics of Metal–Insulator–Semiconductor Microelectronic Systems* (Naukova dumka, Kiev, 1078).
[34] V. M. Koleshko, P. P. Goĭdenko, and L. D. Buĭko, *Monitoring in Microelectronics Technology* (Nauka i tekhnika, Minsk, 1979).
[35] M. Lampert and P. Mark, *Current Injection in Solids* [Academic Press, New York, 1970; Mir, Moscow, 1973].
[36] S. R. Hofstein, IEEE Trans. Electron Devices **ED-13**, 222 (1966).
[37] G. Greeuw and J. F. Verwey, J. Appl. Phys. **56**(8), 2218 (1984).
[38] E. H. Snow, A. S. Grove, B. E. Deal, and C. T. Sah, J. Appl. Phys. **36**(5), 1664 (1965).
[39] R. J. Kriegler and T. F. Devenyi, Thin Solid Films **36**, 435 (1976).
[40] V. N. Vertoprakhov, B. M. Kuchumov, and E. G. Sal'man, *The Structure and Properties of* Si–SiO_2–*M Structures* (Nauka, Novosibirsk, 1981).
[41] W. A. Pliskin, D. R. Kerr, and J. A. Perri, in *Physics of Thin Films*, Vol. 4 [Academic Press, New York, 1967, pp. 257–324; Mir, Moscow, 1970, No. 4, p. 303].
[42] M. Kuch and D. J. Silversmith, J. Electrochem. Soc.: Sol. St. Sci. N 6, 966 (1971).
[43] M. L. Reed, Semicond. Sci. Technol. **4**, 980 (1989).

Translated by M. E. Alferieff

LOW-DIMENSIONAL SYSTEMS

Transformation of a metal–oxide–silicon structure into a resonance-tunneling structure with quasi-zero-dimensional quantum states

G. G. Kareva*)

Scientific-Research Institute of Physics, St. Petersburg State University, 198904 St. Petersburg, Russia
(Submitted March 16, 1998; accepted for publication January 20, 1999)
Fiz. Tekh. Poluprovodn. **33**, 969–972 (August 1999)

A metal–oxide–silicon structure was converted into a double-barrier nanostructure by decreasing the thickness of the insulator and the extent of the depleted space-charge region of *p*-type Si to nanometers. Room-temperature resonant electron tunneling through a miniband of a quantum well of the surface depleted region of silicon was obtained; this was indicated by the measured current–voltage characteristics. The number of features reached 10 because of the large depth (more than 1.1 eV) of the quantum well. The maximum peak-to-valley current ratio is 500. © *1999 American Institute of Physics.* [S1063-7826(99)01708-1]

Resonance-tunneling semiconductor nanostructures with artificial periodicity and a low-dimensional electron gas have now been studied extensively for the last two decades.[1–6] These structures are produced by varying the composition and doping of the constituent components. The most interesting qualities of the structures are their high-speed response time, the possibility of controlling the energy structure with the resultant control of their properties, the negative differential resistance, and charge phenomena. The drawbacks of the structures are due to structural complexity: complex technologies and methods are required to fabricate and monitor them. No mention has been made of metal–oxide–silicon (MOS) structures in their simplest structural variant as resonance-tunneling structures. At the same time, MOS structures are some of the most important elements in modern electronics, and their sizes continue to decrease as modern electronics advances. When the nanometer limit is overcome, MOS structures can be qualitatively altered and converted into resonance-tunneling structures. As a result, it is possible to solve another pressing problem of producing quantum dots on a silicon surface. The present paper is devoted to a discussion of these issues.

To convert a MOS structure into an artificially periodic nanostructure, specifically, a double-barrier structure, the thickness of the oxide grown and the extent of the space-charge region (SCR) of *p*-Si (Ref. 7) were decreased to the nanometer range without complicating the construction by adding layers or inclusions, as done in Refs. 4 and 5. The method used to produce the oxide provides a possibility for estimating its thickness.[7] The thickness of the oxide was also estimated using capacitive and ellipsometric measurements. To ensure a nanometer-size SCR, Si strongly doped with boron was chosen. KDB-0.07, KDB-0.01, and KDB–0.005 with (100) or (111) surface orientation were investigated. With such doping of Si, its depleted SCR can be regarded as a tunneling-transparent barrier, connected in series with a quantum well possessing a series of quantum minibands (Fig. 1). In addition, this quantum well lies between two tunneling–transparent barriers, one of which (left-hand barrier) is the barrier of the depleted SCR of *p*-Si, while the other (right-hand barrier) is the oxide barrier. Therefore the result is a double barrier which, as a rule, is asymmetric. The quantum well is deep (its depth is greater than $E_g = 1.1$ eV) and its dimensions are quite small (of the order of nanometers). These circumstances give a quite large (much greater than kT) energy splitting between the neighboring quantum minibands, making it possible to observe resonance tunneling at room temperature.

Let us examine the operation of a structure with an external voltage polarity such that Si is negative with respect to the metal (Fig. 1a). As one can see from the figure, as the applied voltage increases, the quantum minibands of the SCR line up successively, one after another, with the Fermi level in the interior volume of *p*-Si and resonance tunneling

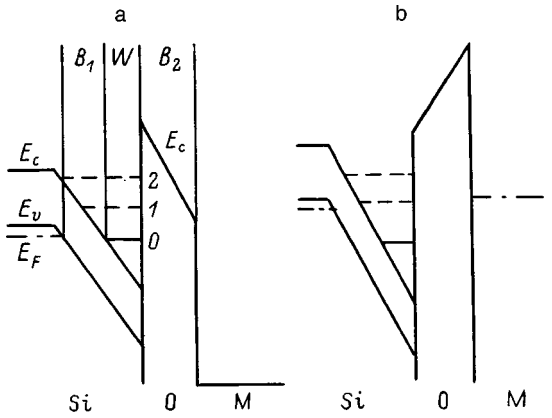

FIG. 1. Energy diagrams of a metal–oxide–*p*-Si nanostructure: a — For a negative bias above the threshold value $-V_{th}$, b — for a positive bias applied to a structure that is initially under a negative bias with magnitude greater than $V_{th.}$ As a result, an electron charge accumulates in quasi-zero-dimensional quantum wells.

from silicon into the metal via a miniband of the SCR becomes possible when the voltage exceeds the value $-V_{th}$ — the threshold voltage at which the lowest miniband (0) lines up with the Fermi level in the interior volume of Si. As previous investigations of the capacitance–voltage characteristics of such structures have shown,[8] two characteristic voltage ranges, the classical and the quantum range, where the behavior of the structures is qualitatively different, can be singled out. In the classical range there are no conditions for resonance tunneling and the capacitance–voltage characteristics, which are featureless, are identical to those calculated in Ref. 9 with allowance for the structural parameters employed. In the quantum range the characteristics exhibited resonance-tunneling features — steps and peaks.

Similarly to the above-described behavior of the capacitance–voltage characteristics, the current–voltage characteristics (IVCs) are featureless in the classical range, where the conditions for resonance tunneling are not satisfied (see dashed curves in Fig. 2). The classical range corresponds to the initial state of the structure and, taking into account this fact, it includes the entire range of positive voltages and the range of negative voltages from 0 to $-V_{th}$. In the classical range, the smoothness of the IVC is independent of the voltage sweep program. Such a dependence appears

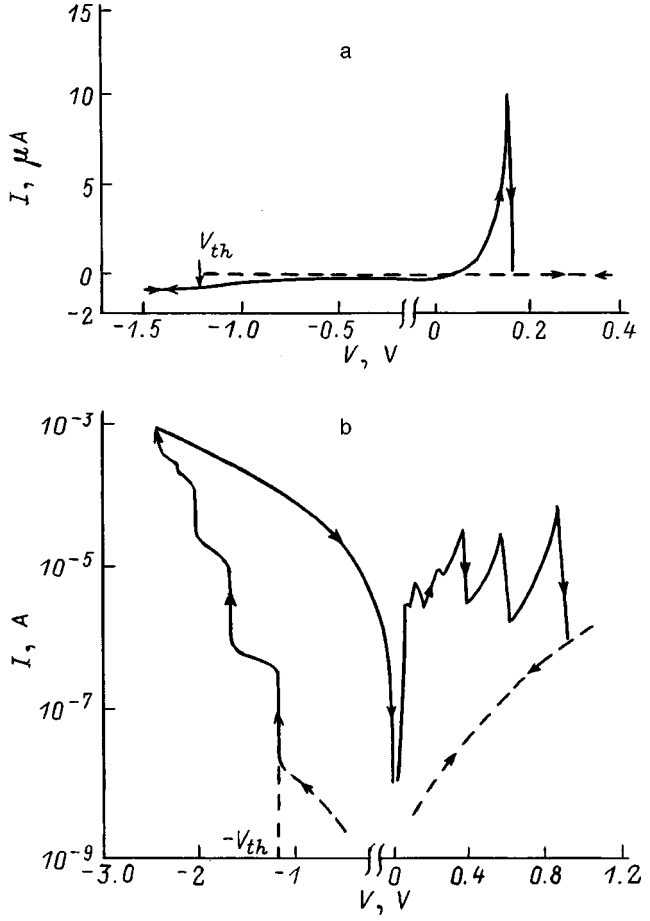

FIG. 2. Typical current–voltage characteristics of a metal–oxide–*p*-Si [KDB-0.01 (100)] structure, measured at room temperature with a sweep of about 10 V/min. The solid curve in Fig. 2a in the voltage range from 0 to −0.9 V is vertically separated from the dashed curve, but in reality both characteristics are the same.

after the transition into the quantum range as a result of crossing the boundary $-V_{th}$, where a qualitative change in the behavior of the characteristics occurs. For $V=-V_{th}=-1.2$ V the current increases sharply, forming a step on the IVC, attesting to switching of the structure into a more highly conducting state, which remains even when the voltage crosses 0 and increases to $V=+0.16$ V (Fig. 2a). At this voltage the IVC, having demonstrated a peak with peak-to-valley current ratio 200, returns to the initial (dashed) curve, which is again abandoned when the negative voltage exceeds $-V_{th}$ and then restored with a corresponding positive voltage.

Current–voltage characteristics, similar to those shown in Fig. 2a, have been observed in Ref. 10 for a structure consisting of a bank of resonance-tunneling columnar diodes based on a structurally highly complex AlAs/GaAs heterostructure (artificially multilayered and columnar at the same time). In Ref. 10 only one step and one peak were observed on the IVC, while the IVC of the resonance-tunneling MOS structure under discussion can demonstrate more features. When the applied voltage increases to values sufficient to line up the next miniband in the quantum well with the Fermi level in the interior volume of the semiconductor (Fig. 1a), resonance tunneling via this miniband gives rise to the second step on the IVC at a negative voltage (Fig. 2b) and to a corresponding additional peak at positive voltage. The process of increasing the number of resonance-tunneling features can be continued and can lead, for example, to the characteristic shown in Fig. 2b. The decrease in the range of voltages between neighboring steps as the voltage increases is a natural reflection of the fact that, according to the shape of the quantum well, the energy splittings between successive minibands decrease from deeper to shallower minibands.

In the quantum range, the shape of the IVC depends on the voltage sweep program. At positive voltage the number of peaks increases with increasing negative voltage with respect to $-V_{th}$ and hence increasing number of steps (compare Figs. 2a and 2b). Based on the observed hysteresis of the IVC, on the whole, the negative and positive voltages have opposite effects. Negative voltages cause the characteristics to deviate from their initial state, which is described by the dashed curve, while positive biases facilitate the structure to return to its initial state, and when these voltages reach the required magnitude, the structure completely returns to its initial state, which is represented by the dashed line in Fig. 2. However, when the negative bias exceeds $-V_{th}$, the initial state can be abandoned repeatedly, and in turn it can be restored by a corresponding positive bias. Such hysteresis cycles with a different number of resonance-tunneling features can be repeated many times.

We emphasize that a negative voltage in the quantum range, i.e., a voltage greater than $-V_{th}$, gives rise to the described hysteresis of IVCs, which can be explained by charge effects that accompany resonance tunneling in the asymmetric double barrier which we are studying. Since in the majority of cases the second part of the barrier, specifically, the insulator, is less penetrable than the first one (semiconductor), favorable conditions are created for filling the

quantum well with electrons by resonance tunneling from silicon into the metal. As the negative bias increases above the value $-V_{th}$, the quantum wells cross the Fermi level one after another, and their state changes from an unfilled state to one that is filled with electrons. We note that in all figures the dashed curves correspond to unfilled states, while the solid curves correspond to filled states. As follows from the results obtained by us, the electrons filling a quantum well at negative voltages remain in the well even when the voltages that cause the quantum well to fill are removed. The asymmetry of the double barrier mentioned above and the nonuniformity of the barrier along the surface facilitate electron conservation in the quantum well. We are dealing here with the naturally occurring nonuniformities, such as surface states. Nonuniformities give rise to fluctuations of the potential in directions parallel to the surface, and they facilitate quasi-zero-dimensional occurrence of the quantized states that operate in resonance tunneling. In this manner, quantum dots can be produced on the silicon surface in MOS structures. Their sizes in directions along the surface are determined by the sizes and distribution of the nonuniformities. The size parameters in a direction normal to the surface of the structure are determined by the size parameters of the double-barrier, and therefore they are controlled by the doping level N_A in silicon, the thickness d of the insulator, and the applied voltage V and can be easily controlled.

Because of the electron charge stored in the quantum dots, the band diagram of the structure in the absence of an applied voltage changes in such a way that minibands appear below the Fermi level. These changes, which are produced by the stored charge, must be taken into account in order to understand the band diagram in Fig. 1b.[1)] As one can see from Fig. 1, for positive voltages there is now a possibility of resonance tunneling occurring from the metal into the semiconductor via a miniband of the quantum well, when in the process of increasing voltage one miniband lines up with the energy gap between the Fermi level and the valence-band top. This possibility is vividly revealed in the peaks of the measured IVCs in Fig. 2. The different form of the resonance-tunneling features with opposite voltage polarities arises naturally as a result of the difference in the energy band diagrams in these cases, especially the difference in the energy diagram of the collector. Another difference between the two polarities of the applied voltage occurs for oppositely directed charge processes in quantum dots. For positive voltages, as the voltage increases in magnitude, quantum dots are discharged as a result of successive emptying of quantum minibands as they cross the Fermi level, instead of charging of quantum dots with the reverse motion of their quantum minibands with respect to the Fermi level as the negative voltage increases. When the required positive charge is reached, all minibands are emptied and the structure returns to its initial state, where it stays until the next negative voltage exceeds $-V_{th}$ and the structure starts to pass through various quasistable states with different magnitude of the charge stored in the quantum wells. Thus, resonance tunneling from the semiconductor into the metal is accompanied by writing electron charges in the MOS nanostructure, while resonance tunneling from the metal into the semiconductor is accompanied by erasure of the electron charges stored beforehand and the structure is characterized by multistability and can be used as a system with long-time memory.

We have established that a metal–oxide–*p*-Si structure is converted into a resonance-tunneling nanostructure with quasi-zero-dimensional quantized states. First of all, a double barrier capable of realizing resonance tunneling of electrons can be created only by decreasing to nanometer sizes the thickness of the insulator and the length of the depleted region of the space charge. Fluctuations of the potential caused by the nonuniformity of the structure in directions along the surface lead to an additional decrease of the dimensionality of the electron gas to quasi-zero-dimension. As a result, quantum dots, whose size parameters in a direction normal to the surface can be monitored and controlled, are organized on the silicon in MOS nanostructure. The room-temperature current–voltage characteristics demonstrate resonance-tunneling features: peaks and steps, whose number can reach 10. The maximum peak-to-valley current ratio is 500. The observed hysteresis of the current–voltage characteristics, explained by charging of quantum dots as a result of resonance tunneling from the semiconductor into the metal and discharging of quantum dots that accompany resonance tunneling from the metal into the semiconductor, shows that the structure with long-time memory and the ability to write and erase charges is multistable.

*)E-mail: apver@onti.niif.spb.su; Fax: (812)428 7240.

1)A structure subjected to a negative voltage greater than the value $-V_{th}$ passes into a state whose structure is different from that in the initial state and is characterized, in particular, by a different charge distribution. An excess negative charge appears in the quantum well, and compensation of the action of this charge by application of a negative voltage produces an excess negative charge in the semiconductor. This built-in charged region remains even after the external voltage is removed; this results in the appearance of a negative charge at $V=0$ on the metal, which is an excess charge compared with the initial state of the structure. The band diagram, shown in Fig. 1b, is constructed in this manner.

[1] L. L. Chang, L. Esaki, and R. Tsu, Appl. Phys. Lett. **24**, 593 (1974).
[2] F. Capasso, K. Mohammed, and A. Y. Cho, IEEE J. Quant. Electron. **QE-22**, 1853 (1986).
[3] L. Esaki, IEEE J. Quant. Electron. **QE-22**, 1611 (1986).
[4] S. L. Wu, C. L. Lee, and T. E. Lei, Appl. Phys. Lett. **63**, 24 (1993).
[5] E. H. Nicollian and R. Tsu, J. Appl. Phys. **74**, 4020 (1993).
[6] F. Capasso, S. Sen, and F. Beltram, *High-Speed Semiconductor Devices* (Interscience Publishers, New York, 1990).
[7] G. G. Kareva, Russian Federation Patent No. 2062529 (1995).
[8] G. G. Kareva, Zh. Tekh. Fiz. **23**, 71 (1997) [Tech. Phys. **23**, 157 (1997)].
[9] S. M. Sze, *Physics of Semiconductor Devices* [Wiley, New York; Mir, Moscow, 1984].
[10] B. W. Alphenaar, Z. A. K. Durrani, A. P. Heberie, and M. Wagner, Appl. Phys. Lett. **66**, 1234 (1995).

Translated by M. E. Alferieff

Formation of two-dimensional islands in the deposition of ultrathin InSb layers on a GaSb surface

A. F. Tsatsul'nikov, D. A. Bedarev, B. V. Volovik, S. V. Ivanov, M. V. Maksimov, Yu. G. Musikhin, N. N. Ledentsov, B. Ya. Mel'tser, V. A. Solov'ev, and P. S. Kop'ev

A. F. Ioffe Physicotechnical Institute, Russian Academy of Sciences, 194021 St. Petersburg, Russia

A. Yu. Chernyshov and M. V. Belousov

St. Petersburg State University (Physics Institute), 198904 Petrodvorets, St. Petersburg, Russia
(Submitted December 29, 1998; accepted for publication December 30, 1998)
Fiz. Tekh. Poluprovodn. **33**, 973–975 (August 1999)

It is shown that an array of two-dimensional islands is formed during the growth of ultrathin (~1.5 monolayers) InSb layers on a GaSb (100) surface by molecular beam epitaxy. After the deposition of several InSb layers separated by narrow barriers, islands of subsequent rows are formed on top of islands of the first row (vertical correlation effect). The formation of islands is confirmed by analysis of the photoluminescence spectra. © *1999 American Institute of Physics.* [S1063-7826(99)01808-6]

1. INTRODUCTION

Major progress has been made to date in the preparation and investigation of the properties of quantum dot (QD) heterostructures. Of utmost interest are arrays of QDs formed *in situ* during the growth of thin strained layers in heteroepitaxy.[1] The phenomenon of self-organization of QDs can be exploited to obtain ordered arrays of three-dimensional (3D), coherent, nanosize islands with low dispersion in size. Today the greatest process has been achieved in the preparation of (In,Ga)As/(Al,Ga)As quantum dots.[2–5] There is interest both in studies of the fundamental physical properties of QD structures and in the creation of optoelectronic devices utilizing QDs. For example, lasers incorporating QDs have been constructed, exhibiting temperature stability of the threshold current and high material gain.[6,7]

Another intriguing prospect in addition to 3D QDs, however, is the formation of two-dimensional islands in the deposition of a strained layer with an effective thickness smaller than one monolayer (ML). In this case a high-density array of islands is formed. Owing to the marked homogeneity in height of such islands, the photoluminescence line associated with them is characterized by small inhomogeneous broadening. This feature, along with the high exciton oscillator strength, produces a pronounced resonance increase in the refractive index and the possibility of the formation of an exciton waveguide, which holds considerable promise for the construction of injection lasers based on such systems. The formation of arrays of 2D nanoislands has been demonstrated for II–VI (CdSe/ZnSSe; Ref. 8) and III-V [InAs/(Al,Ga)As; Refs. 9 and 10] systems.

In earlier papers[11] we have shown that when thin InSb layers are deposited on a GaSb(100) surface, the shape and dimensions of the resulting islands depend very strongly on the effective thickness of the deposited InSb layer. Whereas the formation of QDs takes place in a fairly broad interval of InAs layer thicknesses (up to four monolayers) for a strained InAs/GaAs system, in the case of an InSb/GaSb system 3D clusters are already formed after the deposition of ~2 ML of InSb, resulting in catastrophic degradation of the optical properties. After the deposition of ~1.7 ML of InSb islands are formed with lateral dimensions ~30 nm (Ref. 11). In this paper we investigate the formation of an array of 2D InSb islands in a GaSb host with the deposition of several InSb layers having an effective thickness ~1.5 ML in each deposition cycle.

2. EXPERIMENTAL

The investigated structures were grown by molecular beam epitaxy on a Riber-32 MBE machine. We have grown samples with one, three, and five InSb layers deposited on a GaSb host. The effective thickness of each InSb layer was ~1.5 ML. In multilayer deposition the InSb layers were separated by 5-ML GaSb barriers. The temperature of growth of the active zone was 420 °C for all the samples. The InSb-containing region was bounded on both sides by short-period 20 Å GaSb-20 Å AlSb superlattices to prevent the transport of nonequilibrium carriers to the sample surface and to the interface with the substrate.

Transmission electron microscope (TEM) examinations were made in a Philips EM 420 electron microscope with an accelerating voltage of 100 kV. Photoluminescence was excited by an Ar^+ laser ($\lambda = 514.5$ nm, excitation density $\sim 100\ mV/cm^2$) and was detected by a cooled InSb photodiode.

3. RESULTS AND DISCUSSION

Figure 1 shows TEM images for samples with one and three InSb layers (in-plane and cross-sectional images). It is evident from these images that 3D clusters containing dislocations are not formed. The formation of 2D islands with lateral dimensions of approximately 50 nm is evident from

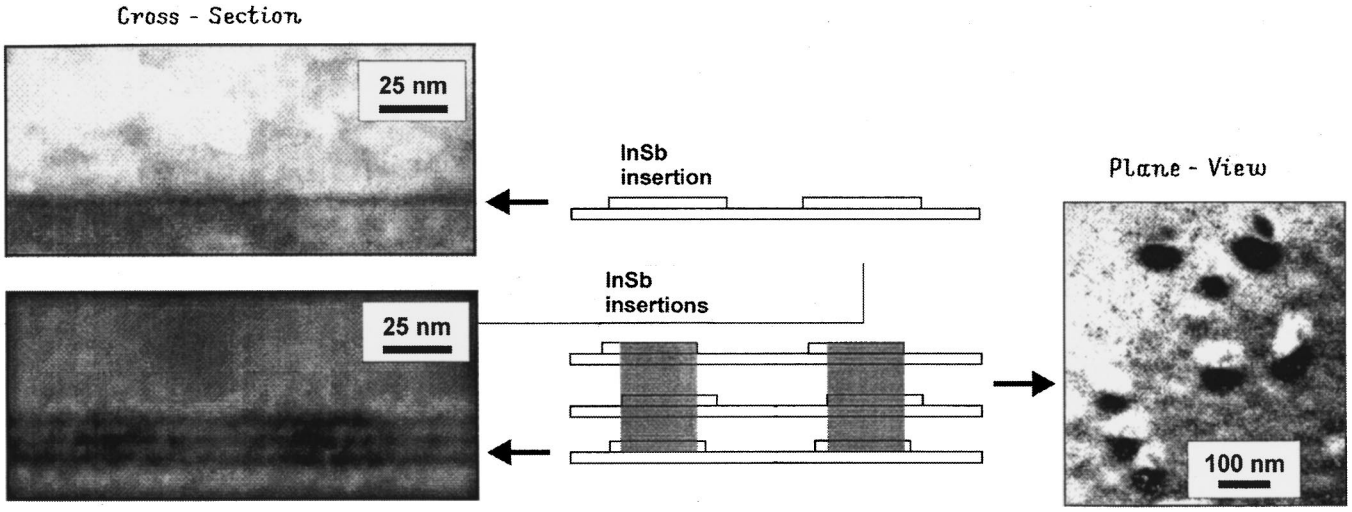

FIG. 1. TEM images obtained in the growth plane and in the cross section for structures with one and three InSb layers.

imaging in the growth plane and in the cross section. It is evident from the image of the cross section of a structure with three InSb layers that islands of the top layers are formed above islands of the first layer (vertical correlation effect).

Figure 2 shows the photoluminescence spectra of the indicated samples. Clearly, an increase in the number of InSb layers causes the optical transition energy to drop significantly, owing to an increase in carrier localization energy due to tunneling interaction between adjacent InSb planes. Figure 3 shows the optical transition energies calculated on the assumption that an InGaSb solid solution is formed in the investigated structures.[12] The average composition of the solution has been determined from the effective thickness of the InSb in each deposition cycle; this thickness was assumed to be either 1.5 ML or 2 ML. It is evident that for samples with one and three InSb layers the experimental optical transition energy is close to the calculated value obtained as a result of approximating the solid solution by a sequence of InSb layers of thickness 2 ML. We can therefore assume that when three InSb layers are deposited, the resulting 2D layer of thickness 1 ML is accompanied in each deposition cycle by the formation of local zones having a greater thickness (2D islands). The overlap of the islands in the growth direction leads to electronic interaction between them and an increase in the localization energy. An increase in the degree of localization is also indicated by the increase in the

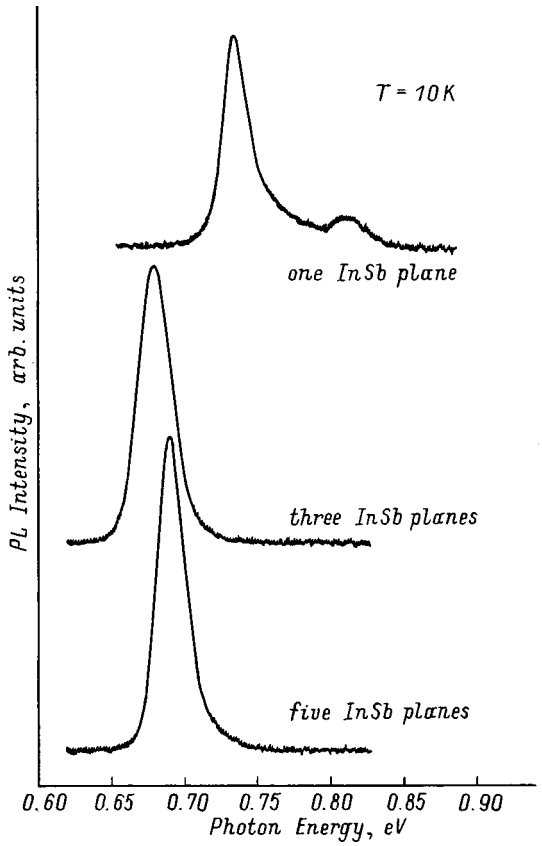

FIG. 2. Photoluminescence spectra of structure with different numbers of InSb layers.

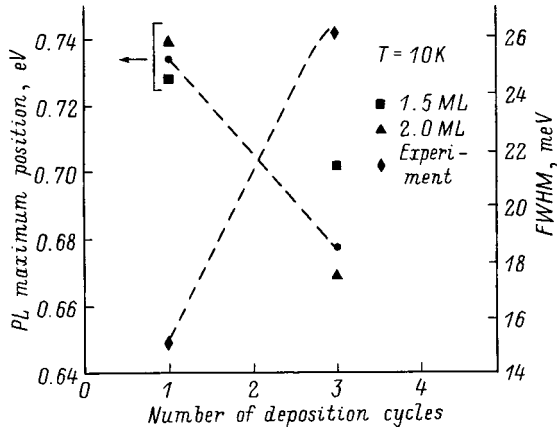

FIG. 3. Experimental values of the position of the maximum and width of the photoluminescence line and calculated values of the optical transition energy with the layers approximated by an InGaSb solid solution. For the determination of the composition of the solid solution the thickness of the InSb layers was assumed to be equal to 1.5 Ml or 2 ML.

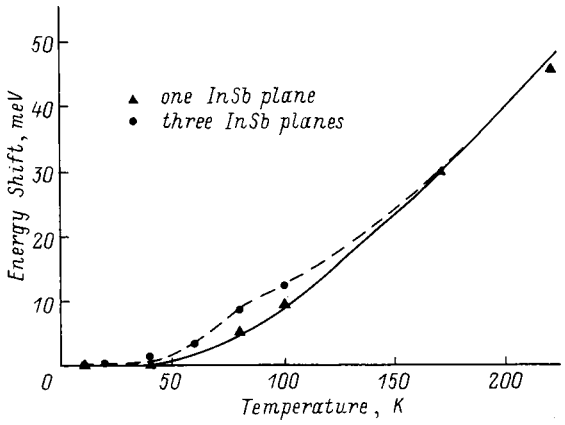

FIG. 4. Temperature dependence of the shift of the maximum of the photoluminescence line for structures with one and three InSb layers.

width of the photoluminescence line as the InSb deposition cycles are increased (Fig. 3).

The formation of islands in the structure with three InSb layers is also confirmed by the temperature dependence of the position of the maximum of the photoluminescence line (Fig. 4). As the temperature is raised, the photoluminescence band is observed to shift more abruptly into the low-energy range as a result of thermal ejection of carriers from islands having a smaller localization energy, which are associated with the short-wavelength branch of the photoluminescence line. This temperature behavior of the photoluminescence line is typical of QD structures.[13] For a sample with one InSb layer the temperature shift of the photoluminescence is much smaller, indicating the weaker influence of carrier localization in the islands on the shape of the photoluminescence line.

4. CONCLUSION

We have investigated the properties of structures with ultrathin InSb inclusions in a GaSb host. We have shown that an array of vertically connected islands having a height of ~2 ML and lateral dimensions of ~50 nm is formed in the deposition of several InSb layers with an effective thickness of ~1.5 ML.

This work has received support from the Russian Fund for Fundamental Research (RFFI Grant 97-02-18175).

[1] L. Goldstein, F. Glas, J. Y. Marzin, M. N. Charasse, and G. Le Roux, Appl. Phys. Lett. **47**, 1099 (1985).
[2] P. M. Petroff and S. P. DenBaars, Superlattices Microstruct. **15**, 15 (1994).
[3] Q. Xie, A. Madhukar, P. Chen, and N. Kobayashi, Phys. Rev. Lett. **75**, 2542 (1995).
[4] J. M. Moison, F. Houzay, F. Barthe, L. Leprince, E. Andre, and O. Vatel, Appl. Phys. Lett. **64**, 196 (1994).
[5] N. N. Ledentsov, M. Grundmann, N. Kirstaedter, O. Schmidt, R. Heitz, J. Buhrer, D. Bimberg, V. M. Ustinov, V. A. Shchukin, P. S. Kop'ev, Zh. I. Alferov, S. S. Ruvimov, A. O. Kosogov, P. Werner, U. Richter, U. Gösele, and J. Heydenreich, Solid-State Electron. **40**, 785 (1996).
[6] Zh. I. Alferov, N. A. Bert, A. Yu. Egorov, A. E. Zhukov, P. S. Kop'ev, A. O. Kosogov, I. L. Krestnikov, N. N. Ledentsov, A. V. Lunev, M. V. Maksimov, A. V. Sakharov, V. M. Ustinov, A. F. Tsatsul'nikov, Yu. M. Shernyakov, and D. Bimberg, Fiz. Tekh. Poluprovodn. **30**, 351 (1996) [Semiconductors **30**, 194 (1996)].
[7] D. Bimberg, N. Kirstaedter, N. N. Ledentsov, Zh. I. Alferov, P. S. Kop'ev, and V. M. Ustinov, IEEE J. Sel. Top. Quantum Electron. **3**(2), 196 (1997).
[8] M. Strassburg, V. Kutzer, U. W. Pohl, A. Hoffmann, I. Broser, N. N. Ledentsov, D. Bimberg, A. Rosenauer, U. Fischer, D. Gerthsen, I. L. Krestnikov, M. V. Maximov, P. S. Kop'ev, and Zh. I. Alferov, Appl. Phys. Lett. **72**, 942 (1998).
[9] V. Bressler-Hill, A. Lorke, S. Varma, P. M. Petroff, K. Pond, and W. H. Weinberg, Phys. Rev. B **50**, 8479 (1994).
[10] B. V. Volovik, A. Yu. Egorov, P. S. Kop'ev, A. R. Kovsh, I. E. Kozin, I. L. Krestnikov, M. V. Maximov, A. V. Sakharov, A. F. Tsatsul'nikov, V. M. Ustinov, A. E. Zhukov, Zh. I. Alferov, N. N. Ledentsov, M. Strassburg, A. Hoffmann, D. Bimberg, I. P. Soshnikov, and P. Werner, in *Proceedings of the International Conference on Physics of Semiconductors (ICPS24), Jerusalem, 1998* (World Scientific, 1998).
[11] A. F. Tsatsul'nikov, S. V. Ivanov, P. S. Kop'ev, A. K. Kryganovskii, N. N. Ledentsov, M. V. Maximov, B. Ya. Mel'tser, P. V. Nekludov, A. A. Suvorova, A. N. Titkov, B. V. Volovik, M. Grundmann, D. Bimberg, and Zh. I. Alferov, J. Electron. Mater. **27**, 414 (1998).
[12] M. P. C. M. Krijn, Semicond. Sci. Technol. **6**, 27 (1991).
[13] A. F. Tsatsul'nikov, N. N. Ledentsov, M. V. Maksimov, A. Yu. Egorov, A. E. Zhukov, S. S. Ruvimov, V. M. Ustinov, V. V. Komin, I. V. Kochnev, P. S. Kop'ev, Zh. I. Alferov, and D. Bimberg, Fiz. Tekh. Poluprovodn. **30**, 1797 (1996) [Semiconductors **30**, 953 (1996)].

Translated by James S. Wood

Submillimeter photoconductivity of two-dimensional electron structures in Corbino geometry

S. D. Suchalkin, Yu. B. Vasil'ev, S. V. Ivanov, and P. S. Kop'ev

A. F. Ioffe Physicotechnical Institute, Russian Academy of Sciences, 194021 St. Petersburg, Russia
(Submitted January 22, 1999; accepted for publication January 26, 1999)
Fiz. Tekh. Poluprovodn. **33**, 976–978 (August 1999)

The photoconductivity of a two-dimensional electron gas in the far IR range in a quantizing magnetic field is investigated for samples in Corbino geometry, which eliminates transport by edge states. It is shown that the photoelectric effect is more than simply the bolometric response of the system, acquiring a component induced by the direct involvement of photoexcited carriers in low-energy scattering processes. © *1999 American Institute of Physics.*
[S1063-7826(99)01908-0]

Apart from investigations of cyclotron absorption, researchers have long been fascinated by the photoconductivity of a two-dimensional (2D) electron gas as a promising experimental technique for the study of 2D electron systems.[1–7] However, the applications of this method are currently limited by the lack of a clear picture of current flow in the presence of the quantum Hall effect. The edge state formalism propounded by Buttiker[8] has stimulated several photoconductivity studies of how radiation with a frequency close to the cyclotron frequency influences transport via edge states in the regime of the integer-valued quantum Hall effect.[6] Measurements of this kind are carried out with low currents I_b through the structure ($I_b<1\ \mu$A). The distributions of the potential and the current density in the structure vary as the current is increased,[9] as do the relative contributions of edge and ''bulk'' states to the transport processes.[10] In addition to the photoelectric effect associated with edge state, it is also important to investigate photoconduction processes in the presence of transport via so-called bulk states situated far from the edges of the sample.

The objective of the present study is to investigate the photoconductivity under conditions of the quantum Hall effect using samples in Corbino geometry. One of the characteristic features of this geometry is the elimination of edge states from the transport processes.[11] Photoconductivity experiments can be used to discern the role of bulk states in the mechanism underlying the formation of the photoresponse in this case.

We have investigated the variation of the conductivity of a 2D electron gas in a GaAs/AlGaAs heterostructure in a quantizing magnetic field under the influence of far infrared radiation. The radiation source was a tunable submillimeter germanium laser operating in the wavelength range from 100 μm to 300 μm. The samples configured in Corbino geometry consisted of solitary heterojunctions with a carrier density of $2.3\times10^{11}\,\mathrm{cm}^{-2}$ and a mobility $\mu=1.2\times10^5\,\mathrm{cm}^2/(\mathrm{V}\cdot\mathrm{s})$ at $T=4.2$ K. The Hall field does not exist in this geometry, and the measured quantity is the current through the structure at constant voltage. The current is proportional to the diagonal component of the conductivity tensor in a magnetic field σ_{xx}. During the measurements a constant dc voltage of 0.1 V was maintained at the sample contacts. The variation of the current through the structure under the influence of radiation pulses having a duration of 0.2 μs and a repetition rate of 2 Hz was recorded.

The results of the measurements are shown in Fig. 1. The magnetic field dependence of the photoresponse $\Delta\sigma_{xx}$ represents a series of peaks, which correlate with the minima of the $\sigma_{xx}(B)$ curve. The voltage-off signal amplitude is equal to zero for all magnetic field strengths, indicating zero photovoltage associated with rectification at the contacts. The presence of an appreciable photoresponse in the range of magnetic fields far from the resonance region, in which the cyclotron frequency is close to the probe frequency, is evidence of heating of the electron gas. In this region the $\Delta\sigma_{xx}(B)$ curve is essentially independent of the radiation frequency. The photoresponse reflects the magnetic field dependence of the temperature sensitivity $\partial\sigma_{xx}/\partial T(B)$ (Ref. 4). The field dependence of the signal has a more complex structure in the vicinity of resonance. It is evident from Fig. 2 that, in addition to the ''heated'' component, there also emerges a component that depends on the magnetic field and comprises a peak that shifts toward higher fields as the radiation frequency is increased. The behavior of the spectral curves of the photoresponse also differs in the resonance and off-resonance regions. In the range of magnetic fields where the cyclotron frequency falls within the laser tuning range, the spectrum of the photoresponse represents a peak whose position depends linearly on the magnetic field. In the region far from resonance the spectrum broadens considerably and is essentially independent of the magnetic field (Fig. 3).

The current through the sample in Corbino geometry drops to zero at certain magnetic field strengths. This happens when the Fermi level is situated in the mobility gap between Landau levels, where the probability of low-energy scattering is lowered, and $\sigma_{xx}=0$. Only when a Landau level is partially filled, when carriers vulnerable to low-energy scattering are present, is it possible to have a nonzero conductivity σ_{xx} and, as a result, a finite current flow through the structure. The absorption of radiation — both resonance,

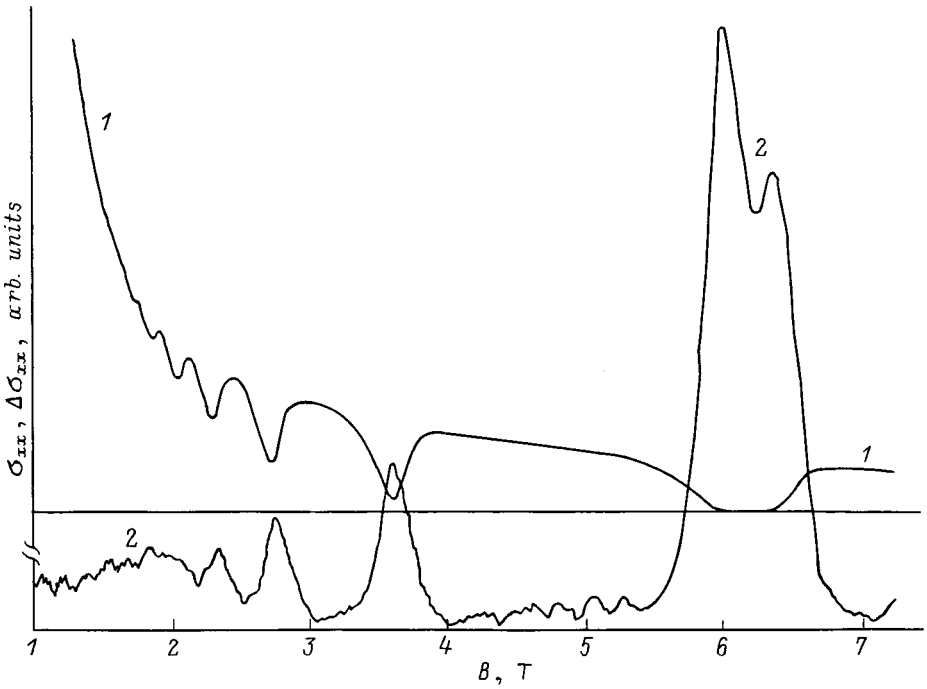

FIG. 1. Dependence of the diagonal component of the conductivity tensor σ_{xx} (*1*) and the photoresponse $\Delta\sigma_{xx}$ (*2*) on the magnetic field *B*. Laser photon energy: $\hbar\omega = 8.36$ meV.

i.e., the direct transition of electrons between Landau levels, and nonresonance absorption at various kinds of sample inhomogeneities — induces a change in the electron distribution function. When the Fermi level is situated between Landau levels, carriers (electrons and ''holes'' in the sense of voids at the almost-filled Landau level) can be generated under the influence of radiation at the mobility threshold.

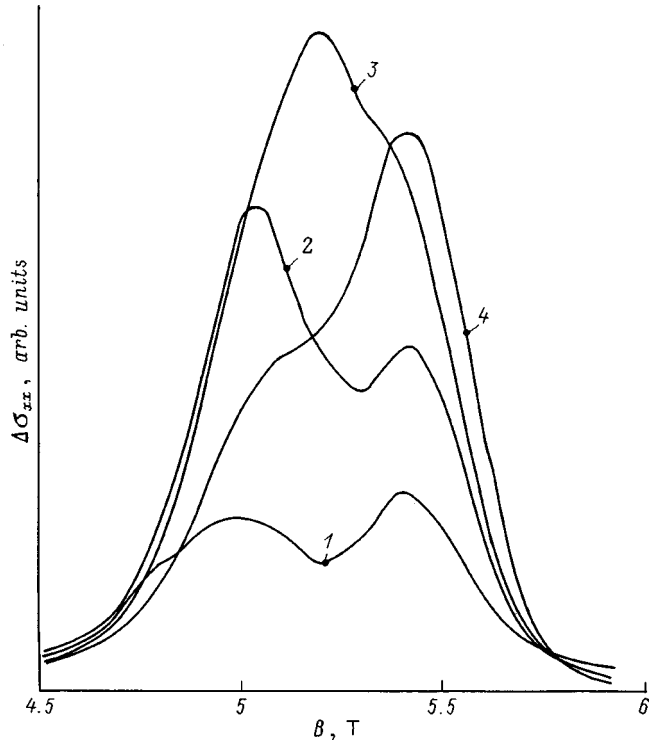

FIG. 2. Dependence of the photoconductivity signal $\Delta\sigma_{xx}$ on the magnetic field *B* in the resonance region for various laser photon energies: (*1*) $\hbar\omega = 7.91$ meV; (*2*) 8.28 meV; (*3*) 8.66 meV; (*4*) 9.26 meV.

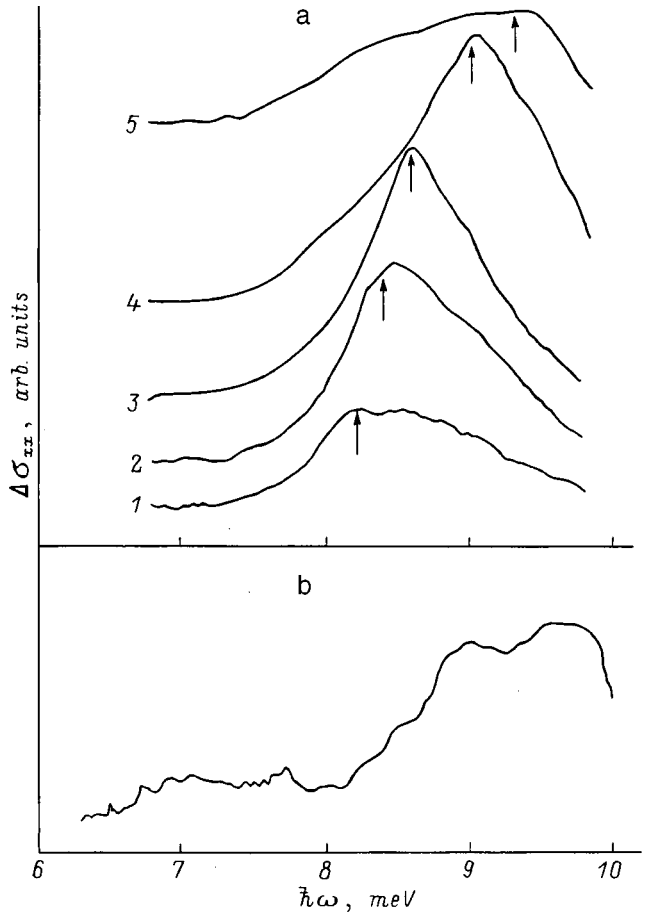

FIG. 3. Spectral curves of the photoconductivity $\Delta\sigma_{xx}$ in the resonance region (a) and in the off-resonance region (b) for various magnetic fields: (*1*) $B = 4.84$ T; (*2*) 5.02 T; (*3*) 5.19 T; (*4*) 5.36 T; (*5*) 5.54 T. The arrows indicated the calculated values of the cyclotron energy corresponding to the effective mass $m^* = 0.68m_0$. In graph b the magnetic field is $B = 2.57$ T.

This gives rise to a finite conductivity σ_{xx}, which depends on the number of carriers vulnerable to low-energy scattering and on the efficiency of energy exchange processes between the electron system and the lattice.

If the quasi-equilibrium relaxation time in the electron system is much shorter than the characteristic time of energy exchange between the electron system and the lattice, the effect of radiation reduces to elevation of the electron temperature by a certain increment ΔT (the notion of ''temperature'' is not interpreted here as simply a measure of the average carrier kinetic energy, but as a specific parameter in the equilibrium distribution function) and, associated with it, the thermal generation of carriers at the mobility threshold. Now in the case where the Fermi level is situated between Landau levels the signal must be a minimum, because the derivative $\partial\sigma_{xx}/\partial T$ is equal to zero in this case. It is evident from Fig. 2 that the component of the photoresponse associated with electron heating, being independent of the magnetic field, has a minimum at the midpoint of the field interval corresponding to $\sigma_{xx}=0$. However, when the energy exchange between the system of carriers and the lattice is sufficiently efficient, the photoresponse can acquire a component associated with the directly involvement of photoexcited carriers: electrons and holes in scattering processes.

The photoresponse created by this mechanism is a maximum when the Fermi level is situated between Landau levels, because then the absorption of resonance photons qualitatively alters the pattern of filling of the Landau levels.[12] In our case this component is comparable with the ''heating'' component (Fig. 2). The spectral curves of the signal in the resonance region comprise a cyclotron resonance peak in the photoconductivity, probably induced by a second mechanism associated with the scattering of photoexcited carriers. This conjecture is evinced by the correspondence of the maximum signal to the magnetic field at which the Fermi level is situated between Landau levels. The photoresponse in the range of magnetic fields far from cyclotron resonance is possibly induced by heating of the samples as radiation is absorbed by inhomogeneities of the structure. The spectral dependence of the photoelectric effect in this case can mirror the dependence of the radiation intensity of a tunable cyclotron laser on the emission frequency.[13]

This work has received support from the program ''Physics of Solid State Nanostructures,'' Grant No. 97-1042.

[1] C. F. Lavine, R. J. Wagner, and D. C. Tsui, Surf. Sci. **113**, 112 (1982).
[2] P. Stein, G. Ebert, K. von Klitzing, and G. Weimann, Surf. Sci. **142**, 406 (1984).
[3] J. C. Maan, Th. Englert, D. C. Tsui, and A. C. Gossard, Appl. Phys. Lett. **40**, 609 (1982).
[4] R. E. Horstman, E. G. van den Broek, J. Wolter, R. W. van der Heijden, G. L. J. A. Rikken, H. Sigg, P. M. Frijlink, J. Maluenda, and J. Hallais, Solid State Commun. **50**, 753 (1984).
[5] M. J. Chou, D. C. Tsui, and A. Y. Cho, in *Proceedings of the 18th International Conference on the Physics of Semiconductors*, Stockholm, Sweden (1986) p. 437.
[6] E. Diezel, G. Muller, D. Weiss, K. von Klitzing, K. Ploog, H. Nickel, W. Schlapp, and R. Losch, Appl. Phys. Lett. **58**, 2331 (1991).
[7] S. Suchalkin, Yu. B. Vasilyev, Yu. Ivanov, S. Ivanov, P. Kop'ev, B. Meltser, and T. Ohyama, Solid-State Electron. **40**, 469 (1996).
[8] M. Buttiker, Phys. Rev. B **38**, 9375 (1988).
[9] P. F. Fontein, P. Hendriks, F. A. P. Bloom, J. H. Walter, L. G. Giling, and C. W. J. Beenaker, Surf. Sci. **263**, 91 (1992).
[10] V. T. Dolgonolov, N. B. Zhitenev, and A. A. Shashkin, JETP Lett. **52**, 196 (1990).
[11] E. Yahel, A. Palevski, and H. Shtrikmann, in *Proceedings of the 23th International Conference on the Physics of Semiconductors*, Vol. 3, Berlin (1996), p. 2523.
[12] Yu. B. Vasil'ev, S. D. Suchalkin, Yu. L. Ivanov, S. V. Ivanov, P. S. Kop'ev, and I. G. Savel'ev, JETP Lett. **56**, 379 (1992).
[13] Yu. L. Ivanov, Yu. B. Vasil'ev, and S. D. Suchalkin, Fiz. Tekh. Poluprovodn. **27**, 1997 (1993) [Semiconductors **27**, 1097 (1993)].

Translated by James S. Wood

Interaction of surface acoustic waves with a two-dimensional electron gas in the presence of spin splitting of the Landau bands

I. L. Drichko,*) A. M. D'yakonov, and I. Yu. Smirnov

A. F. Ioffe Physicotechnical Institute, Russian Academy of Sciences, 194021 St. Petersburg, Russia

V. V. Preobrazhenskiĭ and A. I. Toropov

Institute of Semiconductor Physics, Siberian Branch of the Russian Academy of Sciences, 630090 Novosibirsk, Russia

(Submitted February 2, 1999; accepted for publication February 2, 1999)
Fiz. Tekh. Poluprovodn. **33**, 979–985 (August 1999)

The absorption and variation of the velocity of a surface acoustic wave of frequency $f=30$ MHz interacting with two-dimensional electrons are investigated in GaAs/AlGaAs heterostructures with an electron density $n=(1.3-2.8)\times 10^{11}\text{cm}^2$ at $T=1.5-4.2$ K in magnetic fields up to 7 T. Characteristic features associated with spin splitting of the Landau level are observed. The effective g factor and the width of the spin-split Landau bands are determined: $g^*\cong 5$ and $A=0.6$ meV. The greater width of the orbital-split Landau bands (2 meV) relative to the spin-split bands is attributed to different shielding of the random fluctuation potential of charged impurities by 2D electrons. The mechanisms of the nonlinearities manifested in the dependence of the absorption and the velocity increment of the SAW on the SAW power in the presence of spin splitting of the Landau levels are investigated. © *1999 American Institute of Physics.* [S1063-7826(99)02008-6]

1. INTRODUCTION

In a magnetic field H the energy spectrum of a two-dimensional (2D) electron gas represents a set of discrete levels with energies

$$E_N=(N+1/2)\hbar\omega_c\pm(1/2)(g_0\mu_B H+E_{ex}),$$
$$E_{\text{ex}}=E_{\text{ex}}^0(n\uparrow-n\downarrow). \quad (1)$$

The first term describes the orbital splitting of the Landau levels N enumerates the Landau levels, $\hbar\omega_c\equiv\hbar eH/m^*c$ is the cyclotron energy, $g_0\mu_B H$ is the Zeeman splitting energy, g_0 is the g factor in bulk GaAs, and μ_B is the Bohr magneton. In the 2D case electron-electron interactions increase the initial spin splitting (relative to the 3D case). As a result, Eq. (1) acquires an additional term E_{ex}, which describes the exchange interaction of electrons at the Landau level. The presence of exchange interaction is equivalent to an increase in the equivalent g factor[1]

$$g^*\mu_B H=g_0\mu_B H+E_{\text{ex}}^0(n\uparrow-n\downarrow).$$

It has been observed experimentally[2] that the g factor in a GaAs/AlGaAs heterostructure is $|g^*|=6.23$, which is an order of magnitude higher than the value $|g_0|=0.44$ in bulk GaAs. An increase in the g factor in 2D objects relative to their bulk counterparts has also been observed in Si/SiO_2 (Ref. 3), GaInAs/AlInAs (Ref. 4), InAs/AlSb/GaSb (Ref. 5), and AlAs (Ref. 6) heterostructures.

It is evident from Eq. (1) that the energy E_{ex} depends on the relative population of two spin states; therefore, if the Fermi level is situated between Landau levels of order $(N,\downarrow)$ and $(N,\uparrow)$, the difference $(n\uparrow-n\downarrow)$ is a maximum, and the quantity g^* assumes a certain maximum value. But if the Fermi level is between Landau levels of order $(N,\downarrow)$ and $(N+1,\uparrow)$, then g^* assumes a minimum value equal to g_0. Consequently, the value of g^* is an oscillating function of the magnetic field.[1] Indeed, oscillations of the g^* factor in a magnetic field have been observed in Ref. 5.

In this paper we report measurements of the absorption Γ and velocity increments $\Delta V/V$ of surface acoustic waves (SAWs) in a piezoelectric material as a result of their interaction with 2D electrons in GaAs/AlGaAs heterostructures in a magnetic field in the presence of spin splitting of the Landau levels.

2. EXPERIMENTAL PROCEDURE

The details of the procedure used to measure the SAW absorption are described in Ref. 7 Here we mention only that the SAWs were generated by means of an interdigital transducer situated on the surface of a $LiNbO_3$ (lithium niobate) piezoelectric insulator, into which an rf pulse (30–150 MHz) of length 1.5 μs and repetition rate 50 Hz was propagated. This pulse was chopped from the continuous output signal of a microwave oscillator. The signal transmitted through the sample was received by an analogous transducer formed on the same surface.

A modified version of the pulse-interference method was used to measure $\Delta V/V$. The duty phases of two pulses were compared in a phase detector: the SAW-generating pulse on the lithium niobate surface and the pulse arriving at the receiving transducer, attenuated by interaction with 2D electrons. The error signal at the output of the phase detector was sent to the SAW-generating oscillator and thus altered its frequency in such a way as to reduce the difference between

the duty phases of the indicated pulses to zero. This tracking system was operative throughout the entire experiment with a frequency meter continuously tracking the phase difference between the indicated pulses. The frequency change recorded by this technique was converted into the corresponding velocity change.

The sample was held firmly against the lithium niobate surface by a spring, where the distance of the 2D channel from the lithium niobate surface was shorter than the SAW wavelength ($\lambda = 100\,\mu$m at $f = 30$ MHz). With this mounting of the sample a random gap a is formed between it and the lithium niobate surface, its width ($\sim 0.5\,\mu$m) most likely being governed by the roughnesses of the surfaces of the sample and the lithium niobate. The SAW-induced strain in the sample is not transferred in our experimental configuration. The alternating electric field accompanying the SAW penetrates into the channel carrying 2D electrons, inducing currents in the 2D channel and, accordingly, Joule losses, causing not only SAW energy to be absorbed, but also changing the velocity of the wave. The receiving transducer detects the amplitude of the SAW signal transmitted through the sample. This procedure can therefore be used to introduce an alternating electric field into the sample without having to use contacts.

The absorption Γ and velocity increment $\Delta V/V$ were measured in a vacuum chamber in a magnetic field up to 7 T at temperatures of 1.5–4.2 K in the linear regime (the acoustic power did not exceed 10^{-6} W) and at $T = 1.5$ K in the measurements, depending on the acoustic power.

The GaAs/AlGaAs heterostructures were fabricated by molecular-beam epitaxy with carrier densities $n = (1.3 - 2.8) \times 10^{11}\,\mathrm{cm}^{-2}$ and mobilities $\mu_0 \sim (1-2) \times 10^5\,\mathrm{cm}^2/(\mathrm{V}\cdot\mathrm{s})$. The density and mobility of 2D electrons were determined by a contactless acoustical method.[8]

3. EXPERIMENTAL RESULTS AND DISCUSSION

3.1 Linear regime

In our experimental configuration the absorption coefficient Γ and the velocity increment $\Delta V/V$ are given by the equations[9]

$$\Gamma\,[\mathrm{dB/cm}] = 8.68\frac{K^2}{2}qA \times \frac{[4\pi\sigma_1 t(q)/\varepsilon_s V]}{[1+4\pi\sigma_2 t(q)/\varepsilon_s V]^2 + [4\pi\sigma_1 t(q)/\varepsilon_s V]^2},$$

$$A = 8b(q)(\varepsilon_1+\varepsilon_0)\varepsilon_0^2\varepsilon_s \exp[-2q(a+d)],$$

$$\frac{\Delta V}{V} = \frac{K^2}{2}A\frac{[1+4\pi\sigma_2 t(q)/\varepsilon_s V]}{[1+4\pi\sigma_2 t(q)/\varepsilon_s V]^2 + [4\pi\sigma_1 t(q)/\varepsilon_s V]^2},$$

$$b(q) = [b_1(q)[b_2(q) - b_3(q)]]^{-1},$$

$$t(q) = [b_2(q) - b_3(q)]/[2b_1(q)],$$

$$b_1(q) = (\varepsilon_1+\varepsilon_0)(\varepsilon_s+\varepsilon_0) - (\varepsilon_1-\varepsilon_0)(\varepsilon_s-\varepsilon_0)\exp(-2qa),$$

$$b_2(q) = (\varepsilon_1+\varepsilon_0)(\varepsilon_s+\varepsilon_0) + (\varepsilon_1+\varepsilon_0)(\varepsilon_s-\varepsilon_0)\exp(-2qd),$$

$$b_3(q) = (\varepsilon_1-\varepsilon_0)(\varepsilon_s-\varepsilon_0)\exp(-2qa) + (\varepsilon_1-\varepsilon_0)(\varepsilon_s+\varepsilon_0)\exp[-2q(a+d)], \quad (2)$$

where K^2 is the electromechanical coupling constant of $LiNbO_3$, q and V are the wave vector and velocity of the SAW, respectively, a is the distance between the insulator and the investigated heterostructure, d is the depth of the 2D layer, ε_1, ε_0, and ε_s are the dielectric constants of lithium niobate, vacuum, and gallium arsenide, respectively, and σ_1 and σ_2 are the components of the rf conductivity of 2D electrons, which is complex-valued: $\sigma_{xx}^{\mathrm{rf}} = \sigma_1 - i\sigma_2$ (Ref. 10). These equations can be used to determine the values of σ_1 and σ_2 from the experimentally measured quantities Γ and $\Delta V/V$.

It is evident from Eq. (2) that the dependence of Γ and $\Delta V/V$ on the magnetic field H is determined by the H dependence of the components of the dissipative conductivity σ_{xx}, so that the quantization of the electron spectrum in a magnetic field, inducing Shubnikov-de Haas resistance oscillations, also generates oscillations in our measured effects.

Figure 1 shows experimental curves of Γ and $\Delta V/V$ as functions of the magnetic field for samples AG49 ($n = 2.7 \times 10^{11}\,\mathrm{cm}^{-2}$), AG106 ($n = 1.3 \times 10^{11}\,\mathrm{cm}^{-2}$), and BP92 ($n = 2.8 \times 10^{11}\mathrm{cm}^{-2}$) at $T = 4.2$ K and 1.5 K. It is evident from the figures that Γ and $\Delta V/V$ oscillate in a magnetic field; additional peaks, nonexistent or faint at $T = 4.2$ K, are observed at $T = 1.5$ K for $H = 2.2$ T and 3.65 T (AG49), $H = 2.4$ T and 4 T (BP92), and $H = 5.5$ T (AG106).

The emergence of these peaks is associated with spin splitting of the Landau zones, because for samples AG49 and BP92 their magnetic field positions correspond to occupation numbers $\nu = 3$ and $\nu = 5$, whereas for sample AG106 they correspond to $\nu = 1$, where

$$\nu = nch/eH,$$

c is the speed of light, h is Planck's constant, and e is the electron charge. We are convinced that the SAW absorption peak in a magnetic field corresponding to spin splitting of the Landau level has been observed in Ref. 11, but was not identified by the authors.

Regarding the temperature dependence, in sample AG49 the absorption peaks corresponding to $\nu = 3$ are not observed at $T = 4.2$ K and begin to appear at $T \simeq 3.2 - 3.7$ K for different mountings of the sample, while the peak corresponding to $\nu = 5$ is observed only at $T = 1.5$ K. The energy of spin splitting of the Landau levels is $E_g = g^*\mu_B H$, so that phenomena associated with spin splitting can occur only when the condition $E_g > kT$ holds; consequently, the smaller the value of ν, the higher is the temperature at which they are observed.

The profile of the curves for $\Gamma(H)$ in strong magnetic fields (splitting in two of the Γ peak in the vicinity of even occupation numbers) is attributable to the relaxation behavior of the absorption and is analyzed in detail in Ref. 7. Moreover, it is evident from Fig. 1 that at $T = 1.5$ K the value

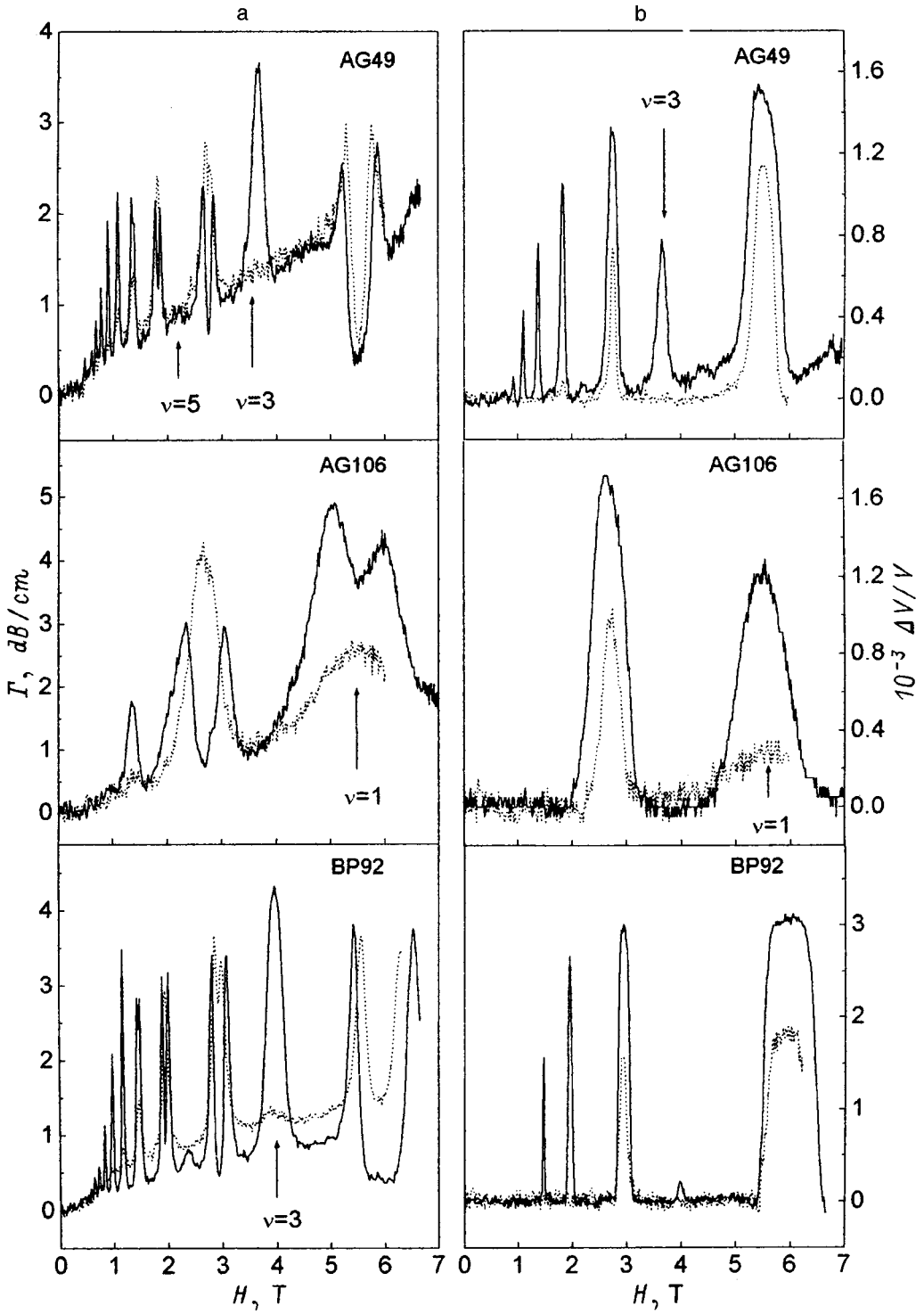

FIG. 1. Dependence of the SAW absorption coefficient Γ (a) and the relative SAW velocity increment $\Delta V/V$ (b) on the magnetic field H for different samples at temperatures of 4.2 K (dashed lines) and 1.5 K (solid lines); the SAW frequency is $f=30$ MHz.

of the Γ peak for odd occupation numbers, $\nu=1$ (AG106) and $\nu=3$ (AG49) is higher (in spin splitting) than the maximum value of the absorption peak for even values $\nu=2, 4, 6$, which correspond to orbital splitting. This fact is very important in regard to understanding the nature of the interaction of SAWs with 2D electrons in heterostructures in the regime of the quantum Hall effect. And indeed it has been reported in several papers (e.g., Refs. 11 and 12) that the experimentally measured value of Γ for all magnetic fields is given by an equation of the type (2), where the role of σ can be taken by the conductivity $\sigma_{xx}^{\mathrm{dc}}$ measured for a direct current. Here the maximum absorption $\Gamma^{\max}$ does not depend on σ_{xx}, i.e., is universal. It has been shown[7] that the dependence $\Gamma(H)$ is described by the conductivity determined from static measurements only when the 2D electrons are delocalized. In the regime of the integer-valued quantum Hall effect the Fermi level is situated half-way between two consecutive Landau

levels, the electrons are localized, and the dc and ac conductivity mechanisms differ, so that $\sigma_{xx}^{rf} > \sigma_{xx}^{dc} = 0$. In this case allowance must be made for the fact that σ_{xx}^{rf} has a complex form. It is difficult to analyze the conditions for attaining the maximum Γ^{max} according to Eq. (2) as a function of the magnetic field in this case, but experiment shows that it is achieved when $\mathrm{Re}\,\sigma_{xx} = \sigma_1 \approx \mathrm{Im}\,\sigma_{xx} = \sigma_2$. The maximum Γ^{max} can then be calculated according to Eq. (2) with $\sigma_1 = \sigma_2 = \sigma$, and if, as experiment shows, $4\pi\sigma/\varepsilon_s V > 1$ in this case, the maximum absorption is $\Gamma^{max} \simeq 1/2\sigma$, i.e., depends on the conductivity.

To understand the nature of the magnetic field dependence of $\Delta V/V$, we must look once again at the physical phenomena associated with interaction between SAWs and 2D electrons. For $H = 0$ electrons are delocalized in the investigated samples, and the 2D electron gas has a high conductivity, so that the rf electric fields accompanying SAW propagation are completely shielded. Here the SAW velocity in lithium niobate has a certain value V. In magnetic fields corresponding to the position of the Fermi level between two consecutive Landau levels the conductivity in the 2D channel diminishes, and the sample essentially becomes an insulator; the shielding of the piezoelectric fields in lithium niobate decrease in this event, disappearing altogether at the conductivity minimum. According to theory,[13,14] piezoelectric materials have a sound velocity increment, which increases the velocity by an amount proportional to the electromechanical coupling constant K^2, so that for a piezoelectric material the SAW velocity $V_0 > V$. The quantity $\Delta V/V = (V_0 - V)/V$ is measured in experiment. It is evident from Fig. 1 that for all the samples the inequality $(\Delta V/V)_{spin} < (\Delta V/V)_{orb}$ always holds in the entire temperature range. This means that the conductivity of the 2D electron system in spin splitting is always higher than in orbital splitting. If we compare the $(\Delta V/V)_{spin}$ curves for samples AG49 and BP92, which have close electron densities, we find that for $\nu = 3$ the second sample does not exhibit the $(\Delta V/V)_{spin}$ peak. This means that the conductivity of the 2D channel is higher in the second sample than in the first.

To analyze the results, it is more practical to work with the rf conductivity σ_{sp} in magnetic fields corresponding to occupation numbers $\nu = 1$ and 3, which is calculated from the experimentally measured quantities Γ and $\Delta V/V$. For this purpose it is necessary to know the random gap a between the sample and the surface of the piezoelectric substrate. The gap a can be determined from the solution of Eq. (3). If we assume that in relatively weak magnetic fields, where electrons are delocalized,[8] the quantity $\sigma_{xx} = \sigma_1 = \sigma_{xx}^{dc}$ does not depend on the frequency, while $\sigma_2 = 0$ and $4\pi\sigma_{xx}/\varepsilon_s V \gg 1$, we then have $\Gamma \sim 1/\sigma_{xx}$; we now infer from Eq. (2) that the ratio of the absorption coefficients in these fields at two different frequencies for the same sample mounting (i.e., for the same gap) can be written in the form

$$\frac{\Gamma(q_1)}{\Gamma(q_2)} = \frac{[q_1 b(q_1) t(q_2)]}{[q_2 b(q_2) t(q_1)]} e^{-2(a+d)(q_1 - q_2)}. \quad (3)$$

Here q_1 and q_2 are wave vectors corresponding to two different SAW frequencies. In our experiments we have found that $a \simeq 0.5\,\mu$m for different sample mountings.

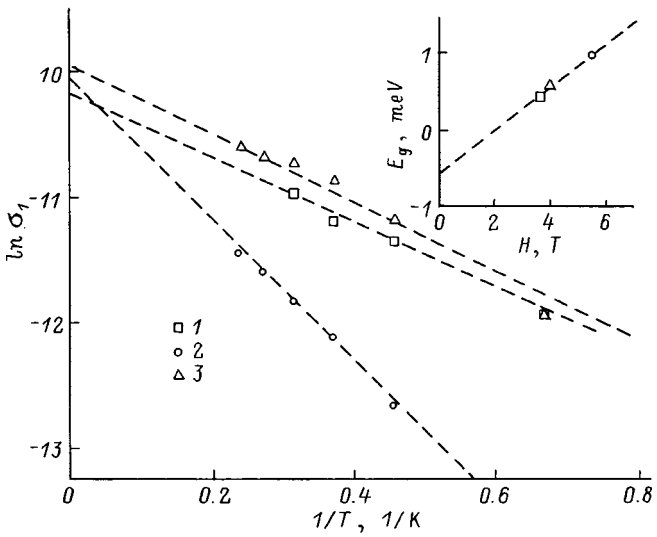

FIG. 2. Dependence of $\ln\sigma_1$ on $1/T$ for samples AG49 (*1*), AG106 (*2*), and BP92 (*3*). Inset: dependence of the activation energy E_g on the magnetic field.

Consequently, from acoustical measurements we have calculated $\mathrm{Re}\,\sigma_{sp} = \sigma_1$ and $\mathrm{Im}\,\sigma_{sp} = \sigma_2$, along with their dependences on the temperature, the magnetic field, and the SAW power. At $T = 1.5$ K we find that σ_1/σ_2 has the values 9.7 ($\nu = 3$) for sample AG49, 17 ($\nu = 3$) for BP92, and 0.9 ($\nu = 1$) for AG106.

As mentioned, the maximum value of the absorption coefficient Γ^{max} is attained for $\sigma_1 = \sigma_2$. Consequently, if $\sigma_1 > \sigma_2$ in a magnetic field corresponding to the absorption peak, the maximum absorption Γ^{max} is still not attained. This case occurs in magnetic fields with $\nu > 8$ in all the samples, and in sample AG49 it also occurs for $\nu = 3$, even at $T = 1.5$ K. Experiment shows that the conductivity $\sigma_1 = \sigma_2 = \sigma$ at which the absorption attains its maximum value Γ^{max} is greater for even values of ν than for odd values, which correspond to spin splitting, and since $\Gamma^{max} \sim 1/\sigma$, the maximum absorption for spin splitting is found to be greater than for orbital splitting. This result is clearly evident in Fig. 1 for sample AG106.

The temperature dependence of $\mathrm{Re}\,\sigma_{sp} \equiv \sigma_1$ ($\nu = 1,3$) for all the samples in the investigated temperature range is well described by the law

$$\mathrm{Re}\,\sigma_{sp} = \sigma_1 \sim \exp(-E_g/2kT). \quad (4)$$

This law is confirmed by the linearity of the plots of $\ln\sigma_1$ as a function of $1/T$ ($f = 30$ MHz) shown in Fig. 2 for all the investigated samples. From the slopes of these lines we have determined the activation energies $E_g = g^* \mu_B H$, which are determined by the spin splitting energy. The inset in Fig. 2 shows the magnetic field dependence of E_g. It is evident that E_g is a linear function of the magnetic field, so that the g^* factor can be determined from the slope of $E_g(H)$, $g^* = 5$. This value agrees with the results of other studies.[2,15,16] It is evident from the figure that the $E_g(H)$ line does not pass through the origin when extrapolated to $H = 0$, probably be-

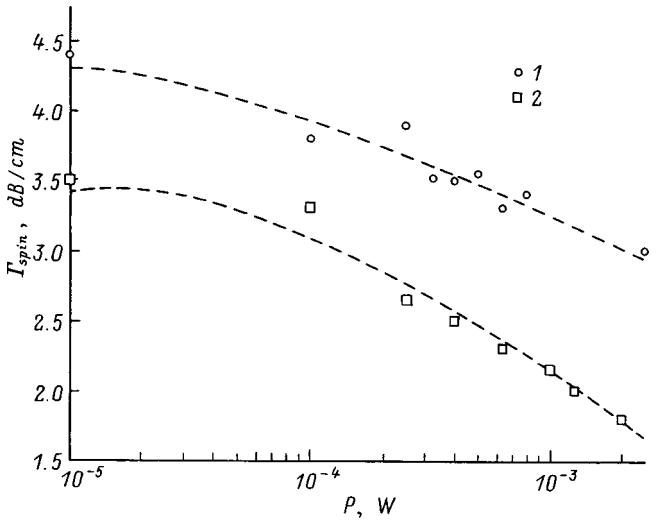

FIG. 3. Dependence of the SAW absorption coefficient Γ_{spin} on the oscillator output power P for samples AG49 (*1*) and AG106 (*2*) at $T=1.5$ K.

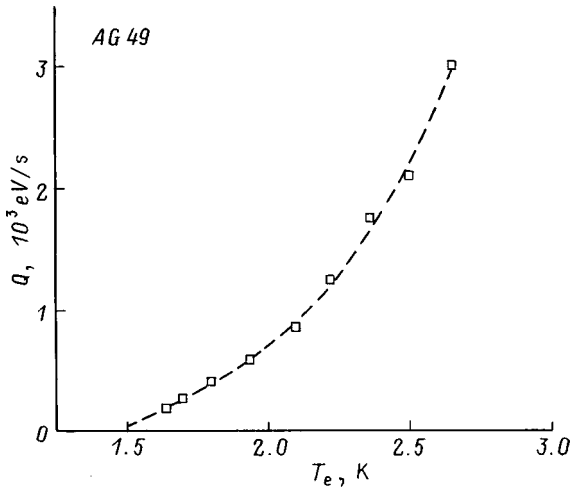

FIG. 4. Dependence of the energy losses Q on the electron temperature T_e for sample AG49 at $T=1.5$ K.

cause the Landau level broadens as a result of the impurity fluctuation potential.[15] We have determined the width of the spin-split Landau levels from the intercept of the $E_g(H)$ line with the energy axis at $H=0$: $A=0.58$ meV. We have previously[17] determined the widths of the bands in the case of orbital splitting for the same samples: $A\approx 2$ meV (AG49). Consequently, the width of the Landau bands is greater in orbital splitting than in spin splitting. As mentioned above, the conductivity of the 2D electron system is always greater in spin splitting than in orbital splitting (for low occupation numbers). Accordingly, the greater the conductivity, the more effective is the shielding of the impurity fluctuation potential and, as a result, the smaller is the width of the band.

3.2 Nonlinear regime

Figure 3 shows the dependence of Γ_{spin} on the oscillator output power P ($f=30$ MHz) for samples AG49 ($\nu=3$) and AG106 ($\nu=1$) at $T=1.5$ K. It is evident from the figure that as the power is increased, the absorption associated with spin splitting of the Landau band, Γ_{spin}, decreases and becomes equal to zero at a certain power level. The relatively small value of $\Delta V/V$ for sample AG49 for $\nu=3$, in contrast with $\nu=2,4$, implies that the conductivity of the 2D system is already fairly high, i.e., a large number of delocalized electrons is present. In this case the behavior of $\Gamma_{spin}(P)$ can be attributed to heating of the electron gas by the SAW electric field, where $\Gamma_{spin}(P)\to 0$ as $kT_e\to g^*\mu_B H$. To describe the heating of the electron gas, we need to know the electron temperature $T_e>T$ (T is the temperature of the lattice), which can be determined by comparing the $\Gamma(P)$ and $\Gamma(T)$ curves. The SAW electric field that penetrates into the channel containing the 2D electron gas is given by the expression

$$|E|^2=K^2\frac{32\pi}{V}(\varepsilon_1+\varepsilon_0)\frac{zq\exp[-2q(a+d)]}{\left(1+\frac{4\pi\sigma_2}{V\varepsilon_s}t\right)^2+\left(\frac{4\pi\sigma_1}{V\varepsilon_s}t\right)^2}W, \quad (5)$$

$$z=[(\varepsilon_1+\varepsilon_0)(\varepsilon_s+\varepsilon_0)-\exp(-2qa)(\varepsilon_1-\varepsilon_0)(\varepsilon_s-\varepsilon_0)]^{-2}, \quad (6)$$

where W is the input SAW power normalized to the width of the sound track. The energy losses in this case are $Q=e\mu E^2=4W\Gamma$ (Ref. 18). The experimental plot of $Q(T_e)$ is shown in Fig. 4. It is found to be well described by the function $Q=A_5(T_e^5-T^5)$. A similar dependence has been obtained in an investigation of nonlinearities in weak magnetic fields, when the electrons exist in delocalized states,[18] corresponding to the relaxation of energy at piezoacoustic phonons in the presence of strong shielding.[19] The value obtained for the coefficient A_5 from this experiment is $25\,eV/(s\cdot \mathrm{K}^5)$, in contrast with the theoretical value determined from equations in Ref. 19 for this sample: $62\,eV/(s\cdot \mathrm{K}^5)$. The difference in the coefficients can be attributed to errors in the determination of the absolute value of the SAW power.

In sample AG106 ($\nu=1$) the same mechanism could not account for the behavior of $\Gamma_{spin}(P)$. Indeed, we can infer from the profile of the peak of the absorption coefficient and the increment $\Delta V/V$ that the conductivity in this sample at $T=1.5$ K is smaller than in sample AG49, where the splitting in two of the absorption peak indicates the localization of carriers situated in the upper band with an oppositely directed spin (relative to the lower band). In this situation we can assume that the nonlinear effects are associated with a decrease in the activation energy in the SAW electric field[20] for electrons existing in localized states at the Fermi level (Poole-Frenkel effect). Now the dependence of the real part of the conductivity on the SAW electric field is given by the expression

$$\sigma_1=\mathrm{Re}\,\sigma_{spin}\propto n(E)=n_0\exp(2e^{3/2}E^{1/2}\varepsilon_s^{-1/2}/kT), \quad (7)$$

where n_0 is the carrier density in the upper Landau band in the linear regime at $T=1.5$ K. The linear behavior of $\ln\sigma_1$ as a function of $E^{1/2}$, with slope $9.5\,(\mathrm{cm}\cdot\mathrm{s}^2/\mathrm{g})^{1/4}$, corroborates this assumption (Fig. 5). The slope calculated from Eq. (7) is $28\,\mathrm{cm}\cdot\mathrm{s}^2/\mathrm{g})^{1/4}$.

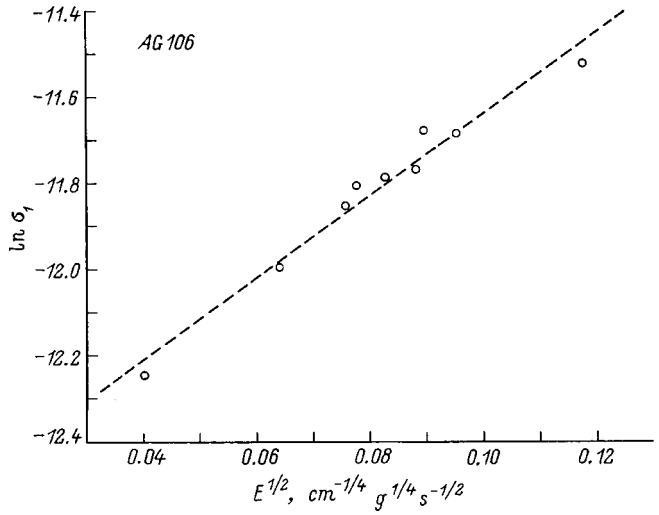

FIG. 5. Dependence of $\ln\sigma_1$ on $E^{1/2}$ for sample AG106 at $T=1.5$ K.

We assume that both of the above-mentioned effects responsible for the dependences $\Gamma(P)$ and $\Delta V/V(P)$ actually coexist, but when delocalized electrons dominate the upper, spin-split-off band, heating of the 2D electron gas plays a greater role; on the other hand, if free electrons are few in number, the dominant mechanism of nonlinearity at first is a reduction of the activation energy in the SAW electric field, causing the number delocalized electrons to increase in the upper band of the spin-split Landau bands, which are heated by the SAW electric field.

4. CONCLUSIONS

In our investigations of the absorption and velocity increment of surface acoustic waves ($f=30$ MHz) due to interaction with two-dimensional electrons in GaAs/AlGaAs heterostructures (with electron densities $n=1.3\times10^{11}$ cm^{-2}, 2.7×10^{11} cm^{-2}, and 2.8×10^{11} cm^{-2} at $T=1.5-4.2$ K in magnetic fields up to 7 T, we have:

1) observed peaks associated with spin splitting of the Landau levels;

2) evaluated the effective g factor, $g^*\cong5$.

3) determined the width of the Landau bands associated with spin splitting: 0.6 meV, which is found to be smaller than the width of the Landau bands for orbital splitting: 2 meV; we have shown that the conductivity of the 2D electron system in spin splitting is always greater than in orbital splitting, so that the fluctuation potential of charged impurities, which governs the width of the Landau bands, is shielded more effectively in spin splitting;

4) investigated the mechanisms of the nonlinearities manifested in the dependences of the absorption coefficient and the SAW velocity increment on the SAW power in the presence of spin splitting of the Landau levels.

The authors are grateful to V. D. Kagan for many discussions, to A. V. Suslov for helping with the measurements, and to D. A. Pristinskiĭ for carrying out the numerical computations.

This work has been supported by grants from the Russian Fund for Fundamental Research, RFFI Grant No. 98-02-18280, and from the Ministry of Science, No. 97-1043.

*)E-mail: Irina.L.Drichko@shuvpov.ioffe.rssi.ru; FAX: (812) 515 6747

[1] T. Ando and Y. Uemura, J. Phys. Soc. Jpn. **37**, 1044 (1974).
[2] R. J. Nicholas, R. J. Haug, K. V. Klitzing, and G. Weimann, Phys. Rev. B **37**, 1294 (1988).
[3] F. F. Fang and P. J. Stiles, Phys. Rev. **174**, 823 (1968).
[4] R. J. Nicholas, M. A. Brummel, J. C. Portal, K. Y. Cheng, A. Y. Cho, and T. P. Pearsall, Solid State Commun. **45**, 911 (1983).
[5] E. E. Mendez, J. Nocera, and W. I. Wang, Phys. Rev. B **47**, 13 937 (1993).
[6] S. P. Papadakis, E. P. de Poorte, and M. Shayegan, *Preprint cond-mat* / 9808158 (1998).
[7] I. L. Drichko, A. M. D'yakonov, A. M. Kreshchuk, T. A. Polyanskaya, I. G. Savel'ev, I. Yu. Smirnov, and A. V. Suslov, Fiz. Tekh. Poluprovodn **31**, 451 (1997) [Semiconductors **31**, 384 (1997)].
[8] I. L. Drichko and I. Yu. Smirnov, Fiz. Tekh. Poluprovodn **31**, 1092 (1997) [Semiconductors **31**, 933 (1997)].
[9] V. D. Kagan, Fiz. Tekh. Poluprovodn. **31**, 470 (1997) [Semiconductors **31**, 407 (1997)].
[10] I. L. Aleiner and B. I. Shklovskii, Int. J. Mod. Phys. B **8**, 801 (1994).
[11] R. Boulet, P. Coleridge, F. Guilon, M. D. 'Iorio, and A. Sachrajda, Can. J. Phys. **69**, 461 (1992).
[12] A. Wixforth, J. Scriba, M. Wassermeier, J. P. Kotthaus, G. Weimann, and W. Schlapp, Phys. Rev. B **40**, 7874 (1989).
[13] V. L. Gurevich, Fiz. Tverd. Tela (Leningrad) **4**, 909 (1962) [Sov. Phys. Solid State **4**, 668 (1962)].
[14] A. R. Hutson and D. L. White, J. Appl. Phys. **33**, 40 (1962).
[15] A. Usher, R. J. Nicholas, J. J. Harris, and C. T. Foxon, Phys. Rev. B **41**, 1129 (1990).
[16] D. R. Leadley, R. J. Nicholas, J. J. Harris, and C. T. Foxon, *Preprint cond-mat* / 9805332 (1998).
[17] I. L. Drichko, A. M. Diakonov, V. D. Kagan, I. Yu. Smirnov, and A. I. Toropov, in *Proceedings of the 24th Conference on Physics of Semiconductor*, on CD-ROM, Jerusalem, Israel (1998).
[18] I. L. Drichko, A. M. D'yakonov, V. D. Kagan, A. M. Kreshchuk, T. A. Polyanskaya, I. G. Savel'ev, I. Yu. Smirnov, and A. V. Suslov, Fiz. Tekh. Poluprovodn. **31**, 1357 (1997) [Semiconductors **31**, 1170 (1997)].
[19] V. Karpus, Fiz. Tekh. Poluprovodn. **22**, 439 (1988) [Sov. Phys. Semicond. **22**, 268 (1988)].
[20] L. S. Stil'bans, *Physics of Semiconductors* [in Russian], Sov. Radio, Moscow (1967).

Translated by James S. Wood

New approach to the analysis of negative magnetostriction in two-dimensional structures

G. M. Min'kov,*) S. A. Negashev, O. É. Rut, and A. V. Germanenko

Ural State University, NIIFPM, Ekaterinburg, Russia

O. I. Khrykin, V. I. Shashkin, and V. M. Danil'tsev

Institute of Physics of Microstructures, Russian Academy of Sciences, Nizhny Novgorod, Russia
(Submitted January 22, 1999; accepted for publication February 18, 1999)
Fiz. Tekh. Poluprovodn. **33**, 986–989 (August 1999)

It is shown that the Fourier transform of the negative magnetoresistance associated with the interference correction to the conductivity contains information about the distribution function of the closed trajectories with respect to their areas and about the dependence of the length of the closed trajectories on their area $\bar{L}(S)$. On the basis of this result a method is proposed for analyzing the negative magnetoresistance. It is used to process experimental results in a two-dimensional structure with a doped barrier. It is shown that the function $\bar{L}(S)$ in the investigated structure is largely determined by the scattering anisotropy. © *1999 American Institute of Physics.* [S1063-7826(99)02108-0]

The anomalous magnetostriction observed in ''dirty'' semiconductors and metals at low temperatures has been adequately explained since the development of the theory of quantum corrections to the conductivity.[1–3] In two-dimensional (2D) systems in weak magnetic fields the main contribution to the anomalous magnetoresistance is from interference corrections to the conductivity. They are attributable to the interference of electron waves transmitted along closed segments of trajectories in opposite directions, which enhances backscattering and lowers the conductivity accordingly. A magnetic field perpendicular to the 2D layer changes the phase of the wave functions of electrons transmitted in opposite directions, thereby decreasing the interference correction and, hence, creating a negative magnetoresistance.

A theory that takes the interference conductivity corrections into account has been developed subject to the condition $k_F l \gg 1$ (k_F is the electron momentum on the Fermi surface, and l is the mean free trajectory). The quasi-classical approach is applicable in this case, and the interference conductivity increment can be represented by the sum of the contributions from the closed trajectories[4]

$$\Delta\sigma = 2\pi l^2 G_0 \sum_i W_i \exp\left(-\frac{L_i}{l_\varphi}\right), \tag{1}$$

where $G_0 = e^2/2\pi^2\hbar$, W_i is the probability density function for the existence of an electron at the starting point after transmission along the ith trajectory of length L_i, $l_\varphi = v_F \tau_\varphi$, v_F is the velocity at the Fermi level, τ_φ is the relaxation time of the phase of the wave function, and the factor $\exp(-L_i/l_\varphi)$ takes into account the probability of phase slip of the wave function in motion along the ith trajectory.

To calculate the field dependence of the negative magnetoresistance, we write the sum (1) as the sum of the contributions from closed trajectories with different numbers of collisions N (Refs. 1, 5, and 6)

$$\begin{aligned}\Delta\sigma(B) &\equiv \sigma(B) - \sigma(0) \\ &= 2\pi l^2 G_0 \sum_N \sum_i W_i^N \exp\left(-\frac{L_i}{l_\varphi}\right) \\ &\quad \times \left[1 - \cos\left(\frac{2\pi S_i^N B}{\Phi_0}\right)\right],\end{aligned} \tag{2}$$

where S_i^N is the area of the ith trajectory with N collisions, $\Phi_0 = 2\pi c\hbar/e$ is the fluxon (flux quantum), and the factor $[1-\cos(2\pi S_i^N B/\Phi_0)]$ takes into account the variation of the interference due to variation of the phase of the electron wave function in the magnetic field as it moves along this trajectory. A diagramming technique[1,6] can be used to calculate this sum and to obtain an analytical result subject to two conditions: a random distribution of scatterers and isotropic scattering, which correspond to scattering by a short-lived potential. In the diffusion approximation (when the number of collisions on the actual trajectories is large) these conditions yield[1]

$$\begin{aligned}\Delta\sigma(B) &= a G_0 \, F(B, \tau_\varphi, \tau_p), \\ F(B, \tau_\varphi, \tau_p) &= \Psi\left(\frac{1}{2} + \frac{B_{\rm tr}}{B}\frac{\tau_p}{\tau_\varphi}\right) - \ln\left(\frac{B_{\rm tr}}{B}\frac{\tau_p}{\tau_\varphi}\right),\end{aligned} \tag{3}$$

where $\Psi(x)$ is the logarithmic derivative of the Γ-function, τ_p is the momentum relaxation time, and $B_{\rm tr} = \hbar c/2el^2$. (If electron-electron interaction is ignored, we have $a = 1$.) Beyond the limits of the diffusion approximation the function $F(B, \tau_\varphi, \tau_p)$ has a more complex form and has been calculated in Ref. 6.

Equation (3) is used specifically in analyzing experimental results on the negative magnetoresistance. It fairly well

describes the field dependence of the negative magnetoresistance and provides a means for determining the relaxation time of the phase of the wave function, along with its temperature dependence. The causes of the noticeable field dependence of the negative magnetoresistance in many cases from Eq. (3) in this approach to the analysis of the experimental results are still not clear. They could be related to the presence of correlation in the impurity distribution, scattering anisotropy, etc.

The proposed method of analyzing the negative magnetoresistance can be used to obtain additional information directly about the statistics of the closed trajectories due to scattering anomalies and correlation in the distribution of impurities. To explain the essential part of the method, we rewrite Eq. (1), separating the contributions of self-crossing trajectories of identical area:

$$\Delta\sigma(B)=2\pi\, l^2\, G_0 \sum_S W(S)\, \exp\left(-\frac{\overline{L}}{l_\varphi}\right) \times\left[1-\cos\left(\frac{2\pi SB}{\Phi_0}\right)\right], \tag{4}$$

where

$$W(S)=\sum_i W_i^S$$

is the areal distribution function of the closed trajectories, W_i^S is the distribution function of trajectories of area S by lengths, and the symbol $\overline{L}=\overline{L}(S,l_\varphi)$ is introduced so that

$$\exp\left(-\frac{\overline{L}(S,l_\varphi)}{l_\varphi}\right)=\frac{1}{W(S)}\sum_i W_i^S\, \exp\left(-\frac{l_i^S}{l_\varphi}\right). \tag{5}$$

It follows from Eq. (4) that the Fourier transform of the negative magnetoresistance is

$$\Phi(S)=\sqrt{\frac{\pi}{2}}2\pi l^2 G_0\, W(S)\, \exp\left[-\frac{\overline{L}(S,l_\varphi)}{l_\varphi}\right]. \tag{6}$$

It is evident, therefore, that the Fourier transform of the negative magnetoresistance contains information about the areal distribution of the closed trajectories $W(S)$ and about the dependence of $\overline{L}$ on S and L_φ. For the subsequent analysis we make only one assumption, that $\overline{L}=\overline{L}(S,l_\varphi)=S^\alpha f(l_\varphi)$. Numerical calculations of the function $\overline{L}(S,l_\varphi)$ (to be published separately) and an analysis of Eq. (3) show that such a dependence of $\overline{L}$ on S and L_φ is valid with good accuracy over a broad range of S and L_φ. For isotropic scattering in this case we have $\alpha\simeq 0.67$. It might appear at first glance that the length of the closed trajectories, on the average, should be proportional to the square root of their area, but it must be taken into consideration that trajectories of large area are more sinuous than small-area trajectories, resulting in a stronger dependence $\overline{L}(S)$. In scattering by ionized impurities, which is the principal mechanism of momentum dissipation at low temperatures, the scattering is anisotropic, so that small-angle scattering is prevalent. Clearly, on the average, large-area trajectories become less sinuous in this case than in isotropic scattering, so that the dependence $\overline{L}(S)$ is weakened, and in the case of strong scattering anisotropy $\overline{L}\propto S^{0.5}$, i.e., $\alpha=0.5$. Consequently, α is determined by scattering anisotropy.

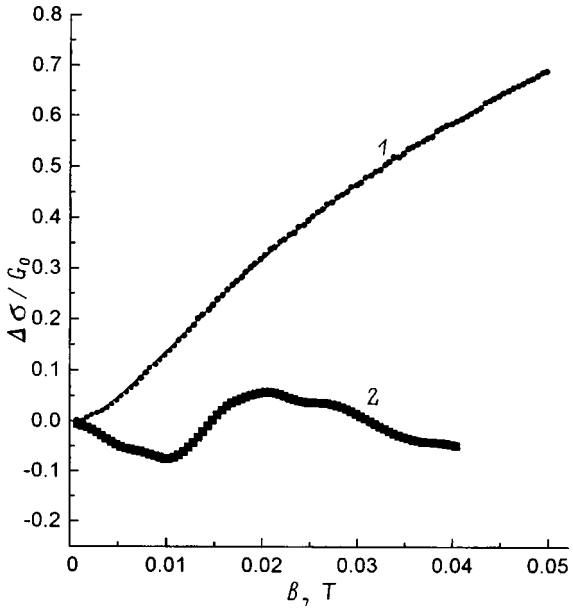

FIG. 1. (*1*) Graph of $\Delta\sigma(B)/G_0$ at a temperature $T=1.5$ K: The points represent experimental data; the solid curve represents the theoretical dependence (3) for $a=0.7$ and $\tau_\varphi=5.4\times10^{-12}$ c. (*2*) Difference between the theoretical and experimental dependences $20\times(\Delta\sigma_{\rm th}-\Delta\sigma_{\rm exp})/G_0$.

For the experimental determination of α it is possible, given the dependence $\Delta\sigma(B)$ at two temperatures, i.e., for different values of l_φ, to find

$$A(S)\equiv\ln\left[\frac{\Phi(S,T_1)}{\Phi(S,T_2)}\right]=S^\alpha[f(l_\varphi^1)-f(l_\varphi^2)] \tag{7}$$

and, hence, to determine α from $A(S)$.

We now analyze the experimental results. They have been obtained for a $(0.3\,\mu\text{m})n^-$-GaAs/$(50\,\text{Å})$In$_{0.1}$Ga$_{0.9}$As/$(0.3\,\mu\text{m})n^-$-GaAs heterostructure. The n^--GaAs had a δ-doped Si layer on each side at a distance of 125 Å from the quantum well. Measurements over a wide range of magnetic fields (up to 6 T) and temperatures (1.5–40) K show that the main contribution to the conductivity is from carriers in the In$_{0.1}$Ga$_{0.9}$As quantum well. In this case one quantum-well subband is filled, wherein the density of electrons is $n=2.5\times10^{11}\,\text{cm}^{-2}$, and their mobility is $\mu=1.1\times10^4\,\text{cm}^2/(\text{V}\cdot\text{s})$.

Figure 1 shows the field dependence of the negative magnetoresistance. Normally, in analyzing the negative magnetoresistance, the field dependence of the resistance is compared with Eq. (3) with the prefactor a and τ_φ treated as fitting parameters. The solid curve in Fig. 1 has been plotted by this technique and at first glance appears to provide a good description of the negative magnetoresistance in a magnetic field up to $B<B_{\rm tr}\simeq0.038$ T for $a=0.7$ and $\tau_\varphi=5.4\times10^{-12}$ s. However, a more careful analysis makes it clear that an appreciable discrepancy exists between the experimental and theoretical dependences (Fig. 1, curve *2*). This

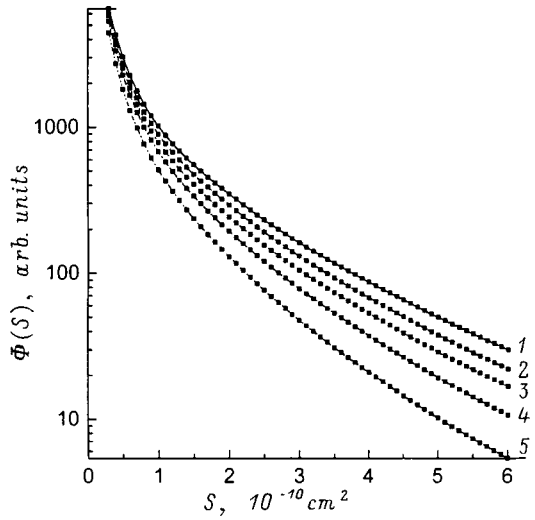

FIG. 2. Fourier transforms of the experimental $\Delta\sigma(B)$ curves at various temperatures: (*1*) $T=1.6$ K; (*2*) 2 K; (*3*) 2.5 K; (*4*) 3 K; (*5*) 4.2 K.

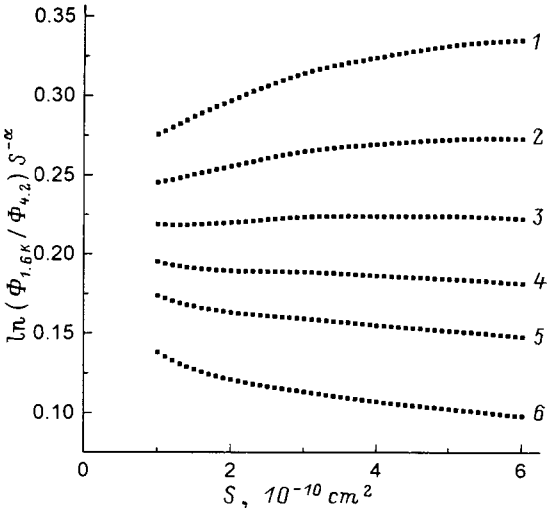

FIG. 3. Graphs of the function $A(S)S^{-\alpha}=\ln[\Phi_{1.6\ \mathrm{K}}(S)/\Phi_{4.2\ \mathrm{K}}(S)]\,S^{-\alpha}$ for: (*1*) $\alpha=0.4$; (*2*) 0.45; (*3*) 0.5; (*4*) 0.55; (*5*) 0.6; (*6*) 0.7.

discrepancy makes the values of the parameters a and τ_φ vary in the intervals 0.65–0.88 and $(4.4-6)\times10^{-12}$ s, respectively, in different parts of the interval $0<B<B_{\mathrm{tr}}$ when expression (3) is used for the fitting. Consequently, the error of determination of a and τ_φ in such a comparison does not exceed 15–20%. In many papers the prefactor smaller than unity is attributed to the contribution of electron-electron interaction (Maki-Thompson correction) (Ref. 7); in our opinion, however, the deviation of a from unity in the investigated sample is attributable to poor compliance with the condition for applicability of the diffusion approximation, $\tau_\varphi/\tau_p\gg1$. In our case $\tau_\varphi/\tau_p\simeq5-10$, and it follows from an analysis of previously published results[6] of calculations of the negative magnetoresistance beyond the scope of the diffusion approximation that for the given relation between a and τ_φ the negative magnetoresistance, as before, is adequately described by Eq. (3), but with a prefactor smaller than unity.

We now look at the outcome of using the above-proposed method. Figure 2 shows the Fourier transforms of $\Delta\sigma(B)$ at several temperatures. It follows from Eq. (7) that by plotting $\ln[A(S)]$ as a function of $\ln S$ it is possible to evaluate α, which is found to have a value of 0.52 ± 0.05. To illustrate the accuracy of determination of α, Fig. 3 shows graphs of $A(S)\,S^{-\alpha}$ for various values of α, plotted at temperatures of 1.6 K and 4.2 K. (Similar results are obtained for any pair of temperatures.)

As mentioned, $\alpha=0.67$ for isotropic scattering. This result can be confirmed by analyzing (in the same way as in our processing of the experimental results) the function $\Delta\sigma(B)$ given by Eq. (3), which has been derived for isotropic scattering. The analysis shows that: 1) the dependence $L(S,L_\varphi)=S^\alpha f(l_\varphi)$ holds over a wide range of S and l_φ; 2) $\alpha=0.67$. In our opinion, the significantly smaller value of α in the investigated sample, is attributable to strong scattering anisotropy. Indeed, the principal momentum dissipation mechanism in our case is scattering by the potential of charged impurities of the δ-doped layers, which is smooth in the quantum well region. Estimates show that the probability of small-angle scattering in this case is 15–20 times the probability of backscattering.

In principle, knowing the dependence $\Delta\sigma(B)$ over a wide range of temperatures, one can experimentally determine the areal distribution function of the closed trajectories $W(S)$. In fact, since l_φ tends to infinity in the limit $T\to0$, it follows from Eq. (6) that the extrapolation of $\Phi(S,T)$ to $T=0$ gives $W(S)$.

Thus the above-proposed method of analyzing the negative magnetoresistance can be used to obtain information about the statistics of the closed trajectories and, hence, about the scattering anisotropy, correlation in the impurity distribution, etc.

This work has been supported by grants from the Russian Fund for Fundamental Research (RFFI Grants 97-02-16168, 98-02-16624, and 98-02-17286) and by the programs ''Physics of Solid State Nanostructures'' (Grant 97-1091) and ''Universities of Russia — Basic Research (Grant 420).

*)E-mail: Grigori.Minkov@usu.ru

[1] S. Hikami, A. Larkin, and Y. Nagaoka, Prog. Theor. Phys. **63**, 707 (1980).
[2] B. Altshuler, D. Khmelnitskii, A. Larkin, and P. Lee, Phys. Rev. B **22**, 5142 (1980).
[3] V. L. Al'tshuler, A. G. Aronov, A. I. Larkin, and D. E. Khmel'nitskiĭ, Zh. Éksp. Teor. Fiz. **81**, 768 (1981) [Sov. Phys. JETP **54**, 411 (1981)].
[4] L. P. Gor'kov, A. I. Larkin, and D. E. Khmel'nitskiĭ, JETP Lett. **30**, 228 (1979); S. Chakravarty and A. Schmid, Phys. Rep. **140**, 193 (1986).
[5] M. I. Dyakonov, Solid State Commun. **92**, 711 (1994).
[6] H.-P. Wittmann and A. Schmid, J. Low Temp. Phys. **69**, 131 (1987).
[7] A. I. Larkin, JETP Lett. **31**, 239 (1980).

Translated by James S. Wood

Long-wavelength emission in structures with quantum dots formed in the stimulated decomposition of a solid solution at strained islands

B. V. Volovik, A. F. Tsatsul'nikov, D. A. Bedarev, A. Yu. Egorov, A. E. Zhukov, A. R. Kovsh, N. N. Ledentsov, M. V. Maksimov, N. A. Maleev, Yu. G. Musikhin, A. A. Suvorova, V. M. Ustinov, P. S. Kop'ev, and Zh. I. Alferov

A. F. Ioffe Physicotechnical Institute, Russian Academy of Sciences, 194021 St. Petersburg, Russia

D. Bimberg

Institut für Festkörperphysik, Technische Universität Berlin, D-10623 Berlin, Germany

P. Werner

Max-Planck-Institut für Mikrostrukturphysik, 06120 Halle, Germany

(Submitted February 15, 1999; accepted for publication February 18, 1999)
Fiz. Tekh. Poluprovodn. **33**, 990–995 (August 1999)

When an array of strained InAs nanoislands formed on a GaAs surface is overgrown by a thin (1–10 nm) layer of an indium-containing solid solution, stimulated decomposition of the solid solution is observed. This process causes the formation of zones of elevated indium concentration in the vicinity of the nanoislands. The volume of newly formed InAs quantum dots increases as a result of this phenomenon, producing a substantial long-wavelength shift of the photoluminescence line. This effect is enhanced by lowering the substrate temperature, and it depends weakly on the average width of the band gap of the solid solution. The indicated approach has been used successfully in achieving room-temperature emission at a wavelength of 1.3 μm. © *1999 American Institute of Physics.* [S1063-7826(99)02208-5]

INTRODUCTION

The self-organizing phenomena responsible for the creation of semiconductor heterostructures with quantum dots (QDs) and quantum wires[1] are intriguing not only from the standpoint of revealing fundamental aspects of epitaxial growth, but also in regard to the fabrication of new-generation optoelectronic and microelectronic devices. The greatest progress in device applications is achieved utilizing the phenomenon of spontaneous conversion of a strained thin film to an array of coherent islands.[2–4] Injection lasers have been constructed utilizing QDs and exhibiting extremely high temperature stability of the threshold current density J_{th}, a low value of J_{th} (Refs. 4–6), and continuous-wave lasing at room temperature with a power output in excess of 3 W (Ref. 7).

One advantage of using QD structures is the possibility of broadening the optical range of emission in comparison with structures based on quantum wells. For example, structures containing In(Ga)As/(Al)GaAs QDs are capable of lasing in the range $1-1.6$ μm (Refs. 4 and 8–10). In particular, QD structures hold considerable promise for the fabrication of devices emitting at a wavelength of 1.3 μm (Refs. 9 and 10). Lasers utilizing InGaAs QDs and emitting at a wavelength of 1.3 μm have now been constructed.[10] Nonetheless, because of rapid gain saturation, lasing via the ground state of QDs has been achieved only by means of very long cavities and with the deposition of high-reflectivity coatings. The problems of attaining the 1.3-μm range for structures utilizing InGaAs/GaAs QDs stem from the rather large average thickness of InAs in the active zone and the high probability of formation of misfit dislocations. It is therefore critical at this time to look for new approaches to the construction of QD devices emitting at 1.3 μm, with a need to minimize the quantity of In in the active zone. Huffaker *et al.*[10] have deposited 5.5 InAs monolayers to achieve emission at a wavelength of 1.3 μm. In the present study we have reduced this number to four monolayers.

We have investigated the structural and optical properties of QD arrays overgrown by a layer of an (In, Ga, Al)As solid solution. The resulting QDs stimulate decomposition of the solid solution, thereby increasing the In concentration in the vicinity of the QDs and producing a long-wavelength shift of the emission line. This approach can be used to achieve emission from InAs QDs at wavelengths up to 1.32 μm while significantly reducing the total content of In in the active zone.

EXPERIMENT

The investigated structures were grown by molecular-beam epitaxy on GasAs (100) semi-insulating substrates by means of a Riber 32P MBE machine. The active zone was placed in a GaAs host and consisted of an array of quantum dots formed in the deposition of an InAs thin film. The effective thickness of the InAs QD layer d_{QD} varied from two to three monolayers (ML) for different structures. The QDs were overgrown by an InGaAs or InGaAlAs solid solution. The thickness of the (In, Ga, Al)As layer (L) varied from 2.5 nm to 8 nm, and the In concentration in the solid solution (x)

varied from 0.1 to 0.4. To prevent the transport of nonequilibrium carriers into the surface zone and into the substrate zone during optical investigations, the active zone was bounded on both sides by short-period AlAs/GaAs superlattices. The growth temperature was 485 °C for the active zone and 600 °C for the rest of the structure. The formation of QDs was monitored from the fast-electron diffraction pattern in reflection.

Transmission electron microscope (TEM) examinations were made on a Philips EM 420 electron microscope with an accelerating voltage of 100 kV. Photoluminescence was excited by an Ar^+ laser ($\lambda = 514.5$ nm, excitation density $\sim 100\,\mathrm{mV/cm^2}$). In the measurement of the luminescence excitation spectrum light from a halogen lamp was transmitted through a monochromator. The luminescence was detected by a cooled Ge photodiode.

RESULTS AND DISCUSSION

Today the greatest progress in the fabrication of (In, Ga)As/GaAs QD lasers is achieved using QDs in the initial stage of their formation,[6,7] which are characterized by a high density, an absence of dislocations, and short carrier trapping and relaxation times. For the implementation of long-wavelength emission in the InAs QD structures the QD arrays were overgrown with a layer of $In_xGa_{1-x}As$ solid solution during the initial stage of their formation ($d_{QD} \sim 2$ ML).

Figure 1a shows the photoluminescence spectra of InAs QD structures prepared by the deposition of ~ 2 ML of InAs and overgrown by a layer of $In_xGa_{1-x}As$ solid solution with various In concentrations (x). The thickness of the $In_xGa_{1-x}As$ layer for all the structures was 4 nm. The photoluminescence spectrum contains a line, labeled *QW* in Fig. 1, in addition to the *QD* line associated with carrier recombination in the resulting QDs. To investigate the nature of this line, we have analyzed the luminescence excitation spectra (Fig. 1b). In the excitation spectra of the *QD* line there are discernible peaks $P1$, $P2$, and $P3$, which on the energy scale are situated at distances from the detection energy of 35 meV, 74 meV, and 102 meV, respectively. This form of the luminescence excitation spectra is typical of QD structures[11] and is associated with a multiphonon mechanism of carrier relaxation from excited QD states. The luminescence excitation spectra also reveal a *QW* line whose position coincides with the position of the *QW* line in the photoluminescence spectra and does not depend on the detection energy. This result shows that the *QW* line is associated with carrier excitation in the continuum of the InGaAs solid solution.

It is evident from the photoluminescence spectra (Fig. 1) that when the In concentration in the InGaAs solid solution increases, the *QW* line exhibits a long-wavelength shift and, accordingly, is shifted toward the long-wavelength end relative to the wetting-layer line observed in the spectrum of ordinary InAs/GaAs QDs (*WL* line in Fig. 1a). Consequently, the QDs reside in the InGaAs matrix, which is a narrower-gap medium than GaAs.

Note that despite the overgrowth of the QDs by the narrower-gap (in comparison with GaAs) material, the energy distance between the QD photoluminescence maximum (*QD* line) and the *QW* peak is roughly 200 meV, which is comparable with the values obtained for ordinary QDs in a GaAs host.[4] It also shows that the carriers localize effectively in the QDs.

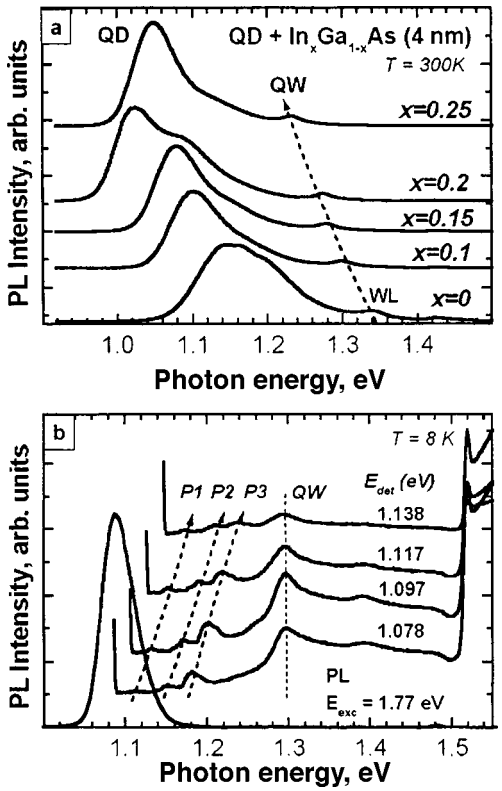

FIG. 1. (a) Photoluminescence spectra for structures containing InAs QDs ($d_{QD} = 2$ ML) overgrown by an $In_xGa_{1-x}As$ layer, $L = 4$ nm. (b) Photoluminescence spectrum and luminescence excitation spectra for structures containing InAs QDs ($d_{QD} = 2$ ML) overgrown by an InGaAs layer. The excitation and detection energies are indicated alongside the spectra.

It is evident from the photoluminescence spectra (Fig. 1a) that as x increases in the interval from 0 to 0.2, the photoluminescence *QD* line is observed to shift toward lower photon energies. However, when x is further increased to 0.25, the *QD* line shifts toward the short-wavelength end. On the other hand, when the thickness of the InGaAs layer is increased from 4 nm to 8 nm at a constant concentration x (0.15 or 0.2), we also observe a short-wavelength shift of the *QD* peak. The variation of the energy positions of the *QD* and *QW* lines in the photoluminescence spectra as functions of the parameters of the $In_xGa_{1-x}As$ layer is shown in Fig. 2a. A further increase in the In concentration to 0.35–0.4 at $L = 4$ nm still enabled us to achieve emission at a wavelength of 1.3 μm, but the TEM examinations show that the density of penetrating dislocations increases sharply in this case.

Figure 2b shows the dependence of the total photoluminescence intensity on the effective InAs thickness in the active zone ($d_{eff} = d_{QD} + L \times x$), which for the given samples increases as a result of the increase of the In concentration in the solid solution. It is evident that for concentrations $x > 0.3$ (which corresponds to $d_{eff} = 18$ Å for $d_{QD} = 2$ ML and $L = 4$ nm), the photoluminescence intensity decreases considerably.

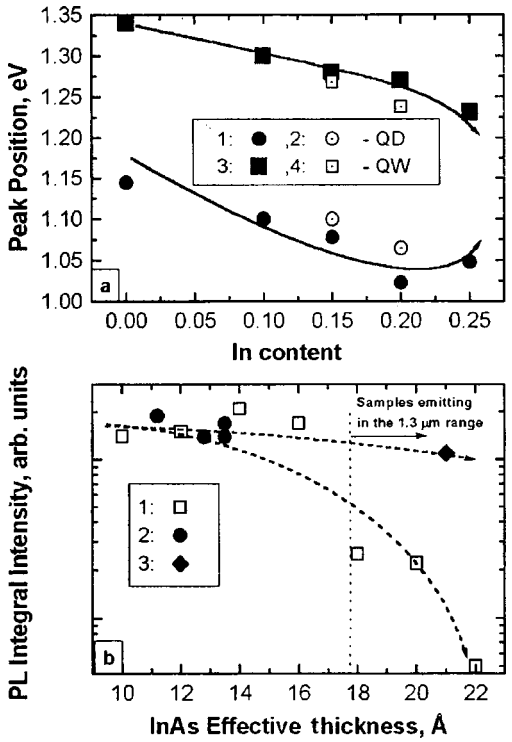

FIG. 2. (a) Positions of the QD photoluminescence peaks (*QD* line) and an InGaAs layer (*QW* line) versus the In concentration in the InGaAs layer: (*1, 3*) $L=4$ nm; (*2, 4*) $L=8$ nm. (b) Dependence of the total photoluminescence intensity on the effective thickness of the InAs layer: (*1*) Structures with $d_{QD}=2$ ML, $L=4$ nm, and various In concentrations in the solid solution; (*2*) structures with various effective InAs thicknesses in the active zone (the parameters of the structures are given in Table I; (*3*) structures with InAs QDs ($d_{QD}=3$ ML) deposited in the middle of an $In_{0.12}Ga_{0.88}As$ layer.

It is evident from the investigations that for structures with 2 ML of InAs QDs with overgrowth of the QDs by an InGaAs solid solution it is possible to obtain long-wavelength emission, but for a certain critical In concentration in the InGaAs layer ($x\sim0.25$ in the given situation) the resulting effect is such as to produce a short-wavelength shift of the QD photoluminescence line. To obtain long-wavelength emission in this case requires a significant increase of the In concentration in the InGaAs layer, but this leads to the formation of dislocations and, in the final analysis, degradation of the optical properties of the structures (Fig. 2b).

An alternative possibility for achieving emission at a wavelength of 1.3 μm is to increase the effective thickness of the InAs layer (d_{eff}) without increasing the In concentration in the solid solution. We have grown a series of samples in which the effective thickness of the InAs layer was varied by varying the amount of InAs during deposition of the QDs (d_{QD}) and by varying the thickness of the InGaAs layer (L) without the value of x ever exceeding 21 %. Table I gives the parameters of the active zone of these structures, along with TEM data [the density and diameters of the QDs and the density of misfit dislocations formed at the interface in the plane of the QDs]. Figure 3 shows the photoluminescence spectra of these samples. The following conclusions can be drawn from a comparison of the TEM and photoluminescence results. First, increasing the total quantity of In during the successive deposition of QDs and the InGaAs layer increases the size of the islands and produces a long-wavelength shift of the QD photoluminescence line. However, at a certain critical concentration of In atoms ($d_{QD}=2.7$ ML, $L=25$ Å, and $x=21$ % in the given situation) the density of misfit dislocations increases, accompanied by a 25-meV shift of the QD photoluminescence line toward higher photon energies. This effect is similar to the effect observed for 2 ML of QDs.

TABLE I.

Sample	d_{QD} (ML)	x	L, nm	Lateral QD diameter, nm	QD density, cm^{-2}	Density of misfit dislocations, cm^{-1}
A	~2.2	0.18	2.6	15	3.4×10^{10}	2.3×10^{4}
B	~2.7	0.18	2.6	18	4.3×10^{10}	2.7×10^{4}
C	~2.7	0.18	3	18	4.5×10^{10}	3.2×10^{4}
D	~2.7	0.21	2.6	17	4.6×10^{10}	6.5×10^{4}

We assume that when the QD array is overgrown by an InGaAs layer, the In atoms are distributed nonuniformly in the growth plane, owing to QD-induced stresses. As a result, zones of elevated In concentration form in the vicinity of the resulting QDs, in effect increasing the size of the QDs. The phenomenon of decay of a quantum well under the influence of a QD array is described in Refs. 12 and 13 for various materials. If the In content exceeds a certain value, the In concentration near the largest dots can exceed the critical value, and misfit dislocations are formed in the plane of the QDs. Since radiative recombination does not take place at these dots, the intensity of the long-wavelength part of the photoluminescence spectrum decreases, and the photoluminescence line shifts toward the short-wavelength end. Another cause of the short-wavelength shift of the QD photoluminescence line with a simultaneous long-wavelength shift of the photoluminescence line of the InGaAs layer could be a change in the growth kinetics as the islands are overgrown by an InGaAs solid solution having a higher In content. In this event the fraction of In atoms deposited in the vicinity of the QDs decreases, raising the average In content.

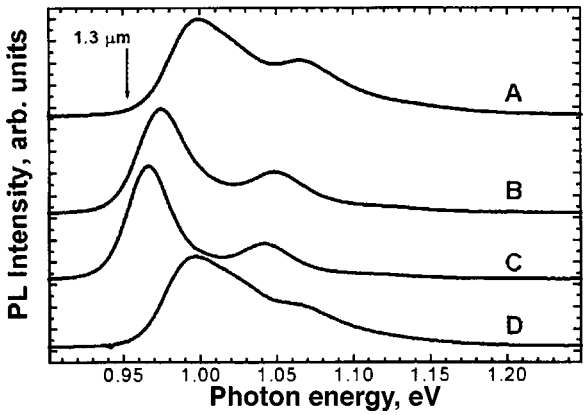

FIG. 3. Photoluminescence spectra for structures with various effective InAs thicknesses in the active zone. The parameters of the structures $A-D$ are given in Table I.

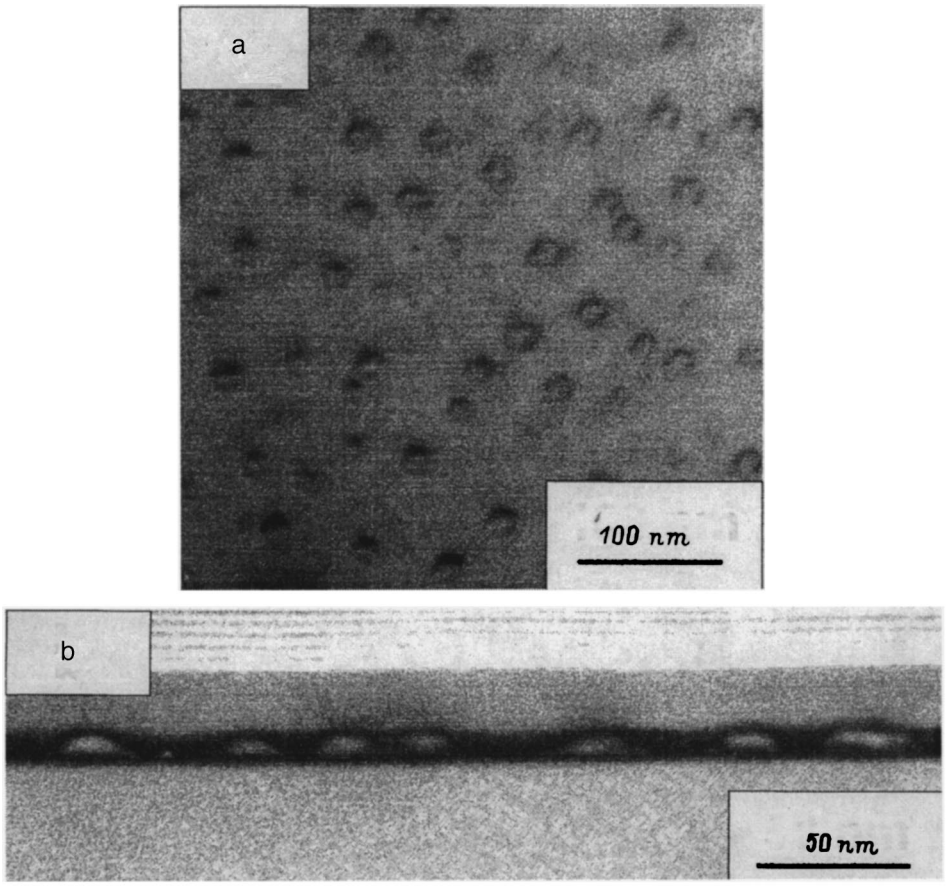

FIG. 4. TEM images in the growth plane (a) and in the cross section (b) of a structure with InAs QDs ($d_{QD}=3$ ML) deposited in the middle of an $In_{0.12}Ga_{0.88}As$ layer.

Since the increase in the QD diameter as the InAs content in the QDs increases from 2.2 Ml to 2.7 ML does not cause the density of misfit dislocations to increase, we have sought to further increase the long-wavelength shift by growing a structure with 3 ML of InAs QDs deposited in the middle of a wide (10 nm) $In_{0.12}Ga_{0.88}As$ layer. Figure 4 shows TEM images in the growth plane and in the cross section for the indicated structure. It is evident from the image of the cross section that the height of the resulting islands is comparable with the thickness of the InGaAs layer, indicating essentially complete overgrowth of the QDs by the InGaAs layer. The newly formed QDs therefore reside in the narrow-gap InGaAs host. Moreover, a comparison of the TEM images in the growth plane for structures containing 3 ML of InAs with and without[4] a layer of InGaAs solid solution shows that the deposition of InGaAs increases the lateral dimensions of the QDs from ~15 nm to ~20 nm.

The indicated structure exhibits emission at a wavelength of 1.3 μm at room temperature (Fig. 5). We also note that when the effective thickness of the InAs layer increases as the result of an increase in d_{QD} and L and a simultaneous lowering of the In concentration in the solid solution, the total photoluminescence intensity is essentially unchanged (Fig. 2b). This approach can therefore be used to achieve emission at 1.3 μm and at the same time to avoid degradation of the optical properties of the structures.

We subsequently attempted to lower the total quantity of In in the active zone while maintaining long-wavelength emission at a wavelength of approximately 1.3 μm. To do so, we investigated the influence of the growth temperature during overgrowth of the QDs by an InGasAs layer on the optical properties of the structures. Figure 6 shows the photoluminescence spectra of samples with the InGaAs layer grown at temperatures of 485 °C and 455 °C, respectively. It is evident that lowering the growth temperature imparts a long-wavelength shift to the emission. This result can be attributed to the influence of temperature on the decay kinetics of the InGaAs layer and demonstrates the feasibility of achieving a further long-wavelength shift of the photoluminescence line with the right choice of temperature regimes.

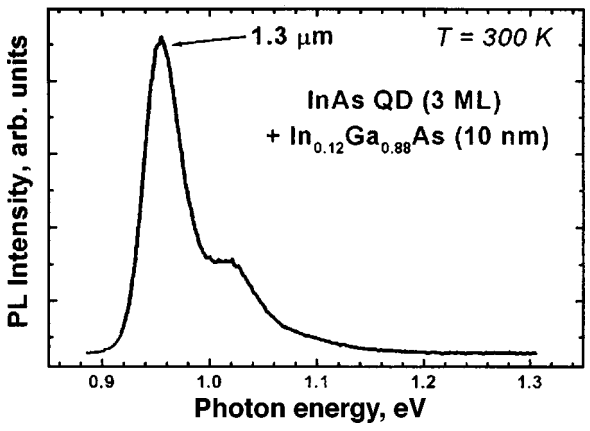

FIG. 5. Photoluminescence spectrum for a structure with InAs QDs ($d_{QD}=3$ ML) deposited in the middle of an $In_{0.12}Ga_{0.88}As$ layer.

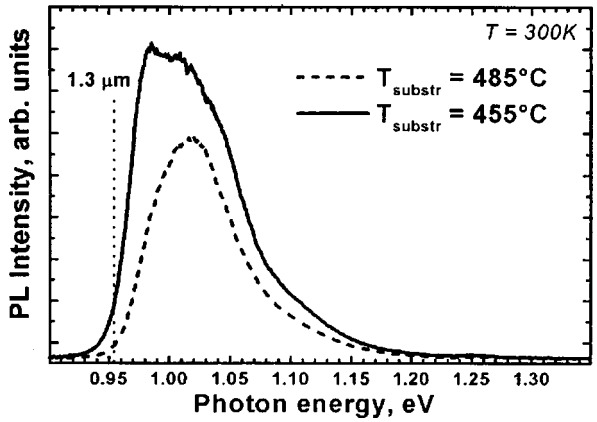

FIG. 6. Photoluminescence spectra for InAs QDs ($d_{QD}=2.2$ ML) overgrown by an $In_{0.12}Ga_{0.88}As$ layer at various temperatures. The overgrowth temperatures are indicated alongside the spectra.

In addition, we proposed to exploit a phenomenon that we had observed previously for spontaneously decomposing layers[1,14]: decomposition of an InGaAlAs/GaAs layer. We grew structures with InAs QDs overgrown by an InGaAlAs solid solution. The investigations show that the introduction of Al into the solid solution produces a significant long-wavelength shift of the QD emission line despite major broadening of the band gap of the host. This effect can be explained on the assumption that the introduction of Al significantly enhances the decomposition of the solid solution and increases the In concentration in the vicinity of the QDs. It should be noted that the total quantity of In in the active zone for this structure corresponds to 12.5 Å of InAs, which is far below the value of 16.5 Å given in Ref. 10, in which lasing at a wavelength of 1.3 μm is reported. We have thus succeeded in substantially lowering the total quantity of In in the active zone while achieving emission at a wavelength greater than 1.3 μm at room temperature.

CONCLUSIONS

The reported investigations have shown that the overgrowth of an array of InAs quantum dots by a thin film of (In, Ga, Al)As solid solution leads to decomposition of the solid solution and the formation of local zones near the QDs with an elevated concentration of In atoms. This phenomenon produces an effective increase in the size of the QDs and a significant long-wavelength shift of the photoluminescence emission line to 1.3 μm at room temperature. We have investigated the dependence of the optical properties of such structures on the growth conditions and have demonstrated the feasibility of achieving a long-wavelength shift of the emission without degradation of the optical properties of the structures. We have shown that the addition of small concentrations of Al to the solid solution can significantly reduce the total quantity of InAs in the active zone while maintaining an emission wavelength greater than 1.3 μm. This result demonstrates the possibility of constructing lasers utilizing InAs QDs on GaAs substrates and emitting at a wavelength of 1.3 μm.

This work has received support from the Russian Fund for Fundamental Research, the International Association for the Promotion of Cooperation with Scientists from the Independent States of the Former Soviet Union (INTAS) (Grants 96-0467 and 94-1028-YSF-41), the Ministry of Science Program ''Physics of Solid State Nanostructures,'' and the Volkswagen Foundation.

[1] N. N. Ledentsov, Prog. Cryst. Growth Charact. **35**, 289 (1997).
[2] L. Goldstein, F. Glas, J. Y. Marzin, M. N. Charasse, and G. Le Roux, Appl. Phys. Lett. **47**, 1099 (1985).
[3] P. M. Petroff and S. P. DenBaars, Superlattices Microstruct. **15**, 15 (1994).
[4] N. N. Ledentsov, M. Grundmann, N. Kirstaedter, O. Schmidt, R. Heitz, J. Böhrer, D. Bimberg, V. M. Ustinov, V. A. Shchukin, P. S. Kop'ev, Zh. I. Alferov, S. S. Ruvimov, A. O. Kosogov, P. Werner, U. Richter, U. Gösele, and J. Heydenreich, Solid-State Electron. **40**, 785 (1996).
[5] N. Kirstaedter, N. N. Ledentsov, M. Grundmann, D. Bimberg, V. M. Ustinov, S. S. Ruvimov, M. V. Maximov, P. S. Kop'ev, Zh. I. Alferov, U. Richter, P. Werner, U. Gösele, and J. Heydenreich, Electron. Lett. **30**, 1416 (1994).
[6] M. V. Maksimov, N. Yu. Gordeev, S. V. Zaĭtsev, P. S. Kop'ev, I. V. Kochnev, N. N. Ledentsov, A. V. Lunev, S. S. Rubimov, A. V. Sakharov, A. F. Tsatsul'nikov, Yu. M. Shernyakov, Zh. I. Alferov, and D. Bimberg, Fiz. Tekh. Poluprovodn. **31**, 162 (1997) [Semiconductors **31**, 124 (1997)].
[7] A. R. Kovsh, D. A. Livshits, A. E. Zhukov, A. Yu. Egorov, M. V. Maximov, V. M. Ustinov, N. N. Ledentsov, P. S. Kop'ev, Zh. I. Alferov, and D. Bimberg, in *Proceedings of the Seventh International Symposium on Nanostructures: Physics and Technology*, St. Petersburg, Russia, 1999 (in press).
[8] M. V. Maximov, A. F. Tsatsul'nikov, B. V. Volovik, D. A. Bedarev, A. Yu. Egorov, A. E. Zhukov, A. R. Kovsh, N. A. Bert, V. M. Ustinov, P. S. Kop'ev, Zh. I. Alferov, N. N. Ledentsov, D. Bimberg, I. P. Soshnikov, and P. Werner, in *Proceedings of the International Conference on Physics of Semiconductors (ICPS24)*, Jerusalem, 1998 (World Scientific, 1998).
[9] R. P. Mirin, J. P. Ibbetson, K. Nishi, A. C. Gossard, and J. E. Bowers, Appl. Phys. Lett. **67**, 3795 (1995).
[10] D. L. Huffaker, G. Park, Z. Zou, O. B. Shchekin, and D. G. Deppe, Appl. Phys. Lett. **73**, 2564 (1998).
[11] R. Heitz, M. Grundmann, N. N. Ledentsov, L. Eckey, M. Veit, D. Bimberg, V. M. Ustinov, A. Yu. Egorov, A. E. Zhukov, P. S. Kop'ev, and Zh. I. Alferov, Appl. Phys. Lett. **68**, 361 (1996).
[12] A. F. Tsatsul'nikov, A. Yu. Egorov, A. E. Zhukov, A. R. Kovsh, V. M. Ustinov, N. N. Ledentsov, M. V. Maksimov, A. V. Sakharov, A. A. Suvorova, P. S. Kop'ev, Zh. I. Alferov, and D. Bimberg, Fiz. Tekh. Poluprovodn. **31**, 109 (1997) [Semiconductors **31**, 88 (1997)].
[13] M. Sopanen, H. Lispanen, and J. Ahopelto, Appl. Phys. Lett. **66**, 2364 (1995).
[14] I. L. Krestnikov, A. V. Sakharov, N. N. Ledentsov, I. P. Soshnikov, Yu. G. Musikhin, A. R. Kovsh, V. M. Ustinov, I. V. Kochnev, P. S. Kop'ev, Zh. I. Alferov, and D. Bimberg, in *Proceedings of the Sixth International Symposium on Nanostructures: Physics and Technology*, St. Petersburg, Russia (1999), p. 257.

Translated by James S. Wood

AMORPHOUS, GLASSY AND POROUS SEMICONDUCTORS

Pulsed breakdown of chalcogenide glass semiconductor films in a magnetic field

É. N. Voronkov

Moscow Power Institute, 111250 Moscow, Russia
(Submitted November 23, 1998; accepted for publication February 2, 1999)
Fiz. Tekh. Poluprovodn. **33**, 996–1000 (August 1999)

The application of an external magnetic field during the breakdown of chalcogenide glass semiconductor films provides a means for space-time tracing of the evolution of the current channel and for the separation of electronic and thermal effects. The rapid movement of the current channel along the sample tends to cool it, substantially abating the influence of Joule heat and making it possible to increase the power. It is shown that breakdown is driven by a leader-streamer mechanism. © *1999 American Institute of Physics.* [S1063-7826(99)02308-X]

One of the most interesting phenomena accompanying electrical breakdown in chalcogenide glass semiconductors (CGSs) is the switching effect discovered and investigated by Kolomiets *et al.*,[1] Ovshinsky,[2] and Kostylev and Shkut[3] have proposed a number of applications of this effect in microelectronics, stimulating vigorous research on CGSs in the late 1970s and early 1980s, along with the development of models of the switching effect.[1–3] It should be noted, on the other hand, that the complex nature of the effect has yet to be fully revealed. We believe that the flagging interest in this phenomenon pursuant to the development of silicon memory microcircuits, which have superseded CGS memory elements, is unwarranted, because the switching effect is one of the most efficient techniques for generating an electron-hole plasma, and it is applicable for the development of various functional electronic devices and possibly light emitters utilizing films doped with rare-earth metals.

The objective of the present study is to investigate the breakdown dynamics of CGSs and to separate the contributions of electronic and thermal effects underlying the phenomenological model of the switching effect.[1–3] To achieve this goal, we apply an external magnetic field, which enables us to trace in both space and time the evolution of the current channel.

In a previous paper[4] we have shown that when a CGS film breaks down in a magnetic field, a curved track is formed by molten or crystallized material, reminiscent of a track in a Wilson cloud chamber. From the shape of this track we have estimated the hypothetical particle velocity, which was found to be extremely high, but we did not advance any assumptions as to the possible nature of the track. Consequently, part of the objective of the present study is to ascertain the nature of the ''track'' and to explain its shape.

In the investigation we have observed that the main stages of breakdown of CGS thin films in a magnetic field coincide with the main stages of the switching effect. This result has brought us to the conclusion that the switching effect and our investigated breakdown are based on identical processes.

The measurements were carried out on samples with planar and coplanar (''sandwich'') electrode configurations. The distance between the planar electrodes was $100-200\,\mu$m, and the length of the electrodes was 70 mm. The sandwich structures had an electrode area of $0.1-1.0\,\text{mm}^2$. The thickness of the CGS films was in the interval $1-3\,\mu$m. Measurements performed on different CGS compositions did not exhibit any fundamental differences. The results given below are for As_2SeTe_2 films.

The experimental arrangement is shown schematically in Fig. 1. A sample consisting of a glass substrate with a CGS film *1*) deposited on it and metal strip electrodes (*2*) was placed in a magnetic field (*3*). A pulsed voltage from an oscillator (*4*) was applied through a current-limiting resistor (*5*) between a pair of adjacent electrodes, one of which was grounded. In a few cases experiments were performed on samples with coaxial annular electrodes. Approximately the same results were obtained here as for the strip electrodes.

The amplitude of the rectangular pulse applied to the sample was varied in the interval 5–50 V for the sandwich

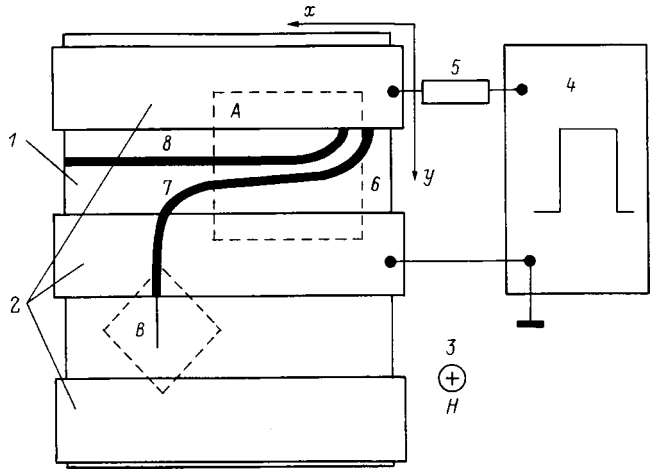

FIG. 1. Schematic diagram of the experimental arrangement: (*1–5*) explained in text; (*6–8*) alternative paths of the observed tracks.

structures and in the interval 100–800 V for the samples with planar electrodes. The pulse duration was 1–3 ms, with a leading edge of duration $0.1-1\ \mu$s. During the measurements the sample was placed in the gap of a magnet with an induction of 2 T.

Figure 2 shows typical oscillograms of the voltage on the sample (upper graph) and the current through it (lower graph) without (a) and with (b) a magnetic field. Several characteristic segments are discernible in the oscillograms: a lag time, during which the voltage drop across the sample and the current through it do not change; fast switching-on with a sudden jump in the current and a simultaneous drop in the sample resistance by several orders of magnitude (breakdown or switching on); the switched-on state. The part of the oscillogram corresponding to the switched-on state contains two segments exhibiting an additional (secondary) increase in the sample conductivity after a certain time, with a jump in the conductivity. In the switched-on state for compositions exhibiting a strong tendency to crystallize (e.g., $Ge_{15}Te_{84}As_4$) the first of these segments corresponds to the storage time, i.e., if the pulse terminates before the onset of the secondary jump, the resistance of the sample remains high; otherwise, it maintains a low resistance even after the voltage is removed.

The main stages of breakdown represented in Fig. 2 occur both for sandwich structures and for planar structures, even though the oscillograms can differ considerably for individual samples of the same kind. For example, the current in individual samples is observed to increase gradually in the intervals of the switched-off and switched-on states; moreover, there is often only one segment in the switched-on state.

A comparison of Figs. 2a and 2b shows that for the most part a magnetic field does not alter the form of the oscillogram (the storage time increases somewhat in the magnetic field), implying that the film breakdown mechanism in the presence of a magnetic field is the same as without it. This inference permits us to generalize the conclusions for breakdown in a magnetic field to the zero-field case.

Electrical breakdown in a magnetic field results in the formation of a track channel, which is observable by virtue of burnout, melting, or crystallization of the material (depending on the pulse power). In zero field the track is linear (track *6* in Fig. 1), whereas in a magnetic field it curves (*7*) and does not always join up with the electrodes (*8*). This result indicates that in a magnetic field the track does not conform to the configuration of the current channel. The current channel remains linear, but it moves between the electrodes along the film. Its rate of displacement is proportional to the current in the channel and could exceed 10^4 cm/s in our experiments. The movement of the filament can be judged from the erosion of the electrodes in the regions through which it passes. Rapid movement of the current channel along the film helps to cool it and eliminates the possibility of thermal breakdown. An analysis of many photographs has shown that a track which persists after breakdown is formed by a hot spot moving from the anode toward the cathode.

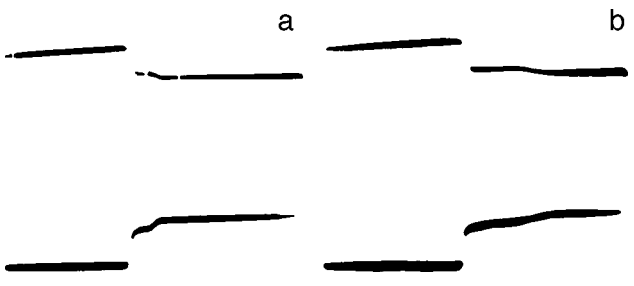

FIG. 2. Oscillograms of the voltage (upper graph) and current (lower graph) without (a) and with (b) a magnetic field.

Figure 3a shows a photograph of the initial segment of one of the tracks formed in a film after breakdown in a magnetic field (see track *8* in Fig. 1). It is evident from Fig. 3a that a hot spot (flare-up) gradually evolves and, at the same time, moves toward the cathode (at an average rate of the order of 100 cm/s) while concurrently moving together with the current filament along the substrate. The velocity of the filament (velocity of the hot spot along the x axis) can be several times the velocity of the spot within the filament (in the y direction.

When the hot spot actually attains the cathode, the electrode burns up and, what is particularly intriguing, a track in the form of a crystallized filament propagates into a zone where the electric field is zero (zone *B* in Fig. 1). A relevant photograph, showing the directional propagation of the excitation over a great distance after the grounded electrode, is given in Fig. 3b. Most likely the energy in this zone is transported by an acoustic oscillatory process involving oscillations of a coherent nature, as confirmed by the absence of divergence in the track.

The observed phenomena are nicely explained on the basis of the leader-streamer mechanism.[5] In this case the lag time (Fig. 2) corresponds to the rise time of the space charge of the tip of the streamer. It is important to understand that this time ranges from a few microseconds to several milliseconds, depending on the pulse amplitude, and the transit time of the streamer between the contacts does not exceed 100 nm, whereas for the leader it can vary from a few microseconds to several milliseconds. The density of free carriers in the channel left in the wake of the leader is close to $10^{18}\,\mathrm{cm}^{-3}$, which is approximately the same as the uncompensated charge density at the tip of the leader.

The newly formed streamer fills up the electron-hole plasma channel almost instantaneously (switching-on time in Fig. 2), whereupon the hot tip of the leader (hot spot) begins to form, and the tip begins to move slowly from the anode toward the cathode. The electrons and holes generated in the vicinity of the leader tip are transported into the channel, making it highly conducting. The flare-up of the spot at the anode corresponds to the formation of the leader tip, which consists of a charge double layer. It should be mentioned that the onset of the ''hot spot'' associated with the tip of the leader is accompanied by radiation in the near infrared range, which has previously[6] been interpreted as a recombination process in the switching effect.

The channel is heated by the movement of the hot spot associated with the leader tip. This effect is confirmed by the

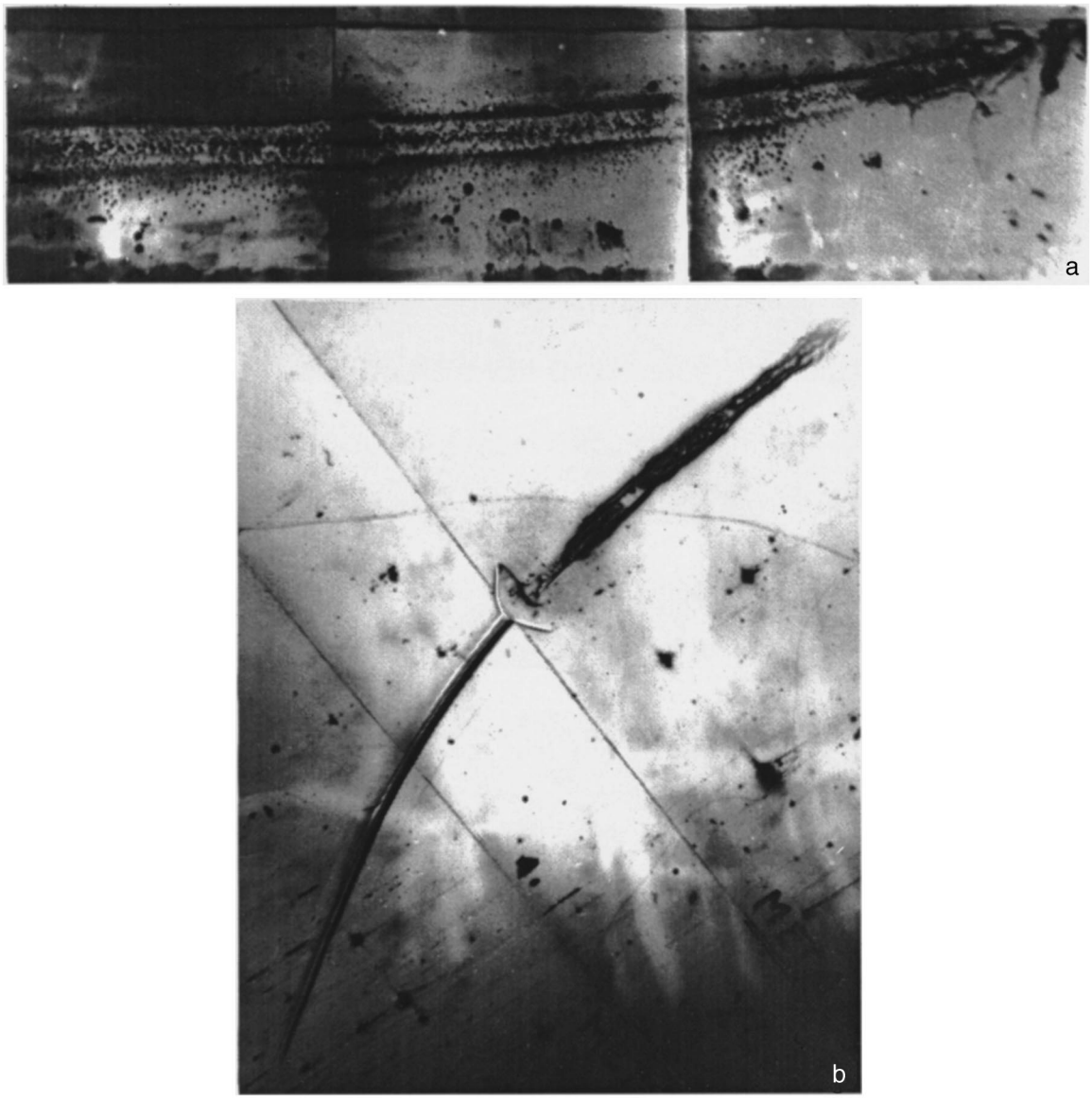

FIG. 3. Photographs of the initial (a) and final (b) parts of a track after breakdown in a magnetic field.

fact that melting, crystallization, and burnout take place only in the region of the channel through which the tip of the leader passes (Fig. 3a). As the tip approaches the cathode, the space-charge region vanishes. In this case the plasma-filled, conducting wake of the leader closes the contacts, which corresponds to a small current jump in the switched-on state. Since the track of the leader in memory switches is filled with highly conducting crystallizing material, the low interelectrode resistance is preserved after termination of the electrical pulse.

Since the current does not change or changes only very slightly after streamer breakdown (Fig. 2), we can assume that the velocity of the channel is approximately constant, and the observed features of the track are associated with variations of the leader velocity. The velocity is then a maximum in the stages of formation and decay of the leader tip in the direction toward the cathode. The velocity is approximately constant in the remaining time interval.

Figure 4 shows individual parts of the sample for the cases in which the movement of the leader tip leads to burnout, as witnessed by the strip in the middle of the sample (a), and to melting of the CGS (b). These photographs show that despite the invariance of the average velocity of the leader, its tip pulsates, flaring up and dying out, i.e., ostensibly moves in spurts, as is especially visible in Fig. 4b. It is possible that the onset of a soliton-type acoustic excitation (Fig. 3b) with a wavelength of the order of 10^{-3} cm is specifically associated with the energy pulsation distinguished in the leader tip.

In conclusion, looking once again at the switching effect, in our opinion, it is based on the leader streamer mechanism, which accounts quite well for all the known properties of this effect. Discrepancies can be attributed to the fact that in the switching effect, as a rule, the short-channel condition holds, and the space-charge region can fill up the entire interelectrode space.

The sum-total of these considerations is indicative of the potential practicality of the switching effect in applications

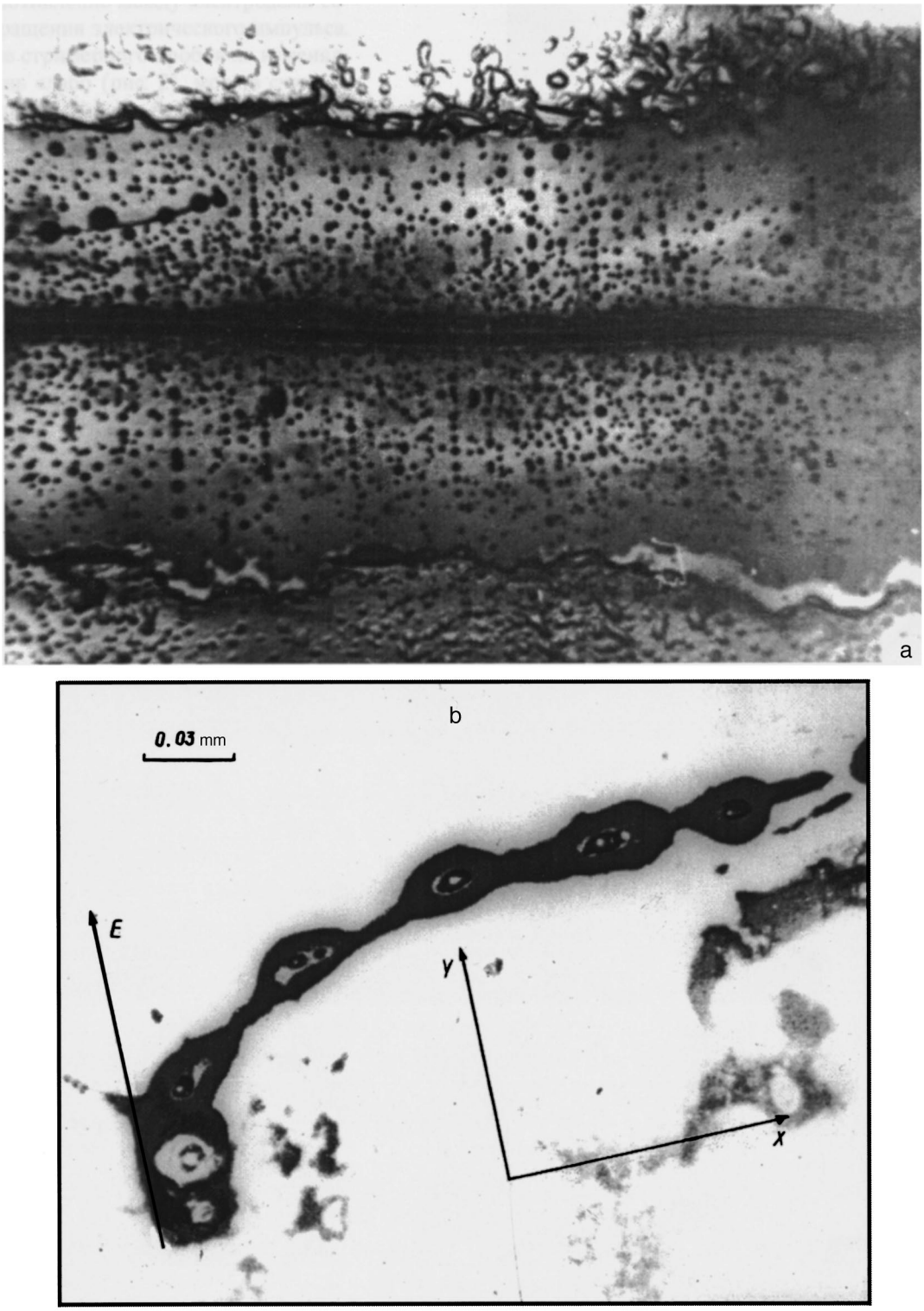

FIG. 4. Photographs of parts of the samples exhibiting intermittent motion of the leader tip when the track is formed by burnout (a) and melting (b) of the material.

for the construction of high-power solid-state plasma generators. If short pulses are used, it is theoretically feasible to eliminate the filamentation stage,[7] thereby affording the possibility of building solid-state analogs of gas-discharge devices with good potential applications in the development of miniature pulse radiators.

[1] B. T. Kolomiets and É. A. Lebedev, Radiotekh. Élektron. **8**, 2097 (1963); B. T. Kolomiets, É. A. Lebedev, I. A. Taksami, and K. D. Tséndin, Fiz. Tekh. Poluprovodn. **17**, 119 (1983) [Sov. Phys. Semicond. **17**, 75 (1983)].

[2] S. R. Ovshinsky, U.S. Patent, Cl. 307-885, No. 3281591 (1963); D. Adler, M. S. Shur, M. N. Silver, and S. R. Ovshinsky, J. Appl. Phys. **51**, 3289 (1980).

[3] S. A. Kostylev and V. A. Shkut, *Electronic Switching in Amorphous Semiconductors* [in Russian], Naukova Dumka, Kiev (1978).
[4] G. I. Borovov and É. N. Voronkov, Fiz. Tekh. Poluprovodn. **10**, 750 (1976) [Sov. Phys. Semicond. **10**, 445 (1976)].
[5] V. Ya. Ushakov, *Pulsed Electrical Breakdown of Liquids* [in Russian], Izd. Tomsk. Univ., Tomsk (1966).
[6] M. J. Thompson, D. Pooladej, and P. J. Walsh, J. Non-Cryst. Solids **35/36**, 1111 (1980).
[7] A. M. Minarsky and P. B. Rodin, Solid-State Electron. **41**, 813 (1997).

Translated by James S. Wood

Multiple bonds in hydrogen-free amorphous silicon

A. I. Mashin*) and A. F. Khokhlov

N. I. Lobachevskiĭ State University, 603600 Nizhny Novgorod, Russia
(Submitted November 13, 1998; accepted for publication March 3, 1999)
Fiz. Tekh. Poluprovodn. **33**, 1001–1004 (August 1999)

The short-range-order structure and electron paramagnetic resonance of amorphous silicon prepared by vacuum sublimation and by ion implantation are investigated. It is found that amorphous silicon with atoms in the sp^2 hybrid state is formed in the annealing of evaporated silicon at 500 °C or in the irradiation of a silicon single crystal with neon at a dose greater than or of the order of $10^{17}\,\mathrm{cm}^{-2}$. In the latter case the amorphous material is depthwise inhomogeneous and contains a layered structure consisting of silicon atoms with a period of 5.16 Å. In each case an ESR signal with a g factor $g \simeq 2.0048$, which corresponds to a dangling bond of a silicon atom in the sp^2 state, is observed. © *1999 American Institute of Physics.* [S1063-7826(99)02408-4]

INTRODUCTION

In studying the influence of annealing on the short-range-order structure and properties of amorphous silicon prepared by the decomposition of silane in an rf glow discharge, we have synthesized silicon with a nontetrahedral short-range-order structure. The new material, called silicyne,[1,2] is amorphous. According to electron-diffraction studies and ultrasoft x-ray spectroscopy data, it has a low coordination number (approximately 2), a large valence angle (almost 180°), and a shorter average interatomic distance (2.1 Å) in comparison with crystalline silicon. In our opinion, it is the silicon analog of carbyne and consists mainly of linear chains of silicon atoms with multiple bonds of the type $(-\mathrm{Si}\equiv\mathrm{Si}-\mathrm{Si}\equiv\mathrm{Si})_n$ and $(=\mathrm{Si}=\mathrm{Si}=\mathrm{Si}=\mathrm{Si}=)_n$. The atomic chains, in turn, are bonded together by van der Waals forces or bridges of ordinary covalent bonds. In the formation of silicyne a major role is played by hydrogen, whose concentration in the as-prepared silicon films has attained 12–40 at. %.

The objective of the present study is to investigate the influence of annealing on the structural transformations and properties of hydrogen-free amorphous silicon (a-Si).

EXPERIMENTAL PROCEDURE

The initial amorphous films were prepared mainly by the vacuum sublimation of silicon[3] and by the irradiation of crystalline silicon with inert gas ions.

For the structural measurements silicon films of thickness 70–80 nm were deposited on a freshly cleaved chip of a NaCl crystal. The deposition rate did not exceed 0.3 nm/s. The temperature of the substrate was 250 °C. The resulting amorphous silicon had an almost-tetrahedral structure.

Crystalline silicon, mark BKD-1000, was irradiated with neon ions of energy up to 80 keV at doses ranging from 6×10^{14} ions/cm^2 to 2×10^{17} ions/cm^2 at room temperature. In every case the ion current density did not exceed $10\,\mu$A/cm^2.

Transmission electron diffraction patterns from the evaporated films were recorded by means of an ÉMR-102 recording electron diffraction camera. Conversion from electron scattering intensity to the radial distribution function of the electron density was achieved by the conventional Fourier transform technique[4] and by optimization of the information functional.[5] The short-range order parameter was calculated from the areas and positions of the radial distribution function by a procedure similar to that in Ref. 6. In the case of films prepared by ion implantation the electron diffraction patterns were recorded in reflection by means of an ÉG-100M electron diffraction camera. The structure was checked after each successive etching of silicon layers having a thickness of the order of 120 Å.

The first derivatives of the electron spin resonance absorption line were recorded on a three-centimeter homodyne spectrometer. The magnetic scan was calibrated by recording the third and fourth lines of the Mn^{++} spectrum in MgO powder, which are separated from each other by 85.5 G. The g factor of the paramagnetic centers was measured relative to the resonance absorption of a KCl standard with $g=2.0028$. The density, linewidth, and g factor of the paramagnetic centers in relative measurements were determined within error limits of 8%, 0.1 G, and 0.0002, respectively.

RESULTS AND DISCUSSION

Figure 1 shows how the electron scattering intensity varies in films prepared by the vacuum sublimation of silicon as the anneal temperature is varied. It is evident that recrystallization does not begin until the anneal temperature attains 700 °C. At lower temperatures the films remain amorphous, but structural transformation takes place. This process can be visualized more intuitively from Table I, which shows the results of calculations of the short-range-order structure of the films. As in the case of a-Si:H (Ref. 1), a significant change in the short-range-order structure of the still amorphous material is observed at an anneal temperature $T_a = 500$ °C. At this temperature the first coordination number

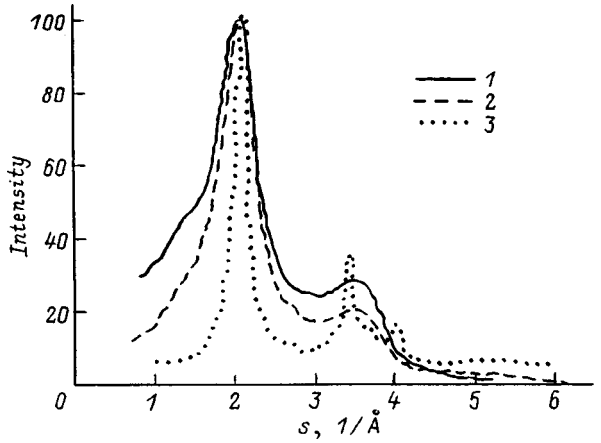

FIG. 1. Angular dependence of the electron scattering intensity for *a*-Si annealed at: (*1*) room temperature; (*2*) 500 °C; (*2*) 700 °C.

k_1 decreases from 3.8 ± 0.2 to 2.8 ± 0.2, and the interatomic distance r_1 decreases to 2.15 ± 0.04 Å. The valence angle, however, undergoes a notably smaller change than in *a*-Si:H films: $\varphi=(132\pm6)°$. Even though the variations of all the short-range order parameters are less pronounced than for hydrogenated silicon, they cannot be written off as experimental error. Measurements of the structure of evaporated, hydrogen-free, amorphous silicon films prepared by electron-beam evaporation and ion-plasma sputtering reveal the absence of any appreciable variations of the parameters of the first coordination sphere in annealing up to the partial recrystallization temperature.

As in Ref. 1, these data on the variation of the short-range-order structure of *a*-Si can be attributed to the formation of silicon multiple bonds during annealing. However, the structure of the molecules will necessarily differ. We have calculated possible stable nontetrahedral silicon structures by the nonempirical restricted Hartree-Fock method in basis 6-311$G(d)$ [RHF/6-311$G(d)$] with the correlation energy taken into account by second-order Møller-Plesset perturbation theory [MP2/6-311$G(d)$]. The geometry was optimized by the gradient method. The stationary points of the surface potential energy were characterized by calculating the vibrational frequencies. We have confined the present study to clusters of atoms existing only in the singlet spin state. All the calculations have been carried out by means of PC Games-4.5.1 software.[7] We used silicon chain structures as the basic cluster models. The chain length was varied from 2 to 12 silicon atoms. Our calculations have shown that, in addition to a tetrahedral structure, silicon can form stable chained cluster structures. The stationary point determined by us is a local minimum in the case of full optimization. The resulting data are further corroborated by the vibrational frequency calculations. The silicon atoms in such structures are situated in one plane, but not in one straight line. The distance between these local and global — corresponding to a tetrahedral configuration of atoms — energy minima of different forms of clusters is of the order of 20 kcal/atom. The optimized angles between silicon atoms are varied in the range from 115° to 127°.

TABLE I. Short-range-order parameters of amorphous silicon prepared by vacuum sublimation before and after annealing at temperature T_a.

T_a, °C	k_1	r_1, Å	φ, deg
No anneal	3.8	2.33	111
450	3.6	2.31	115
500	2.8	2.15	136
600	2.8	2.18	132

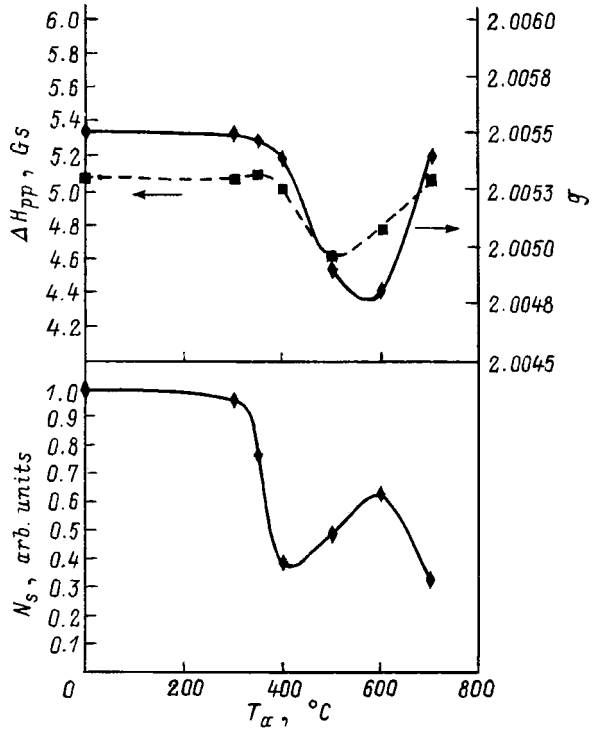

FIG. 2. Influence of annealing on the density of paramagnetic centers N_s, the g factor, and the linewidth ΔH_{pp} of amorphous silicon evaporated by vacuum sublimation.

It is also interesting to note that each silicon atom in these clusters has a double bond, but the total order of the bonds per silicon atom is only three. We can therefore assume that each silicon atom in a real amorphous silicon film can utilize its free valence to form a bond with another chain and thus promote the formation of a three-dimensional disordered network. The silicon atoms in this case exist in an sp^2 hybrid state and have ordinary and double bonds with lengths of 2.29 Å and 2.11 Å, respectively. We see that the calculated bond lengths and valence angles are in good agreement with the results of the structural measurements. It is entirely admissible that some of the silicon atoms can be left with a single unused bond. But then the corresponding material will have to have a high density of unpaired spins.

Figure 2 shows the results of ESR measurements of *a*-Si films prepared by the vacuum sublimation of silicon. The as-prepared *a*-Si films had a density of unpaired spins $N_s=7.5\times10^{18}\,\mathrm{cm}^{-3}$. The measured ESR line with a g factor of 2.0055 corresponds to a dangling bond in tetrahedral amorphous silicon. The density of paramagnetic centers decreases as anneal temperature is raised. However, in the range of anneal temperatures $500-600$ °C an increase in N_s, which

is accompanied by a decrease in the g factor and the linewidth ΔH_{pp}, is observed. It is reasonable to assume that at these temperatures the observed reverse anneal stage is associated with structural transformation of the amorphous semiconductor and the generation of paramagnetic centers. Since the paramagnetic resonance line has a different g factor and a different linewidth, we are encountering a new paramagnetic center. In our opinion, the role of this new center can be identified exclusively with the same dangling bond of the silicon atom, but now existing in an sp^2 hybrid state. The influence of the short-range-order parameters on the g factor of defects in amorphous semiconductors has been reported in a theoretical study.[8] Similar experimental data had been obtained in earlier work.[9–11] In contrast with our work, in Ref. 9 the increase in N_s at temperatures $T_a = 500 - 600\,^\circ$C was not accompanied by a variation of the g factor or the linewidth ΔH_{pp}. It is entirely conceivable that the authors of Ref. 9 were unable to observe the variations of these parameters of the ESR line on account of a relatively large error of their experiments. In particular, the authors themselves remarked that the error of determination of the g factor attained values of 0.0005.

The reverse annealing effect has been observed[10,11] in a-Si prepared by ion implantation. In this case both an increase in N_s and a decrease in the g factor was noted, along with an increase in the linewidth. The authors of Ref. 10 assumed that centers with a g factor of 2.0046, which they called $C8$ centers, exist in addition to paramagnetic centers with a g factor of 2.0055 (VV centers) in silicon irradiated with gaseous impurities. They postulated that the $C8$ centers are situated on the inner surface of inert gas bubbles, which can be formed both during implantation and during annealing of the implanted silicon. The breakup of the bubbles at high anneal temperatures is responsible for the onset of the reverse annealing effect. Finally, in Ref. 11 we have advanced the hypothesis that the increase in N_s in reverse annealing is not associated with the generation of VV centers, but with the breakdown of magnetic ordering in amorphous silicon as the density of paramagnetic centers decreases on the whole. As in Ref. 10, the postanneal properties and behavior of this kind of silicon are significantly influenced by the high concentration of injected gas. Thus, the authors of Refs. 10 and 11 concur as to the important role of the inert gas in the formation of amorphous silicon by ion implantation, but they submit different explanations for the behavior of such a material during annealing. In the present study we have taken yet another look at this problem and, to gain more insight into the processes involved in the implantation of inert gas ions in silicon, we have investigated the structure of amorphous silicon prepared in this way.

It is generally known that silicon layers obtained with irradiation doses not too far above the amorphization level are amorphized over their entire depth. At ultrahigh implantation doses greater than or of the order of $10^{17}\,\mathrm{cm}^{-2}$ the amorphous layer becomes depthwise inhomogeneous, and traces of crystallinity appear in the interior of the irradiated layer (see Fig. 3). The given electron diffraction pattern was

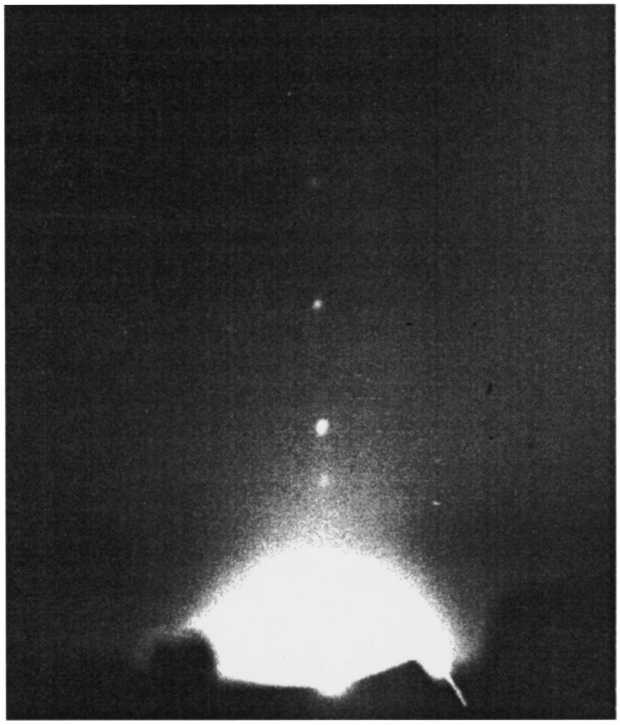

FIG. 3. Electron diffraction pattern in reflection after etch-peeling of 200 Å from the surface of silicon irradiated with Ne^+ ions at a dose of $2 \times 10^{17}\,\mathrm{cm}^{-2}$ and an ion energy of 40 keV.

recorded from the surface of a sample after a layer of thickness of the order of 200 Å had been peeled from it. According to data in Ref. 10, this is precisely the depth at which $C8$ centers are found, whereas according to our data,[11] there is a layer with ferromagnetic spin ordering. The character of the point reflections occurring periodically along one line suggests that the observed diffraction originates from planes situated parallel to one another with a period of 5.16 Å. We see that the period differs from the lattice constant of crystalline Si ($a = 5.43$ Å). In-plane ordering does not exist. In Ref. 11 we have postulated that layered compounds of the Si_xNe_y type are formed. They are planar structures similar to graphite intercalates, in which inert gas atoms fill the voids between silicon planes. The silicon atoms no longer have four, but three silicon neighbors, and the type of hybridization of the valence electrons changes from sp^3 to sp^2. Van der Waals forces act between planes consisting of neon and silicon atoms. Some of the silicon atoms, however, have unused bonds. According to ESR data, such a layered structure has paramagnetic centers whose concentration attains a value of the order of $10^{21}\,\mathrm{cm}^{-3}$. The measurements have been carried out at room temperature. The ESR line has a g factor equal to 2.0047 and a linewidth $\Delta H_{pp} = 14$ G. Our ESR data are in good agreement with the parameters of the $C8$-center,[10] but structural measurements indicate that this paramagnetic center is more consistent with a dangling bond of a silicon atom existing in an sp^2 hybrid state. This conclusion is further supported by our experiments on the annealing of evaporated amorphous silicon films. Such material does not

contain inert gas atoms, and the good agreement (within the measurement error limits) of the g factors of the ESR lines leads to the assumption that both cases involve the same paramagnetic center. The appreciable difference in the linewidths of the ESR signals is associated with exchange broadening of the line at a high density of these centers in the implanted silicon.

CONCLUSIONS

In summary, when hydrogen-free amorphous silicon is annealed at temperatures of $500-600\,^{\circ}\mathrm{C}$, a structural transformation is observed, creating a disordered network of silicon atoms in the sp^2 hybrid state. This situation corresponds to a high density of dangling bonds and plasticity of amorphous silicon at such temperatures.[12] A structure consisting of alternating layers of silicon and neon atoms arises in amorphous silicon prepared by the implantation of an ultrahigh dose of inert gas ions. The atoms in the silicon planes are randomly distributed, but exhibit sp^2 hybridization of the valence electrons.

We wish to thank V. V. Karzanov and A. G. Razuvaev for assisting with the EPR measurements and quantum-chemical calculations.

*)E-mail: mashin@phys.unn.runnet.ru

[1] A. F. Khokhlov, A. I. Mashin, and D. A. Khokhlov, JETP Lett. **67**, 646 (1998).
[2] P. F. Schewe and B. Stein, AIP Bull. Phys. News, No. 388 (Story #3) (September, 1998).
[3] D. A. Pavlov, V. G. Shungurov, D. V. Shengurov, and A. F. Khokhlov, Fiz. Tekh. Poluprovodn. **29**, 286 (1995) [Semiconductors **29**, 142 (1995)].
[4] L. I. Tatarinova, *Electron Diffraction Analysis of Amorphous Substances* [in Russian], Nauka, Moscow (1972).
[5] S. I. Ovsetsin, D. A. Khokhlov, E. A. Soldatov, and A. I. Mashin, in *Proceedings of the All-Russian Conference ''Sixteenth N. V. Belov Scientific Lectures,'' December 15–16, 1997* [in Russian], Nizhny Novgorod (1997), p. 105.
[6] V. N. Gordeev, A. I. Popov, and V. A. Filikov, Izv. Akad. Nauk SSSR, Neorg. Mater. **16**, 1773 (1980).
[7] M. W. Schmidt, K. K. Baldridge, J. A. Boatz, S. T. Elbert, M. S. Gordon, J. J. Jensen, S. Koseki, N. Matsunaga, K. A. Nguyen, S. Su, T. L. Windus, M. Dupuis, and J. A. Montgomery, J. Comput. Chem. **14**, 1347 (1993).
[8] N. Ishii, M. Kumeda, and T. Shimizu, Jpn. J. Appl. Phys. **20**, L673 (1981).
[9] A. V. Dvurechensky and I. A. Ryazantsev, Radiat. Eff. **46**, 129 (1980).
[10] A. F. Khokhlov and A. I. Mashin, in *Proceedings of the All-Union Conference on Radiation Defects in Solids* [in Russian], Ashkhabad (1977), p. 154.
[11] A. F. Khokhlov, A. A. Ezhevskiĭ, A. I. Mashin, and D. A. Khokhlov, Dokl. Akad. Nauk **339**, 370 (1994).
[12] J. E. Mayer, L. Eriksson, and J. A. Davies, *Ion Implantation in Semiconductors: Silicon and Germanium*, Academic Press, New York (1970).

Translated by James S. Wood

Current-voltage characteristics of Si:As blocked impurity band photodetectors with hopping conductivity (BIB-II)

D. G. Esaev,*) S. P. Sinitsa, and E. V. Chernyavskiĭ

Institute of Semiconductor Physics, Siberian Branch of the Russian Academy of Sciences, 630090 Novosibirsk, Russia

(Submitted February 8, 1999; accepted for publication February 18, 1999)
Fiz. Tekh. Poluprovodn. **33**, 1005–1009 (August 1999)

The current-voltage characteristics of Si:As blocked impurity band (BIB) structures are investigated. The behavior of the dark current in the temperature range 4.2–25 K and in the range of bias voltages −3 to +3 V is analyzed. It is shown that the main features of the $I-V$ characteristics are governed by the thermal-field injection of charge carriers from the contacts to the BIB structure. The details of the $I-V$ characteristics for bias voltages of both polarities are attributed to generation-recombination processes between the conduction band and the impurity band of the N^+ photoconductive layer. It is established that the blocking layer can accumulate charge of both signs, influencing the formation of the dark $I-V$ characteristics. © *1999 American Institute of Physics.* [S1063-7826(99)02508-9]

INTRODUCTION

The behavior of the dark current in a blocked impurity band (BIB) structure is discussed in Refs. 1–3. However, the experimental data given in these papers are inadequate for drawing straightforward conclusions as to the prevalent mechanisms underlying the evolution of the dark conductivity. To bridge this gap, we have performed systematic dark-current measurements in Si:As BIB structures.[4]

The resulting experimental data show that the principal features of the current-voltage ($I-V$) characteristics are governed by contact injection, as postulated in an earlier paper.[1] However, while the injection model discussed in that paper gives a correct determination of the threshold voltage for injection from the contact, it fails to predict either the field dependence or the temperature dependence of the current. The condition stated in Ref. 1, that the electric field is zero at the injection contact, leads to an infinite density of injected electrons, which is not a physically tenable result. Consequently, the mechanisms of contact injection in a BIB structure remains an open question.

We have established the existence of characteristic kinks in the $I-V$ characteristics of the structures and have postulated that generation-recombination processes between the principal band (the conduction band in our case) and the impurity band play a principal role in their formation. The role of these processes has been noted previously for structures of the $N^{++}-N^{+}-N^{++}$ type.[5] In BIB structures these processes act in conjunction with hopping conduction through the impurity band to produce the particular features of the $I-V$ characteristics for both polarities of the bias voltage.

Finally, under certain conditions both a negative charge and a positive charge can accumulate in the blocking layer of a BIB structure, where hopping conduction is stopped as a result of the low concentration of the principal dopant (arsenic in our case). These processes also influence the behavior of the $I-V$ characteristics and are discussed below.

1. POTENTIAL BARRIERS IN THE BIB STRUCTURE

It has been shown[4] that for both polarities the current is mainly an exponential function of the bias voltage, where for negative biases this dependence begins to appear in fields $E<10^2$ V/cm. It leads to the assumption that the current in the BIB structure is governed by contact injection. For this reason the nature of the potential barriers at the contacts and their dependence on the bias voltage and temperature are decisive in regard to the subject of carrier injection.

We now consider the contact zones in greater detail. Figure 1 shows diagrams of the characteristics of the contacts to the N^+ and I layers of a Si:As BIB structure. The contacts are formed by diffusion phosphorous doping of the surface of the I layer and by means of an epitaxial ''blockaded'' contact of the Si:As N^{++} layer to the N^+ photoconductive layer (see Fig. 1 in Ref. 4). The impurity concentration in these contacts is greater than the required concentration for the Mott transition.[6] Such contacts are customarily referred to as ohmic contacts, because at temperatures above the transition temperature to hopping conduction, T_h, they render the current linear with respect to the field as electrons move through the principal conduction band. The contacts convert to the injection type as the temperature is lowered, producing superlinear characteristics; this phenomenon has been established previously for $P^{++}-I-N^{++}$ diodes.[7]

An analysis of the temperature and field dependences of the current has shown[7] that the principal mechanism by which electrons pass through the barrier in the $N^{++}-I$ contacts in the temperature interval 10−25 K is the Richardson emission of electrons from the N^{++} contact in the I layer through the barrier, which is lowered by the applied voltage.

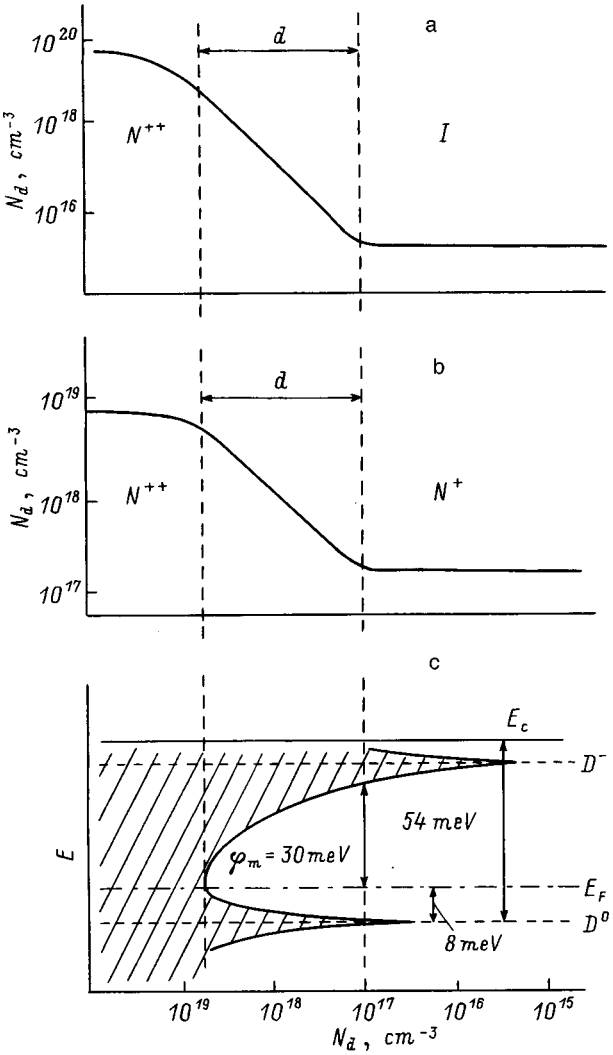

FIG. 1. Distribution of the dopant concentration: (a) in a diffusion contact to the blocking layer; (b) in an epitaxial ''blockaded'' contact to the photoconductive layer; (c) diagram of the formation of the potential barrier for injected electrons in the $N^{++}-I$ and $N^{++}-N^{+}$ contacts. Here D^0 is the electron level at an isolated neutral As atom in Si, D^- is the electron level at an isolated, negatively biased As atom in Si; d is the thickness of the region of variable concentration, which is bounded on the left by the concentration for the Mott transition.

2. CURRENT-VOLTAGE CHARACTERISTIC FOR A NEGATIVE NEGATIVE BIAS

To investigate the $I-V$ characteristics, in addition to the BIB structures we prepared ''resistor'' $N^{++}-N^{+}-N^{++}$ structures from the BIB type by etching the blocking I layer and fabricating a diffusion N^{++} layer to the N^{+} layer under the same conditions as to the I layer of the BIB structure. Figures 2 and 3 show $I-V$ characteristics and temperature curves of the current I for the $N^{++}-N^{+}-N^{++}$ structure. Clearly, the $I-V$ characteristics are symmetric and up to a voltage $V=1$ V are almost exponential:

$$I \propto \exp(-\varepsilon_a/kT)\exp(qlE/kT),$$

where $E=V/l$, V is the bias voltage, l is the thickness of the N^{+} layer, and q is the electron charge. The temperature dependence of the current indicates that at temperatures above $T_h=18$ K the conduction of band electrons excited from the

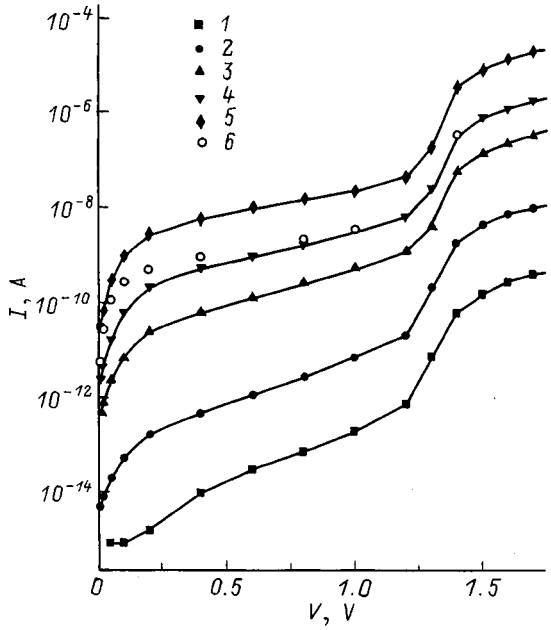

FIG. 2. The current-voltage characteristics of an $N^{++}-N^{+}-N^{++}$ structure. The area is $S=340\times500\ \mu$m^2. (*1–5*) Forward branches; (*6*) reverse branch. Temperature: (*1*) $T=4.2$ K; (*2*) 5.7 K; (*3*) 8 K; (*4, 6*) 9.6 K; (*5*) 13 K.

impurity level is predominant. At $T<T_h$ hopping conductivity prevails because of holes ejected into the peak of the density of states of neutral donors. The activation energy is $\varepsilon_a=8.3$ meV, which is close to its theoretical value $\varepsilon_3=0.99q^2N_d^{1/3}/\chi=8$ meV (χ is the dielectric permittivity of silicon). The hopping distance determined from the $I-V$ curve is close to $L_h\cong200$ Å, which corresponds to the average distance between donors in the density-of-states peak.

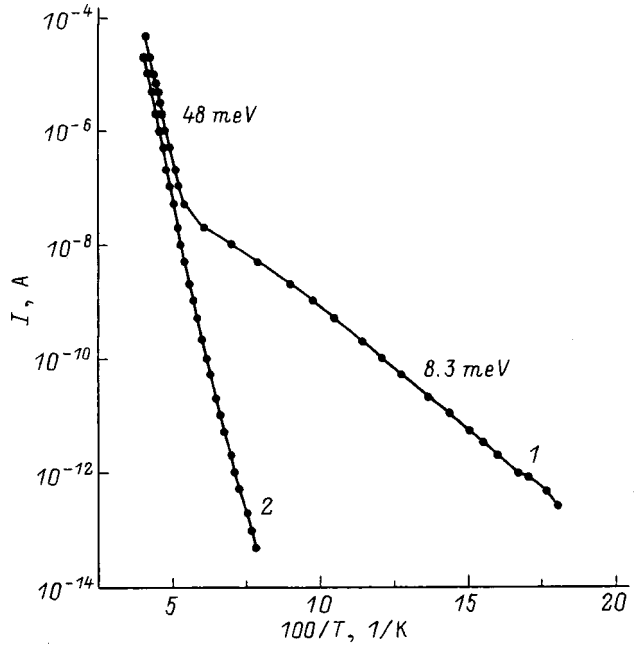

FIG. 3. Current versus temperature in: (*2*) a BIB structure; (*1*) an $N^{++}-N^{+}-N^{++}$ structure made from it. Area $S=340\times500\ \mu$m^2; bias voltage 0.4 V.

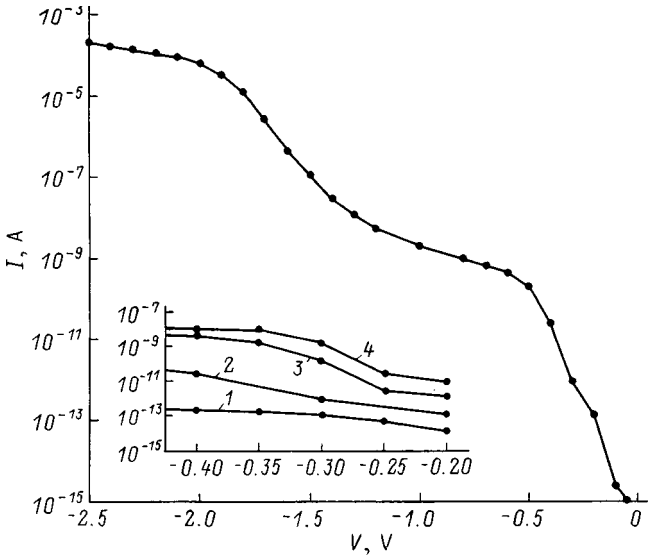

FIG. 4. Current-voltage characteristic of a negatively biased BIB structure at a temperature $T=9$ K. Area $S=650\times650\ \mu\text{m}^2$. Inset: $I-V$ characteristics in the low-voltage range at: (*1*) $T=5.6$ K; (*2*) 9 K; (*3*) 13 K; (*4*) 14.7 K. The coordinate axes are the same as in the main figure.

In a negatively biased BIB structure holes flow through the impurity band of the N^+ layer to the interface with the I layer, and the entire bias voltage is across the blocking layer. When a current appears in the structure after an increase in the voltage, it can only be associated with electrons injected through the barrier (Fig. 1c) into the conduction band, because an impurity band does not exist in the I layer.

Figure 4 shows the $I-V$ characteristic of a BIB structure for $V<0$. In the initial interval the current depends exponentially on the voltage and the temperature, and can be described by the relation

$$I(V,T)=I_0\ \exp[-(\varphi_m-qVd/W)/kT],$$

where $\varphi_m=30$ meV, $W=5\ \mu$m, and $d=8\times10^{-6}$ cm. Here φ_m is the height of the contact barrier, W is the thickness of the I layer, d is the thickness of the transition contact zone between the I layer and the N^{++} layer. These results are consistent with those of Ref. 7 and deviate from the conclusions of Ref. 5 as to the tunneling character of the injection current in an $N^{++}-N$ contact (Si:As) at a temperature of 10 K.

As the injected electrons reach the interface of the I and N^+ layers, they enter the region of As^+ ions. The As^+ electron capture cross section in silicon, determined from the recombination coefficient $B=2.2\times10^{-6}\ \text{cm}^3\cdot\text{s}^{-1}$ at $T=5.5$ K and $E=100$ V/cm, is $\sigma=10^{-11}\ \text{cm}^2$ (Ref. 8). For this value of σ and the surface concentration of As^+ at the level $N_{\text{As}}^+=10^8\ \text{cm}^{-2}$ (at $V=0.1$ V and $W=5\ \mu$m) a large fraction of the electrons passes through the charged layer without being captured. The fraction of the electron current transformed by capture at this interface into hole current through the impurity band is only $10^{-3}-10^{-2}$.

In addition to the capture of electrons at the interface of the I and N^+ layers, capture also takes place in the entire N^+ layer, where the density of As^+ atoms is equal to the density of acceptors. The fraction of the injection electron current that can transform in this region into hole current through the impurity band is $\eta=[1-\exp(-N_{\text{As}}^+L\sigma)]\cong0.3$, where $N_{\text{As}}^+=2\times10^{13}\ \text{cm}^{-3}$, and the thickness of the N^+ layer is $L=20\ \mu$m, i.e., the fraction can be large. The latter process can be limited by the rate of transition of holes from conducting states in the peak of the density of states of neutral donors — $g(\varepsilon)$ — into states of donors nearest to acceptors — $g_1(\varepsilon)$ — and second charged donors near the first complexes — $g_2(\varepsilon)$ (the notation corresponds to Ref. 9). We can therefore expect the hole current through the impurity band in the kink region to be from 10^{-2} to 1 times the injection current.

As long as the recombination current is small in comparison with the maximum possible hole current through the impurity band, the charge at the $I-N^+$ interface does not change, and a current that depends exponentially on the bias voltage is observed. However, as the injection current increases exponentially, the recombination current also increases exponentially. When it approaches the maximum possible current that can pass through the impurity band,

$$I=I_0\ \exp(-\varepsilon_a/kT)\ \exp(qlE/kT),$$

the surface charge begins to decrease. Here $I_0=q\mu N_aES$, μ is the effective hole conductivity through the impurity band of As in Si, estimated for the given doping level as $\mu_p=1\ \text{cm}^2/(\text{V}\cdot\text{s})$ (Ref. 10), and S is the area of the BIB structure. The reduction of the charge causes the voltage to be redistributed between the space-charge region W and the total thickness of the N^+ layer L and equalizes the electric field in the structure.

After the kink region the $I-V$ characteristic enters a second exponential interval. Here the current is again given by the above relation, but now with W replaced by the total thickness of the BIB structure $(W+L)$.

3. CURRENT-VOLTAGE CHARACTERISTIC FOR A POSITIVE BIAS

For a positive bias lower than the contact injection voltage[1] the field does not penetrate to the interface of the N^+ and N^{++} layers, and there is no injection current from the blockaded N^{++} contact. A range of biases extending from several tenths of a volt to several volts (depending on the configuration and parameters of the BIB structure) is observed. Here the current is less than 10^{-15} A (Fig. 5). When a certain bias lower than the contact injection voltage is attained, there emerges a current that depends exponentially on the bias voltage and the temperature. This current then begins to be limited, and the $I-V$ characteristic acquires a kink. The temperature dependence of the current in the interval where it flattens out corresponds to the dependence in an $N^{++}-N^+-N^{++}$ structure. Since the current in structures of this kind for $V<1$ V and $T<18$ K is governed by the hopping conductivity through the impurity band, it is natural to assume that the current in the vicinity of the kink will also be limited by the hopping conduction current through the impurity band. The carriers move through the impurity band to the interface of the N^+ and I layers, and then electrons transfer into the conduction band by one of the thermal-field-

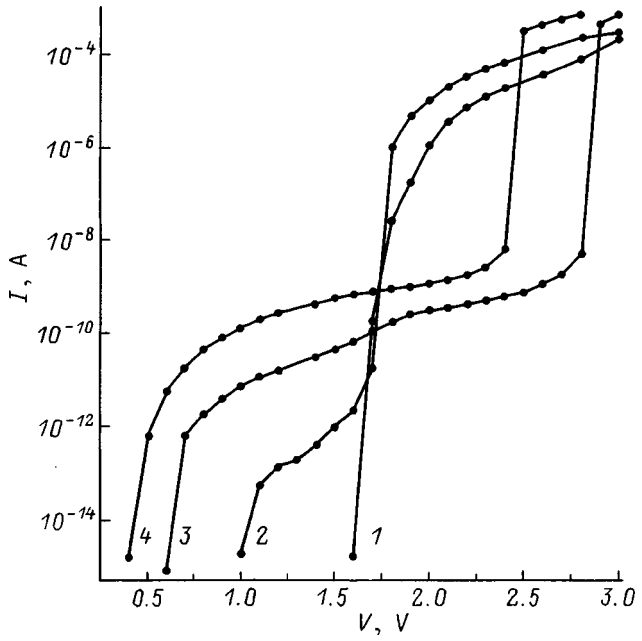

FIG. 5. Current-voltage characteristic of a positively biased BIB structure at temperatures: (*1*) $T=4.2$ K; (*2*) 5.6 K; (*3*) 7.4 K; (*4*) 11.6 K.

ionization mechanisms. The low accuracy of the $I-V$ characteristics in this zone makes it impossible to choose between the Poole–Frenkel mechanism and thermally facilitated electron tunneling from the donor into the conduction band, but the estimation of the observed quantities admits the proposed explanation.

The current in the hopping conduction region for a positive bias is lower than the corresponding negative-bias current. The difference between the two currents in the vicinity of the kink for opposite bias polarities in a BIB structure and the deviation of these currents from the corresponding current in an $N^{++}-N^{+}-N^{++}$ structure are attributable to the fact that the current through the impurity band flows in a uniform field $E=V/L$ in the ''resistor'' structure. In a BIB structure with either polarity the electric field in the N^{+} layer varies from $E=V/(W+L)$ to the minimum value of E. In a BIB structure, therefore, the current through the impurity, while preserving the temperature dependence of the hopping conductivity of the N^{+} layer, has a lower value, which is controlled by the minimum-field part of the N^{+} layer.

With a further increase in the bias, an exponential dependence of the current on the voltage is again observed. It has been suggested[11,12] that the $I-V$ characteristic in this field range is controlled by impact ionization of the impurity band of the N^{+} photoconductive layer. However, the parallel shift of the $I-V$ characteristics in this region, exhibiting an exceedingly strong temperature dependence of the current, cannot be explained in the impact ionization model either in regard to the reduction of the current as the temperature is lowered or in regard to the parallel shift of the $I-V$ characteristics toward diminishing the bias voltage. Our proposed explanation is as follows.

The increase in the current with the bias voltage in this region is induced by injection from a ''blockaded'' N^{++} contact and is controlled by the same mechanism as injection from an N^{++} contact into the I layer for a negative bias. Electrons entering the I layer are captured by As^{+} ions, causing the negative charge to increase and, naturally, inducing a parallel shift of the $I-V$ characteristics toward increasing the voltage. The limiting shift of the $I-V$ characteristics is determined by the density of acceptors and the thickness of the I layer and for the investigated samples is approximately 1 V, which agrees with the observed $I-V$ characteristics.

This explanation is confirmed in experiment when the temperature is further decreased to 5.6 K and 4.2 K. It is evident that when the temperature is lowered to 5.6 K or lower, the shift of the $I-V$ characteristics changes sign. This behavior can be logically explained if we allow for the fact that after all the As^{+} centers have been filled with electrons, a further decrease in the temperature and increase in the voltage must be accompanied by the onset of cumulative ionization of neutral donor centers in the I layer; i.e., a positive charge sets in. The change of sign of the charge is a trigger-type effect due to the positive feedback of the charge with the contact injection current, as is in fact observed in experiment. Switching from high to low voltages takes place as the $I-V$ characteristics vary during successive lowering of the temperature. If the measurements are initiated at the temperature $T=4.2$ K, then when the temperature is raised to $T=7.4$ K, switching to higher voltages takes place, and the injection voltage then decreases as the temperature increases. A similar parallel shift of the $I-V$ characteristics toward lower bias voltages has been observed previously[5] in measurements of the $I-V$ characteristics at 4.2 K on silicon resistors with an $N^{++}-N^{+}-N^{++}$ structure. In this paper, in contrast with our own investigations, a spin generator with a linear rise and decay of the voltage was used. This resulted in the formation of a hysteresis loop in the $I-V$ characteristics. We have used a step-voltage generator with an adjustable time of application of the bias to the sample and a constant manual bias. In both cases the voltage only increased from zero to the maximum value (dictated by the maximum current), so that only part of the hysteresis loop was recorded.

The variation of the charge on As atoms in the I layer due to the capture of electrons from the conduction band and the resulting modulation of the injection current also account for the high current-power sensitivity of highly biased BIB photodetectors.[13]

CONCLUSIONS

The reported investigation has made it possible for the first time to establish the role of all the elements of a BIB structure in the formation of its current-voltage characteristic.

1. The contact N^{++} regions together with the asymmetry of the structure form the main exponential dependence of the current on the bias voltage.

2. The kink regions on the $I-V$ characteristics for negative and positive bias voltage and the onset of current after the blocking region (for a positive bias) are associated with generation-recombination processes between the impurity band and the conduction band of the N^{+} photoconductive layer.

3. The behavior of the $I-V$ characteristics in the high-current range for a positive bias can be attributed to the accumulation of negative or positive charge in the blocking I layer of the BIB structure.

*)E-mail: esaev@thermo.isp.nsc.ru

[1] B. G. Martin, Solid-State Electron. **33**, 427 (1990).
[2] V. V. Bolotov, G. N. Kamaev, G. N. Feofanov, and V. M. Émekskuzyan, Fiz. Tekh. Poluprovodn. **24**, 1697 (1990) [Sov. Phys. Semicond. **24**, 1061 (1990)].
[3] V. M. Emekskuzyan, G. N. Kamaev, G. N. Feofanov, and V. V. Bolotov, Fiz. Tekh. Poluprovodn. **31**, 311 (1997) [Semiconductors **31**, 255 (1997)].
[4] D. G. Esaev, S. P. Sinitsa, and E. V. Chernyavskiĭ, Fiz. Tekh. Poluprovodn. **33**, 614 (1999) [Semiconductors **33**, 574 (1999)].
[5] E. Simoen, B. Dierickx, L. Deferm, C. Claeys, and G. Declerck, J. Appl. Phys. **68**, 4091 (1990).
[6] W. N. Shafarman and T. G. Castner, Phys. Rev. B **33**, 3570 (1986).
[7] Y. N. Yang, D. D. Coon, and P. F. Shepard, Appl. Phys. Lett. **45**, 752 (1984).
[8] N. Sclar, J. Appl. Phys. **55**, 2972 (1984).
[9] B. I. Shklovskiĭ and A. L. Éfros, *Electronic Properties of Doped Semiconductors*, Springer-Verlag, Berlin-New York (1984).
[10] M. D. Petroff, M. G. Stapelbroek, and W. A. Kleinhaus, Appl. Phys. Lett. **51**, 406 (1987).
[11] F. Szmulowicz and F. L. Madarsz, J. Appl. Phys. **62**, 2533 (1987).
[12] F. Szmulowicz, F. L. Madarsz, and J. Diller, J. Appl. Phys. **63**, 5583 (1988).
[13] S. B. Stetson, D. B. Reynolds, M. G. Stapelbroek, and R. L. Stermer, Proc. SPIE **686**, 48 (1986).

Translated by James S. Wood

THE PHYSICS OF SEMICONDUCTOR DEVICES

Gadolinium-doped InGaAsSb solid solutions on an InAs substrate for light-emitting diodes operating in the spectral interval $\lambda = 3-5\ \mu$m

N. V. Zotova, S. A. Karandashev, B. A. Matveev, M. A. Remennyĭ, N. M. Stus', and G. N. Talalakin

A. F. Ioffe Physicotechnical Institute, Russian Academy of Sciences, 194021 St. Petersburg, Russia
(Submitted December 2, 1998; accepted for publication December 8, 1998)
Fiz. Tekh. Poluprovodn. **33**, 1010–1013 (August 1999)

The influence of a gadolinium impurity on the electrical and luminescence characteristics of epitaxial structures made from narrow-gap *n*-InGaAsSb solid solutions grown by liquid-phase epitaxy on InAs substrates is investigated. The addition of gadolinium to the flux solution in the interval of concentrations $0 < X^l_{Gd} \leqslant 0.14$ at. % has the effect of lowering the density of electrons in the InGaAsSb layers from $(3-6)\times 10^{16}\,\mathrm{cm}^{-3}$ to $(7-8)\times 10^{15}\,\mathrm{cm}^{-3}$ and increasing the carrier mobility from $32\,000\,\mathrm{cm}^2/(\mathrm{V}\cdot\mathrm{s})$ to $61\,500\,\mathrm{cm}^2/(\mathrm{V}\cdot\mathrm{s})$ ($T = 77$ K). Also observed are a decrease in the half-width of the photoluminescence spectra from 25 meV to 12 meV and as much as a tenfold increase in their intensity ($T = 77$ K). The electroluminescence intensity of LEDs fabricated from gadolinium-doped *n*-InGaAsSb/*p*-InAs epitaxial structures ($T = 300$ K) increases approximately a factor of 2 relative to the undoped samples.
 [S1063-7826(99)02608-3]

1. INTRODUCTION

The capabilities of liquid-phase epitaxy (LPE) technology in application to the fabrication of efficient optoelectronic devices, including those based on III–V solid solutions, are often known to be limited by the presence of residual silicon, carbon, and oxygen impurities in the melt. Of special interest in this regard are papers in which possible avenues are offered for the purification of semiconductor materials doped with rare-earth elements Yb, Gd, Sc, Sm, etc.[1–7]

The objective of the present study is to prepare and investigate the electrical and luminescent properties of narrow-gap solid solutions n-$In_{1-x}Ga_xAs_{1-y}Sb_y$ and light-emitting diodes (LEDs) utilizing them, grown by LPE from the gadolinium-doped flux melt on the basis of these solid solutions and emitting in the spectral interval $\lambda = 3-5\ \mu$m ($T = 300$ K).

2. SAMPLES AND EXPERIMENTAL PROCEDURE

The samples were epitaxial layers of the solid solution n-$In_{1-x}Ga_xAs_{1-y}Sb_y$ of thickness $d = 10-20\ \mu$m grown by LPE at a temperature $T = 635-654\,^\circ$C from: a) the undoped liquid phase; b) from the Gd-doped solution in the range of concentrations $0 < X^l_{Gd} \leqslant 0.14$ at. %. The substrates were single-crystal *n*-InAs and *p*-InAs wafers of industrial purity with a carrier density $n,p(77\,\mathrm{K}) = (1-3)\times 10^{16}\,\mathrm{cm}^{-3}$, mobility $U_n(77\,\mathrm{K}) = (4-5)\times 10^4\,\mathrm{cm}^2/(\mathrm{V}\cdot\mathrm{s})$, and $U_p(77\,\mathrm{K}) = (0.7-1.0)\times 10^3\,\mathrm{cm}^2/(\mathrm{V}\cdot\mathrm{s})$, and a dislocation density of $5\times 10^3 - 1\times 10^4\,\mathrm{cm}^2$. According to an interpolative estimate using data on the composition of the layers, the lattice periods of the epitaxial films and the InAs substrate are well matched (see Table I). The *n*-InGaAsSb epitaxial layers had a sufficiently perfect morphology [planarity, high-quality surface and (110) cleavage plane] with a dislocation density of $10^4 - 10^5\,\mathrm{cm}^{-2}$, with no abrupt increase in the dislocation density observed up to $X^l_{Gd} = 0.14$ at. %.

The electrical parameters of the *n*-InGaAsSb epitaxial films grown on *p*-InAs substrates were measured on rectangular samples with six indium contacts by the standard dc procedure in a magnetic field of 4.9 kOe at $T = 77$ K. The carrier density (n_{77}) and mobility (U_{77}) were calculated from the results of measurements of the electrical conductivity (σ) and the Hall coefficient (R).

The photoluminescence spectra ($T = 77$ K) were measured in a reflection geometry (radiation excited and recorded from the surface of the *n*-InGaAsSb layer). The excitation source was an LPI-14 semiconductor laser ($\lambda = 0.8\ \mu$m, $P_{pls} \sim 50$ W).

3. EXPERIMENTAL RESULTS AND DISCUSSION

The electrical parameters of the investigated samples are shown in Table II. The measurement results show that the density of free carriers n_{77} decreases as the Gd content in the flux melt is increased in the interval $0 < X^l_{Gd} \leqslant 0.14$ at. % in *n*-InGaAsSb epitaxial layers. The most abrupt decrease, from $n_{77} = (3-6)\times 10^{16}\,\mathrm{cm}^{-3}$ to $n_{77} = 1\times 10^{16}\,\mathrm{cm}^{-3}$, is observed in the interval $0 < X^l_{Gd} \leqslant 0.005$ at. %. When the Gd content in the flux solution is further increased to $X^l_{Gd} = 0.14$ at. %, the $n_{77} = f(X^l_{Gd})$ curve in Fig. 1 reaches saturation, attaining values $n_{77} = (7-8)\times 10^{15}\,\mathrm{cm}^{-3}$. Concurrently, at $X^l_{Gd} \cong 0.005$ at. % the electron mobility (U_{77}) increases 1.5

TABLE I.

No.	X^l_{Gd}, at. %	Solid solution composition	$\overline{\alpha}$, Å	$\delta\overline{\alpha}$
H_{23}-2	0.0022	$In_{0.935}Ga_{0.065}As_{0.94}Sb_{0.06}$	6.057	-1.6×10^{-4}
HN-4	0.0030	$In_{0.951}Ga_{0.049}As_{0.946}Sb_{0.054}$	6.061	$+4.9\times10^{-4}$
H_{18}-2	0.022	$In_{0.93}Ga_{0.07}As_{0.939}Sb_{0.061}$	6.054	-4.9×10^{-4}

-1.8-fold relative to the mobility in the undoped samples, attaining a value $U_{77}=61\,500\,cm^2/(V\cdot s)$ at $n_{77}=1.3\times10^{16}\,cm^{-3}$ (Fig. 1)

Using the results of the Hall measurements and assuming that the carrier mobility is mainly determined by scattering at optical phonons and impurity ions, we have calculated the densities of impurity ions (N_1), donors (N_D), and acceptors (N_A) and the degree of compensation $K=N_A/N_D$.

An analysis of the results shows that the densities of impurity ions (both N_A and N_D) decrease significantly with increase in the Gd content in the flux solution, attaining minimum values $N_D=(1-2)\times10^{16}\,cm^{-3}$ and $N_A=(3-5)\times10^{15}\,cm^{-3}$ at $X^l_{Gd}=0.004-0.005$ at. % (Fig. 2). With a further increase in X^l_{Gd} to 0.14 at. %, the density N_D scarcely changes at all, while N_A and N_1 increase somewhat at $X^l_{Gd}=0.005-0.013$ at. % and reach saturation under doping conditions $X^l_{Gd}=0.01-0.14$ at. %.

The decrease in the donor density as the Gd content in the liquid phase is increased can be attributed to a decrease in the background impurity concentration of group-VI elements due to their interaction with the gadolinium and the formation of high-melting compounds.[3] On the other hand, the saturation of the $N_d=f(X^l_{Gd})$ curve implies that the InGaAsSb solid solution film contains another species of impurity at the level of $1.5\times10^{15}\,cm^{-3}$, which does not enter into interaction with the gadolinium.

This kind of dependence of the density N_A on the gadolinium content in the liquid phase attests to the complex nature of the interaction of Gd with uncontrollable impurities. In particular, the increase of N_A at $X^l_{Gd}=0.005$ at. % can be attributed to the acquisition of acceptor properties by the Gd itself (an effect similar to that observed in Ref. 4 for GaAs ⟨Sc⟩) or by compounds formed with Gd, or it can be identified with the decomposition of acceptor-binding complexes. The latter process could probably occur at X^l_{Gd}

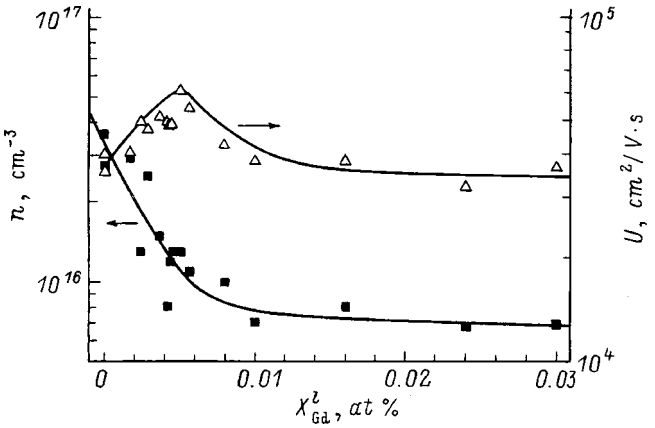

FIG. 1. Dependence of the carrier density n and mobility U on the gadolinium content X^l_{Gd} in the flux solution ($T=77$ K).

>0.005 at. %, when the above-postulated processes begin to prevail over the basic extractive influence of Gd.

We can infer from the foregoing analysis of the Hall measurement results that the total density of charge carriers effectively decreases as Gd is added up to the level $X^l_{Gd}=0.005$ at. %, owing to a decrease in the background densities of both donors and acceptors. A further reduction in the carrier density with the addition of Gd above 0.005% is due to an increase in the degree of impurity compensation $K=N_A/N_D$.

Figure 3 shows typical photoluminescence spectra of the samples. Their short-wavelength and long-wavelength parts and the half-width are similar to the characteristics of the spectrum of a homogeneous perfect crystal, for example, InAs. Only the photoluminescence edge line is observed for doped and undoped heterostructures. The position of the spectral maximum $h\nu_m$ as a function of the doping level varies in the interval $h\nu_m=397-405$ meV. At a density $n_{77}=8\times10^{15}\,cm^{-3}$ the position of the Fermi level in the *n*-InGaAsSb layer coincides with the bottom of the conduction band, so that $h\nu_m$ corresponds to band-to-band optical transitions. Consequently, the minimum value $h\nu_m=397$ meV obtained from the photoluminescence spectra, within error limits 1/2 kT, can be regarded as corresponding to the width of the band gap of the investigated solid solution $In_{0.935}Ga_{0.065}As_{0.94}Sb_{0.06}$. The increase of $h\nu_m$ to $h\nu_m$

TABLE II.

No.	X^l_{Gd}, at. %	$n\cdot10^{-16}$, cm^{-3}	U, $cm^2/(V\cdot s)$	$N_1\cdot10^{-16}$ cm^{-3}	$N_D\cdot10^{-16}$, cm^{-3}	$N_A\cdot10^{-16}$, cm^{-3}	K
H_7-1	0	4.5	32000	6.81	5.66	1.15	0.20
H_{22}-1	0	3.6	40000	4.85	4.23	0.62	0.15
H_7-2	0.0017	2.9	40400	4.54	3.72	0.82	0.22
H_4-3	0.0037	1.5	52000	2.45	1.98	0.47	0.23
H_7-3	0.0042	0.81	50000	2.14	1.48	0.66	0.45
H_{22}-3	0.0051	1.3	61500	2.0	1.65	0.35	0.21
H_{22}-4	0.0074	1.6	52000	2.62	2.11	0.51	0.24
H_{22}-5	0.0160	0.8	44000	2.70	1.8	0.9	0.50
H_{22}-6	0.030	0.69	38000	2.57	1.63	0.94	0.58
H_{21}-6	0.140	0.69	33000	3.0	1.85	1.15	0.62

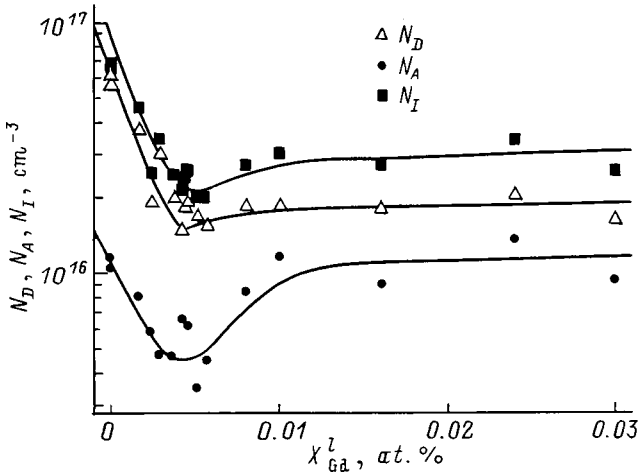

FIG. 2. Dependence of the densities N_D, N_A, and N_1 on the gadolinium content in the flux solution ($T=77$ K).

$=405$ meV is caused by a change in the position of the Fermi level in the conduction band due to an increase in the density of majority carriers in the investigated samples.

The measurements show that as the Gd content is increased, the photoluminescence intensity is observed to increase, attaining a maximum at a concentration $X^l_{Gd}=0.004-0.005$ at. %. In the corresponding series of samples I_0 is interpreted as the photoluminescence intensity of control samples grown under the same conditions but not doped with Gd. To illustrate the dependence $(I/I_0)=f(X^l_{Gd})$, Fig. 4 shows curves for samples grown on *n*-InAs substrates (*1*) and for samples of the standard H_{22} series grown on *p*-InAs substrates (*2*). It is evident from Fig. 4 that an increase in the concentration to $X^l_{Gd}=0.016$ at. % is accompanied by a decrease in the radiation intensity, probably due to elevation of the role of nonradiative channels in the recombination processes, owing to an increase in the acceptor density (N_A) and the degree of compensation ($K=N_A/N_D$).

As the gadolinium content is increased, the half-width of the photoluminescence spectra $\Delta h\nu_{0.5}$ decreases by a factor

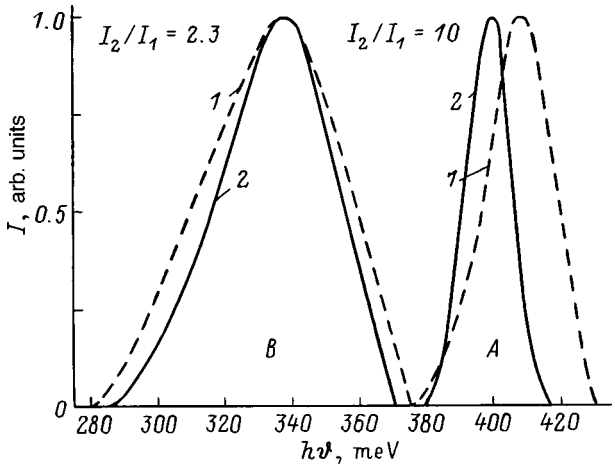

FIG. 3. *A*) Photoluminescence spectra ($T=77$ K) of *n*-InGaAsSb: (*1*) $X^l_{Gd}=0$; (*2*) $X^l_{Gd}=0.005$ at. %. *B*) Electroluminescence spectra ($T=300$ K) of *n*-InGaAsSb/*p*-InAs: (*1*) $X^l_{Gd}=0$; (*2*) $X^l_{Gd}=0.005$ at. %.

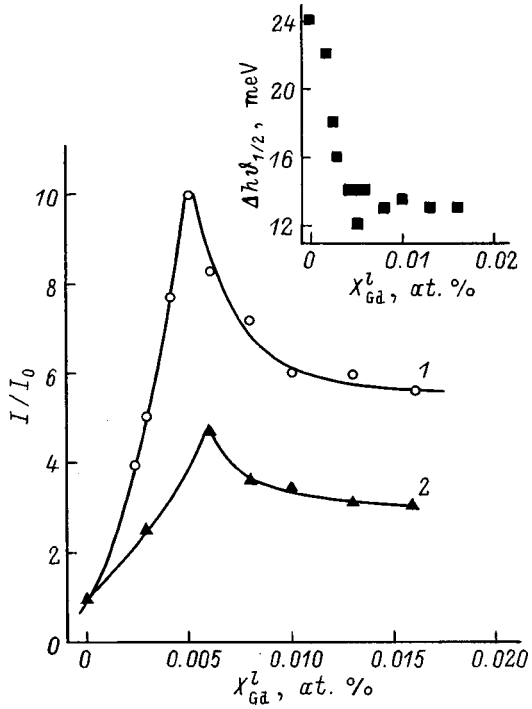

FIG. 4. Dependence of the photoluminescence intensity I/I_0 and the half-width of the photoluminescence spectra $\Delta h\nu_{0.5}$ (inset) on the gadolinium content in the flux solution ($T=77$ K). Substrates: (*1*) *n*-InAs; (*2*) *p*-InAs.

of 1.3–1.8 (see the inset in Fig. 4), saturating at a concentration $X^l_{Gd}\cong 0.005$ at. % and thus repeating the behavior of the carrier density in Gd-doped samples (Fig. 1). It is important to note that the photoluminescence intensity is observed to decrease by one half in *n*-InGaAsSb/*p*-InAs heterostructures relative to control samples grown on *n*-InAs substrates (Fig. 4, curve *1*). This fact suggests that the epitaxial layers could be contaminated with acceptors contained in the *p*-InAs substrates.

Consequently, the results of an analysis of the spectral characteristics of the investigated samples made from the solid solution $In_{0.935}Gd_{0.065}As_{0.94}Sb_{0.06}$ confirm the conclusions as to the purifying effect, based on galvanomagnetic measurements.

In the course of the study we have also measured the electroluminescence characteristics of model LEDs ($\lambda=3.7\ \mu$m at $T=300$ K) fabricated from the Gd-doped material. Selected *n*-InGaAsSb/InAs samples in the form of diode structures with a hetero-p'–n junction situated at the layer-substrate interface were used for this purpose, along with structures incorporating a homo-p–n junction in a layer of *n*-InGaAsSb/*p*-InGaAsSb/*p*-InAs solid solution. The electroluminescence spectra are shown in Fig. 3. Table III gives the spectral characteristics of LEDs fabricated from Gd-doped and undoped material. It is evident from the table that the radiation intensity decreases by approximately one half for devices based on Gd-doped structures.

CONCLUSIONS

We have established that the doping of a flux melt with gadolinium to concentrations $X^l_{Gd}=0.004-0.005$ at. % low-

TABLE III.

No.	X^l_{Gd}, at. %	$h\nu$(300 K), meV	$\Delta h\nu_{0.5}$, meV	λ(300 K), μm	I/I_0	Structure
H_{22}-1	0	333	39	3.72	1	*n*-InGaAsSb / *p*-InAs
H_{22}-2	0.0029	329	39	3.77	2.3	*n*-InGaAsSb / *p*-InAs
H_{21}-3	0.022	332	51	3.73	2.1	*n*-InGaAsSb / *p*-InAs
SD-1	0	336	41	3.69	1	*n*−*p*-InGaAsSb/*p*-InAs
SD-2	0.005	339	39	3.66	1.8	*n*−*p*-InGaAsSb/*p*-InAs

ers the density of electrons in the layers to $n_{77}\approx 10^{16}\,\mathrm{cm}^{-3}$ and increases the mobility to $U\approx 6\times 10^4\,\mathrm{cm}^2/(\mathrm{V}\cdot\mathrm{s})$. The concentrations of all other impurities decrease in this case as a result of decrease in the densities of both donors and acceptors. When the Gd content in the liquid phase is increased from 0.005 at. % to 0.010 at. %, the electron density decreases further to $n_{77}=(7-8)\times 10^{15}\,\mathrm{cm}^{-3}$ by virtue of an increase in the acceptor density and the overcompensation of impurities, while the carrier mobility decreases to $U=(3-4)\times 10^4\,\mathrm{cm}^2/(\mathrm{V}\cdot\mathrm{s})$. Beginning with $X^l_{Gd}=0.01$ at. %, the dependences of n, N_I, N_D, and N_A on X^l_{Gd} reach saturation with scarcely any change up to $X^l_{Gd}=0.14$ at. %.

With Gd doping in the interval of concentrations $X^l_{Gd}=0.004-0.005$ at. % a 4 to 10-fold increase in the photoluminescence intensity and a 1.3 to 1.8-fold decrease in the half-width of the spectra are observed relative to the undoped samples. A further increase in the Gd content from 0.005 at. % to 0.14 at. % causes the photoluminescence intensity to decrease, whereas the half-width of the spectra remains constant, assuming a value $\Delta h\nu_{0.5}\approx 12$ meV.

A 1.8 to 2.3-fold increase in the electroluminescence intensity of the model LEDs based on gadolinium-doped *n*-InGaAsSb/*p*-InAs heterodiode structures and *n*-InGaAsSb/*p*-InGaAsSb/*p*-InAs structures with emission wavelengths $\lambda\sim 3.7\,\mu$m ($T=300$ K) is observed relative to emission sources utilizing the undoped material. This result bears witness to the promising potential of the Gd-doped material for the fabrication of efficient optoelectronic devices operating in the spectral interval $3-5\,\mu$m.

*)E-mail: bmat@iropt3.ioffe.rssi.ru; Fax: +7(812) 247 43 24

[1] K. A. Gatsoev, A. T. Gorelenok, S. A. Karpenko, V. V. Mamutin, and R. P. Seĭsyan, Fiz. Tekh. Poluprovodn. **17**, 2148 (1983) [Sov. Phys. Semicond. **17**, 1373 (1983)].
[2] N. T. Bagraev, L. S. Vlasenko, K. A. Gatsoev, A. T. Gorelenok, A. V. Kamanin, V. V. Mamutin, B. V. Pushnyĭl, V. K. Tibilov, Yu. P. Tolparov, and A. E. Shubin, Fiz. Tekh. Poluprovodn. **18**, 83 (1984) [Sov. Phys. Semicond. **18**, 49 (1984)].
[3] A. T. Gorelenok, V. G. Gruzdov, R. Kumar, V. V. Mamutin, T. A. Polyanskaya, I. G. Savel'ev, and Yu. V. Shmarev, Fiz. Tekh. Poluprovodn. **33**, 35 (1999) [Sov. Phys. Semicond. **33**, 21 (1999)].
[4] T. I. Voronina, T. S. Lagunova, B. E. Samorukov, and N. A. Strugov, Fiz. Tekh. Poluprovodn. **22**, 147 (1988) [Sov. Phys. Semicond. **22**, 91 (1988)].
[5] V. V. Vorob'eva, M. V. Egorova, L. M. Kreshchuk, S. V. Novikov, and I. G. Savel'ev, Fiz. Tekh. Poluprovodn. **23**, 1699 (1989) [Sov. Phys. Semicond. **23**, 1051 (1989)].
[6] A. N. Baranov, T. I. Voronina, T. S. Lagunova, M. A. Sipovskaya, V. V. Sherstnev, and Yu. P. Yakovlev, Fiz. Tekh. Poluprovodn. **27**, 421 (1993) [Semiconductors **27**, 236 (1993)].
[7] A. T. Gorelenok and M. V. Shpakov, Fiz. Tekh. Poluprovodn. **30**, 488 (1996) [Semiconductors **30**, 269 (1996)].

Translated by James S. Wood

Spatial beam oscillations in stripe lasers utilizing InAsSb/InAsSbP heterojunctions

A. P. Danilova, T. N. Danilova, A. N. Imenkov, N. M. Kolchanova, M. V. Stepanov, V. V. Sherstnev, and Yu. P. Yakovlev*)

A. F. Ioffe Physicotechnical Institute, Russian Academy of Sciences, 194021 St. Petersburg, Russia
(Submitted February 8, 1999; accepted for publication February 15, 1999)
Fiz. Tekh. Poluprovodn. **33**, 1014–1019 (August 1999)

Anomalously narrow, single-lobe and double-lobe beam directivity patterns in the plane of the *p-n* junction have been observed in lasers constructed from InAsSb/InAsSbP heterojunctions emitting at a wavelength of approximately 3.3 μm. Theoretical near-field and far-field radiation distributions for the laser emission of two beams oscillating across the stripe are obtained on the basis of new concepts of the lasing processes. The single-lobe directivity pattern is obtained for the emission of in-phase beams, and the double lobe is obtained for antiphase beams. Correspondence of the theory with experiment is established. © *1999 American Institute of Physics.* [S1063-7826(99)02708-8]

The spatial distribution of laser radiation in heterostructures and its variation are essential to our understanding of the physical processes and modulation effects.

1. INTRODUCTION

The spatial distribution of radiation in stripe heterolasers has usually been formed by virtue of an abrupt decrease in the refractive index at the edges of the stripe.[1] It has been described theoretically by wave functions corresponding to rectangular potential wells. Eliseev and Bogatov have shown that the dependence of the refractive index on the radiation intensity leads to self-focusing of the laser beam due to optical self-confinement of the beam.[2,3] We have observed the self-focusing of radiation in lasers utilizing InAsSb/InAsSbP heterojunctions, accompanied by a variation of the radiation wavelength.[4] We have shown that raising the injection flux density toward the edges of the stripe in such lasers makes the radiation wavelength dependent on the current, owing to the formation of a waveguide whose dielectric permittivity is a quadratic function of the coordinate.[5] Such a dependence of the permittivity on the coordinate in the waveguide of narrow-gap lasers requires a new approach to laser beam-forming and an investigation of the near-field and far-field radiation distributions.

In this paper we have posed the problem of constructing lasers with various distributions of the light beams along the width of the stripe, analyzing the directivity patterns, and ascertaining the behavior of the beams in lasers with different stripe widths.

2. OBJECTS OF INVESTIGATION

The investigated P-$InAs_{0.48}Sb_{0.17}P_{0.35}$/$n$-$InAs_{0.95}Sb_{0.05}$/$N$-$InAs_{0.48}Sb_{0.17}P_{0.35}$ laser heterojunctions (Fig. 1) were grown on *p*-InAs substrates of thickness $h=300\ \mu$m with a hole density of $5-8\times10^{18}\,\mathrm{cm}^{-3}$. The thickness of the narrow-gap active zone of the laser was $1-3\ \mu$m, and the thickness of the wide-gap emitters was $\sim3\ \mu$m. The active zone was left undoped, and the density of electrons in it was $\sim10^{16}\,\mathrm{cm}^{-3}$. The *N*-InAsSbP was doped with Sn to an electron density $n\sim2-5\times10^{18}\,\mathrm{cm}^{-3}$, and the *P*-InAsSbP–Zn layer was doped to a hole density $p\sim1\times10^{18}\mathrm{cm}^{-3}$. The substrate was polished to a thickness of 100 μm. Mesa stripes having widths of 10 μm and 18 μm were formed on the resulting structures by photolithography. Fabry-Perot cavities of length $200-400\ \mu$m were fabricated by the cleavage technique. The width of the laser structure in the substrate zone was 500 μm.

Judging from our previous work,[6,7] in the lasers with a stripe width of 10 μm lasing was expected to take place predominantly in a longitudinal spatial mode, and in those with a stripe width of 18 μm lasing was assumed to take place in the first transverse mode. Owing to the large difference in the widths of the substrate and the stripe, an elevated injection density was obtained at the edges of the stripe in comparison with its middle.[5]

The investigations were carried out at liquid-nitrogen temperature with the laser driven by rectangular current pulses of the ''meander'' type having an off-duty factor of 2 and a repetition rate of 80 Hz. We investigated the spectra and directivity patterns of the radiation in the current interval from one to three times the threshold level.

3. EXPERIMENTAL RESULTS

The directivity pattern of the lasers with a stripe width of 10 μm (Fig. 2) with the current I slightly above the threshold I_{th} ($I\approx1.05\cdot I_{th}$) has the characteristic profile for a cosine distribution of the electromagnetic wave amplitude at the exit mirror of the cavity. The width of the pattern at half the intensity (half-width) is $\Delta\Theta_{0.5}=22°$. As the current is increased, $\Delta\Theta_{0.5}$ initially decreases to $\sim17°$ at $I\approx2-2.5I_{th}$ and then again increases slightly to $18-19°$ at $I\approx3I_{th}$. We have remarked previously[6] that the minimum half-width of the directivity pattern corresponds to a uniform distribution of the electric field of the light wave on the cavity mirror.

The radiation pattern of lasers with a stripe width of 18 μm (Fig. 3) for the same above-threshold current levels

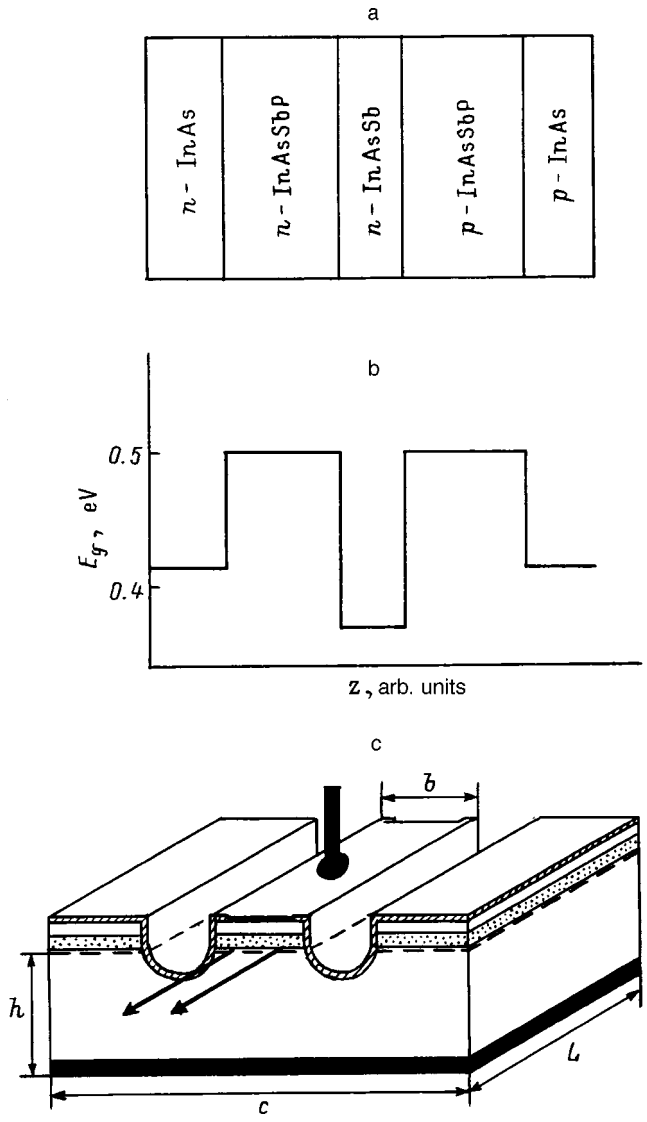

FIG. 1. Structure of the investigated diode laser: (a) arrangement of the epitaxial layers; (b) layered profile of the width of the band gap; (c) schematic view of the structure of the mesa stripe diode laser.

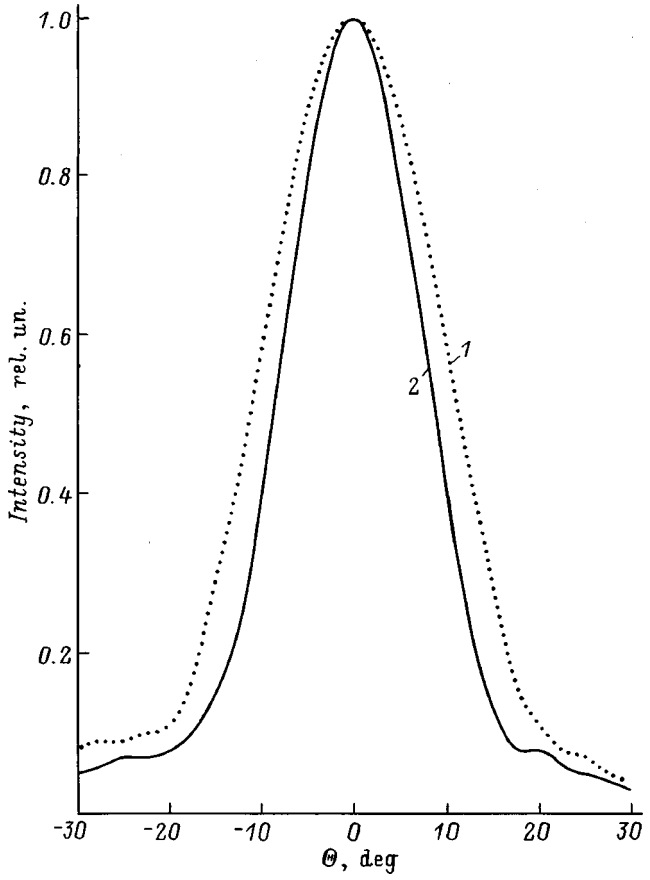

FIG. 2. Directivity patterns of the V12192 laser No. 1 in the plane of the *p-n* junction for various excesses of the current I above the threshold I_{th}: (*1*) 1.05; (*2*) 2.5.

has two maxima separated by an angular distance $\sim 11°$, whereas the distance between the maxima for predominance of the first transverse spatial mode should be 20°. The depth of the minimum between the peaks decreases as the current is increased, and the angular positions of the maxima remain almost constant.

Consequently, in lasers with a stripe width of 18 μm the directivity pattern comprises two sharp peaks separated by almost half the angular distance that should occur in the presence of the first transverse mode.

4. DISCUSSION OF THE EXPERIMENTAL RESULTS

For lasers with a stripe width of 10 μm the correspondence of the half-width of the directivity pattern to a uniform distribution of the electric field amplitude of the light wave at the cavity mirror does not mean that such a distribution actually occurs. It cannot occur, because the wave amplitude at the edge of the stripe must be essentially equal to zero by virtue of the large difference between the refractive indices of the crystal and air. Moreover, the wave amplitude cannot change discontinuously with the coordinate. Such a half-width could also be given by parallel light beams with a spacing ~ 6 μm if the beams were stable. They appear spatially well defined if they oscillate from one edge of the stripe to the other, changing places. We have shown previously[5] that oscillations of one beam in a laser are possible if the dielectric permittivity decreases according to a square law in the direction from the middle of the stripe toward its edges. The linearity of the differential equation describing the oscillating beam allows it to be summed with another beam having a different amplitude and a different phase.

It should be noted that in Ref. 5 a linear equation has been derived from the nonlinear equation under a simplifying assumption. In real lasers, therefore, it is possible to have limitations on the number of spectral and spatial modes associated with nonlinearity.

In lasers with a stripe width of 18 μm the angular spacing of the directivity maxima, equal to 11°, could be obtained in the presence of opposing beams with a spacing of 17 μm if this positioning of the beams were stable. However, this is only a hypothetical limit. We therefore encounter the problem of oscillations even in opposing beams.

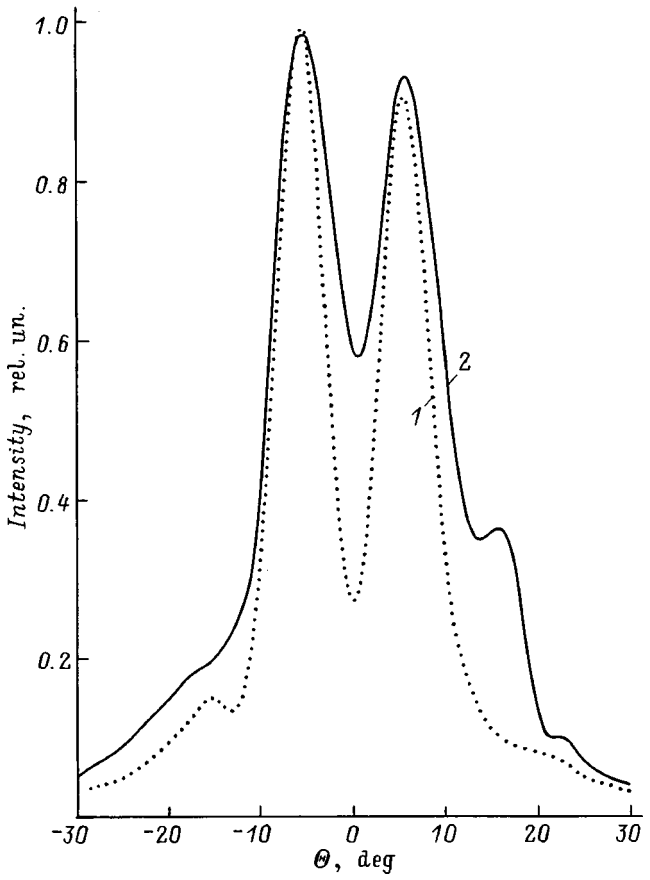

FIG. 3. Directivity patterns of the V1109 laser No. 3 in the plane of the *p-n* junction for various excesses of the current I above the threshold I_{th}: (*1*) 1.14; (*2*) 1.8.

5. DIRECTIVITY PATTERN OF A STRIPE HETEROLASER GENERATING TWO SPATIALLY OSCILLATING BEAMS

We confine our discussion to the case in which the resistance of the substrate is higher than the differential resistance of the *p-n* junction in the lasing regime and is lower than in the prelasing regime, and we assume that the flow of charge carriers along the width of the stripe is slight.

We express the time-dependent amplitude distribution of the light wave at the cavity mirror, in accordance with Refs. 5 and 8, by the equation

$$u(\xi,\omega_c t)=\exp\left[-\frac{1}{2}\xi^2+\xi\xi_0\cos\omega_c t-\frac{1}{2}\xi_0^2\cos^2\omega_c t - i\left(\frac{1}{2}\omega_c t+\xi\xi_0\sin\omega_c t-\frac{1}{4}\xi_0^2\sin 2\omega_c t\right)\right], \quad (1)$$

where we have introduced the following notation: $\xi=\alpha y$ is the dimensionless coordinate, y is the coordinate in the direction of the width of the cavity, measured from its middle, α is a coefficient characterizing the dependence of the permittivity on y:

$$\alpha=2\left(\frac{\pi}{\lambda b}\right)^{1/2}\left(k\frac{i_0}{i_0+1}0\right)^{1/4}, \quad (2)$$

λ is the wavelength of the radiation in vacuum, b is the width of the cavity, ξ_0 is the relative deviation of the centroid of the beam from the origin, k is a coefficient that depends on the ratio of the width c to the thickness h of the substrate and on the distribution of the radiation intensity along the width of the stripe,

$$k=\frac{c}{2h}-1, \quad (3)$$

for a uniform distribution of the radiation intensity along the width of the stripe, $i_0=(J-J_{\text{th}})/(J_{\text{th}}-J_i)$ is the relative current density of the pump in the middle of the stripe, J is the current density in the middle of the stripe, J_i and J_{th} are the current densities at the inversion and lasing thresholds, respectively, t is the time, ω_c is the angular frequency of the beam oscillations,

$$\omega_c=\frac{c_0\alpha^2\lambda}{\pi}, \quad (4)$$

and c_0 is the speed of light.

The intensity distribution of the radiation at the mirror for an oscillating beam depends on the time:

$$|u|^2\approx\exp\{-(\xi-\xi_0\cos\omega_c t)^2\}. \quad (5)$$

To find the average distribution, it is necessary to integrate over time. If two beams are used with opposite signs of y_0, then for in-phase beams we obtain

$$|u^2|\approx\gamma\exp(-\xi^2-\xi_0^2\cos^2\omega_c t)[\sinh^2\varphi+\cos^2\psi], \quad (6)$$

and for out-of-phase beams we have

$$|u|^2\approx\gamma\exp(-\xi^2-\xi_0^2\cos^2\omega_c t)[\sinh^2\varphi+\sin^2\psi], \quad (7)$$

where γ is the ratio of the beam amplitudes, and

$$\varphi=\xi\xi_0\cos\omega_c t-\frac{1}{2}\ln\gamma, \quad \psi=\xi\xi_0\sin\omega_c t. \quad (8)$$

Figure 4 shows the time-averaged distributions of the radiation intensity (the values of the parameters $\xi_0=1$ and $\alpha=0.2\times10^4\ \text{cm}^{-1}$ are taken from Ref. 5). It is evident from the figure that two in-phase beams (curve *4*) provide greater localization of radiation in the middle of the stripe than a single beam (curve *1*).

Out-of-phase beams (curves *2* and *3*) form an intensity minimum in the middle of the stripe, its depth decreasing as the difference in the beam amplitudes diminishes. The angular frequency of the beam oscillations ω_c, calculated from Eq. (4), is 1.3×10^{13} Hz. The nature of the distribution of the radiation intensity over the cavity mirror directly influences the value of the parameter k, the probability of the existence of one or more beams, the phase difference, and the amplitude ratio as functions of the stripe width and the perfection of its boundaries.

The frequency tuning interval of the laser is also bound by these conditions.

We calculate the directivity pattern approximately, disregarding the finiteness of the stripe dimensions, from the equation

$$|D_u|^2\sim(1+\cos\Theta)^2\left|\int_{-\infty}^{\infty}U(y,\omega_c t)\exp\left(i\frac{2\pi y}{\lambda}\sin\Theta\right)dy\right|^2, \quad (9)$$

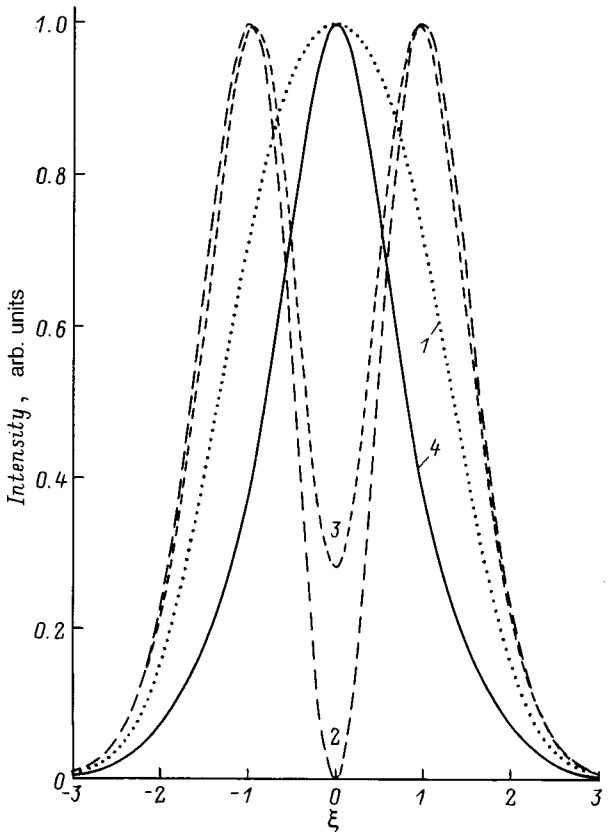

FIG. 4. Calculated intensity distribution of a laser beam along the width of the stripe for various combinations of spatially oscillating beams with $\xi_0=1$, $\alpha=0.2\times10^4\ \mathrm{cm}^{-1}$, and $\lambda=3.3\ \mu$m: (*1*) single beam; (*2*) two equal-amplitude, out-of-phase beams; (*3*) two out-of-phase beams with a twofold difference in amplitudes; (*4*) two equal-amplitude, in-phase beams.

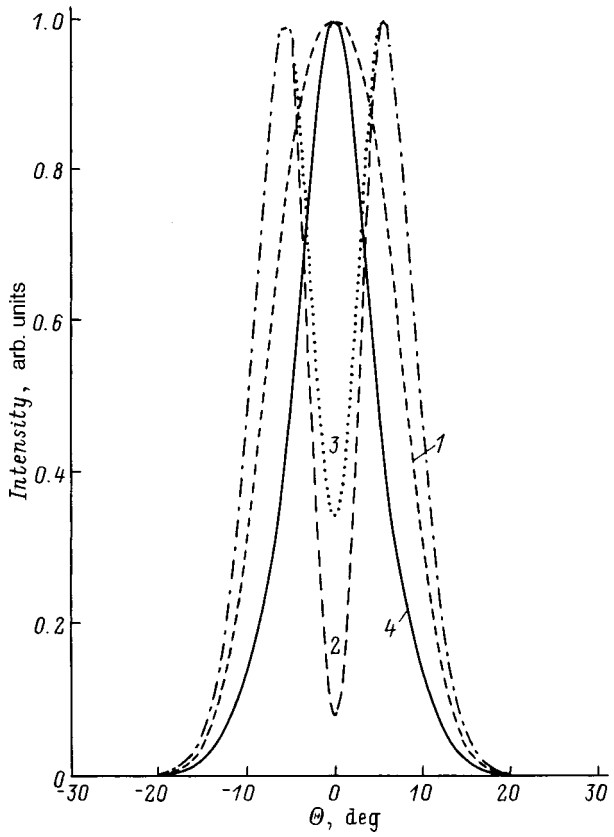

FIG. 5. Calculated directivity pattern of a laser beam in the plane of the *p-n* junction for the same combinations of spatially oscillating beams and values of the parameters as in Fig. 4.

where Θ is the angle between the projection of the direction of observation onto the plane of the active zone and the normal to the cavity mirror in this plane.

For one beam we obtain

$$|D_u|^2\sim(1+\cos\Theta)^2\exp\left\{-\left(\frac{2\pi\sin\Theta}{\lambda\alpha}-\xi_0\sin\omega_c t\right)^2\right\}. \tag{10}$$

In the presence of two in-phase beams with opposite signs of y_0 we have

$$|D_u|^2\sim(1+\cos\Theta)^2\gamma\exp\left\{-\left(\frac{2\pi\sin\Theta}{\lambda\alpha}\right)^2-\xi_0^2\sin^2\omega_c t\right\}\times[\sinh^2\varphi+\cos^2\psi], \tag{11}$$

and for two out-of-phase beams

$$|D_u|^2\sim(1+\cos\Theta)^2\gamma\exp\left\{-\left(\frac{2\pi\sin\Theta}{\lambda\alpha}\right)^2-\xi_0^2\sin^2\omega_c t\right\}\times[\sinh^2\varphi+\sin^2\psi]. \tag{12}$$

Here φ and ψ are given by the equations

$$\varphi=\frac{2\pi\sin\Theta}{\lambda\alpha}\xi_0\sin\omega_c t-\frac{1}{2}\ln\gamma,$$

$$\psi=\frac{2\pi\sin\Theta}{\lambda\alpha}\xi_0\cos\omega_c t+\frac{1}{4}\sin 2\omega_c t. \tag{13}$$

To obtain the averaged beam directivity pattern, it is necessary to integrate over time.

The result of the summation of $|D_u|^2$ as $\omega_c t$ varies from 0 to 2π is shown in Fig. 4 for the same values of the parameters $\xi_0=1$ and $\alpha=0.2\times10^4\ \mathrm{cm}^{-1}$ as in Ref. 5. It is evident from the figure that a single beam (curve *1*) and two in-phase beams (curve *4*) provide a single lobe in the directivity pattern. In the presence of two beams the half-width of the lobe is 1.7 times smaller than for a single beam. Out-of-phase beams (curves *2* and *3*) form a double-lobe directivity pattern with a minimum at $\Theta=0$. The depth of the trough decreases as the difference between the beam amplitudes increases.

6. COMPARISON OF THEORY AND EXPERIMENTAL DATA

The single-lobe experimental directivity pattern of a laser with a stripe width of 10 μm and currents 2–2.5 times the threshold level is comparable in half-width and profile with the pattern calculated for two in-phase beams. This experimental curve is found to be close in profile and half-width to the theoretical curve for two in-phase beams with $\alpha=0.2\times10^4\ \mathrm{cm}^{-1}$, $\gamma=0.3$, and $\xi_0=1$. The deviation of γ from unity indicates a difference in the amplitudes of the oscillating beams. The second beam is conducive not only to narrowing of the directivity pattern (Fig. 5), but also to nar-

rowing of the intensity distribution of the beam at the cavity mirror (Fig. 4). The latter consideration make this lasing regime the most probable in narrow cavities.

The double-lobe experimental directivity pattern of a laser with a stripe width of 18 μm is comparable in profile and angular spacing of the maxima to the directivity pattern for two out-of-phase beams with $\alpha = 0.2 \times 10^4$ cm^{-1} and $\xi_0 = 1$. The depth of the minimum at the midpoint of the experimental curve corresponds to a two- to threefold difference in the amplitudes of two oscillating out-of-phase beams. The ratio γ is equal to 0.5 for $I = 1.14 I_{\text{th}}$ and to 0.35 for $I = 1.8 I_{\text{th}}$. The second beam improves the uniformity with which the cavity is filled by the generated beam (Fig. 4). This lasing regime should be the most probable in wide-stripe lasers. It is important to note that for a stripe width greater than 20 μm in lasers emitting at a wavelength of 3.3 μm spatial mode orders higher than the zeroth and first will occur; we have taken them into account. The maximum relative deviation of the beam from the origin ξ_0 will increase and the theoretical curves will change in this case. Consequently, lasers having a stripe width greater than 20 μm require special consideration.

We can therefore attribute the anomalously narrow experimental single-lobe and double-lobe beam directivity patterns to the generation of several spatially oscillating beams.

7. CONCLUSIONS

Anomalously narrow beam directivity patterns in the plane of the *p-n* junction with one and two lobes have been observed in lasers based on InAsSb/InAsSbP heterojunctions emitting in the spectral range of 3.3 μm. To account for the anomalies, we have taken into account the increase in the density of nonequilibrium charge carriers and the corresponding decrease in the dielectric permittivity from the middle of the laser stripe toward its edges due to the increase in the pump density and decrease of the laser intensity in this direction. From the linearization of the Helmholtz equation for the radiant flux we have postulated that several beams separated in space and in phase can be generated, and that they oscillate along the width of the stripe. We have obtained theoretical near-field and far-field radiation distributions. Single-lobe directivity patterns are obtained in the generation of in-phase beams. Lasing of this kind is more probable for a narrow stripe, because it tends to confine the beam within the limits of the stripe. Double-lobe directivity patterns are obtained in the generation of out-of-phase beams, which is more probable in wide-stripe lasers, because it promotes uniform filling of the stripe by the beam. The beam amplitudes differ. The theoretical directivity patterns are consistent with the experimental in their general features.

This work has been supported in part by INCO-Copernicus Contract No. 1C15-CT97-0802 (DG12-CDPF) and in part by a grant from the Ministry of Science of the Russian Federation Program ''Optics and Laser Physics.''

*)E-mail: yak@ioptl.ioffe.rssi.ru

[1] O. V. Bogdankevich, S. A. Darznyak, and P. G. Eliseev, in *Semiconductor Lasers* [in Russian], Nauka, Moscow (1976), p. 139.
[2] A. P. Bogatov and P. G. Eliseev, Kvantovaya Élektron. **12**, 465 (1985) [Sov. J. Quantum Electron. **15**, 308 (1985)].
[3] P. G. Eliseev and A. P. Bogatov, Tr. Fiz. Inst. Akad. Nauk SSSR **166**, 15 (1986).
[4] T. N. Danilova, O. I. Evseenko, A. N. Imenkov, N. M. Kolchanova, M. V. Stepanov, V. V. Sherstnev, and Yu. P. Yakovlev, Pis'ma Zh. Tekh. Fiz. **22**(16), 7 (1996) [Tech. Phys. Lett. **22**, 645 (1996)].
[5] T. N. Danilova, A. P. Danilova, A. N. Imenkov, N. M. Kolchanova, M. V. Stepanov, V. V. Sherstnev, and Yu. P. Yakovlev, in *Proceedings of the Conference on Physics at the Threshold of the Twenty-First Century* [in Russian], St. Petersburg (1998).
[6] T. N. Danilova, A. P. Danilova, O. G. Ershov, A. N. Imenkov, V. V. Sherstnev, and Yu. P. Yakovlev, Fiz. Tekh. Poluprovodn. **32**, 373 (1998) [Semiconductors **32**, 339 (1998)].
[7] A. N. Baranov, T. N. Danilova, O. G. Ershov, A. N. Imenkov, V. V. Sherstnev, and Yu. P. Yakovlev, Pis'ma Zh. Tekh. Fiz. **19**(17), 30 (1993) [Tech. Phys. Lett. **19**, 543 (1993)].
[8] L. I. Schiff, *Quantum Mechanics*, McGraw-Hill, New York (1955).

Translated by James S. Wood .

Lasing at a wavelength close to 1.3 μm in InAs quantum-dot structures

A. R. Kovsh, A. E. Zhukov, N. A. Maleev, S. S. Mikhrin, V. M. Ustinov,
A. F. Tsatsul'nikov, M. V. Maksimov, B. V. Volovik, D. A. Bedarev, Yu. M. Shernyakov,
E. Yu. Kondrat'eva, N. N. Ledentsov, P. S. Kop'ev, and Zh. I. Alferov

A. F. Ioffe Physicotechnical Institute, Russian Academy of Sciences, 194021 St. Petersburg, Russia

D. Bimberg

Institut für Festkörperphysik, Technische Universität Berlin, D- 10623 Berlin, Germany
(Submitted March 23, 1999; accepted for publication March 25, 1999)
Fiz. Tekh. Poluprovodn. **33**, 1020–1023 (August 1999)

The feasibility of lasing at a wavelength close to 1.3 μm is demonstrated in InAs quantum-dot structures placed in an external InGaAs/GaAs quantum well. It is shown that the required wavelength can be attained with the proper choice of thickness of the InAs layer deposited to form an array of three-dimensional islands and with a proper choice of mole fraction of InAs in the InGaAs quantum well. Since the gain attained in the ground state is insufficient, lasing is implemented through excited states in the temperature interval from 85 K to 300 K in a structure based on a single layer of quantum dots. The maximum attainable gain in the laser structure can be raised by using three rows of quantum dots, and this configuration, in turn, leads to low-threshold (70 A/cm^2) lasing through the ground state at a wavelength of 1.26 μm at room temperature. © *1999 American Institute of Physics.* [S1063-7826(99)02808-2]

The fabrication of laser diodes on gallium arsenide substrates with an emission wavelength of 1.3 μm for applications in fiber-optic communication lines poses a timely problem in view of the quest for an alternative to the indium phosphide lasers used currently. The main drawbacks of the latter are low temperature stability[1] and complications in the construction of Bragg mirrors for vertically emitting lasers[2] due to the small discontinuity of the band gaps and an insufficient difference between the refractive indices of the InGaAsP compounds used in the devices.

When strained InGaAs/GaAs quantum wells are used, the emission wavelength is limited to ~1.1 μm by requirements imposed on the width and composition of the quantum wells by pseudomorphic growth limits.[3] To broaden the emission spectral range of gallium arsenide structures, two approaches are currently under intensive development. The first is based on the application of InGaAsN quantum wells with a low nitrogen content[4]; the second approach relies on the concept of In(Ga)As island growth on a GaAs surface, which permits localized, dislocation-free objects to be fabricated from a narrow-gap material with lateral dimensions of the order of 100 Å (Refs. 5 and 6). The lowest threshold current densities obtained using InGaAsN/GaAs quantum wells and InGaAs/GaAs quantum dots (QDs) are equal to 675 A/cm^2 and 270 A/cm^2, respectively (see Refs. 7 and 8). In the latter case the InGaAs/GaAs QDs were formed by depositing eleven monolayers (ML) of InGaAs by molecular-beam epitaxy (MBE) with the alternating deposition of indium and gallium atoms and arsenic molecules.

We have previously proposed an alternative method for the production of QD laser structures, the basic idea consisting in the placement of InAs QDs formed in the standard MBE regime in an external InGaAs quantum well.[9] This method can be used to increase the emission wavelength up to 1.35 μm at room temperature.[10] Here we report the achievement of lasing at a wavelength of 1.26 μm with a threshold current density of 70 A/cm^2 in a structure whose active region is formed by the indicated method.

The investigated structures were grown by MBE in a Riber 32P MBE machine with a solid-state As source. The active zone of the test samples intended for photoluminescence measurements as well as the laser structures comprised an array of InAs QDs overgrown by an InGaAs quantum well having a specific composition and thickness. The temperature of deposition of the QDs and the quantum well and the adjoining gallium arsenide of thickness 5 nm was equal to 485 °C. The rest of the structure was grown at a temperature of 600 °C. Standard MBE arsenic enrichment conditions were established during growth. The transition from two-dimensional to three-dimensional growth during the deposition of InAs was observed directly in the course of growth through the onset of a line pattern in the diffraction of fast electrons in reflection. The laser diodes were constructed in a geometry with four cleaved faces to minimize radiation output losses. Contacts were formed by the spray deposition and alloying (at 450 °C) of AuGe/Ni/Au and AuZn/Ni/Au metal layers to an n^+-GaAs substrate and to a p^+-GaAs contact layer, respectively. Electroluminescence investigations were carried out with a pulsed pump (frequency 5 kHz, pulse duration 1 μs). A germanium photodiode was used to record the signal.

The structural and optical properties of such structures have been studied in detail.[11] The emission wavelength depends both on the size of the QDs themselves and on the composition of the InGaAs layer adjoining the QDs. The size of the QD, in turn, increases as the quantity of deposited

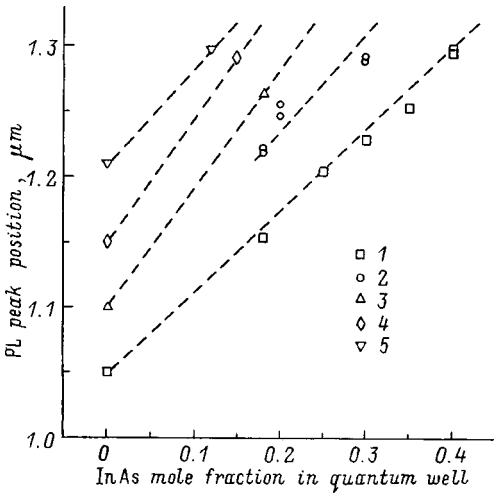

FIG. 1. Position of the photoluminescence peak of structures utilizing InAs quantum dots in an external InGaAs quantum well on GaAs substrates at room temperature versus the mole fraction of InAs in the InGaAs quantum well for various thicknesses of the InAs layer used to form the QDs: (*1*) $Q_{\mathrm{InAs}}=2.0$ ML; (*2*) 2.2 ML; (*3*) 2.4 ML; (*4*) 2.7 ML; (*5*) 3.0 ML. The thickness of the InGaAs quantum well varies in the interval from 5 nm to 8 nm.

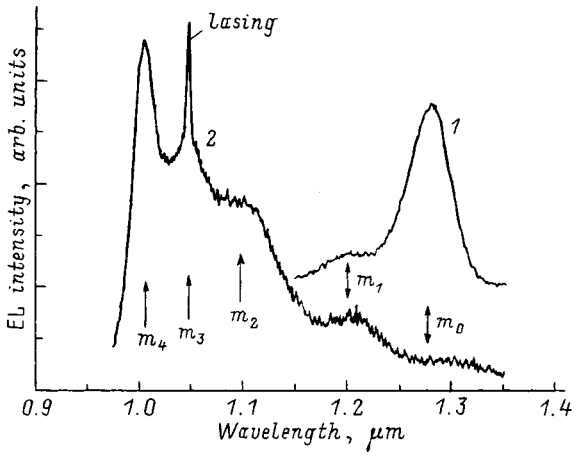

FIG. 3. Room-temperature electroluminescence spectra of a structure with an active zone based on a single layer of InAs/InGaAs/GaAs QDs. At a low pump level $J=4.5$ A/cm^2 (*1*) the spectrum is dominated by a spontaneous emission peak through the QD ground state (m_0), and at a high excitation level $J=2.1$ kA/cm^2 (*2*) one ground state and four excited states are singled out (their positions are indicated by arrows). Lasing with a threshold current density $J_{\mathrm{th}}\simeq 2$ kA/cm^2 occurs in the third excited state.

InAs (Q_{InAs}) spent in their formation is increased. Figure 1 shows the position of the photoluminescence maximum of structures with InAs/InGaAs/GaAs QDs for various values of Q_{InAs} and for various compositions of the InGaAs quantum well. We have observed that the position of the photoluminescence maximum remains essentially unchanged as the thickness of the quantum well is varied from 5 nm to 8 nm. Clearly, either ''large'' QDs overgrown by an $In_xGa_{1-x}As$ layer with a small In content (e.g., $Q_{\mathrm{InAs}}=3$ ML, $x\simeq 0.2$) or the opposite, ''small'' QDs with a large In content in $In_xGa_{1-x}As$ ($Q_{\mathrm{InAs}}=2$ ML, $x\simeq 0.35-0.4$), can be used to attain an emission wavelength of 1.3 μm.

For the electroluminescence investigation an InGaAs/AlGaAs laser structure was grown in the standard double heterostructure geometry characterized by separate confinement of the carriers and the light wave by a graded-index waveguide. The dopants used to obtain *n*-type and *p*-type conductivities were Si and Be, respectively. A schematic diagram of the structure is shown in Fig. 2. The active zone was

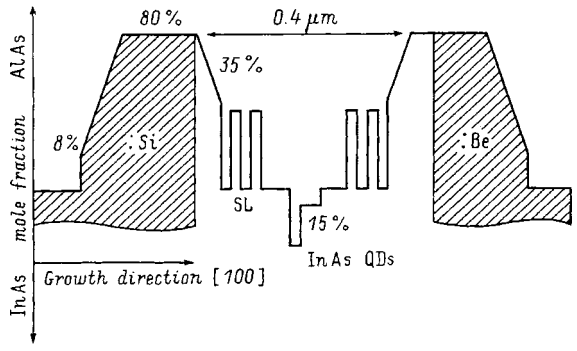

FIG. 2. Schematic diagram of a laser structure with an active zone based on InAs/InGaAs/GaAs quantum dots (QDs). The vertical axis represents the percentage content AlAs(InAs), and SL denotes the superlattice.

an array of InAs QDs ($Q_{\mathrm{InAs}}=2.7$ ML) overgrown with an $In_{0.15}Ga_{0.85}As$ layer of thickness 8 nm. Figure 3 shows the electroluminescence spectra of the structure at 300 K for various current densities. At a low pump level the spectrum is dominated by a spontaneous emission peak in the vicinity of 1.3 μm, which is associated with recombination through the ground state of the QDs (m_0). As the pump current is increased, it rapidly saturates, and the intensities of the peaks of the excited states begin to increase considerably. At a pump current density ($J=2.1$ kA/cm^2 four excited states are clearly distinguished in the spectrum (m_1, m_2, m_3, m_4), and a stimulated emission peak is observed through the state m_3. The threshold current density (J_{th}) has a value of 2 kA/cm^2.

The curves in Fig. 4a represent the temperature dependence of the positions of the spontaneous emission peaks for various states, and the points correspond to the lasing wavelength. Figure 4b shows the dependence of J_{th} on the observation temperature T. The graphs exhibit a jump-like behavior. Lasing takes place through state m_1 at temperatures from 85 K to 150 K, then beginning at $T=195$ K and up to $T=240$ K lasing through state m_2 is observed, accompanied by an abrupt increase in J_{th}, and when the temperature is raised further, lasing passes through state m_3.

To explain the physical nature of this behavior, we refer to Fig. 5, which shows schematically the dependence of the gain on the current density of the pump for QD lasers. Each state is characterized by a definite transmission current ($J_{\mathrm{tr}}^{m_i}$) and saturated gain ($g_{m_i}^{\mathrm{sat}}$). These quantities are directly proportional to the number of QDs *per se*, the degree of degeneracy of the state, and the oscillator strength. Previously we have observed that for structures with a QD array, owing to the fourfold degeneracy of the first excited state (m_1) with respect to the ground state (m_0), the transmission current, exactly like the saturated gain, is four times higher for the excited state.[12] Higher-level states have an even higher order of degeneracy and, hence, are characterized by still higher

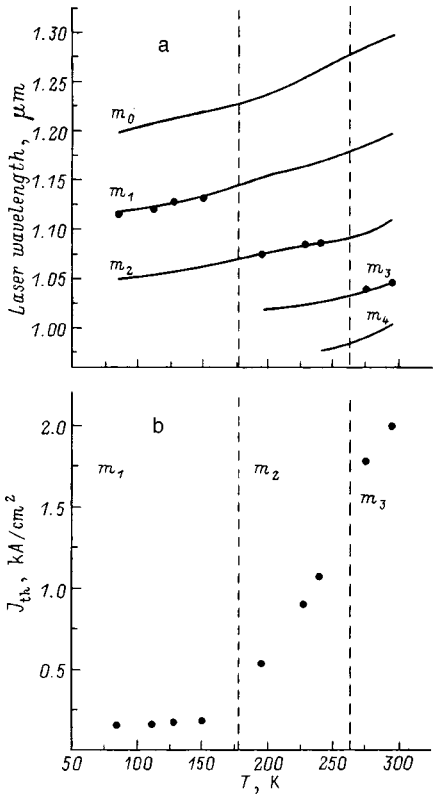

FIG. 4. Temperature dependence of the emission wavelength (a) and the threshold current density J_{th} (b) of a structure with an active zone based on a single layer of InAs/InGaAs/GaAs QDs. The solid curves (a) represent the electroluminescence from various states, and the points (a, b) represent lasing. The vertical dashed lines separate the temperature intervals of lasing through definite states.

transmission current and saturated gain. The condition for the onset of lasing stipulates that the attained gain (g_{QD}) must be equal to the sum of the internal losses (α_{in}) and the radiation output losses (α_{out}). If the maximum attainable gain ($g^{sat}_{m_i}$) for state (m_i) is below the threshold gain (G_{th} $=\alpha_{in}+\alpha_{out}$), lasing does not take place through this state. Since $g^{sat}_{m_{i+1}} > g^{sat}_{m_i}$, lasing can begin at state m_{i+1}, accompanied by a jump of the emission wavelength and an abrupt increase in J_{th} due to the increase in the transmission current (see the inset in Fig. 5). Consequently, the jump-like behavior of the emission wavelength and the threshold current density for the investigated laser structure can be attributed to an increase in the threshold gain with the temperature. As a matter of fact, with an increase in the observation temperature, owing to thermal ''dispersing'' of the carriers among higher states, a higher pump current must be applied in order to maintain the same gain, and this operation, in turn, causes α_{in} to increase as a result of the increase in free-carrier losses, so that the threshold gain increases accordingly (loss multiplication regime).

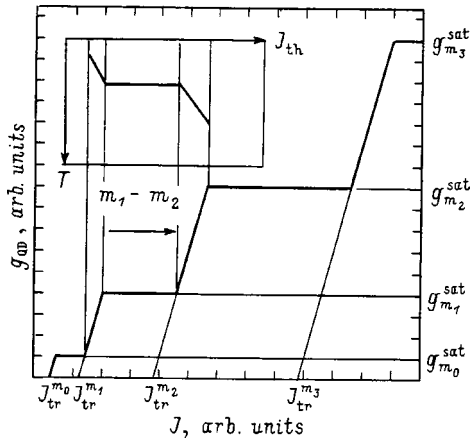

FIG. 5. Schematic diagram showing the dependence of the gain (g_{QD}) on the pump current density (J) in QD structures, assuming the presence of one ground state and four excited states (m_0, m_1, m_2, m_3, m_4). Inset: temperature dependence of the threshold current density (J_{th}) (schematic representation). The transition of lasing from state m_i to m_{i+1} is accompanied by an abrupt increase in J_{th}.

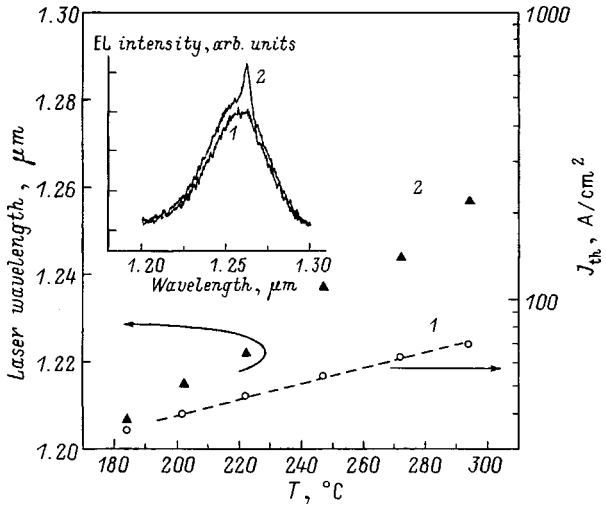

FIG. 6. Temperature dependence of J_{th} (*1*) and the emission wavelength (*2*) in a structure with an active zone based on three rows of InAs/InGaAs QDs separated by GaAs layers of thickness 30 nm. Inset: room-temperature electroluminescence spectra of the structure below ($J=65$ A/cm^2) (*1*) and above ($J=75$ A/cm^2) (*2*) the lasing threshold. The threshold current density at $T=293$ K is $J_{th}=70$ A/cm^2, the emission wavelength is 1.26 μm, and the characteristic temperature is $T_0=160$ K.

Thus, inadequate saturated gain on the basis of the state of the QDs ($g^{sat}_{m_0}$) makes it impossible to achieve lasing close to 1.3 μm at room temperature. The gain $g^{sat}_{m_0}$ can be increased by increasing the number of QDs themselves, and this, in turn, can be achieved by using several QD planes separated by GaAs layers.

In the second laser structure investigated here the active zone comprised three rows of InAs QDs overgrown by an $In_{0.15}Ga_{0.85}As$ layer. The thickness of the GaAs spacer layers was 30 nm, and the thickness of the $In_{0.15}Ga_{0.85}As$ layers was 5 nm. The variations of J_{th} and the laser emission wavelength for such a structure are shown in Fig. 6. The inset to the figure shows the room-temperature electroluminescence spectra recorded near the lasing threshold. In the given situation lasing takes place through the ground state of the QDs over the entire investigated temperature range. At room temperature the wavelength is 1.26 μm, and the threshold current density is $J_{th}=70$ A/cm^2. The characteristic temperature is $T_0=160$ K. We note that J_{th} is close to the all-time record

for QD lasers,[13] which shows that the proposed concept for the implementation of lasing at a wavelength of 1.3 μm has a promising future.

To summarize, an array of InAs quantum dots situated in an external InGaAs quantum well can be used to achieve lasing at a wavelength of 1.3 μm in structures grown on GaAs substrates. Since the gain attained in the ground state is insufficient, lasing in a structure with an active zone based on a single QD array takes place through excited states at a wavelength of 1.05 μm. Increasing the maximum gain in the ground state by using three rows of QDs leads to lasing at a wavelength of 1.26 μm with a threshold current density of 70 A/cm^2. Such a low threshold current density suggests the possibility of further optimizing the active zone to achieve lasing at a wavelength of 1.3 μm.

This work has received support from a program of the International Association for the Promotion of Cooperation with Scientists from the Independent States of the Former Soviet Union (INTAS Grant 96-0467).

[1] S. Seki, H. Oohasi, H. Sugiura, T. Hirono, and K. Yokoyama, J. Appl. Phys. **79**, 2192 (1996).
[2] Y. Qian, Z. H. Zhu, Y. H. Lo, D. L. Huffaker, D. G. Deppe, H. Q. Hou, B. E. Hammons, W. Lin, and Y. K. Tu, Appl. Phys. Lett. **71**, 25 (1997).
[3] J. W. Matthews and A. E. Blakeslee, J. Cryst. Growth **27**, 118 (1974).
[4] M. Kondow, K. Uomi, A. Niwa, T. Kitatani, S. Watahiki, and Y. Yazawa, Jpn. J. Appl. Phys. **35**, 1273 (1996).
[5] K. Mukai, N. Ohtsuka, M. Sugawara, and S. Yamazaki, Jpn. J. Appl. Phys. **33**, L1710 (1994).
[6] A. Yu. Egorov, A. E. Zhukov, P. S. Kop'ev, N. N. Ledentsov, M. V. Maksimov, V. M. Ustinov, A. F. Tsatsul'nikov, Zh. I. Alferov, D. L. Fedorov, and D. Bimberg, Fiz. Tekh. Poluprovodn. **30**, 1345 (1996) [Semiconductors **30**, 707 (1996)].
[7] K. Nakahara, M. Kondow, T. Kitatani, M. C. Larson, and K. Uomi, IEEE Photonics Technol. Lett. **10**, 487 (1998).
[8] D. L. Huffaker, G. Park, Z. Zou, O. B. Shchekin, and D. G. Deppe, Appl. Phys. Lett. **73**, 2564 (1998).
[9] A. E. Zhukov, A. R. Kovsh, A. Yu. Egorov, N. A. Maleev, V. M. Ustinov, B. V. Volovik, M. V. Maksimov, A. F. Tsatsul'nikov, N. N. Ledentsov, Yu. M. Shernyakov, A. V. Lunev, Yu. G. Musikhin, N. A. Bert, P. S. Kop'ev, and Zh. I. Alferov, Fiz. Tekh. Poluprovodn. **33**, 180 (1999) [Semiconductors **33**, 153 (1999)].
[10] K. Nishi, H. Saito, S. Sugou, and J.-S. Lee, Appl. Phys. Lett. **74**, 1111 (1999).
[11] B. V. Volovik, A. F. Tsatsul'nikov, D. A. Bedarev, A. Yu. Egorov, A. E. Zhukov, A. R. Kovsh, N. N. Ledentsov, M. V. Maksimov, N. A. Maleev, Yu. G. Musikhin, A. A. Suvorova, V. M. Ustinov, P. S. Kop'ev, Zh. I. Alferov, D. Bimberg, and P. Werner, Fiz. Tekh. Poluprovodn. **33**, 990 (1999) [Semiconductors **33**, 901 (1999)].
[12] A. R. Kovsh, A. E. Zhukov, A. Yu. Egorov, V. M. Ustinov, N. N. Ledentsov, M. V. Maksimov, A. F. Tsatsul'nikov, and P. S. Kop'ev, Fiz. Tekh. Poluprovodn. **33**, 215 (1999) [Semiconductors **33**, 184 (1999)].
[13] V. M. Ustinov, A. Yu. Egorov, A. R. Kovsh, A. E. Zhukov, M. V. Maksimov, A. F. Tsatsul'nikov, N. Yu. Gordeev, S. V. Zaitsev, Yu. M. Shernyakov, N. A. Bert, P. S. Kop'ev, Zh. I. Alferov, N. N. Ledentsov, J. Böhrer, D. Bimberg, A. O. Kosogov, P. Werner, and U. Gösele, J. Electron Spectrosc. Relat. Phenom. **175/176**, 689 (1997).

Translated by James S. Wood